DISSERTATION

Titel der Dissertation

Supernova-Produced Radionuclides in Deep-Sea Sediments Measured with AMS

verfasst von

Mag. Jenny Feige, Bakk.

angestrebter akademischer Grad

Doktorin der Naturwissenschaften (Dr. rer. nat.)

Wien, 2014

Abstract

Massive stars, with masses larger than eight times the mass of the sun, explode as so-called supernovae. In their ejected envelopes, the signatures of stellar nucleosynthesis processes are transported: long-lived radionuclides, such as ^{26}Al, ^{53}Mn, and ^{60}Fe, which were created during the life-time and in the late phases of such massive stars as well as during their explosion. If a supernova occurs close to the Solar System, it is possible that these radionuclides are incorporated into terrestrial archives.

In this work, approximately 100 samples from four deep-sea sediment cores were analyzed for traces from recent supernovae. A measurement of a ferromanganese crust from the Pacific Ocean by Knie et al. (2004) indicated, that such a nearby supernova could have happened 2-3 Myr ago. The deep-sea sediments used for my work have a time resolution of a factor 1000 higher than the crust. Therefore, it should be possible to constrain the time period, in which the supernova traces arrived on Earth.

With accelerator mass spectrometry (AMS), a very sensitive method to detect extremely low concentrations of long-lived radionuclides, the supernova-produced isotopes ^{26}Al, ^{53}Mn, und ^{60}Fe were measured. Three different AMS facilities were available: the VERA accelerator in Vienna (Austria), the DREAMS facility in Dresden-Rossendorf (Germany), and the HIAF facility in Canberra, (Australia).

For confirmation of the existing paleomagnetic chronology of the deep-sea sediments, ^{10}Be was measured as well. This long-lived radionuclide is produced in the Earth's atmosphere. Difficulties of measuring the low concentrations of stable ^{9}Be with ICP-MS became apparent. These concentrations are required to obtain an age dating. Because of the extraordinarily good depth profile for the deep-sea sediments from the measured ^{26}Al data, this radionuclide was instead used for age determinations. Like ^{10}Be, ^{26}Al is dominantly produced in the Earth's atmosphere. Isotope ratios of ^{26}Al/^{10}Be were calculated in this work, which are in agreement with the value expected from atmospheric production.

Additionally to atmospheric production, a possible in-situ production generates ^{26}Al within the sediments itself. The AMS results show, that supernova-produced ^{26}Al may indeed be hidden behind the large terrestrial background.

Further, interplanetary ^{53}Mn is transported to Earth by extraterrestrial dust particles. For ^{53}Mn test measurements were performed in the course of this work. The chromium content (with the isobar ^{53}Cr) in the deep-sea sediment samples, interfering with the AMS measurement of ^{53}Mn, could not be suppressed sufficiently during chemical sample preparation.

The AMS measurements of ^{60}Fe, which is not produced in-situ on Earth, successfully showed an enhanced concentration of this radionuclide in a time range of 1.7-3.2 Myr. The large extension of this signal over ~1.5 Myr was surprising. From a single supernova, a much narrower signal would be expected. The measured data was used to calculate limits on theoretical nucleosynthesis models from measured ^{60}Fe/^{26}Al ratios. Furthermore, the hypothesis of a constant ^{60}Fe input via interplanetary dust particles in deep-sea sediments could not be confirmed.

Zusammenfassung

Sehr massereiche Sterne von mehr als acht Sonnenmassen explodieren also sogenannte Supernova. In der bei einem solchen Ereignis ausgeschleuderten Sternenhülle befinden sich die Signaturen der vorangegangenen Nukleosynthese: langlebige Radionuklide wie ^{26}Al, ^{53}Mn und ^{60}Fe, die in solch massereichen Sternen sowie während deren Explosionen erzeugt wurden. Findet eine Supernova in der Nähe des Sonnensystems statt, ist es möglich, dass diese Radionuklide in terrestrische Archive eingebaut werden.

Im Rahmen dieser Arbeit wurden etwa 100 Proben aus vier Tiefseesedimentbohrkernen auf Spuren jüngster Supernova-Ereignisse untersucht. Eine Messung des Supernova-Radionuklids ^{60}Fe in einer pazifischen Tiefseemangankruste von Knie et al. (2004) zeigte, dass solch eine nahe Supernova vor 2-3 Myr Jahren stattgefunden haben könnte. Die Tiefseesedimente aus dem Indischen Ozean, die in dieser Arbeit vermessen wurden, haben eine 1000 mal höhere Zeitauflösung. Daher sollten es möglich sein, den Zeitraum, in dem die Supernova-Spuren auf die Erde eingetragen wurden, einzuschränken.

Mit Beschleunigermassenspektrometrie (AMS), einer sehr sensitiven Methode zur Detektion extrem niedriger Konzentrationen von langlebigen Radionukliden, wurden die Supernova-produzierten Isotope ^{26}Al, ^{53}Mn, und ^{60}Fe gemessen. Drei verschiedene AMS Anlagen standen dafür zur Verfügung: der VERA-Beschleuniger in Wien (Österreich), die DREAMS-Anlage in Dresden-Rossendorf (Deutschland) und die HIAF-Anlage in Canberra (Australien).

Zur Verfizierung einer existierenden paleomagnetischen Chronologie in den Tiefseesedimenten wurde zusätzlich das atmosphärisch-produzierte Radionuklid ^{10}Be gemessen. Hier zeigten sich Schwierigkeiten bei der Bestimmung der Konzentrationen von stabilem ^{9}Be mit ICP-MS. Diese Konzentrationen sind notwendig, um eine Altersdatierung durchführen zu können. Da jedoch ein ausserordentlich gutes Tiefenprofil der Sedimentbohrkerne aus den ^{26}Al-Messdaten gewonnen werden konnte, wurde dieses zur Altersbestimmung verwendet. Wie ^{10}Be geht ^{26}Al zu einem grossen Anteil ebenfalls aus atmosphärischer Produktion hervor. ^{26}Al/^{10}Be Isotopenverhältnisse in den Sedimenten wurden im Rahmen dieser Arbeit bestimmt, die mit dem erwarteten Wert aus der Atmosphäre übereinstimmen.

Zu dem schon genannten atmosphärischen Eintrag von ^{26}Al kommt eine mögliche in-situ Produktion in den Sedimenten selbst. Die AMS-Messergebnisse zeigten, dass ein mögliches Supernova-Signal in ^{26}Al tatsächlich durch die verhältnismässig hohe terrestrische Produktion überdeckt sein könnte.

^{53}Mn wird durch extraterrestrische Staubpartikel auf die Erde eingetragen. Testmessungen wurden an ^{53}Mn im Rahmen dieser Arbeit durchgeführt. Es stellte sich heraus, dass während der chemischen Probenpräparation der Chrom-Gehalt (mit dem stabilen Isobar ^{53}Cr) der Tiefseesedimente nicht genügend unterdrückt wurde, um eine AMS-Messung durchführen zu können.

Die AMS-Messungen von ^{60}Fe, welches keine terrestrischen Quellen hat, zeigten eine erhöhte Konzentration dieses Radionuklids zwischen 1.7 und 3.2 Myr. Überraschend war die zeitliche Ausdehnung dieses Signals von ~1.5 Myr, da man sich von einer einzelnen Supernova ein viel schmäleres Signal erwartet hatte. Die Daten wurden dazu genutzt, um Rückschlüsse auf Nukleosyntheseprozesse in massereichen Sternen über gemessene Verhältnisse von ^{60}Fe/^{26}Al zu ziehen. Die Hypothese, dass das ^{60}Fe Signal durch eingetragene interplanetare Staubpartikel hervorgerufen worden sein könnte, konnte nicht bestätigt werden.

Contents

1 Introduction

Massive stars (approximately eight times more massive than the sun, $\gtrsim 8$ M$_\odot$) end their lives in highly energetic events called supernova (SN) explosions. Hereby, a fraction of the chemical elements that were produced during the lifetime of the star, in its late phases as well as during its explosion, are ejected into the surrounding interstellar medium (ISM). If a SN occurs close to the Solar System, some of the ejected material might be deposited in terrestrial archives (Figure 1.1, left).

This work concentrates on detecting trace amounts of so-called long-lived radionuclides of SN-origin in deep-sea sediments. In this study, astrophysics is combined with other research fields, such as geology, chemistry, and experimental physics. Due to the interdisciplinary character of this thesis technical terms of different areas are used. For this reason a glossary summarizing the most important terms and abbreviations is given at the end of this work.

1.1 Motivation

SNe are violent events, that release large amounts of freshly synthesized material with kinetic energies of 10^{50}-10^{52} erg into the surrounding space. Such explosions happen with a rate of (1.9±1.1) SNe per century within the Milky Way (Diehl et al., 2006). The ejected matter mixes with the elements already present in the ISM, leading to an enrichment of heavy elements over time. The time evolution of elemental abundances is called chemical evolution of the galaxy.

Long-lived radionuclides, such as ^{26}Al, ^{53}Mn, and ^{60}Fe are produced in massive stars. Their half lifes are in the order of Myr (million years). ^{26}Al is formed in the cores of main sequence stars, during carbon shell-burning in later phases of the star, and in a SN explosion. ^{53}Mn is a nucleosynthesis product of explosive burning processes of a massive star. ^{60}Fe is an slow neutron capture (s-process) nuclide created in the late burning phases and during the stellar explosion (e.g. Limongi and Chieffi (2006)). Stellar winds and SN explosions distribute these radioactive isotopes within the ISM.

Unstable nuclei can be detected via their radioactive decay signatures. ^{26}Al β^+-decays to the stable isotope ^{26}Mg. The transition occurs into an excited state of the ^{26}Mg nucleus, where a γ-ray of 1.8 MeV is emitted. The detection of this γ-ray with space missions such as *COMPTEL* and *INTEGRAL* proves that nucleosynthesis is ongoing in our galaxy (e.g. Diehl et al. (2008)). Similar studies were performed on ^{60}Fe: It β^--decays to ^{60}Co, which subsequently β^--decays with a half-life of 5.3 years to the stable isotope ^{60}Ni.

Here, γ-rays of 1.17 and 1.33 MeV are emitted due to deexcitation of the ^{60}Ni nucleus. Measuring these γ-rays gives also insight to enrichment processes in the ISM of ^{60}Fe from SNe, and its intensity can be compared with measurements on ^{26}Al. A γ-ray flux ratio of $(^{60}$Fe$/^{26}$Al$)_{\gamma,obs}$ = (0.15±0.05) was inferred from the observational data (Wang, 2008). Stellar evolution models of AGB- and SAGB-stars suggest, that such stars usually produce isotope ratios of ^{60}Fe$/^{26}$Al $\geq$ 1, whereas SN models yield lower values than 1 Lugaro and Karakas (2008); Doherty et al. (2014).

In addition to so-called "live" signatures, originating directly from the presence of the radionuclide, extinct radioactivity can be detected in form of decay products of the intrinsic radionuclide. The presumably first particles that condensed to solids in the early Solar System are found as inclusions in meteorites (e.g. Ott and Hoppe (2007)). By studying such Calcium-Aluminium inclusions (CAIs) and chondrules, concentrations of ^{26}Mg, ^{53}Cr, and ^{60}Ni (the decay products of ^{26}Al, ^{53}Mn, and ^{60}Fe) can be quantified. This method extends the use of these long-lived isotopes as radioactive clocks to the beginning of the Solar System, although their half-lifes are much shorter than the age of the Solar System. An excess of ^{26}Mg and ^{60}Ni was interpreted as signature of SN activity at the time of formation of the Solar System. A close SN to the Solar System was suggested to have triggered its formation (e.g. Huss et al. (2009); Dauphas et al. (2008)). However, more recent findings show, that the excess disappears, when considering ^{26}Al and ^{60}Fe also being ejected by stellar winds from Wolf-Rayet stars into star forming regions (Young, 2014). If a single SN had deposited radioactive nuclides into the early Solar System, an overproduction of isotopes such as ^{53}Mn, ^{107}Pd, and ^{182}Hf would be expected (Lugaro et al., 2014), which was not indicated in the meteoritic analyses. The abundance of elements in the early Solar System - as inferred from meteorite studies - represents that of a polluted presolar cloud with late injections of stellar winds and SN explosions.

An indication for much more recent SN activity in the vicinity of the Solar System is the existence of the Local Bubble. This superbubble was presumably generated by a sequence of SN explosions. These push the ambient ISM outwards from the explosion site, leaving a cavity inside and a shell of ejected SN material mixed with swept-up ISM at its boundaries. The LB age is estimated to 14 Myr and a contribution of 14-20 SNe to the formation of this large structure in the local ISM is assumed, the last one occurring a few 100 kyr ago (Fuchs et al., 2006) (1 kyr = 1000 years). The Solar System is embedded within this LB. At some point in time within the past 14 Myr, the LB shell, transporting accumulated ejected SN matter must have overrun the Solar System. If individual SNe occurred afterwards, their expanding shells should have passed the Solar System at a later point in time.

Within these expanding shells (LB and individual SN), the nucleosynthesis signatures of massive stars and their explosions are transported. If the Solar System is encountered to such a shell, these signatures might be carried into terrestrial archives, such as deep-sea sediments. Detection of SN traces on Earth itself might provide an important piece to solve the puzzle how the heavy elements are formed in the universe. It allows constraints

on nucleosynthesis processes of massive stars and might provide answers on transport processes of dust into the Solar System. Furthermore, a positive detection of SN radionuclides, such as ^{26}Al, ^{53}Mn, and ^{60}Fe, helps to gain information on the Earth's history and the local Universe. Finding such traces can help to solve questions such as: When was the last close SN? How close was it? Was there more than one SN, and did it have an impact on the Earth's biosphere?

1.2 Historical Overview and Present Status

Almost 20 years ago two independent studies triggered the search for ^{60}Fe, a long-lived iron-isotope of SN-origin, on Earth. Korschinek et al. (1996) suggested to search for SN traces in deep-sea sediments. The authors state that, detection of an ^{60}Fe signal in such an archive would help to gain information on its abundances in the ISM, on nucleosynthesis processes in SNe, and on transport of ejected SN material.

At the same time Ellis et al. (1996) presented a study proposing not only the presence of ^{60}Fe on Earth as diagnostic tool for nearby SNe, but also other radioactive SN isotopes e.g. ^{26}Al, ^{36}Cl, ^{53}Mn, and ^{59}Ni. With half lifes in the order of Myr, these radionuclides can be detected live in terrestrial archives with ages up to ~10 Myr. In addition to a direct deposition, the longer-lived but less abundant r-process nuclei presumably of SN-origin ^{129}I, ^{146}Sm, ^{244}Pu, as well as ^{182}Hf (Fields et al., 2005) might be detectable on Earth. Their half-lives are in the order of 10-100 Myr. These radionuclides might have a significant abundance in the ISM, as they were ejected during SN explosions of previous star generations. Such long-lived isotopes might be swept up by the expanding shell of a nearby SN and transported to Earth. Furthermore, a nearby SN would result in a temporarily stronger influx of cosmic rays. Therefore, an enhanced production of the isotope ^{10}Be, which is produced in the Earth's atmosphere, might be observed. However, Ellis et al. (1996) state that a SN must be as close as 40 pc to cause a detectable increase of cosmogenic products. Ellis et al. (1996) proposed ice cores and ocean sediments as suitable terrestrial reservoirs for SN traces.

1.2.1 Experimental Findings of Extrasolar Traces

Since 1996 the subject of finding and exploring geological isotopic anomalies of SN origin became a popular matter. The first experimental indication of a SN signal on Earth was published by the Munich AMS group (Knie et al., 1999a). A ferromanganese crust - a very slowly growing deposit on the pelagic sea floor, rich in iron and manganese - originating from the South Pacific from a depth of 1300 m, was examined for SN traces. An ^{60}Fe signal was detected with accelerator mass spectrometry (AMS) in the two upper layers of the crust, corresponding to ages of 0-2.8 and 3.7-5.9 Myr. An older layer (5.9-13 Myr) did not show any signature of this radionuclide.

To obtain a higher time resolution a follow-up measurement of another ferromanganese crust (237KD) was performed a few years later by the same research group (Knie et al., 2004). This crust originated from the equatorial Pacific from a depth of 4830 m. Its

growth rate was determined to be very homogeneous and slow with only 2.5 mm Myr^{-1}. It was cut into layers of 1-2 mm thickness to obtain a continuous depth profile with a time resolution of about 400-800 kyr, reaching back in time to almost 14 Myr. Again, an ^{60}Fe enhancement was found, predominantly in the layer of 6-8 mm corresponding to an age of 2.4-3.2 Myr. This age was obtained by measuring ^{10}Be, a long-lived isotope, which is constantly produced in the Earth's atmosphere and detectable throughout the layers of the crust. Thus, using the exponential decrease of this radionuclide with depth, an age profile could be established. The accepted half-life value of ^{10}Be used for this dating procedure at that time was (1.51±0.06) Myr (Hofmann et al., 1987). However, a later remeasurement of the half-life yielded a lower value of (1.387±0.012) Myr (Chmeleff et al., 2010; Korschinek et al., 2010). Applying this new value, the corresponding age of the layer of 6-8 mm became younger with 1.74-2.61 Myr (Feige et al., 2012). Furthermore, a slightly different growth rate of 2.37 mm Myr^{-1} was measured (Fitoussi et al., 2008). Figure 1.1 (right) presents the $^{60}Fe/Fe$ data from Knie et al. (2004) with the recalculated chronology, and from a second measurement performed by Fitoussi et al. (2008) in the same crust from a drill hole 20 cm off the previous sampling location. In this later study, the ^{60}Fe signal was detected again. The width of this signature might be smaller than the temporal extension of the layer (~800 kyr) it was detected in. Hence, to fully resolve the signal, the time resolution should be further improved.
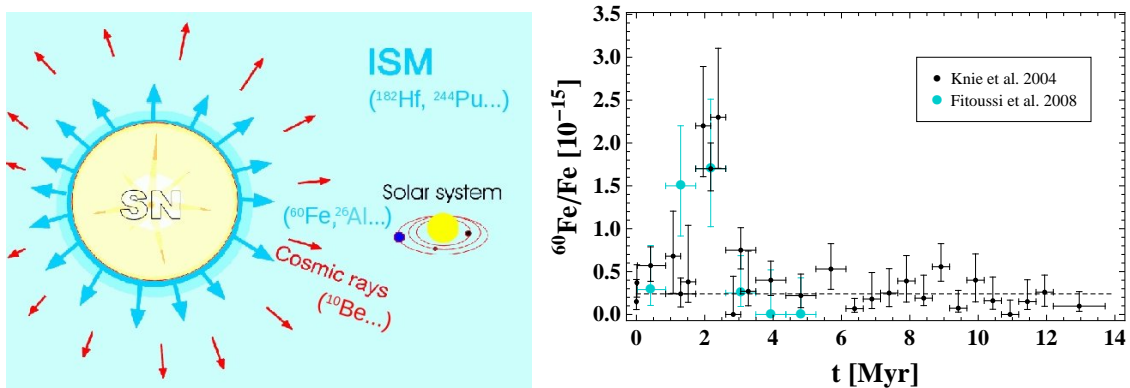
Figure 1.1: Left: This cartoon exemplifies a SN explosion in the solar vicinity ejecting freshly synthesized radionuclides (^{26}Al, ^{60}Fe), which might subsequently become deposited on Earth. Long-lived isotopes already present in the ISM (^{182}Hf, ^{244}Pu) might be swept-up and transported via the expanding SN shell. Additionally, the production of cosmogenic radionuclides in the Earth's atmosphere such as ^{10}Be might increase, if the SN occurs sufficiently close to the Solar System (courtesy of TUM). **Right:** An enhancement of the $^{60}Fe/Fe$ ratio at 2-3 Myr was detected in a ferromanganese crust by Knie et al. (2004) and later confirmed by Fitoussi et al. (2008).

Fitoussi et al. (2008) intended to better resolve the ^{60}Fe signal in a North Atlantic sediment. The exposure time of the solar system to a passing SN shell was assumed to be very small (<50 kyr) compared to the time range contained in a layer of the ferromanganese crust of ~800 kyr. The much larger accumulation rate (3 cm kyr^{-1}) in these Atlantic sediments would allow to fully resolve a narrow SN signal. Fitoussi et al. (2008) calculated

an ^{60}Fe/Fe ratio of $\gtrsim 10^{-14}$ for signal widths between 10 and 50 kyr in these sediments. This ratio is an order of magnitude higher than the signal that was found in the ferromanganese crust by Knie et al. (2004). Instead, the most optimistic interpretations of the ^{60}Fe/Fe measurement results indicated a signal of low significance, on average not higher than 3×10^{-16}, covering a large time range of approximately 1 Myr (Figure 1.2, left). Fitoussi et al. (2008) evaluated the possibility of a deposition time longer than the expected time of <50 kyr for a single SN. They calculated a particle fluence - the number of atoms deposited per cm^2 - for one (or two) signals of ~400 kyr duration, which turned out to be 5 times less than estimated from the signal in the ferromanganese crust. The authors conclude that either their sediment does not represent the average global value or, which is of higher probability, that the uptake-factor estimated for the crust might be wrong. This uptake-efficiency determines the fraction of ^{60}Fe from the overlying water column incorporated into the ferromanganese crust and was calculated to be 0.6 % by Knie et al. (2004).
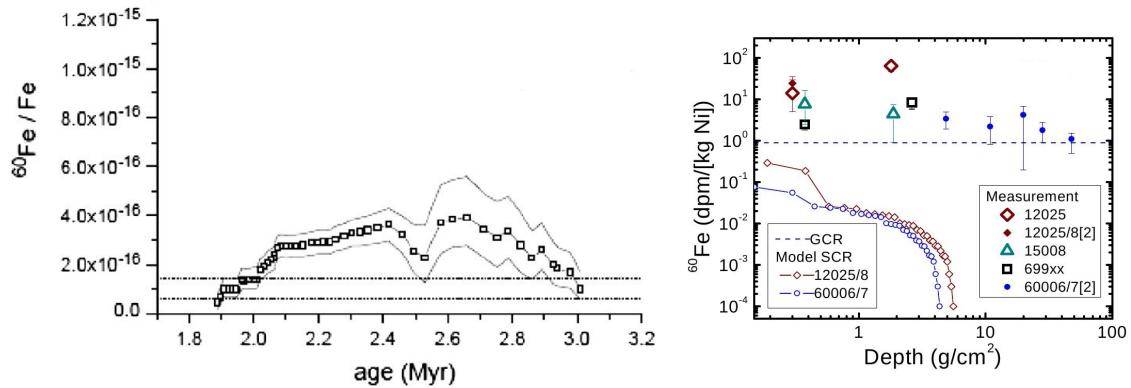
Figure 1.2: Left: A 400 kyr running mean reveals a very broad signal of marginal significance in a deep-sea sediment core analyzed for SN input of ^{60}Fe by Fitoussi et al. (2008). **Right:** Lunar samples analyzed for enhanced ^{60}Fe activity (Fimiani et al., 2012). The blue data points refer to a previous study by Cook et al. (2009), the other data points refer to different lunar cores measured by (Fimiani et al., 2012). Background of ^{60}Fe expected from galactic and solar cosmic rays is displayed as dashed and solid lines (see figure).

For the first time, extraterrestrial evidence of enhanced ^{60}Fe was detected in lunar samples by Cook et al. (2009). The authors state that a potential signal should be concentrated on the lunar surface and not be diluted by stable iron, because of negligible sedimentation. Furthermore, a low ^{60}Fe background is expected. This background is generated from spallogenic production on Ni isotopes, but the abundance of Ni in lunar samples is low (~100 ppm). However, there are processes leading to a dilution of a SN-produced ^{60}Fe. Mixing of the upper centimeters by constant impacts of meteorites, micrometeorites (MMs) and dust, the so called gardening effect, causes dispersion of a signal and a time resolution can not be obtained. Cook et al. (2009) compared their ^{60}Fe results with the ^{60}Fe production estimated from galactic and solar cosmic rays (GCRs and SCRs) and measured an ^{60}Fe activity above the background in the topmost sample. A follow-up study by Fimiani et al. (2012, 2014) reports six samples with signals significantly above the back-

ground (Figure 1.2, right). The interstellar fluence derived in these studies is again lower than expected from the signal in the ferromanganese crust assuming an uptake-factor of 0.6 %.

A different long-lived radionuclide of possible SN origin studied in terrestrial archives is the r-process isotope ^{244}Pu. Wallner, C. et al. (2000, 2004) analyzed layers of the ferromanganese crust 237KD - the same crust analyzed by Knie et al. (2004) - and of a manganese nodule from the equatorial Pacific for anthropogenic (^{239}Pu and ^{244}Pu) and extraterrestrial (^{244}Pu) plutonium. A top layer (0-2 mm, corresponding to 0-0.8 Myr) of the crust and the entire nodule was measured to examine the uptake-factor of Pu into the crust from known anthropogenic ^{239}Pu activities, which yielded (14±8) % for the crust and (160±70) % for the nodule. The two values are orders of magnitudes higher than the uptake-efficiency for ^{60}Fe. The higher uptake of Pu in the nodule compared to the crust is explained by its spherical shape and thus a higher surface area. One event of ^{244}Pu was detected in the crust in layers corresponding to 1-14 Myr containing no anthropogenic Pu. This event was converted into a ^{244}Pu fluence of 3×10^4 ats cm^{-2}. Wallner, C. et al. (2004) conclude, that this signal might originate from direct input of a SN in a distance of a few 10 pc. Furthermore, a fraction of this fluence might be of interstellar origin: ^{244}Pu ejected from previous SNe and swept-up by a nearby SN.

Further measurements of ^{244}Pu were carried out in deep-sea sediments by Paul et al. (2003, 2007). In these studies one single event was detected in a Pacific sediment from a depth of 5800 m. This could not be assigned to SN input, since it did not exceed the concentration expected from nuclear fallout.

The search for extraterrestrial SN signatures on Earth, particularly for the ^{60}Fe signal 2-3 Myr ago, is ongoing. Besides the research performed in this work, AMS measurements of ^{60}Fe in deep-sea sediments from the Pacific Ocean are conducted by the AMS group at TU Munich (e.g. Bishop and Egli (2011) and Ludwig et al. (2013)). Their work concentrates predominantly on extracting magnetite from microfossils and measuring SN-produced ^{60}Fe within these bacteria. These so-called magnetotactic bacteria grow magnetite chains and use them for orientation within deep-sea sediments via the Earth's magnetic field. A first result indicating successful measurements was communicated by Bishop in Witze (2013).

1.3 Possible Causes for a Terrestrial SN Signal

The possible source for an ^{60}Fe excess in the Solar System caused by a close SN was discussed by various authors. Most favor the theory of a nearby SN delivering its freshly synthesized products to Earth. Knie et al. (2004) assumed dust grains as ^{60}Fe carrier, because these can be large enough to overcome the solar wind and be transported into the inner Solar System. A sign of previous SN activity in the local ISM is the existence of the Local Bubble (LB). A sequence of individual SNe presumably formed the LB during the last 14 Myr (Fuchs et al., 2006), possibly encountering the Solar System with a SN

rate of approximately 1 per Myr. One or more of the closest SNe are primary suspects to have directly deposited ^{60}Fe in the crust 2-3 Myr ago (Feige, 2010; Breitschwerdt et al., 2012). The LB, its origin and a possible connection to the ^{60}Fe signal will be discussed in detail below.

A different theory was discussed by Basu et al. (2007) and pursued by Stuart and Lee (2012). They suggest that the ^{60}Fe signal in the crust is not of SN origin, but instead caused by high concentrations of MMs. ^{60}Fe is found in meteorites, where it is cosmogenically produced from Ni isotopes. Basu et al. (2007) infer that the ^{60}Fe signal originates from MMs being incorporated over the last 4-5 Myr. However, Fitoussi et al. (2008) demonstrate that, even if the total Ni-content in the crust was of MM origin, it is too low to produce the necessary amount of ^{60}Fe. It was then pointed out by Stuart and Lee (2012), that ^{60}Fe has not been measured directly in MMs yet and therefore this source cannot be ruled out.

As mentioned above, Fitoussi et al. (2008) did not succeed in detecting an intense narrow ^{60}Fe signal in an Atlantic deep-sea sediment. Instead, a marginal broad signal of low significance appeared. They conclude that this could not be caused by a single SN, because the exposure time of the Solar System to a SN shell carrying ^{60}Fe might be less than 50 kyr. Fitoussi et al. (2008) suggest a scenario of indirect input of SN-produced ^{60}Fe into deep-sea archives. The Solar System today is located in an interstellar cloud denser than surrounding LB medium, called the Local Fluff. It might have traveled through such a cloud in the past, enriched in ^{60}Fe from SNe producing the LB.

1.3.1 Evidence of Recent SN Activity: a Superbubble Embedding our Solar System

The Solar System is located within a structure of thin hot gas surrounded by a shell of denser and cooler medium stretching about 200 pc in the galactic plane and 600 pc perpendicular to it. This cavity in the local ISM is called the Local Bubble (LB) and is characterized by hot temperatures of $\sim 10^6$ K and a low average density of 5×10^{-3} ats cm^{-3} compared to the average ISM density of 1 at cm^{-3} (Berghöfer and Breitschwerdt, 2002; Fuchs et al., 2006).

When a star explodes, it ejects a large fraction of its stellar envelope, leaving behind a neutron star or, in the case of very massive stars from masses above ~ 25 M$_\odot$, a black hole. The ejecta is accumulated in a spherical shell surrounding the residual star, which expands through the ISM. This shell sweeps up ISM material, leaving a cavity of less dense medium inside. One SN would not be strong enough to form a large so-called superbubble, such as the LB. A conglomeration of 14-20 SN explosions, starting ~ 14 Myr ago with a SN rate of ≤ 1 SN Myr^{-1}, - the last SN occurring some 100 kyr ago - presumably created the LB (Fuchs et al., 2006; Breitschwerdt et al., 2012). A slightly lower age of 10-12 Myr and the production of the LB by six SNe was proposed by Maíz-Apellániz (2001).

Fuchs et al. (2006) identified a young OB-association within a volume of radius r = 200 pc around the solar neighborhood, where stars with masses above 8.2 M$_\odot$ appeared to be missing. They concluded that these stars must have already exploded as SNe and the

remaining stars belong today to three subgroups of the Scorpius-Centaurus (Sco-Cen) association: Upper Centaurus Lupus (UCL), Lower Centaurus Crux (LCC), and Upper Scorpius (US). Their trajectories over the past 30 Myr are diplayed in Figure 1.3 (left). The dashed line illustrates the location of the LB in the galactic plane today. The first stars entered this region 10-15 Myr ago, which is consistent with the age of the LB.
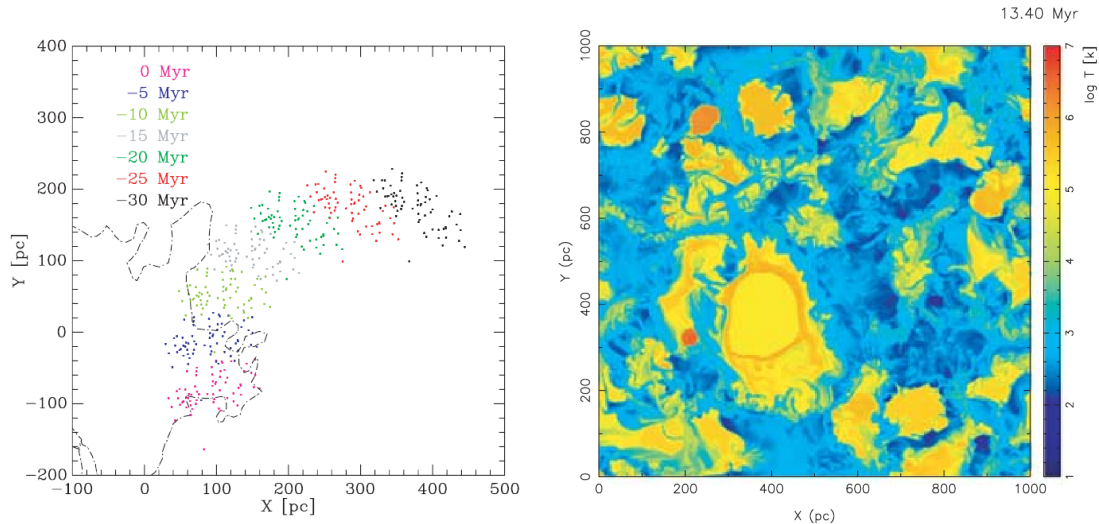
Figure 1.3: Left: The path of a young stellar group moving tracked back 30 Myr into the past. The dashed line indicates the region occupied by the LB today. This figure suggests, that the first stars entered this region 10-15 Myr ago, forming the LB by multiple SN explosions. Remaining stars are now part of the Sco-Cen association (Fuchs et al., 2006). **Right:** A cut through the galactic plane (color-coded temperature distribution) showing formation of two superbubbles: Loop I (nearly circular structure with the center located at approximately (400,400) pc) and our LB (elongated vertical structured left of Loop I) in a turbulent ISM 13.4 Myr after the first explosion (simulation by Breitschwerdt and de Avillez (2006)).

The figure implies that the explosions occurred not directly in the middle of the LB region, but off-center very close to its boundaries. This might be due to the existence of another superbubble in close proximity to our LB, the Loop I, which started to form around the same time. A computer simulation exploring the evolution of the LB and Loop I was performed by Breitschwerdt and de Avillez (2006) (Figure 1.3 (right)). In their model the LB was produced by 19, Loop I by 39 SNe. Due to the stronger energy input into Loop I it pushed the adjacent LB in the direction away from Loop I, leading to its elongated shape. Loop I is still active; another 38 explosions were calculated for the future. The two bubbles are separated by a "wall" - dense swept-up ISM gas built up by SNe within the bubbles. However, due to ongoing SN activity in Loop I this interaction shell is predicted to fragment in about 15 Myr (Breitschwerdt and de Avillez, 2006).

1.3.2 The Link to a Signature on Earth

The LB serves as indicator for recent SN activity in the Solar vicinity. Hence it is possible that one or even more of these SNe deposited radionuclides in terrestrial archives.

First calculations to reproduce the intensity of the ^{60}Fe signal in the ferromanganese crust were performed by Knie et al. (1999a, 2004). These authors estimated a distance of 30-40 pc of the Solar System to the explosion and suggested the existence of the LB as possible explanation for ^{60}Fe deposition on Earth. A direct link between the enhancement of ^{60}Fe in the crust and the LB was then established by Berghöfer and Breitschwerdt (2002) and Benítez et al. (2002). The latter work states that 2-3 Myr ago the center of LCC was located in a distance of ~100 pc, but the closest explosion could have happened at only 40 pc. Fields et al. (2005) inferred a distance of 15-120 pc by combining the measured ^{60}Fe signal with nucleosynthesis models. A similar study was carried out by Feige (2010) and Breitschwerdt et al. (2012), where the possibility of multiple SNe producing the anomaly in the crust was examined. Here, trajectories and explosion times of stars within LCC and UCL were taken into account. Not only the peak, but the whole ^{60}Fe profile in the ferromanganese crust produced from ~16 SNe was modeled. The closest explosion was found to reside between 65 and 85 pc.

Furthermore, estimations of fluences of not only ^{60}Fe but also other potential candidate isotopes such as ^{26}Al, ^{53}Mn, and ^{244}Pu in terrestrial deep-sea sediments and lunar samples were presented by Feige et al. (2012) and Fry et al. (2014) using SN explosion distances of ~100 pc to the Solar System.

The explosion distances might be constrained by finding residual stars of the SNe that formed to LB. Neuhäuser et al. (2012) and Tetzlaff et al. (2013) identified potential neutron stars, which might originate from the SNe that deposited ^{60}Fe on Earth. Two neutron stars were suggested to have birth places relatively close to the Solar System, with distances of 110-150 pc. However, the explosions of the progenitor stars were predicted to have occurred about 1-1.5 Myr ago. Therefore, these SNe are too young to produce an ^{60}Fe signal on Earth 2-3 Myr ago.

1.4 The Search for Supernova-Produced Radionuclides in Deep-Sea Sediments

A ferromanganese crust is a very suitable archive to search for isotopic SN anomalies. Due to its slow growth rate of only $\sim$mm Myr^{-1}, a large time range can be covered to find a first evidence of extraterrestrial input, however, poorly resolved in time. To obtain a better temporal resolution an archive with a higher accumulation rate is chosen for this work. Ice cores and deep-sea sediments fulfill this requirement. Ice cores, with accumulation rates in the order of cm kyr^{-1}, provide a detailed time resolution but require large amounts of sample material to be processed. Furthermore, the time region of interest, 2-3 Myr ago, is out of reach in these archives. Ice cores might date back up to 800 kyr (EPICA community members, 2004), even a core reaching back in time to 1.5 Myr before the present (BP) was recovered from Antarctica (Fischer et al., 2013). However, this does not extend back in time sufficiently long to search for a 2-3 Myr old SN signal, the age of the ^{60}Fe signature detected in the ferromanganese crust (Knie et al., 2004).

In this work, deep-sea sediments with low accumulation rates are chosen for detection

of SN radionuclides. With sedimentation rates in the order of mm kyr^{-1} the amount of sample material becomes limited, because the higher the accumulation rate the more material has to be investigated to cover a certain time range. Furthermore, the amount of stable isotopes, which dilute the concentration of the investigated SN radionuclides, increases with increasing sedimentation rate due to constant intake of stable elements.

The growth rate of the most slowly-growing deep-sea sediments is a factor of 1000 higher than that of a typical ferromanganese crust. Figure 1.4 illustrates the impact of a higher temporal resolution on a potential signal. The major excess of ^{60}Fe in the crust was observed in a layer of only 2 mm thickness corresponding to roughly 800 kyr. With a 1000 times higher deposition rate, the same time range is contained in 2 m of deep-sea sediment. If the width of this signal is much smaller than 800 kyr, it is possible to better constrain the deposition time and therefore the explosion time of the corresponding SN. In addition, conclusions about the structure of such a SN signal might be inferred. Due to the higher time resolution, a change of the signals intensity with time might be observable in the deep-sea sediments.
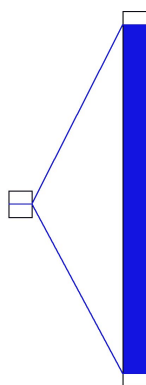
Figure 1.4: Schematic comparison of a layer in the ferromanganese crust and a deep-sea sediment. Its accumulation rate is 1000 times larger the the growth rate of a typical ferromanganese crust. Therefore, the same time range is contained in a 1000 times larger section, allowing a much better time resolution of a potential SN signal.

One goal of this work was to further explore the existence of such a signal and if proven positive, answer the question of its extension and intensity. Here, not only ^{60}Fe, but other SN candidate isotopes namely ^{26}Al and ^{53}Mn were measured with different AMS facilities to obtain a detailed data set of multiple radionuclides within the time period of interest. The AMS labs include VERA (Vienna), DREAMS (Dresden), and HIAF (Canberra). A few targets were measured with the AMS facility at TU Munich. Cosmogenically produced ^{10}Be in the Earth's atmosphere was measured to obtain an age profile of the sediment cores. The structure of this thesis is described in the following:

Formation processes of pelagic accretions such as ferromanganese crusts and nodules as well as different types of deep-sea sediments will be described in chapter 2 for an understanding of mechanisms involved in depositing extraterrestrial material. The sediment

samples chosen for the search for SN signatures will be introduced and characterized for type, composition and location. Several dating techniques are discussed, in particular magnetostratigraphy, which is applied in this work to obtain average accumulation rates of the deep-sea sediments. This stratigraphy will be confirmed with isotopic age dating.

In chapter 3 the SN isotopes analyzed in this work are explored and theoretical estimations of expected signals in the marine sediments are presented. For this purpose nucleosynthesis processes in massive stars producing the radionuclides ^{26}Al and ^{53}Mn, and ^{60}Fe, as well as their possible terrestrial and extraterrestrial background sources are examined. Transport times in SN remnants (SNRs), the exposure time of the Earth to a passing SNR, and the importance of dust formation for final deposition in marine sediments is discussed. Expected SN peaks in the sediments with different signal widths are calculated using two approaches: scaling from the previous signal in the ferromanganese crust and calculating direct input using different nucleosynthesis models.

The chemical extraction techniques for Al, Be, Mn, and Fe are explained in chapter 4. AMS measurement procedures for suppressing interfering isobars in different labs as well as methods for quantifying amounts of stable isotopes within the samples are described. Furthermore, obstacles in the first attempts of sample preparation as well as resulting chemical yields are investigated.

Results and discussions are presented in chapter 5. These are divided into different topics starting with a comparison of ^{10}Be measurement results from two different AMS labs (DREAMS and VERA). Problems in measuring its stable isotope ^{9}Be with ICP-MS are investigated. Subsequently, VERA-results of ^{26}Al are presented and its measurement efficiency is discussed. The next section describes ^{53}Mn and ^{60}Fe measurements at the HIAF lab. Before a SN signal in the sediments is discussed, a dating procedure is carried out. In combination with magnetostratigraphy, isotopic dating with ^{10}Be/^{9}Be and with ^{26}Al/^{27}Al ratios was applied. Subsequently, the ^{26}Al measurement results are related to potential terrestrial background from various sources. Atmospheric ^{26}Al/^{10}Be ratios are compared with results from the marine sediments. This is followed by a discussion of fractionation effects between those two isotopes in correlation with the sediment's carbonate content. The final section explores a SN signal in the analyzed deep-sea sediments and its origin. An uptake-factor of the ferromanganese crust is recalculated and constraints on theoretical nucleosynthesis models from isotopic ratios of ^{60}Fe/^{26}Al are presented.

The last chapter 6 gives a summary of this work and its results. Furthermore, the impact on the Earth's biosphere of a SN in close and moderate distance to the Solar System is discussed.

2 Deep-Sea Archives and Age Dating

Deep-sea sediments, with a higher time resolution than a ferromanganese crust, are chosen for the detection of SN signatures in this work. Samples of four pelagic sediment cores originating from the Indian Ocean are available for the search for SN radionuclides. Differences in formation processes between ferromanganese encrustations and deep-sea sediments are discussed in this chapter. Furthermore, some properties of deep-sea sediments from the Eastern Indian Ocean important for later discussions, namely composition, density and mixing lengths, are investigated.

Preliminary sedimentation rates of the deep-sea sediment cores were estimated in the time range corresponding to the ^{60}Fe signal detected in the Fe-Mn crust with magnetostratigraphic dating. This age model will be complemented in chapter 5.4 with isotopic dating. Therefore, radionuclide dating methods with ^{10}Be/^{9}Be and ^{26}Al/^{27}Al are described in the end of this chapter.

2.1 Types of Pelagic Accretions

Based on Robert (2008), different types of pelagic sediments, crusts, and nodules are described in order to provide an understanding of processes involved in the deposition of extraterrestrial matter on the ocean floor.

2.1.1 Formation of Pelagic Sediments

In the open ocean particles settle onto the sea floor and form pelagic sediments. These particles originate predominantly from three sources: terrigenous, biogenic, and organic sources. The present-day distribution of the major types of oceanic sediments are shown in Figure 2.1.

2.1.1.1 Terrigenous Sediments

Terrigenous sediments are products of particles of continental origin incorporated into the ocean. Physical and chemical weathering processes separate these particles from their parent rock; subsequent erosion mechanisms transport them into marine areas.

Physical weathering processes involve breaking the rock surface into small fragments e.g. due to temperature change, freezing of water within rock pores, and biological activity on the rock surface, such as growth of roots. Chemical weathering includes alteration of the
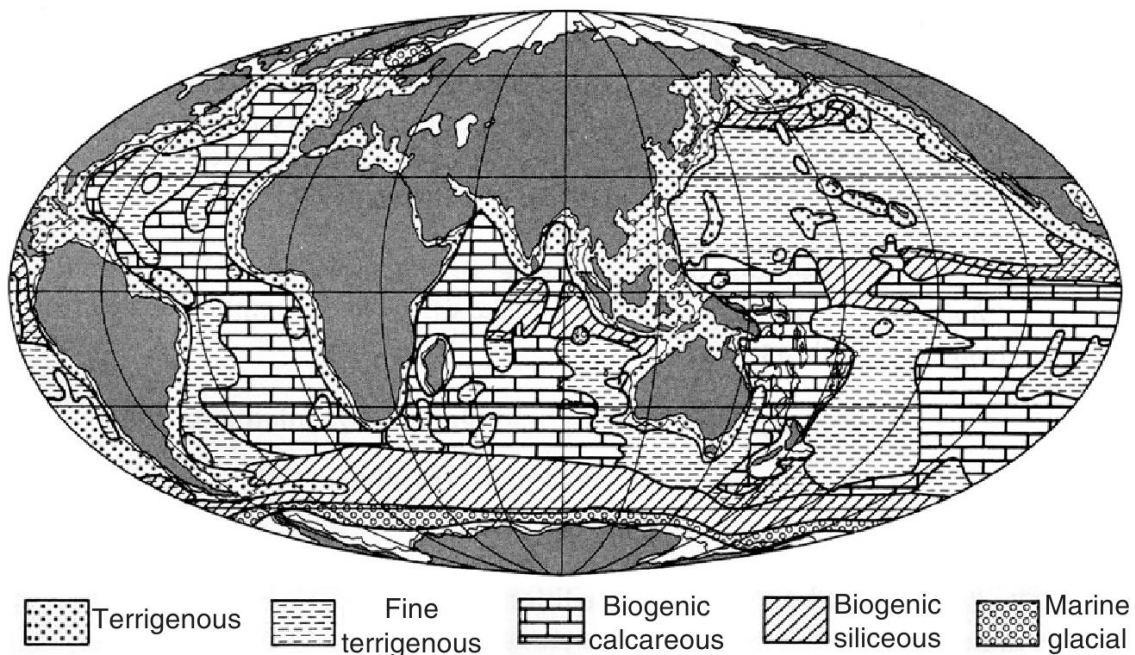
Figure 2.1: Present-day distribution of the major types of sediments (Robert, 2008). For a detailed description see text.

surface by chemical reactions of rain water with rock minerals. Soluble elements such as Ca and B are transported away, and insoluble elements like Al and Fe are enriched in the weathering profiles of the rock.

Particles formed on land, and mobilized and transported by (1) ice (glaciers, icebergs), (2) rivers, (3) wind, eventually reach the oceans.

(1) At high latitudes, surfaces are eroded by glaciers and ice streams. As ice behaves like a very viscous fluid, it is able to transport a wide range of grain sizes. Obstacles, such as rocks, induce pressure on the ice leading to a lower melting temperature. Water streams carrying particles develop and are released at the end of the glacier. Furthermore, icebergs at sea levels fragment and transport terrigenous particles away from the continent before melting (ice-rafting).

(2) Released grains are removed by flows developing for instance after rainfall. Rivers erode and transport particles to ocean shorelines (fluvial erosion), where the major fraction is accumulated.

(3) A third major source of particle input into the ocean is eolian dust. Wind behaves as a low density and low viscous fluid and transports particles over a wide range depending on its velocity and sizes of the suspended grains. Wind with velocities of 0.1-0.3 m s^{-1} is able to erode clay-and silt-sized grains, where high velocities of 20-30 m s^{-1} are needed to remove particles of 2 mm size from the Earth's surface. Only the smallest silt particles, clay or colloids with sizes below 0.016 mm are

transported at high altitudes up to the tropopause to distances of some 1000 km and possibly to the open ocean.

A fraction of terrigenous material that has reached the ocean via rivers is distributed in the ocean via water currents. This fraction mainly consists of fine-grained suspended clay- and silt-sized particles. In addition, eolian dust particles are deposited from the atmosphere in pelagic regions. The components accumulate on the sea floor, where deposition is facilitated by flocculation. Here, the terrigenous matter is mixed with other types of particles, a large fraction stemming from biogenic origin. The greater the distance from the shore the lower becomes the terrigenous component in the sediments, reaching values below 5 % in pelagic sediments. However, the amount of terrigenous particles depends also on the location of the CCD; below this zone the terrigenous fraction might be larger as biogenic material may be dissolved.

2.1.1.2 Biogenic Sediments

Biological activity dominates in the photic zone, a region reaching 100-200 m below the sea surface, where solar energy and nutrients are available. Most biogenic particles stem from marine microorganisms; a large group consists of foraminifera and radiolaria, both protozoa, whose remains are found as microfossils in pelagic sediments.

Foraminifera (Figure 2.2, left) are among the calcareous species, which predominantly produce tests (shells of microorganisms) of calcium carbonate. A minor fraction (deep benthic organisms) uses terrigenic or organic particles to agglutinate their shells.
Foraminifera exist most commonly in zooplanktonic form by mass (not by species). They range between 50 and 400 µm in size (with some exceptions, which reached lengths up to 10 cm in the Permian ages). Dead planktonic foraminifera settle on the sediments surface within a few weeks. Organic matter is dissolved and, depending on the location of the CCD, the remaining tests are also dissolved or reach the ocean floor in partly dissolved form.
In addition, benthic foraminifera being more divers in species populate the area on and in marine sediments, the majority living in the topmost cm. These are only some 100 µm in size (some grow up to 10 mm) and predominantly populate shallow-water areas. However, a fraction is found as pelagic organisms in deep-sea sediments.
Radiolaria (Figure 2.2, right) are zooplanktonic microorganisms living in all water depths available, ranging from the photic zone to abyssal regions of several km. Their exoskeleton consists of amorphous silica (opal A), varying from 40-400 µm in size, some may reach sizes up to 2 mm.
Dissolution of biogenic opal depends among others on silica saturation of the ocean water and on the temperature: the higher the temperature the higher the dissolution rate. Furthermore, the existence of metals in opal, such as Al and Fe, decreases its solubility. The highest dissolution occurs in the photic zone, a significant part also occurs at the sea floor. Eventually only a fraction of the initial biogenic silica are incorporated into the sediment. In addition to zooplanktonic species, remains of autotrophic organisms, namely phytoplanktonic fossils such as coccoliths (calcareous) and diatoms (siliceous) are found in
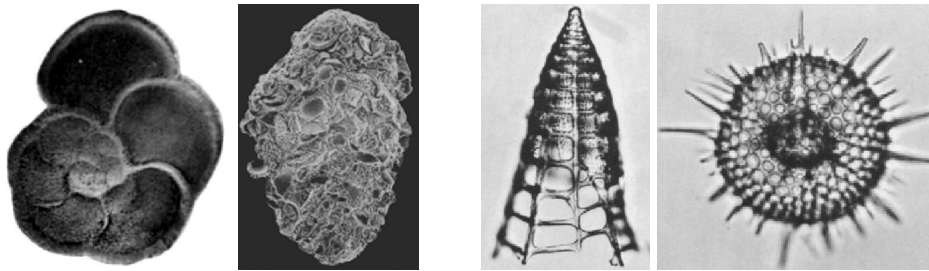
Figure 2.2: Left: planktonic (left) and benthic (right) foraminifer. **Right:** two examples of radiolaria (Robert, 2008).

pelagic sediments. Sinking of particles occurs mainly within aggregates or fecal pellets.

2.1.1.3 Organic Matter in Sediments

Two sources dominate the production of organic components incorporated into sediments. One is continental input from plants and soils, the other one is production from organisms living in the oceanic photic zone. Continental plants and oceanic autotrophs such as phytoplankton (e.g. diatoms) and algae produce organic compounds via photosynthetic processes. Heterotrophic organisms such as foraminifera and radiolaria or fish function as secondary producers of organic matter as they exploit the primary matter produced by the autotrophs.
A large fraction of the organic matter is oxidized or consumed as food in the photic zone. Below, fluxes of organic matter decrease due to remineralization to inorganic compounds. Significantly less than a percent of organic carbon reaches the seafloor of pelagic sediments. Here, benthic organisms such as bacteria, foraminifera, and worms further decompose and oxidize organic matter. Sediments with high accumulation rates contain more organic material than slow-growing sediments, as rapid burial prevents organic carbon from degradation.

2.1.1.4 Other Types of Sediment-Particles

In addition to the types discussed above, other particle types might be deposited in pelagic sediments. A major source is for example volcanic activity on continents, where glass and ashes are transported by run-off and wind into the ocean. In the ocean itself, hot-spots and mid-ocean ridge volcanism releases basaltic magma, which can be transported thousands of km. Critical for this work is the incorporation of extraterrestrial dust grains such as interplanetary dust particles (IDPs) and MMs into marine sediments (see e.g. Brownlee (1985)). If SN traces are deposited on Earth, incorporation of extraterrestrial dust grains might contribute to a significant background to a potential SN signal in the sediments. Most affected is the long-lived isotope ^{53}Mn. This is significantly produced by spallation reactions of cosmic rays on Fe in extraterrestrial dust grains. The amount of radionuclides transported to Earth within extraterrestrial dust grains and their interference with a SN signal is discussed in detail in chapter 3.

2.1.2 Characteristics of Deep-Sea Sediments

As most of the organic matter is dissolved, pelagic sediments predominantly contain biogenic and (mainly fine-grained) terrigenic particles with varying concentrations depending on their location. The amount of biogenic particles increases when moving from coastal to open ocean regions (Figure 2.1). Minor components of deep-sea sediments are for instance authigenic materials such as manganese nodules or MMNs as well as extraterrestrial dust particles.

Types of sediment grains are classified by their sizes. Sand (0.063-2 mm) and gravel (2-256 mm) dominate in coastal areas. Clay and silt (0.0002-0.004 mm and 0.004-0.063 mm, respectively) are found in open ocean sediments. Smaller particles below 0.2 µm are referred to as colloids.

A first classification of sediment types was given by Murray and Renard (1891). If a sediment consists mainly of biogenic matter such as mineral products from pelagic organisms and shells it is identified as "ooze", whereas disintegration products of continental or volcanic particles are called "mud". A sediment referred to as "clay" is of terrigenous origin. These classifications have been developed further, taking into account components like calcareous, siliceous and various terrigenic particles.

When particles are settled on the sea floor, they are not necessarily fixed to their position but might be reworked by external forces such as increasing velocity of bottom water currents and gravity flows at inclined areas (e.g. margins). These are induced by instabilities occurring for instance from seismic activities. Such processes lead to changes in accumulation rate, prevent material from being deposited or even erode previously deposited material. For this reason only the fewest marine sediments have a homogeneous accumulation rate and can show major hiatuses (cavities in the chronology of a sediment), particularly if this rate is already very slow.

Further mixing occurs through bioturbation, which is dominant in the top few cm of the sediment. Here, benthic organisms such as bacteria are actively burrowing, primarily where oxygen is available. Below a few cm, where oxygen is consumed, anaerobic bacteria use up nitrogen, manganese and iron, and sulfur with decreasing depth. Therefore, the composition of the top layers may be altered, as deeper, older material is mixed and transported to the surface and vice versa. This leads to a homogenization in the affected depth, which is referred to as mixing length. The average thickness of this layer is comprised between 4 and 10 cm.

2.1.3 Formation of Ferromanganese Crusts and Nodules

Figure 2.3 displays various types of ferromanganese crusts and nodules in their specific environment at the ocean's floor (Halbach, 1986). Such crusts and nodules are certain types of sediments, and are distinguished from each other by different formation processes: hydrogeneous (or hydrogenetic), diagenetic, and hydrothermal. The individual formation processes are predominantly reflected in their compositions, locations, and

growth rates.
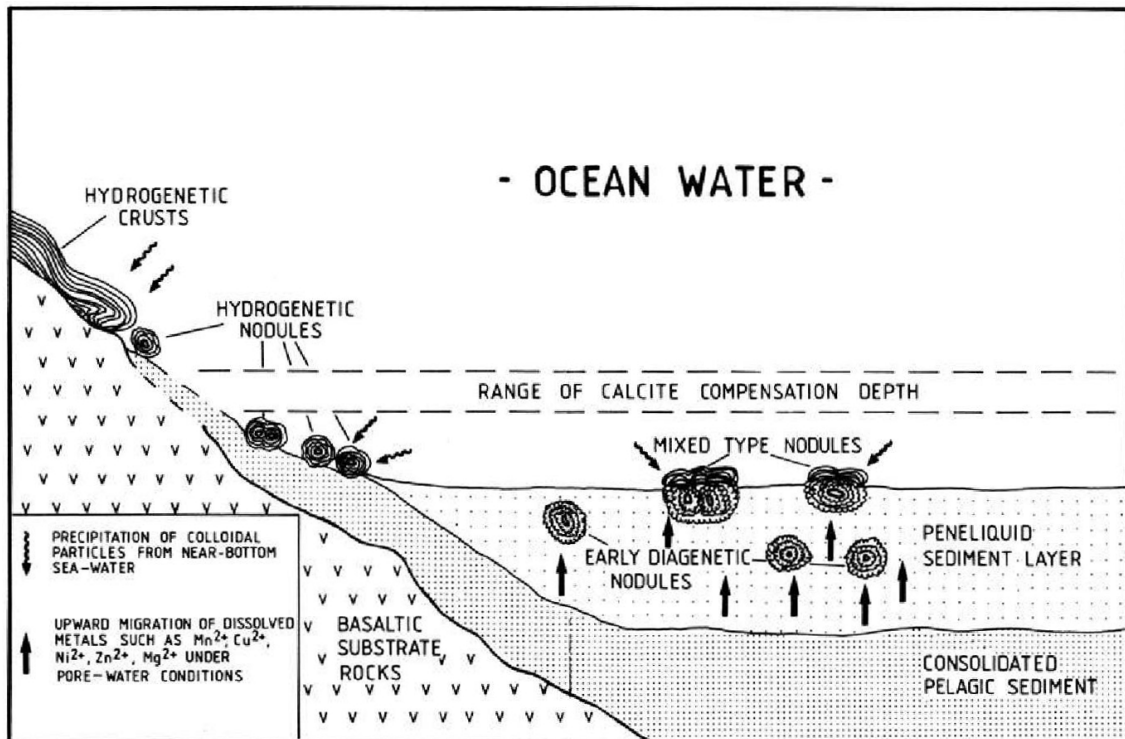
Figure 2.3: Types and locations of ferromanganese crusts and nodules on substrate rocks and in pelagic sediments (Halbach, 1986).

2.1.3.1 Hydrogenetic Ferromanganese Crusts

Hydrogenetic ferromanganese crusts, also called hydrogeneous sediments (Figure 2.4), form mainly on sea mountains, ridges, and plateaus at water depths of 400-7000 m (Hein and Koschinsky, 2014) in regions shielded from terrigenous and biogenic influences, where ocean water currents prevent normal sedimentation (Halbach, 1986). Apart from their slow growth rates between 1 and 5 mm Myr^{-1}, they are characterized by a large mean porosity of 60 % compared to the substrate rocks they are growing on, a mean dry bulk density of 1.3 g cm^{-3} and a mean wet bulk density of 1.9 g cm^{-3} (Hein et al., 2000). Hydrogenetic ferromanganese crusts predominantly consist of iron and manganese (both account roughly to around 20 wt%) with an average ratio of Fe/Mn = 0.7±0.2. They are mainly composed of vernadite and feroxyhyte with minor amounts of detrital minerals such as quartz and feldspar. In general, metals (such as Fe and Mn) enter the ocean from fluvial, eolian, and extraterrestrial sources. Additionally, chemical elements are remobilized from other sediments (Hein et al., 2000). Manganese is easily dissolved and enriched in the oxygen minimum zone (OMZ), a region deficient in oxygen that is located 200-1000 m below the sea surface. In the water column below this zone, where oxygen is enriched by deep-water currents, manganese and other elements that

form oxides and hydroxides generate complexes and build up mixed colloids such as $MnO_2/Fe(OH)_3$ (Koschinsky and Halbach, 1995). The surface of manganese oxyhydroxides $(MnO_2 \times nH_2O)^-$ has a negative charge and attracts cations such as Co, Ni, Zn, etc., whereas the slightly positive charged iron hydroxide $(Fe(OH)_3 \times nH_2O)^+$ surfaces form bonds with complexes containing V, As, P, etc. (Hein et al., 2000).

The colloids precipitate as oxides or hydroxides on substrate rocks, which are free from sediments. This process itself is not fully understood. The first layer on the rock is believed to form through bacterial catalytic processes (Hein et al., 2000). Further precipitation is autocatalytic with a contribution of bacteria to some degree.

Due to this growth process the crusts' composition represents the temporal variation of elements in the ocean. Adsorption of elements in the surrounding water continues after precipitation (Hein et al., 2000). In particular, dust grains containing e.g. radionuclides of different sources (Poutivtsev, 2007) or also micrometeorites of extraterrestrial origin (Stuart and Lee, 2012) are incorporated into the crust.
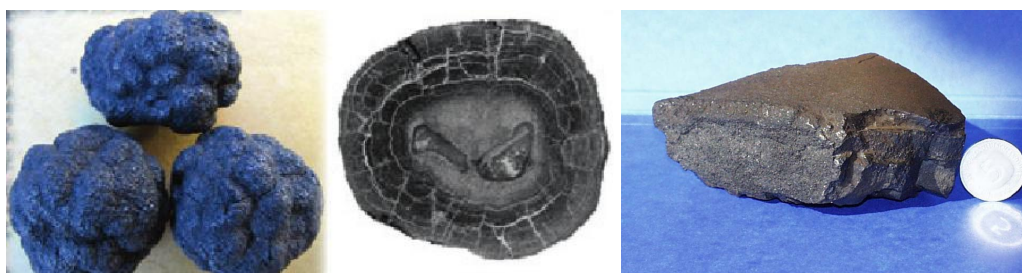
Figure 2.4: Left and middle: Three manganese nodules from the Clarion-Clipperton Zone of the Pacific Ocean with diameters of ~3 cm and a cross section through a nodule from the Blake Plateau in the Atlantic Ocean (Hein and Koschinsky, 2014). **Right:** The hydrogenetic ferromanganese crust 237KD from the Pacific Ocean, in which the extraterrestrial ^{60}Fe signature was detected by Knie et al. (2004) (courtesy of TU Munich).

2.1.3.2 Ferromanganese Nodules

Fe-Mn crusts were defined as manganese seamount nodules until the late 1970's (Hein et al., 2000). However, there are certain differences between crusts and nodules. The most obvious difference is the spherical appearance of nodules in contrast to the flat crust deposits. Figure 2.4 shows three Fe-Mn nodules with a diameter of ~3 cm from the Clarion-Clipperton Zone of the Pacific Ocean (left) and a cross section through a nodule from the Blake Plateau in the Atlantic Ocean (middle). They are mainly classified as two types, distinguishable e. g. by their composition, growth rate, and location. They form in diagenetic or hydrogenetic precipitation processes around a nucleus, which can be rock or authigenic mineral fragments, biogenic fragments such as pieces of bones or shark teeth, or smaller nodules (Hein and Koschinsky (2014), Robert (2008)). Hydrogenetic nodules grow in the same areas as ferromanganese crusts. Diagenetic nodules form in regions

with low sedimentation rates within deep-sea sediments. Mixed forms of the two formation types are more common than either type.

Hydrogeneous Fe-Mn nodules have a comparable chemical and mineral composition to crusts, consisting predominantly of vernadite and feroxyhyte pointing to a similar formation mechanism (Hein and Koschinsky, 2014). Nodules of this type grow with similar rates, however, the higher the diagenetic component the faster a nodule accumulates, with rates up to 250 mm Myr^{-1} (von Stackelberg, 2000).

The main mineral in diagenetic nodules is todorokite, an iron-free manganese oxide (Robert, 2008). If a hydrogenetic component is present, then it occurs along with the mineral vernadite. In addition, they contain minor amounts of detrital aluminosilicate and authigenic minerals (Hein and Koschinsky, 2014). Metals such as Ni, Cu, and Zn are incorporated from pore fluids within the sediment column the nodule is forming in, which consists of chemically modified ocean water.

Manganese nodules exist in regions with low sedimentation rates (<10 mm kyr^{-1}) in depths between 4000 and 6500 m, mainly in abyssal plains such as the Central Indian Ocean Basin (Hein and Koschinsky, 2014). The sizes of most nodules range between 1 and 12 cm, however, there are also microscopically small nodules (with sizes in the range μm up to mm) called manganese micronodules (MMNs). Their abundance in deep-sea sediments correlates inversely with the sedimentation rate. Because of the small accretion rate, nodule growth is inhibited by large sedimentation rates typically encountered above the calcite compensation depth (CCD). This lies between 3500 and 5000 m below the sea surface. Below that depth carbonates are dissolved due to an increase of CO_2 with increasing depth. As a concequence sedimentation rates decrease. Formation processes of MMNs are similar to macronodules (hydrogenetic, diagenetic, and hydrothermal); significant differences in composition seem to originate from a large diagenetic component, which remobilizes manganese and other elements in the sediment column and determines chemistry and distribution of MMNs (Stoffers et al., 1984).

In general, manganese nodules have a mean dry bulk density of 1.35 g cm^{-3} and a mean porosity of 60 %, which is similar to ferromanganese crusts (Jauhari and Pattan, 2000).

2.1.3.3 Other Types of Manganese and Iron Encrustations

Other types of manganese and iron deposits include hydrothermal deposits or shallow-water ferromanganese crusts and nodules. Hydrothermal deposits either consist of Fe oxyhydroxides or Mn oxides. Fe deposits are usually metal-poor, where Mn deposits, which predominantly contain the mineral todorokite, adsorb metals of the ocean water and show incorporated constituents of hydrothermal fluids. These encrustations, which have the form of stratabound layers, are located close to hot-spots and submarine arc volcanoes (Hein and Koschinsky, 2014) and have high growth rates on the order of m Myr^{-1} (Scholten et al., 2004). Shallow-water ferromanganese crusts and nodules that are found for example in the Baltic sea, are metal-poor and grow rapidly (Hein and Koschinsky, 2014).

2.2 Piston Cores from the Indian Ocean

Not any arbitrary terrestrial archive can be used for the search for SN signatures. The advantage of studying deep-sea sediments and crusts over other reservoirs such as continental sediments, is their comparatively undisturbed environment, in which sediments are ideally deposited continuously. In general, conditions might change over time, as indicated above. The sedimentation rate is influenced by the continental influx, tectonics, and changing bottom water velocities, to name just a few.

If existent in deep-sea archives, SN material is only present in trace amounts; concentrations of extraterrestrial radionuclides should be diluted as little as possible by their stable isotope. Therefore, preferred sediments are those with minimal terrigenic input (reduced to primarily eolian dust particles): far from continents, volcanoes and black smokers on the ocean floor. In those sediments the deposition of large amounts of detrital minerals containing stable Al, Fe, and Mn is limited. For this thesis, four sediment cores from the Indian Ocean were chosen.

2.2.1 Properties of *Eltanin* Sediment Cores

The marine sediment cores E45-16, E45-21, E49-53, and E50-02 available for studying SN-produced radionuclides in this work originate from the South Australian Basin. On average, they were located 1000 km south-west of Australia in the south-east Indian Ocean. A map with marked locations is provided in Appendix A. The cores were recovered in the early 1970's during cruises 45, 49, and 50 of the research vessel *Eltanin*, indicated by the capital "E" prior to cruise and core number (Figure 2.5). These cores are stored at the Antarctic Marine Geology Research Facility (ARF) in Florida. Table 2.1 summarizes basic informations on these cores including position, depth below the sea level, total length (Allison and Ledbetter, 1982), and year of recovery (Frakes (1971), Frakes (1973)).

Figure 2.5: Left: research vessel *Eltanin*, courtesy of www.navsource.org. **Right:** A sample of sediment core E45-21.

The cores were taken from a region close to the **A**ntarctic **b**ottom **w**ater (AABW) current (Figure 2.6). Allison and Ledbetter (1982) estimated sediment accumulation rates of

Table 2.1: Positions, depths below sea surface, lengths and dates of recovery of four marine sediments cored by the research vessel *Eltanin*.

Core	Latitude	Longitude	Depth (m)	Length (cm)	Year
E45-16	35°07.00' S	101°58.00' E	4312	680	1970
E45-21	39°00.00' S	103°33.00' E	4237	1182	1970
E49-53	37°51.57' S	100°01.73' E	4248	901	1971
E50-02	39°57.47' S	104°55.69' E	4242	1061	1971

4 mm Myr^{-1} for E45-21 and E50-02, and 3 mm Myr^{-1} for E49-53. E45-16 was not studied in this paper. The sedimentation rate of E45-16 is not of primary relevance as only a few samples are available in the time range, in which the search for a SN signal is performed (2-3 Myr, corresponding to the ^{60}Fe peak found in the ferromanganese crust (Knie et al., 2004)). The samples obtained of E45-16 will be dated independently in chapter 5.4. All sediment cores show hiatuses in time periods with enhanced AABW current velocities. This indicates their sedimentation rates might reside at the lower limit of possible sedimentation.
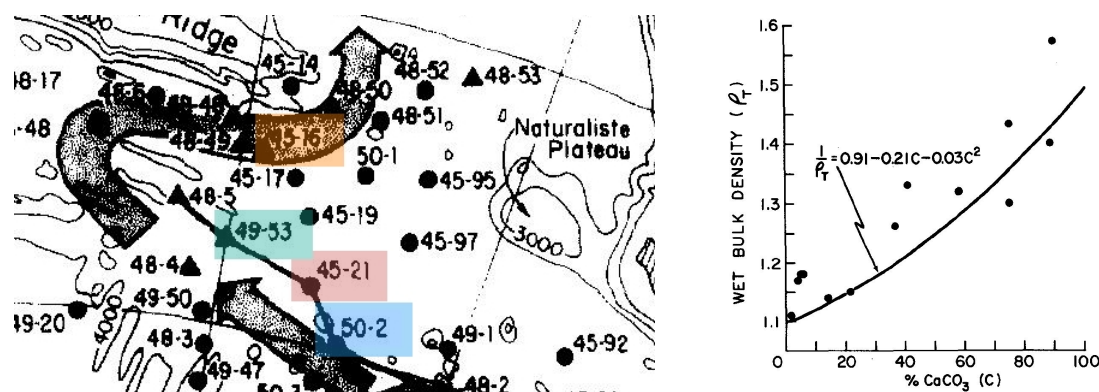
Figure 2.6: Left: Locations of cores E45-16, E45-21, E49-53, and E50-02 with respect to the Antarctic Bottom Water flow (gray arrows). Triangles indicated major hiatuses during the Brunhes and Matuyama chron (Allison and Ledbetter, 1982). **Right:** Relation between CaCO$_3$ content and wet bulk density of pelagic sediments (Lyle and Dymond, 1976). The solid curve does not represent a fit to this data but is an outcome of theoretical estimations.

The four sediments consist mainly of clay and silt particles with varying concentrations of MMNs, foraminifera and radiolarian tests. Furthermore, low abundances of calcareous nannofossils, diatoms, spicules, fish teeth, and pteropods are present (Allison and Ledbetter, 1982). Table B.1 in the Appendix summarizes lithology and most abundant compositions of core sections available for this work (Frakes (1971, 1973)). Due to the proximity of the sediments to the AABW, the majority of the non-biogenic fraction is transported from distant sources, consisting of ice-rafted debris such as quartz- and rock fragments as well as volcanic glass and rock particles (Allison and Ledbetter, 1982).

The mass density of the sediment cores, which is later used to estimate interstellar flu-

ences of SN radionuclides in the cores, was not determined directly in this work. Instead, the wet bulk density is estimated through the percentage of $CaCO_3$ present in the samples, which was found to vary strongly between 50 and 95 % (chapter 5.5). A correlation between $CaCO_3$ and the wet bulk density of abyssal sediments was determined by Lyle and Dymond (1976). Their results are presented in Figure 2.6 (right), which shows the wet bulk density of several Pacific pelagic sediments plotted against their $CaCO_3$ content. The solid line is not a fit through the data but represents a theoretical calculation of this correlation. Though the data is scattered, this plot gives a rough indication on the mass density of deep-sea sediments. In this work, a value of 1.35 g cm^{-3} will be adopted.

The largest set of samples analyzed in this work originates from cores E45-21 and E49-53. Here, almost all samples were obtained from the time period (roughly 2-3 Myr) corresponding to the ^{60}Fe signal in the ferromanganese crust (section 2.3.2). Material available of *Eltanin* core E45-21 included 29 samples spanning a total depth range of 398-697 cm below the sea floor. E49-53 spans a wider range of 120-517 cm; 45 individual samples were available throughout this section. The samples did not cover a continuous section. Instead, each sample corresponded to a length of ~1 cm of sediment core, with distances of 3-17 cm in between.
In addition, surface samples (E45-21 and E50-02) and older samples >4.5 Myr (E45-16) were provided by the ARF for this work. Altogether, 89 samples were available for analysis. In Appendix B.2, individual sample data is listed. This includes top and bottom positions below the sea floor and ages (if available) provided by the ARF.

2.2.2 Piston Coring

The sediment cores were extracted with a piston corer from the sea floor at a depth of more than 4000 m in the Indian Ocean. Figure 2.7 illustrates the setup of such a device. As the piston corer approaches the ocean's floor a trigger weight - by touching the sediment's surface - will signalize the release of a lead weight of several tons by the trigger assembly. The piston corer is also called gravity corer as the coring pipe is accelerated solely by gravity and falls freely until the piston hits the ground. At this point the piston is stopped due to the tightening of the piston cable and the coring pipe slides along the piston into the sediment. As the lead weight hits the piston the pipe is filled with the sediment sample and the corer is pulled up to the research vessel by a cable.
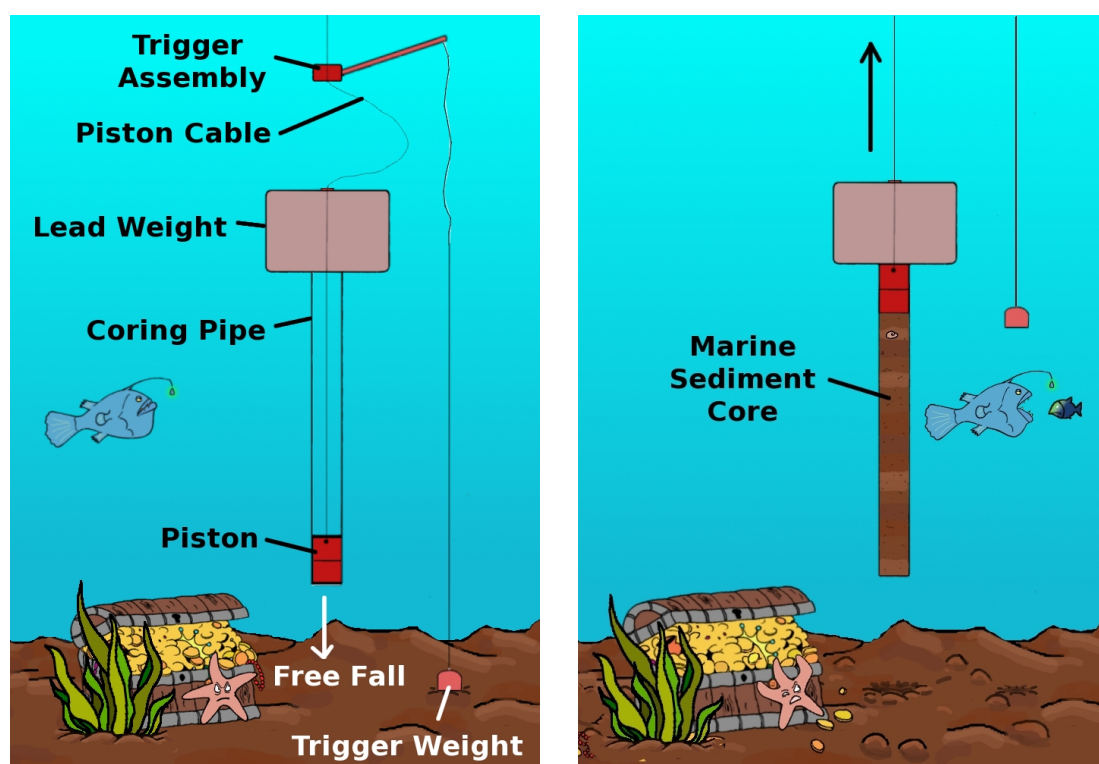
Figure 2.7: A piston coring device before entering the sediment and after the coring process. Further information is available at www.mnhn.fr, www.whoi.edu and www.geochemsol.com.

2.3 Dating Techniques

Several methods exist for dating a sediment core such as magnetostratigraphy (also called paleomagnetic dating), biostratigraphy and radioisotope dating. A magnetostratigraphic chronology of the *Eltanin* cores is presented by Kennett and Watkins (1976) and Allison and Ledbetter (1982). With their data a first estimate of sedimentation rates between major magnetic reversals was obtained (section 2.3.2).

Radioisotope dating is well established using for instance $^{14}C/^{12}C$ ratios (radiocarbon dating). However, for the purpose here this is not a suitable method as samples can be dated only a few $10\,000$ years BP due the short half-life of ^{14}C with ~5700 yr. Therefore it is impossible to date 2-3 Myr old samples with ^{14}C . For such long time periods, the longer-lived radionuclides ^{10}Be and ^{26}Al can be utilized (section 2.3.3). The $^{10}Be/^{9}Be$ and $^{26}Al/^{27}Al$ dating techniques will be applied later in this work and combined with paleomagnetic dating.

2.3.1 Biostratigraphy

The evolution of fossilized organisms can be observed throughout the layers of deep-sea sediments. Changes in species can be assigned to ages and serve for dating of a marine sediment. Various microfossils such as radiolaria, benthic and planktonic foraminifera,

and diatoms are used to obtain a biostratigraphic chronology of deep-sea sediments (Gradstein et al., 2012). Today, foraminifera, which first appeared in the Late Jurassic and evolved during the Cretaceous and subsequently formed more than 400 species, are widely used for dating (Robert, 2008).

However, the *Eltanin* cores E45-21, E49-53, and E50-02 were dated in the 1980s by Allison and Ledbetter (1982), who used radiolarian zones in addition to magnetostratigraphy. Radiolaria developed in the Cambrian and formed about 7000 species since, of which about 300 are found in the modern ocean (Robert, 2008). A radiolarian stratigraphy for Antarctic Seas was established by Hays (1965) and Hays and Obdyke (1967). Fauna from high latitudes, i.e. cold-water regions, differ from equatorial regions in properties such as shell thickness, porosity, and development of spines. Hays (1965) used the distribution of radiolarian antarctic species in correlation with depth of a marine sediment to propose radiolarian zones. These can be assigned to age periods. The most recent species are found in the zone Ω (0 to approximately 0.2 Myr BP), analyzation of species with restricted ranges in depth led to the establishment of three zones below Ω, called Ψ (0.2-0.8 Myr BP), X (0.8-1.8 Myr BP), and Φ (1.8-2.5 Myr BP). The Υ (2.5-4.2 Myr BP) and T (4.2-$\geq$6 Myr BP) zones were developed shortly after by Hays and Obdyke (1967). The combination of biostratigraphy and magnetostratigraphy is a powerful dating tool. In addition to zones established by magnetic reversals, these radiolarian zones are displayed later in this work (Figure 2.10, token from Allison and Ledbetter (1982)).

2.3.2 Magnetostratigraphy Applied to the Cores E45-21 and E49-53

Deep-sea sediment cores contain ferrimagnetic and canted antiferromagnetic particles (mostly magnetite, Fe_3O_4, and hematite Fe_2O_3, with various degrees of Ti-substitution), which hold a magnetic moment that becomes aligned with the Earth's magnetic field during and shortly after sediment deposition. This orientation records the direction of the magnetic field at the time of deposition and is preserved over geological times. Instabilities or changes of the magnetic field can be observed in changes of orientation of magnetized particles. Magnetic reversals occur by chance, therefore a unique pattern consisting of normal and reverse polarity is imprinted with depth of a marine sediment, which can be used for dating.

Figure 2.8 (left) displays the polarity pattern of the Earth's magnetic field over time, i.e. with depth of a marine sediment below the sea floor. Black indicates a normal polarity - the orientation of the magnetic field today - white a reverse polarity. In the history of our Earth there were periods characterized by primarily normal or reverse polarity, which are called chrons. The youngest chron being the Brunhes is characterized by a predominantly normal magnetic field and lasts since 780000 years. Towards older parts of a sediment core the Brunhes chron is followed by Matuyama and Gauss. Regions of inverse polarity within a chron are called subchrons.

Transitions between the chrons and major reversals within those chrons, the subchrons, were used to obtain a first paleomagnetic dating of the four *Eltanin* sediment cores. Kennett and Watkins (1976) identified major polarity changes with depths in the cores (see Figure 2.8, middle) and assigned an age to each reversal. The result is shown in the right part of Figure 2.8, where the expected paleomagnetic pattern is marked with *"Polarity"*.
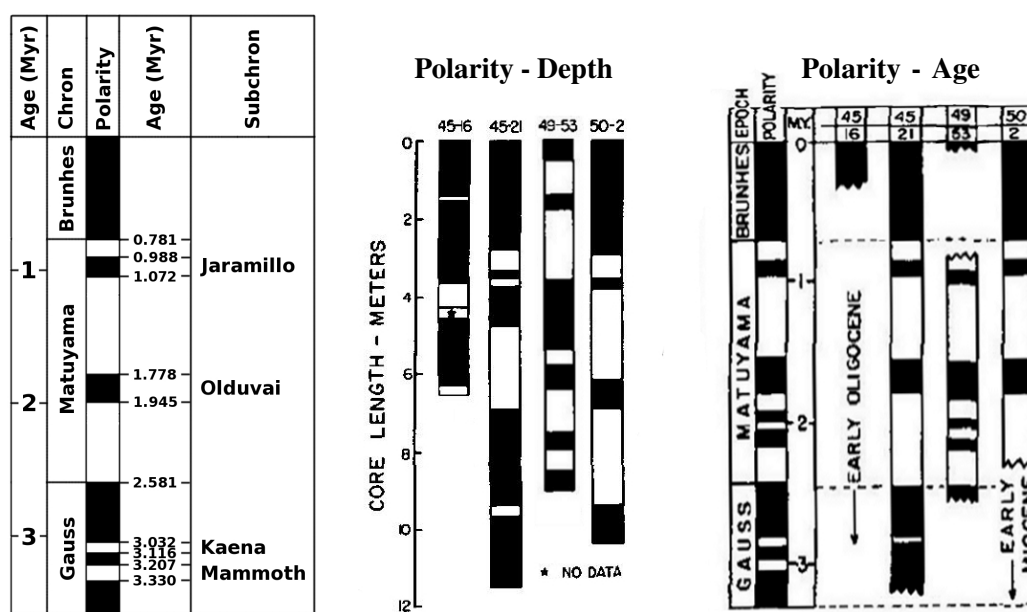
Figure 2.8: Left: A paleochronology, where the major chrons and subchrons are identified by name and age (Gradstein et al., 2012). **Middle:** Magnetostratigraphic chronology of *Eltanin* cores analyzed in this work: magnetic polarity with depth below sea floor. **Right:** Ages are assigned to reversals in the magnetostratigraphic pattern by Kennett and Watkins (1976).

Dating of the *Eltanin* cores E45-21, E49-53, and E50-02 was discussed in detail by Allison and Ledbetter (1982). Their depth profile and assigned ages for E45-21 and E49-53 are displayed in Figures 2.9 and 2.10, respectively. It is noticeable that core E49-53 is shifted by almost a million years towards higher ages due to the inclusion of a missed normal polarity zone in the previous dating procedure by Kennett and Watkins (1976). Allison and Ledbetter (1982) combined their magnetostratigraphic chronology with biostratigraphy using radiolarian zones. This approach was confirmed in this work (section 5.4). The chronology of the cores E45-21 and E50-02 obtained in the studies by Kennett and Watkins (1976) and Allison and Ledbetter (1982) match each other.

In the following, Figure 2.9 is used to obtain a preliminary chronology and averaged sedimentation rates for E45-21 and E49-53 within the major chrons. It shows the inclination of the Earth's magnetic field versus depth of the two cores; major sampling sections are marked with vertical lines (top and bottom). Polarity zones applied for dating are Olduvai (1.778-1.945 Myr) - a normal polarity zone within the Matuyama Chron - the transition of Matuyama to Gauss, which occurred 2.581 Myr ago, and two reverse polarity

zones within the Gauss chron, namely Kaena (3.032-3.116 Myr) and Mammoth (3.207-3.330 Myr), see also Figure 2.8 (left). Based on these tie points - points of a magnetic reversal in time - the associated depths were assigned to the corresponding ages and averaged sediment accumulation rates were calculated between these tie points. Uncertainties of the results were neglected in this first approximation. The results are listed in tables 2.2 and 2.3.
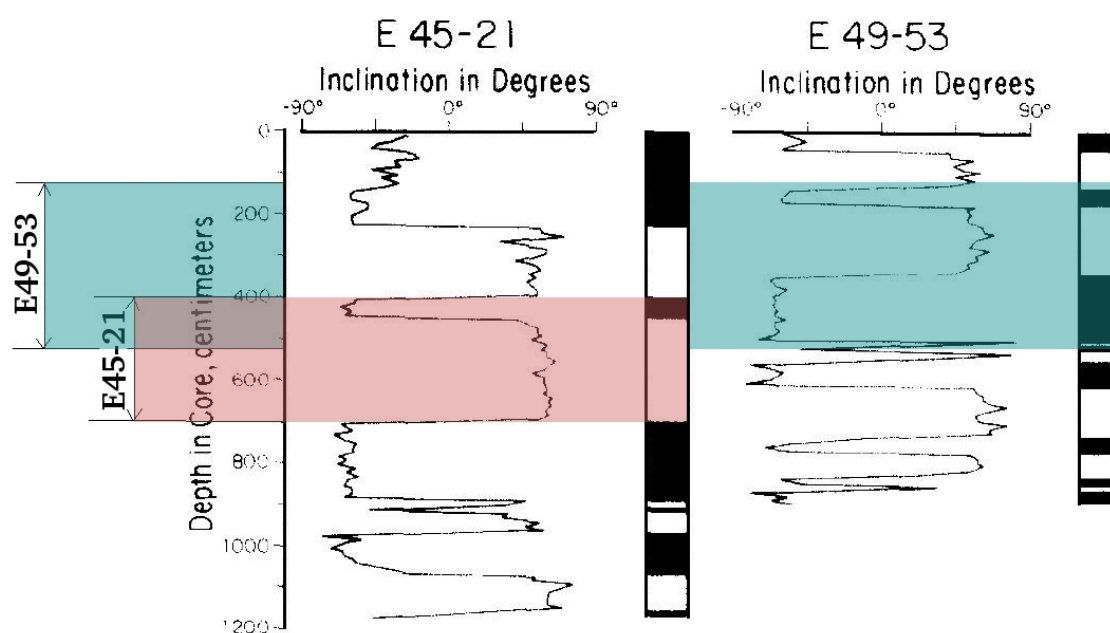
Figure 2.9: The change of inclination of the magnetic field with depth of the sediment cores Allison and Ledbetter (1982). The parts of the cores including samples provided for this work are shown as horizontal lines. A compressed magnetic pattern of E49-53 compared to E45-21 indicates a slower sediment accumulation rate.

It appears that the average sedimentation rates change throughout the cores. This is not surprising as, according to Allison and Ledbetter (1982), all of these four sediment cores are located in close vicinity to or even within an AABW path. Strong bottom water currents may result in a decrease of sedimentation rate or even produce large hiatuses as deposition of sediment material may be inhibited or previously deposited material eroded and transported away. Allison and Ledbetter (1982) identified two major events of high bottom water paleovelocity affecting the formation of the discussed marine sediments. One appeared during the late Matuyama chron and one throughout the Gauss chron.
According to Kennett and Watkins (1976), *Eltanin* core E45-16 shows such a large hiatus between 0.4 and the early Oligocene (approximately 23 Myr ago) (Figure 2.8). This core originates from a location directly within the AABW current (Figure 2.6). Here, only surface material is still intact up to a time of ~0.4 Myr BP and sedimentation continues in the early Oligocene.
The same is observed in *Eltanin* core E49-53. It has a major hiatus starting approximately 0.2 Myr BP, as indicated in Figure 2.10. In contrast to E45-16, this core resided not

Table 2.2: Estimation of average sediment accumulation rates S_{av} in between major magnet reversals of *Eltanin* core E45-21. The total average accumulation rate (weighted by the duration of polarity zones) is 3.70 mm kyr^{-1}. The chron and subchron ages are taken from Gradstein et al. (2012).

Chron/Subchron	Depth (cm)	Age (Myr)	S_{av} (mm kyr^{-1})
Olduvai top	398	1.778	
Olduvai bottom	448	1.945	2.99
Gauss top	695	2.581	3.88

Table 2.3: Estimation of average sediment accumulation rates S_{av} in between major magnet reversals of *Eltanin* core E49-53. The total average accumulation rate (weighted by the duration of polarity zones) is 2.73 mm kyr^{-1}. The chron and subchron ages are taken from Gradstein et al. (2012).

Chron/Subchron	Depth (cm)	Age (Myr)	S_{av} (mm kyr^{-1})
Olduvai top	135	1.778	
Olduvai bottom	180	1.945	2.69
Gauss top	340	2.581	2.52
Kaena top	500	3.032	3.55
Kaena bottom	510	3.116	1.19
Mammoth top	525	3.207	1.64

directly within the bottom-water flow (Figure 2.6), but farther away from the current where velocities were lower. Sedimentation resumes at ~1.3 Myr BP towards higher ages.

Sedimentation rates of *Eltanin* cores E45-21 and E50-02 are affected by a period of strong bottom-water currents during the Gauss chron. Material of both cores was eroded, leaving a hiatus starting of ~3.3 Myr BP for E45-21 and ~2.6 Myr BP for E50-02. The latter core was located closer to the AABW current (Figure 2.6). If the velocity of the water current is not strong enough to prevent sedimentation the grain size structure of the depositing material is altered. This is observed in these two sediment cores between hiatus and ages of ~2.4 Myr BP, as the finer particles are winnowed (Allison and Ledbetter, 1982). Earlier than 2.4 Myr these cores show no discernible hiatuses. They may have been located in an area with lower water velocity or have been shielded by a physical feature on the seafloor.

The total sediment accumulation rates of E45-21 and E49-53 averaged over the whole time periods considered were calculated by weighing the individual average accumulation rates between magnetic field reversals with the duration of each polarity zone. This procedure results in a sedimentation rate of 3.70 mm kyr^{-1} for E45-21. The rate for E49-53 with 2.73 mm kyr^{-1} is slightly lower. These values agree with Allison and Ledbetter (1982), who calculated rates of 4 and 3 mm kyr^{-1} for E45-21 and E49-53, respectively. In section 5.4, this paleomagnetic chronology was combined with isotopic dating and the corresponding uncertainties will be discussed. The difference in sedimentation rates of the two cores is shown in Figures 2.9 and 2.10. Samples obtained from E45-21 cover a length of 299 cm which converts to a time period of 0.8 Myr, whereas E49-53, with a

lower sedimentation rate and a length of 397 cm, covers almost twice the time range of 1.5 Myr. Furthermore, Allison and Ledbetter (1982) estimated a sediment accumulation rate of 4 mm kyr^{-1} for E50-02.

Table 2.4: Depths, assigned ages and numbers of samples provided for this work by the ARF. The column "Dating" indicates the origin of the age estimation. Age estimations were given by the ARF, PMS are the paleomagnetic ages for E45-21 and E49-53 as derived in this work. The total number of samples available was 89.

Core	Depth (cm)	Age (Myr)	Dating	No of samples
E45-16	130-136	~2	ARF	2
	229-235	~4.5	ARF	2
	375-385	~25	ARF	2
E45-21	surface samples			4
	398-697	1.8-2.6	PMS	29
E49-53	120-517	1.7-3.2	PMS	45
E50-02	surface samples			2
	847-854	3-5	ARF	2

Table 2.4 summarizes depths, assigned ages and numbers of samples available of the *Eltanin* cores. It has to be noted that age estimations were provided by the ARF. E45-21 and E49-53 were dated with magnetostratigraphy to confirm the ages by the ARF in the sections, where most samples were available, as explained above. According to ARF, there are two samples from E45-16 with ages of ~2 and ~4.5 Myr, respectively. Comparison with Figure 2.8, where the paleomagnetic chronology with depth and age is displayed, suggests that there are no samples between 0.4 and 23 Myr. The same argument applies for two samples between 3 and 5 Myr of E50-02. This inconsistency will be investigated by means of the ^{10}Be/^{9}Be and ^{26}Al/^{27}Al dating methods later in this work (chapter 5.4).

The ^{60}Fe signal in the ferromanganese crust (Knie et al., 2004) was detected in a time period between 1.74 and 2.61 Myr BP. For this work, samples of the *Eltanin* cores the same time range and beyond were provided by the ARF for the search of SN radionuclides. The preliminary magnetostratigraphic dating confirms that these samples indeed cover time ranges of 1.8-2.6 Myr (E45-21) and 1.7-3.2 Myr (E49-53). The available time periods are indicated by horizontal lines (Figure 2.10). The age profiles of the two *Eltanin* cores are comparable to the age of the ^{60}Fe signature measured in the ferromanganese crust by Knie et al. (2004) and Fitoussi et al. (2008).

The difference between growth rates of a ferromanganese crust (mm Myr^{-1}) and pelagic sediments (mm kyr^{-1}) was already emphasized in Figure 1.4. Almost the whole ^{60}Fe signal in the ocean's crust is contained in a layer of 2 mm thickness, covering a time range of more than 0.8 Myr. The same time range in the *Eltanin* sediments is spread over a length of 2-3 m, a factor of ~1000 higher than for the crust. Here, 29 samples taken from core E45-21 are spread exactly over the peak area of the ferromanganese crust. 45 samples of E49-53 are spread over an even larger time period. If a SN signal narrower than the corresponding layer in the ferromanganese crust is detected, the two sediment
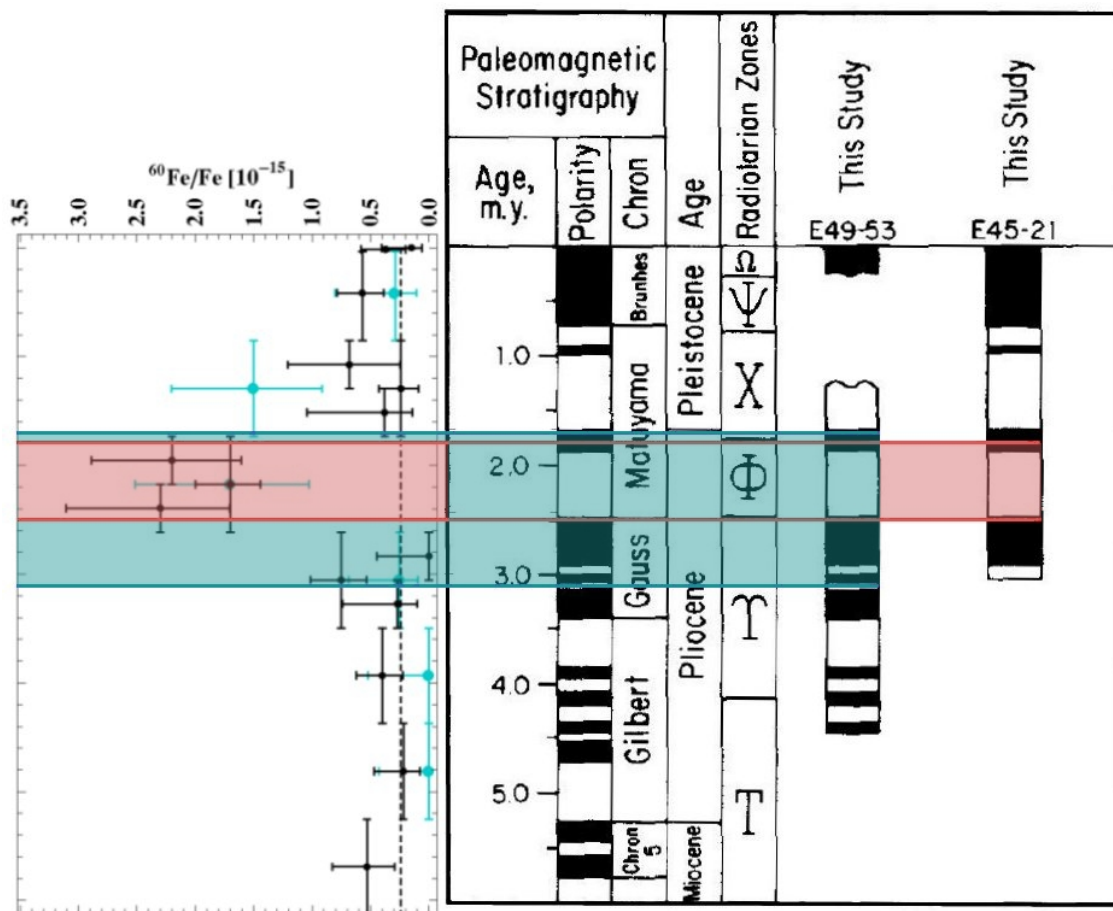
Figure 2.10: The age profile of the *Eltanin* cores E45-21 and E49-53 (adapted Figure from Allison and Ledbetter (1982)). The available time periods provided for analysis in this work are indicated by horizontal lines. Furthermore the $^{60}Fe/Fe$ data (see Figure 1.1, right) by Knie et al. (2004) and Fitoussi et al. (2008) is related to the expected location in the sediment cores.

cores should help to constrain the deposition time of this signal.

Each *Eltanin* sediment sample covers a length of approximately 1 cm. With the preliminary magnetostratigraphic dating, this length equals a time period of roughly 2700 and 3700 yr for E45-21 and E49-53, respectively. There are gaps of 3-17 cm between the samples (see Appendix B.2). These gaps correspond to a minimum of 8 kyr and a maximum of 63 kyr. If an extraterrestrial signature is narrower than those gaps, it might be missed. Theoretical estimations on widths and intensities of a SN signal in deep-sea sediments are given in chapter 3.

Dating with magnetostratigraphy determines average sedimentation rates between major magnetic reversals. Minor instabilities of the earth's magnetic field were not included, therefore finer structures could not be resolved. Allison and Ledbetter (1982) state that, especially during the Matuyama chron the bottom-water current was highly variable leading to variations in the sediment accumulation rate, which is not detectable in the mag-

netostratigraphic data. However, it might be reflected in variations of measured isotopic ratios used as a complementary dating method and applied (see chapter 5.4).

2.3.3 ^{10}Be/^{9}Be and ^{26}Al/^{27}Al Isotopic Ratios for Dating

In the Earth's atmosphere, ^{10}Be and ^{26}Al are produced by spallation of the most abundant elements by cosmic rays. ^{10}Be is mainly produced from nitrogen (a small fraction from oxygen), ^{26}Al is a spallogenic product from argon. ^{10}Be has a half-life of $t_{1/2} = 1.387 \pm 0.012$ Myr (Korschinek et al., 2010; Chmeleff et al., 2010). The half-life of ^{26}Al, with $t_{1/2} = 0.717 \pm 0.017$ Myr is a weighted mean from values reported in four different studies (Samworth et al. (1972); Middleton et al. (1983), Norris et al. (1983), and Thomas et al. (1984)), see (Auer et al., 2009). Thus, these radionuclides are suitable for determining a chronology of millions of years old terrestrial reservoirs. ^{26}Al has not been extensively applied as a dating method for marine deposits. ^{10}Be is commonly used in various applications such as marine sediments (e.g. Bourlès et al. (1989); Wang et al. (1996)), continental sediments (see for instance Lebatard et al. (2008), ferromanganese crusts and nodules (Segl et al., 1984; Sharma and Somayajulu, 1982), and potentially corals (Lal et al., 2005).

2.3.3.1 Beryllium Isotope Stratigraphy

As soon as the particle-reactive ^{10}Be is produced in the Earth's atmosphere, it is quickly attached onto aerosol particles (Ménabréaz et al., 2012). The average atmospheric residence time of ^{10}Be lies between 1 and 3 years (Raisbeck et al., 1981; Baroni et al., 2011), long enough to efficiently smooth out latitudinal variations of the atmospheric production rates of ^{10}Be (Heikkilä et al., 2013) through atmospheric mixing processes. ^{10}Be enters the ocean via settling particles (probably in soluble form) where it resides for 400-4600 years (see Bourlès et al. (1989) and references therein). The ocean mixing time is of ~1000 years. Higher residence times imply a homogenization of ^{10}Be in the ocean water, whereas mixing might be incomplete with lower residence times. In the open ocean ^{10}Be exists mainly in dissolved form. It is preferentially deposited in regions with high particle flux (particle scavenging) such as continental margins and upwelling regions (Henken-Mellies et al., 1990) and primarily adsorbed onto aluminosilicate phases (Sharma et al., 1987b). The scavenging efficiency depends on the composition of the settling particles and their surface area (Lebatard et al., 2008).

Thus, the absolute ^{10}Be concentration is variable within a deep-sea sediment and ^{10}Be and cannot be used for dating by itself. In order to eliminate concentration variations, ^{10}Be is normalized to its stable isotope ^{9}Be. Although ^{10}Be and ^{9}Be have different sources, once in the ocean they behave similarly.
The input of ^{9}Be into the ocean occurs in detrital form, i.e. from particles of weathered rocks. Its input happens mainly through fluvial influx. An insignificant part of ^{9}Be enters the ocean via dust deposition (Willenbring and von Blanckenburg, 2010). A small fraction of ^{9}Be exists in dissolved form. With a residence time in the ocean between 150 and

~4000 years (Bourlès et al. (1989) and references therein), it is likely to be homogenized before deposition and scavenged with the same efficiency as ^{10}Be. For this reason the atomic ratio ^{10}Be/^{9}Be represents a useful dating tool. However, when chemically extracting beryllium from the sediment, it should represent the soluble beryllium in the ocean at the time of deposition (Lebatard et al., 2008). This can be achieved by not fully decomposing the sediment material, but by dissolving only the portion that was adsorbed onto particles or precipitated from the solution, which is called the authigenic beryllium. For this reason, a gentle leaching procedure was applied in the sample preparation of the sediment samples (chapter 4.1).

A chronology of marine sediments with isotopic ratios of ^{10}Be/^{9}Be is obtained with the equation of exponential decay

$$N(t) = N_0 \, e^{-\lambda t}. \tag{2.1}$$

$N(t)$ is the authigenic fraction of the ^{10}Be/^{9}Be ratio in a sediment layer of age t, λ is the decay constant of ^{10}Be. N_0 is the initial ^{10}Be/^{9}Be ratio measured at the sediments top surface. The initial authigenic ratio should be comparable to the soluble ^{10}Be/^{9}Be fraction in the ocean (Lebatard et al., 2008). Bourlès et al. (1989) determined values of (^{10}Be/^{9}Be) = (6.8±0.7)×10^{-8} for the Indian Ocean.

Due to the fact that ^{10}Be and ^{9}Be originate from different sources, their ratio is not globally constant (spatially and temporally). Regions influenced by continental input have lower ^{10}Be/^{9}Be than open oceans regions as the influx of stable beryllium is higher (Lebatard et al., 2008). In general, all deep ocean ratios measured within the work of Bourlès et al. (1989), namely South Atlantic, Pacific and Indian Ocean, fall within (1.0±0.4)×10^{-7}.
Temporal fluctuations of the ^{10}Be/^{9}Be ratio are introduced either by a change of ^{10}Be and/or ^{9}Be. Variations in the ^{10}Be concentration are commonly associated with a modulation in the production rate of ^{10}Be in the Earth's atmosphere, for instance due to changes in the geomagnetic field strength (Ménabréaz et al., 2012) or primary cosmic ray flux variations (Raisbeck and Yiou, 1984). Short term variations induced by the 11-year solar cycle (Beer et al., 1990) are not important for this work as the sampling time resolution of the *Eltanin* samples is in the order of at least a few 10 000 years.
Melting of ice after glacial periods potentially releases ^{10}Be into the ocean. Henken-Mellies et al. (1990) estimated an increase of 2-20% of ^{10}Be in an Atlantic sediment with a sedimentation rate of 1.3 cm kyr^{-1} and a bioturbation zone of 8 cm. A time period of 5000 yr of deglaciation is homogenized within this mixing length. Assuming a similar bioturbation zone and an accumulation rate of 0.3 cm kyr^{-1} for the *Eltanin* cores, the same amount is spread over a four times longer time range. Therefore the increase of ^{10}Be from deglaciation is a factor of 4 lower and can be considered negligible in the *Eltanin* cores.
Any increase of the global erosion rate would lead to higher influx of ^{9}Be and thus a lower ^{10}Be/^{9}Be ratio. In fact, at the same time ^{10}Be is also delivered into the ocean. However, the ^{10}Be/^{9}Be ratio for example in soils is around one order of magnitude lower than the ratio of the open ocean (Henken-Mellies et al., 1990). Willenbring and von Blanckenburg (2010) analyzed soluble ^{10}Be/^{9}Be ratios as a weathering proxy to find the global erosion rate essentially constant for the last 12 Myr.

2.3.3.2 Aluminium Isotope Stratigraphy and Comparison to the ^{10}Be/^{9}Be Dating Technique

After being produced in the Earth's atmosphere, ^{26}Al behaves similar to ^{10}Be. It is adsorbed onto aerosol particles, shares the atmospheric cycle, and enters the ocean due to wet and dry deposition (Auer et al., 2009). Once in the ocean it is scavenged and settles onto the seafloor via sinking particles (Wang et al., 1996).

To obtain a chronology in deep-sea sediment cores with equation (2.1), ^{26}Al is normalized to its stable isotope ^{27}Al. This, like ^{9}Be, is also a weathering product and exists in detrital and authigenic form. The major input source of aluminum in surface water of the open ocean is eolian dust. In coastal regions the input of dissolved aluminum occurs primarily through fluvial influx (Orians and Bruland, 1986). However, the residence time of aluminum in deep ocean water is estimated to be much smaller than of beryllium. With 50-150 years (Orians and Bruland, 1986) it is not homogenized, but quickly scavenged and deposited on the sea floor before having a chance of being transported far away from the point of entry into the ocean. This should result in regional variations of ^{26}Al/^{27}Al ratios (Wang et al., 1996).

In contrast to ^{10}Be, the radionuclide ^{26}Al has not been used extensively for dating yet. Examples of applications are measurements of ^{26}Al/^{27}Al isotope ratios in Pacific deepsea sediments (Wang et al., 1996); Antarctic firn and ice samples were investigated by Auer et al. (2009), and manganese nodules by Sharma et al. (1987a). Ratios obtained in these studies range from 3×10^{-14} (sediments) to 2×10^{-13} (nodules). These are many orders of magnitude lower than the expected ^{10}Be/^{9}Be ratios ($\sim10^{-7}$, see section 2.3.3.1). Auer et al. (2009) measured atomic ratios of ^{26}Al/^{10}Be = 1.89×10^{-3} produced in the Earth's atmosphere. The reason for lower production of ^{26}Al in comparison to ^{10}Be lies in the lower abundance of argon (0.9 %) compared to nitrogen (78 %) in the atmosphere. Stable aluminum is much more abundant in the Earth's crust ($\sim8\%$), whereas beryllium is a trace element. This results in ^{26}Al/^{27}Al ratios in deep-sea deposits 7-8 orders of magnitude lower than ^{10}Be/^{9}Be. Measuring such low ^{26}Al/^{27}Al ratios with AMS is a time consuming task and requires a dedicated AMS facility (section 5.2).

The large amount of stable ^{27}Al can be used as an advantage. In contrast to beryllium, of which only trace amounts are present in a sediment, there is sufficient aluminum to be chemically extracted from the sediment samples without the need of adding a carrier. Addition of a stable ^{9}Be carrier introduces additional sources of uncertainties as on the one hand the carrier amount has to be known, but more importantly the amount of natural stable beryllium needs to be measured independently. Difficulties in measuring these low ^{9}Be concentrations with ICP-MS became apparent in this work and are explored in detail in chapter 5.1.2.

The oldest samples available for this work were assumed to be approximately 25 Myr old. With a half-life of 1.39 Myr ^{10}Be is suitable to date sedimentary deposits as old as 15 Myr (Bourlès et al., 1989; Lebatard et al., 2008). ^{26}Al has a shorter half-life (0.72 Myr), therefore dating is possible only for younger samples. Assuming concentrations of ^{26}Al are

detectable within ages of up to 10 half-lifes of ^{26}Al, samples can be dates back to approximately 7 Myr. This approach is very optimistic: on the one hand due to the expected low surface ratio of ^{26}Al/^{27}Al and on the other hand due to in-situ production of ^{26}Al in marine sediments (Sharma and Middleton, 1989). ^{26}Al from in-situ production might become comparable with atmospherically produced ^{26}Al already at ages of approximately 2 Myr (see chapter 3.1.1.2). Within younger ages the stronger exponential decrease of ^{26}Al/^{27}Al might result in a more accurate dating method than ^{10}Be/^{9}Be. In chapter 5.4 the two isotopic ratios of ^{10}Be/^{9}Be and ^{26}Al/^{27}Al in combination with magnetostratigraphy will be applied for dating of samples from the *Eltanin* cores.

Several studies proposed to utilize the ^{26}Al/^{10}Be ratio as a chronometer (e.g. Wang et al. (1996); Auer et al. (2009) and Shibata et al. (2000)). However, fractionation effects occurring during the incorporation of aluminum and beryllium complicate the use of this ratio in deep-sea sediments (Raisbeck and Yiou, 1984; Wang et al., 1996). Such fractionation effects and their possible cause will be further explored in chapter 5.5.

3 From Massive Stars into Marine Sediments

Four long-lived radionuclides were measured in deep-sea sediment samples with AMS: ^{10}Be, ^{26}Al, ^{53}Mn, and ^{60}Fe. The goal was to detect trace amounts of ^{26}Al, ^{53}Mn, and ^{60}Fe possibly related to recent SN activity in proximity of the Solar System. With half-lifes of a few Myr, these isotopes are ideal candidates to search for a SN signature 2-3 Myr ago. This age corresponds to a possible SN trace measured in a ferromanganese crust (Knie et al., 2004). Due to their short half-life compared to Earth's age, ^{26}Al, ^{53}Mn, and ^{60}Fe present in the early Solar System have already decayed to negligible amounts. Thus, primordial radionuclides with half-lifes of ~Myr no longer existed 2-3 Myr ago and do not represent an interfering background, which would add to a SN signal.

In the following, nucleosynthesis of the SN isotopes ^{26}Al, ^{53}Mn, and ^{60}Fe in massive stars is described. Possible sources causing a constant background of these long-lived isotopes in the deep-sea sediments, which might interfere with a SN signal at 2-3 Myr, are explored. A continuous input of freshly produced radionuclides into deep-sea sediments occurs for example from terrestrial atmospheric or in-situ production as well as from influx of IDPs. While for ^{60}Fe no terrestrial in-situ production and no significant constant extraterrestrial influx is expected, ^{26}Al and ^{53}Mn have various sources of additional input. Such sources are investigated in this chapter and terrestrial production as well as extraterrestrial input of ^{26}Al and ^{53}Mn is quantified. Subsequently, the transport processes involved in depositing long-lived radionuclides in terrestrial archives are examined. In particular, the role of dust grains for SN-produced radionuclides to enter the Solar System is discussed. Model calculations are carried out to quantify the amounts of the SN isotopes ^{26}Al, ^{53}Mn, and ^{60}Fe that could be deposited the deep-sea sediments.
Furthermore, production processes of the long-lived radionuclide ^{10}Be are discussed. However, ^{10}Be measurements in deep-sea sediment archives were performed solely for dating purposes.

3.1 Production Mechanisms of ^{26}Al, ^{53}Mn, ^{60}Fe, and ^{10}Be

In the following the evolution of a star will be discussed in a simple model, based on Diehl et al. (2011).

Stars in their main sequence life-time produce their energy via hydrogen-burning in their core from the pp-chain or the CNO-cycle. Which nuclear process dominates depends on mass and temperature of the star. As hydrogen (H) is exhausted in the core, the star leaves the Main Sequence and enters the RGB (red giant branch) phase. Hydrogen is now enriched in a shell around a He core and continues burning, causing the star to expand. Freshly synthesized He from the H-shell is transported onto the core, which starts to contract and heat. Stars with masses larger than ~0.4 M$_\odot$ start to ignite He in the core, converting most of the He to C via the 3α-process and to O via the reaction ^{12}C(α,γ)^{16}O. Again, when He is exhausted in the core, it continues burning in a shell around the CO core. This is where a star enters the AGB (asymptotic giant branch) phase. The star now consists of three regions: the electron-degenerated CO core, the overlying He-rich shell, and the outer H-rich shell. Stars with masses up to ~6 M$_\odot$ will die as a CO white dwarf. Super-AGB stars fall in the mass range of approximately 7-11 M$_\odot$. These stars are able to start central C-burning and form an ONeMg core. Their final evolution depends on the size of this core: they either end their lives as an ONe white dwarf or explode in an electron capture supernova (ECSN). More massive stars will undergo additional burning stages, first, central oxygen burning converting O to Si, then core silicon burning, where elements of the iron group are formed. Finally, they explode in a highly energetic event such as a core-collapse supernova CCSN.

Massive stars produce nuclides heavier than iron by neutron capture processes. The slow neutron capture- or s-process in the late phases of the star generates nuclides close to the line of stability, starting from iron up to the heaviest stable element bismuth. The rapid neutron capture- or r-process, which occurs in very hot environments with high neutron densities, e.g. in a CCSN, builds up the neutron-rich elements and the actinides. Each process forms about half of the isotopes heavier than iron.
The particular nucleosynthesis processes relevant for ^{26}Al, ^{53}Mn, and ^{60}Fe production in stars are described below.

The main sources for constant input of ^{26}Al and ^{53}Mn into terrestrial archives are either of terrestrial or extraterrestrial origin. Cosmogenic nuclides are produced in the Earth's atmosphere, as well as in meteoroids and comets, micrometeoroids and interplanetary dust particles (IDPs). These sources for additional input of radionuclides, adding to a potential SN signal, are explored in the following sections. First, a short excursion to the definition and origin of small interplanetary particles is given.

According to Genge et al. (2008) (and references therein) the terms ‚dust‘ and ‚micro-meteorites‘ are defined as follows: extraterrestrial dust particles found on the Earth's surface are referred to as micrometeorites (MMs). These are mostly large in size with 30-1000 μm. The smaller particles with less than 30 μm in diameter are collected in the Earth's stratosphere and are known as (IDPs). MMs and most of the IDPs seem to originate from the asteroid belt where they are formed via collisions between the asteroids. 40 % of the IDPs are suggested to originate from comets. Furthermore, interstellar dust particles (ISDs) formed for instance in AGB-stars and SNe can enter the Solar System and can be transported to Earth (section 3.2).

Within the Solar System, dust particles spiral inwards due to the Pointing-Robertson-effect (Robertson, 1937). Because of their proper motion the particles experience an aberration of the solar radiation: the radiation does not interact with the dust particle from a right angle, but seems to come from a slightly different angle in forward direction. The force of the radiation pressure acts against the orbital motion, leading to deceleration of small particles and spiraling towards the center of the solar system.

Whether a particle enters the Earth's atmosphere and survives depends mainly on its size and its entrance velocity and angle. Each dust particle entering the atmosphere experiences deceleration and surface heating, the maximum heating occurring at high altitudes (between 85 and 90 km) (Love and Brownlee, 1991). Materials with high velocities (>15 km/s) may be of cometary or interstellar origin. Low-velocity dust (<15 km/s) spirals in predominantly from the asteroid belt. Particles with very small sizes are efficient radiators due to their large ratio of surface area to mass. Numerical results from Love and Brownlee (1991) show that particles with sizes less than 50 μm (20 μm) and entrance velocities of 12 km/s (20 km/s) do not melt significantly and the original surface is preserved. Larger (100-1000 μm) particles lose at least 90 % of their mass (for an entrance velocity of 15 km/s).

3.1.1 ^{26}Al

With a half-life of $t_{1/2} = 0.72$ Myr, ^{26}Al has the shortest half-life of the radionuclides analyzed in this work. It is generated in massive stars, further production of ^{26}Al occurs on Earth and within extraterrestrial particles.

3.1.1.1 Production in Massive Stars

^{26}Al is dominantly produced in three environments in massive stars: in core H-burning, during the C and Ne convective shell burning and explosive Ne burning. The primarily responsible reaction is the ^{25}Mg(p,γ)^{26}Al reaction in all of these environments. Following (Limongi and Chieffi, 2006), who discussed the processes involved in nucleosynthesis of ^{26}Al for stars in the mass range of 11-120 M$_\odot$, the production of ^{26}Al is briefly outlined.

The massive star starts converting its initial abundance of ^{25}Mg to ^{26}Al as soon as it reaches the Main Sequence. Here, hydrogen burns in the core with temperatures larger than 3×10^7 K. A fraction of freshly produced ^{26}Al is lost due to β^+-decay to ^{26}Mg. In very hot and massive stars (T $> 5 \times 10^7$ K) destruction by ^{26}Al(p,γ)^{27}Si becomes effective towards the end of H burning (Figure 3.1). When the H core is exhausted, ^{26}Al is preserved in the H-rich layers until the explosion of the star. Central He burning destroys most of ^{26}Al via (n,α) and (n,p) reactions. The neutrons are produced by the ^{13}C(α,n)^{16}O process. The final amount of ^{26}Al from the H-rich layers ejected in the SN explosion depends on mass loss of the star prior to the explosion and on dredge-up.

Figure 3.1: Nucleosynthesis processes of ^{26}Al during central H burning (left), ^{53}Mn (middle), ^{60}Fe (right) in massive stars. Green arrows indicate production via proton and neutron capture as well as through decay of a mother isotope, red arrows imply destruction (modified sections of the chart of nuclei).

In the carbon-burning shell ^{26}Al is produced via the ^{25}Mg(p,γ)^{26}Al reaction as well. Here, ^{25}Mg originates from the initial CNO abundance of the star via (CNO)$_{ini}$ $\rightarrow$ ^{14}N $\rightarrow$ ^{22}Ne $\rightarrow$ ^{25}Mg. The protons needed for ^{26}Al production are predominantly made in the ^{12}C(^{12}C,p)^{23}Na(α,p)^{26}Mg process. Destruction by β^+-decay becomes very efficient, since the half-live of ^{26}Al is temperature-dependent. At temperatures between 10^9 K $<$ T $< 10^{9.6}$ K it decreases to 6.5 min. Photodisintegration will be effective at T $> 10^{9.3}$ K. In the C-burning shell ^{26}Al is most efficiently produced at temperatures of T $\sim 10^{9.255}$ K. Such a high temperature increases the cross sections of the ^{25}Mg(p,γ)^{26}Al reaction and of the reactions producing the required protons. Due to the convective environment, freshly synthesized ^{26}Al is quickly transported to regions of lower temperature, where the half-life increases again. Ne-burning in the shell and in the core also produces ^{26}Al. Again, it is the ^{25}Mg(p,γ)^{26}Al reaction, provided with protons from the ^{23}Na(α,p)^{26}Mg channel. Here, ^{25}Mg comes from C burning, where a part is left unburned and ^{23}Na is a product of C burning. During the passage of the SN shock-wave through the C (or Ne/C) convective shell, the fraction of ^{26}Al located close to the iron core is partially destroyed.

During the explosion of the star, ^{26}Al is mainly produced in the C convective shell with temperatures in the order of $\sim 2.3 \times 10^9$ K. Again the ^{25}Mg(p,γ)^{26}Al reaction controls its production, whereas destruction occurs via neutron captures processes. ^{25}Mg needed for the reaction is now produced by neutron capture on ^{24}Mg, which was synthesized in C

and Ne burning.

Figure 3.2 shows the contributions of the C/Ne convective shell, the SN explosion as well as stellar wind to the total amount of ejected ^{26}Al (also called the ^{26}Al yield). In almost all of the stellar progenitor masses explored in this figure explosive nucleosynthesis is the major contributor to the production of ^{26}Al. Stellar wind does not add significantly to the overall yield below masses of ~25 $M_\odot$.
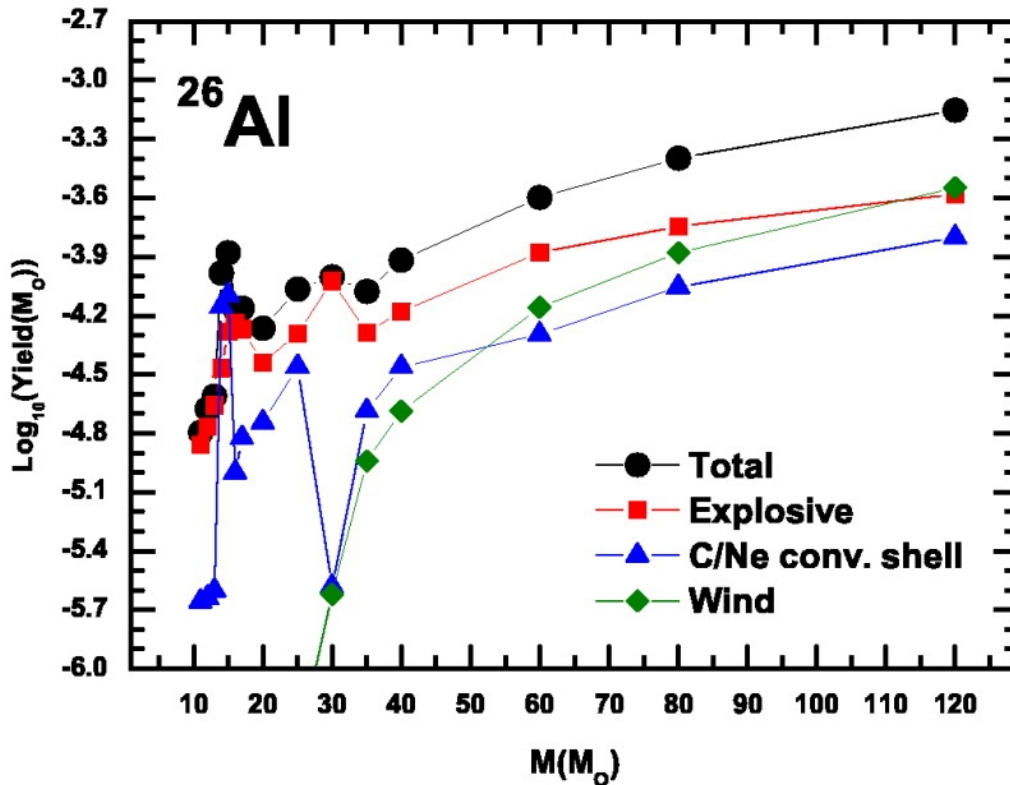
Figure 3.2: Contribution of the ^{26}Al production from different stellar environments to the total nucleosynthesis yield (displayed in logarithmic scale in units of $M_\odot$) as a function of initial stellar mass (in units of $M_\odot$) (Limongi and Chieffi, 2006).

Theoretical SN yields of ^{26}Al have been determined for instance by Timmes et al. (1995), Woosley and Weaver (1995), Rauscher et al. (2002), Limongi and Chieffi (2006) and Woosley and Heger (2007). Chieffi and Limongi (2013) include stellar rotation and its effect upon the computed yields compared to non-rotational models. In all of these studies, ejected ^{26}Al yields range from ~10^{-5} to ~10^{-4} $M_\odot$ in massive stars, with masses between and 11 and 25 $M_\odot$. ^{26}Al yields in this mass range are presented in Figure 3.3.
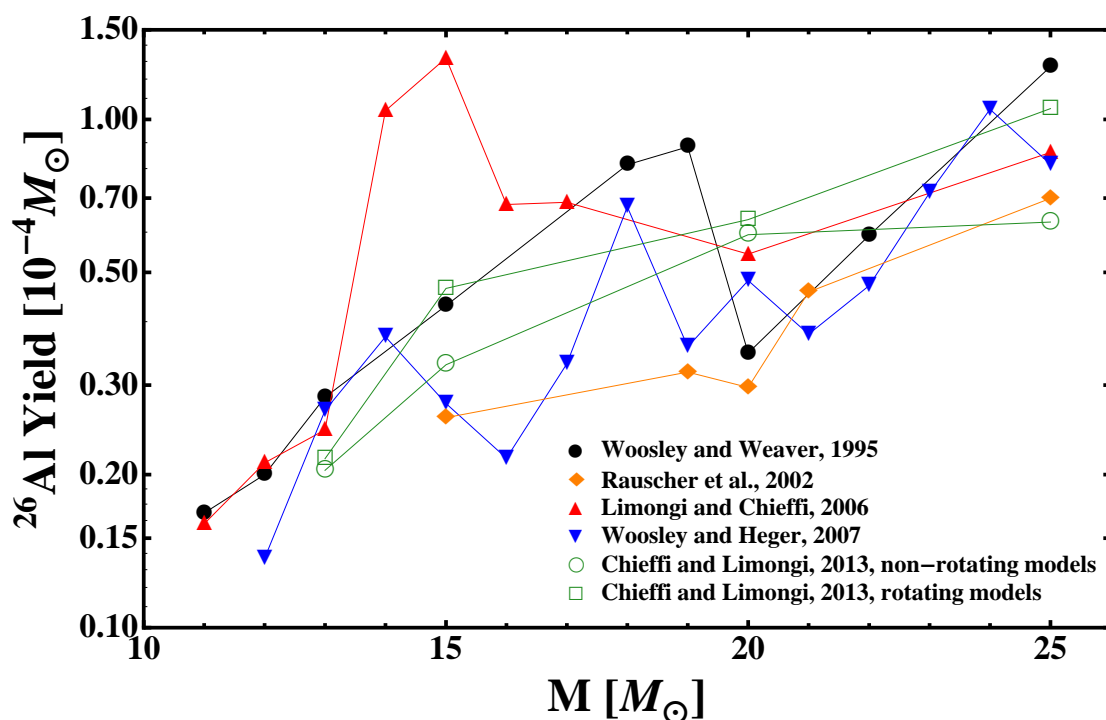
Figure 3.3: Comparison of theoretical ^{26}Al nucleosynthesis yields (displayed in logarithmic scale in units of 10^{-4} M$_\odot$) from several research groups for stellar masses between 11 and 25 M$_\odot$.

3.1.1.2 Terrestrial and Extraterrestrial Input into Deep-Sea Sediments

In addition to a potential SN signal of ^{26}Al, a high input of ^{26}Al from other sources into the *Eltanin* sediment cores is expected. This input may originate from: (i) cosmogenic production of ^{26}Al, (ii) meteoric influx that might carry ^{26}Al, and (iii) in-situ production of ^{26}Al directly in the marine sediment or in the overlying water column. In the following, production/influx of ^{26}Al from these sources is investigated quantitatively.

(i) Cosmogenic Production

A large fraction of ^{26}Al deposited into deep-sea sediments originates from cosmogenic production in the Earth's atmosphere. Here, ^{26}Al is a spallation product of Ar from secondary neutrons from GCRs. Secondary neutrons are generated from primary reactions of incident cosmic ray particles with a target (e.g. an arbitrary atom in the atmosphere). According to Auer et al. (2009), the atmospheric production rate was reported between 1.6 and 4.4 $\times 10^3$ ats cm^2 yr^{-1} (by J. Beer, which was a private communication, and Lal and Peters (1967), respectively). By measuring ^{26}Al/^{10}Be ratios in atmospheric, firn, and Antarctic ice samples, Auer et al. (2009) calculated a global mean atmospheric production rate of ^{26}Al. The authors determined a value of ^{26}Al/^{10}Be = $(1.89\pm0.05) \times 10^{-3}$. Using the theoretical production rate of ^{10}Be of $P_{10,atm} = 6.6 \times 10^5$ ats cm^{-2} yr^{-1} (Masarik and Beer (2009)) this ratio converts to an average amount of $P_{26,atm} = 1280$ ^{26}Al ats cm^{-2} produced per year in the atmosphere.

Applying this production rate, the atmospheric ^{26}Al influx into marine sediments is investigated in the following. The wet bulk density of the cores used in this work is assumed to be $\rho = 1.35$ g cm^{-3} (chapter 2.2.1) and the mean accumulation rate is $S = 0.32$ cm kyr^{-1} (chapter 2.3.2). The concentration C_{atm} of ^{26}Al atoms in a gram of sediment is calculated with

$$C_{atm} = \frac{P_{10,atm}}{S \times \rho} \times \left(\frac{^{26}Al}{^{10}Be}\right) = \frac{P_{26,atm}}{S \times \rho} = 2.87 \times 10^6 \text{ ats g}^{-1}. \qquad (3.1)$$

Taking into account radioactive decay, this concentration decreases with time corresponding to

$$C_{atm}(t) = 2.87 \times 10^6 e^{-\lambda_{26}t} \text{ ats g}^{-1}, \qquad (3.2)$$

where $\lambda_{26} = 9.7 \times 10^{-7}$ yr^{-1} is the decay constant of ^{26}Al. The resulting curve is plotted in Figure 3.4 (green, dashed).
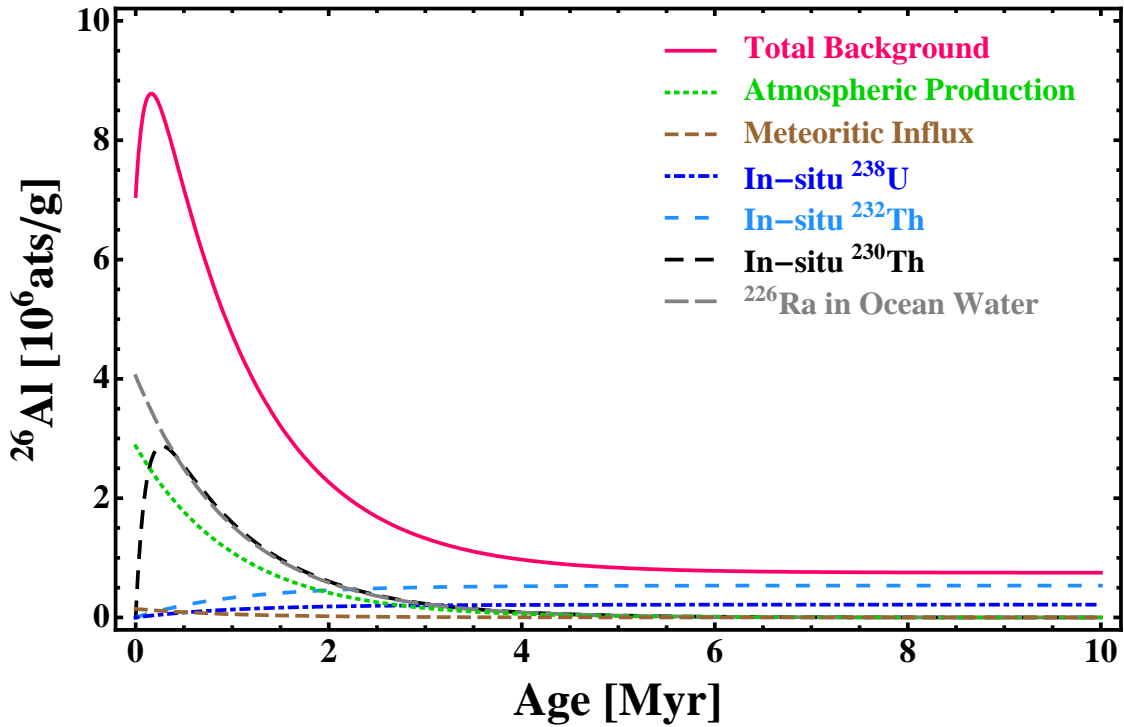
Figure 3.4: Different sources (dashed lines) for input of ^{26}Al into deep-sea sediments at a depth of Z = 4200 m with an accumulation rate S = 0.32 cm kyr^{-1}, and a density $\rho = 1.35$ g cm^{-3}. The total amount of ^{26}Al from all of these sources (solid line) might interfere with a possible SN signal of ^{26}Al located between 2-3 Myr.

(ii) Meteoritic Influx

The extraterrestrial influx of ^{26}Al was determined by Auer et al. (2009) by measuring the atmospheric ratio of ^{26}Al/^{53}Mn. The assumption made in this study is that all ^{53}Mn in the atmosphere is of extraterrestrial origin and none is produced in the atmosphere. The

authors then calculated production rates of ^{26}Al and ^{53}Mn in meteorites and IDPs to obtain the fraction of the atmospheric to the extraterrestrial ^{26}Al/^{53}Mn ratio. They conclude that a fraction of approximately 5 % of ^{26}Al in the atmosphere originates from extraterrestrial influx. Taking this value the calculated meteoric concentration is

$$C_{met}(t) = 1.44 \times 10^5 e^{-\lambda_{26}t} \text{ ats g}^{-1}, \tag{3.3}$$

and can be viewed in Figure 3.4.

(iii) In-situ Production

^{26}Al can not be directly produced from cosmic ray interaction on the ocean floor, as the sediments are shielded by more than 4000 m of water. However, there is another possibility of generating so-called radiogenic ^{26}Al by a reaction occurring within deep-sea sediments, the ^{23}Na(α,n)^{26}Al reaction (Sharma and Middleton, 1989). Plenty of sodium is available; the average salinity of the Indian Ocean is of 3.5 %. The α-particles needed for this reaction are constantly supplied by radionuclides α-decaying in natural decay series. The production rate of ^{26}Al per second and gram of deep-sea sediment is calculated by

$$P_{26} = n_{23} \sum_i A_i \sum_j \int_{E_0}^{E_j} \sigma(E) \left(\frac{dE}{dx}\right)^{-1} dE. \tag{3.4}$$

Here, A_i denotes the specific activity (decays s^{-1} g^{-1}) of the parent nuclide (e.g. ^{232}Th, ^{238}U) of the i-th natural decay chain. A salinity of 3.5 % corresponds to a particle density of $n_{23} = 7.5 \times 10^{20}$ ^{23}Na ats cm^{-3}. $\sigma(E)$ is the cross section of the ^{23}Na(α,n)^{26}Al reaction and dE/dx the energy loss of the j-th α-particle with energy E_j in the i-th decay chain in the sample. The lower limit E_0 of the integral (3.4) is determined from the reaction cross section. It is assumed that the natural decay chain is in equilibrium, then each α-particle contributes to the total production of ^{26}Al by

$$p(\alpha_j) = \frac{\int_{E_0}^{E_j} \sigma(E) \left(\frac{dE}{dx}\right)^{-1} dE}{\sum_j \int_{E_0}^{E_j} \sigma(E) \left(\frac{dE}{dx}\right)^{-1} dE}, \tag{3.5}$$

which is denoted as the production fraction. The α-energies and their production fraction within the natural decay chains of interest are given in Appendix C.1. If more than one α-particle is emitted in a radioactive decay, the intensity weighted mean of their energies was calculated.

^{26}Al production cross sections for the ^{23}Na(α,n)^{26}Al reaction have been determined for different energies by Norman et al. (1982) and are tabulated in Appendix C.2. Figure 3.5 (left, dots) shows the cross sections in mbarn for an energy range of 3 - 9 MeV. Below that energy range, $\sigma(E)$ is negligible. No α-particles generated in the natural decay-chains
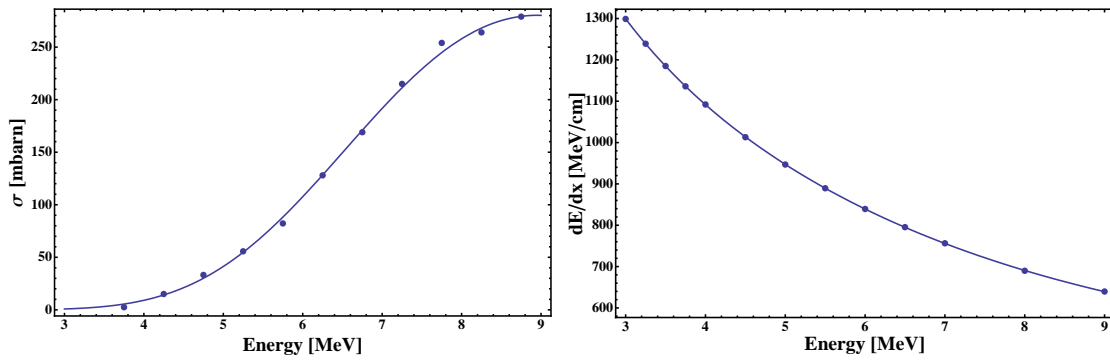
Figure 3.5: Left: Energy-dependent production cross section σ(E) for the ^{23}Na(α,n)^{26}Al reaction (Norman et al., 1982). **Right:** Stopping power of α-particles in a deep-sea sediment using a density of 1.35 g cm^{-1} (determined with SRIM, Ziegler et al. (2010)). Solid lines indicate fits through the data points.

have energies above 9 MeV. To calculate the integral in equation (3.4), the data is fitted with

$$\sigma(E) = 2.58 \times 10^{-5} e^{-1.52\,E}\,E^{13.59}, \tag{3.6}$$

which is shown as a solid line in Figure 3.5 (left).

The stopping power dE/dx of the α-particles in a deep-sea sediment was taken from SRIM (The **S**topping and **R**ange of **I**ons in **M**atter, version 2013, see e.g. Ziegler et al. (2010) or www.srim.org). The simulations of charged particles moving through a medium were carried out for α's in the energy range of 1 - 10 MeV (Figure 3.5, right). The matter simulates a typical pelagic sediment, consisting of a mixture of clay minerals (SiO_4 and Al), calcium carbonate ($CaCO_3$) and water (H_2O). The input and the resulting data is presented in Appendix D. This stopping power of α-particles in deep-sea sediments for different energies was fitted with

$$\frac{dE}{dx}(E) = 1132 + \frac{1512}{E} - 139\,e^{-0.071\,E}\,E \tag{3.7}$$

Figure 3.5 (right) displays the stopping power versus the particle energy as obtained by the SRIM simulation (points) and the fit to the data shown as solid line.

Radiogenic ^{26}Al production rates have been quantified from three parts of natural decay series: α-particles that are generated in the radium and thorium series within a deep-sea sediment and, in addition, α's produced from radioactive decays starting with the mother isotope ^{230}Th in sea water. α-particles from the actinium series do not significantly produce ^{26}Al and were therefore neglected.

^{238}U and ^{232}Th in Minerals

Sharma and Middleton (1989) computed an amount of 6×10^5 ^{26}Al ats g^{-1} being produced in-situ in pelagic clays. It is assumed that uranium, thorium and sodium are homogeneously distributed within the sample. An average concentration of 1 ppm for ^{238}U ($t_{1/2}$

= 4.5 Gyr) and 5 ppm for ^{232}Th ($t_{1/2}$ = 14 Gyr) in deep sea sediments is assumed. Using equation (3.4), the production rates of $P_{26,238}$ = 0.21 ats g^{-1} yr^{-1} and $P_{26,232}$ = 0.52 ats g^{-1} yr^{-1} are obtained. Here, $P_{26,238}$ corresponds to the production of ^{26}Al from α-particles generated in the ^{238}U decay series, $P_{26,232}$ refers to the ^{232}Th decay series. Thus, the concentrations of ^{26}Al generated from the radium and thorium series taking into account exponential decay are calculated with

$$C_{238}(t) = \frac{P_{26,238}}{\lambda_{26}}(1 - e^{-\lambda_{26}t}) = 2.15 \times 10^5(1 - e^{-\lambda_{26}t}) \text{ ats g}^{-1}, \tag{3.8}$$

$$C_{232}(t) = \frac{P_{26,232}}{\lambda_{26}}(1 - e^{-\lambda_{26}t}) = 5.35 \times 10^5(1 - e^{-\lambda_{26}t}) \text{ ats g}^{-1}. \tag{3.9}$$

The corresponding functions are plotted in Figure 3.4. Adding these two concentrations approaches a value of radiogenic ^{26}Al production of almost 7.5×10^5 ats g^{-1} for ages $\gtrsim$3 Myr of the deep-sea sediment. This value is comparable to the concentration estimated by Sharma and Middleton (1989).

^{230}Th from Sea Water

The main source of ^{230}Th ($t_{1/2}$ = 75.4 kyr) in a deep-sea sediment is not the production from ^{234}U located directly within the sediment. Instead, it is predominantly generated from isotope ^{238}U being dissolved in sea water, which decays to ^{234}U and subsequently to ^{230}Th. The latter is then quickly stripped from the overlying water column and built into the sediment (Henderson et al., 1999). An approach on calculating the ^{230}Th concentration in abyssal sediments is discussed in Kadko (1980):

With an average oceanic activity ratio of A(^{234}U)/A(^{238}U) = 1.14 (Koide and Goldberg, 1963) and a concentration of ^{238}U of 2.4 dpm l^{-1} (Ku et al., 1977) the activity of ^{234}U becomes 2.8 decays per minute (dpm) per liter of sea water. As ^{234}U decays to ^{230}Th, this value is equal to the number of ^{230}Th atoms produced per minute per liter, 2.8 min^{-1} l^{-1}. Translating this number into to a column density N_{SW} (the abbreviation SW denotes sea water) yields

$$N_{SW} = (2800 \text{ ats min}^{-1} \text{ m}^{-3}) \times Z \tag{3.10}$$
$$= 0.28\,Z \text{ ats min}^{-1} \text{ cm}^{-2}. \tag{3.11}$$

Here, Z is the height of the water column, which is equal to the depth of the sediment below the sea surface. It is assumed that all ^{230}Th in the water column with height Z is build into the sediment. The sediment cores investigated in this work were located at a depth of Z = 4200 m. Inserting this value for Z into equation (3.11) yields N_{SW} = 1176 ats min^{-1} cm^{-2}. The total input rate of ^{230}Th is

$$A_{SW} = \lambda_{230}N_{SW} + 0.6 = 11.4 \text{ dpm cm}^{-2} \text{ kyr}^{-1}, \tag{3.12}$$

where a constant continental input rate of 0.6 dpm cm^{-2} kyr^{-1} (Ku et al., 1977) is added. With a sedimentation rate of S = 0.32 cm kyr^{-1} and a wet bulk density of ρ = 1.35 g cm^{-3},

the activity of ^{230}Th per gram of sediment is

$$A_{230} = \frac{11.4}{S\rho} = 26.4 \text{ dpm g}^{-1}. \tag{3.13}$$

Two cases have to be considered: a fraction of 50-70 % of the daughter product of ^{230}Th, ^{226}Ra ($t_{1/2} = 1.6$ kyr), diffuses out of the sediment (Kadko, 1980). Such losses of ^{226}Ra are especially effective at low sedimentation rates. Therefore, after decay of ^{230}Th, the decay chain is split into two components. One is the fraction that stays in the sediment, the other is the fraction that diffuses into the ambient sea or pore water. Here, the assumption is made, that half of ^{226}Ra resides in the sediment. Thus, the production rate of ^{26}Al generated from α-decay of ^{230}Th as well 50 % of subsequent decays starting with ^{226}Ra within the deep-sea sediments results in $P_{26,230} = 3.62$ ats g^{-1} yr^{-1} (using equation 3.4). Then, concentrations taking into account exponential decay are written as

$$C_{230}(t) = \frac{P_{26,230}}{\lambda_{26}} \frac{\lambda_{230}}{\lambda_{26} - \lambda_{230}}(e^{-\lambda_{230}t} - e^{-\lambda_{26}t}) = -4.81 \times 10^6(e^{-\lambda_{230}t} - e^{-\lambda_{26}t}) \text{ ats g}^{-1}. \tag{3.14}$$

λ_{26} and λ_{230} are the decay constants of ^{26}Al and ^{230}Th, respectively. The ^{26}Al concentration generated from the decay of ^{230}Th and its daughters, C_{230}, has a maximum at 274 kyr. ^{230}Th itself contributes only a small fraction of 1.4 % to the total production (Appendix C.1).

The portion of ^{226}Ra, which diffused out of the sediment material, produces ^{26}Al in the ambient water. In order to obtain the stopping power dE/dx of α-particles in water, a SRIM simulation was carried out (Appendix D). Then, the production rate of ^{26}Al by α-particles released from ^{226}Ra and its daughter products in water is calculated using equation 3.4. This results in $P_{26,226} = 3.91$ ats g^{-1} yr^{-1}. Assuming all ^{226}Ra isotopes diffuse into the water column above the sediment, an exponential decay function is used for calculating the ^{26}Al concentration,

$$C_{226}(t) = \frac{P_{26,226}}{\lambda_{26}} = 4.05 \times 10^6 e^{-\lambda_{26}t} \text{ ats g}^{-1}. \tag{3.15}$$

Figure 3.4 shows all contributions to the production of ^{26}Al. The total input is plotted as the solid line. According to the curve representing the total amount of ^{26}Al within a deep-sea sediment, its concentration should increase the first 200 kyr. Towards older ages it decreases and approaches a value of 7.5×10^5 ats g^{-1} at approximately 5 Myr.

It has to be noted that the approximations made for the in-situ production of ^{26}Al result from very simplified models, which give an upper limit and probably overestimate the production. Especially the assumption, that U, Th and Na are uniformly distributed is problematic. Na originates from the sea water and is likely to be adsorbed onto mineral particles. ^{238}U and ^{232}Th are residing predominantly inside the mineral phases, where the α-particles are stopped after a few 10 µm. The highest cross-section for producing ^{26}Al via the ^{23}Na(α,n)^{26}Al reaction is for the highest α-energies. Even if the particles reach the mineral surface, where ^{23}Na might be located, they have lower energy left to make a

reaction. For instance, an α-particle with 8 MeV that traveled a distance of 26 μm through sediment matter has a residual energy of 6 MeV (SRIM simulation, Appendix D). However, the cross-section for the ^{23}Na(α,n)^{26}Al for an α-particle of 6 MeV is approximately 40 % of the cross-section for an 8 MeV α. In table C.1 in the Appendix, it is shown, that the few α-particle with the highest energies of 7 and 8 MeV contribute to approximately half of the total production of ^{26}Al.

Within the sea water particles are more likey to be uniformly distributed. Here, α's may be consumed by other reactions (such as ^{35}Cl(α,d)^{37}Ar, (Fabryka-Martin, 1988)) and therefore lost for the production of ^{26}Al .

These simple calculations are compared with measured ^{26}Al data (chapter 5).

3.1.2 ^{53}Mn

^{53}Mn has the longest half-life of the radionuclides investigated in this work. It decays with a half-life of $t_{1/2}$=(3.7±0.4) Myr (Honda and Imamura, 1971) via electron capture to its stable isobar ^{53}Cr. Like ^{26}Al and ^{60}Fe it is produced in massive stars. However, the major contribution to the ^{53}Mn content in deep-sea sediment comes from influx of extraterrestrial particles to Earth, as detailed below.

3.1.2.1 Nucleosynthesis in Massive Stars

When a massive star explodes, a shock wave moves through its interior and passes the silicon and oxygen burning shell. ^{53}Mn is mainly produced during explosive silicon burning in the innermost parts of the star (within a radius of ~6000 km). Here, the temperatures range between 4 and 5×10^9 K. Iron-group isotopes are synthesized producing also ^{53}Fe ($t_{1/2}$ = 8.5 min), which decays to ^{53}Mn (Figure 3.1). A small fraction of ^{53}Mn is synthesized during explosive oxygen burning, where temperatures are lower of 3-4 $\times 10^9$ K (Woosley et al., 2002; Meyer, 2005).

Nucleosynthesis yields were published by Woosley and Weaver (1995), Rauscher et al. (2002), Woosley and Heger (2007), and Chieffi and Limongi (2013). The ejected amounts of ^{53}Mn range from 1×10^{-5} to ~4×10^{-4} M$_\odot$ for progenitor stars with masses between 11 and 25 M$_\odot$ (Figure 3.6).
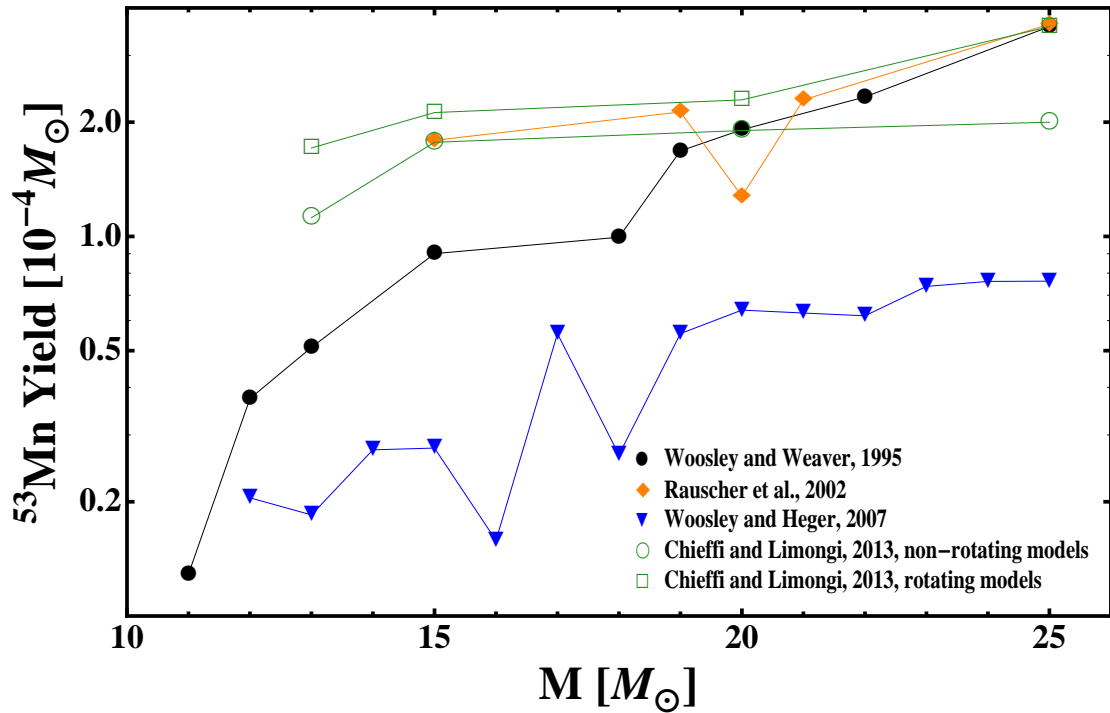
Figure 3.6: Comparison of theoretical ^{53}Mn nucleosynthesis yields (displayed in logarithmic scale in units of 10^{-4} M$_\odot$) from several research groups for stellar masses between 11 and 25 M$_\odot$.

3.1.2.2 Extraterrestrial Influx

The major input of ^{53}Mn into deep-sea sediments originates from extraterrestrial influx of IDPs and MMs. In large objects, such as meteoroids, asteroids, comets as well as the moon, ^{53}Mn is produced by both, SCRs and GCRs. GCRs, with high energies between a few GeV/nucleon and 10^{20} eV/nucleon are able to penetrate several 10's of cm into the target (see e.g. Leya et al. (2000)). SCRs, with lower energies of 1 to some 100 MeV/nucleon, produce ^{53}Mn close to the surface. The main production of ^{53}Mn in large objects occurs from reactions of secondary neutrons with iron in the object. A smaller fraction of ^{53}Mn is obtained from reactions with nickel (Merchel et al., 2000), which contribute to the total production of ^{53}Mn by ~3 % (Leya et al., 2000).
The annual influx of ^{53}Mn has been estimated to be approximately 200 atoms cm^{-2} yr^{-1} by Auer (2008).

Direct in-situ production of ^{53}Mn from cosmic rays is negligible, since the samples of this work were shielded by 4000 m of ocean water.

3.1.3 ^{60}Fe

The long-lived radionuclide ^{60}Fe, with a half-life of (2.62 ± 0.04) Myr (Rugel et al., 2009), is mainly produced during the s-process in massive stars. In contrast to ^{26}Al and ^{53}Mn, no significant terrestrial end extraterrestrial input of ^{60}Fe is expected into marine sediments, which might add to an ^{60}Fe SN signature. The possibility of extraterrestrial particles transporting ^{60}Fe into terrestrial archives will be discussed in the following.

3.1.3.1 Production in Massive Stars

The following description of the nucleosynthesis of ^{60}Fe in massive stars is based on Limongi and Chieffi (2006). ^{60}Fe is mainly synthesized in massive stars by neutron capture on ^{59}Fe during He and C shell burning and during the explosion of the star. Since ^{59}Fe - which itself is created by neutron capture on its stable isotope ^{58}Fe - has a very short half-life of ~44 days, the production of ^{60}Fe competes with the β^--decay of ^{59}Fe to the stable nuclide ^{59}Co (Figure 3.1). Neutron densities larger than 3×10^{10} cm^{-3} are needed to overcome the ^{59}Fe bottleneck at temperatures lower than T = $10^{8.7}$ K. At higher temperatures the half-life of ^{59}Fe decreases significantly, whereas the neutron capture cross section for the ^{59}Fe(n,γ)^{60}Fe reaction is affected only mildly. Therefore the neutron densities have to increase to ~3×10^{11} cm^{-3} at T = 10^9 K and to ~6×10^{12} cm^{-3} at T = $10^{9.3}$ K to produce a significant amount of ^{60}Fe. The half-life of ^{60}Fe has a strong temperature dependence, dropping to half a year at T = 10^9 K and to ~14 min at T = $10^{9.4}$ K. However, because of the high neutron densities, the (n,γ) reaction always overcomes the β^--decay of ^{60}Fe to ^{60}Co. At temperatures higher than 2×10^9 K ^{59}Fe and ^{60}Fe are destroyed by photodisintegration via the (γ,n) and (γ,p) reactions. These reactions and conditions apply to all environments mentioned above, which produce ^{60}Fe.

He-shell burning creates a significant amount of ^{60}Fe only in stars that enter the Wolf-Rayet phase, namely stars with masses larger than 40 M$_\odot$. The main neutron production arises from the ^{22}Ne(α,n)^{25}Mg reaction at temperatures above 4×10^8 K. The He-shell in stars with lower masses does not reach temperatures high enough to produce sufficiently high neutron densities.

In the C convective shell temperatures and neutron densities are high enough to produce ^{60}Fe, also in lower-mass stars. The main neutron donor is again the ^{22}Ne(α,n)^{25}Mg process. The ^{12}C(^{12}C,α)^{20}Ne reaction provides a large amount of α particles at temperatures above 10^9 K. In stars with progenitor masses >20 M$_\odot$, neutron densities between 6×10^{11} and 2×10^{12} cm^{-3} are created. The neutron density drops for lower-mass stars. However, in these stars the production of ^{60}Fe in the C convective shell is still the most effective process, compared with He-shell burning and explosive burning (see Figure 3.7). Again, the convective environment is very important. Freshly synthesized ^{60}Fe is transported to regions with lower temperatures, where its half-life increases and the neutron densities are lower, i.e. ^{60}Fe is not consumed by another neutron-capture process. α particles and ^{22}Ne, needed as neutron donors via the ^{22}Ne(α,n)^{25}Mg reaction, are transported due to convection into the regions where ^{60}Fe is produced.
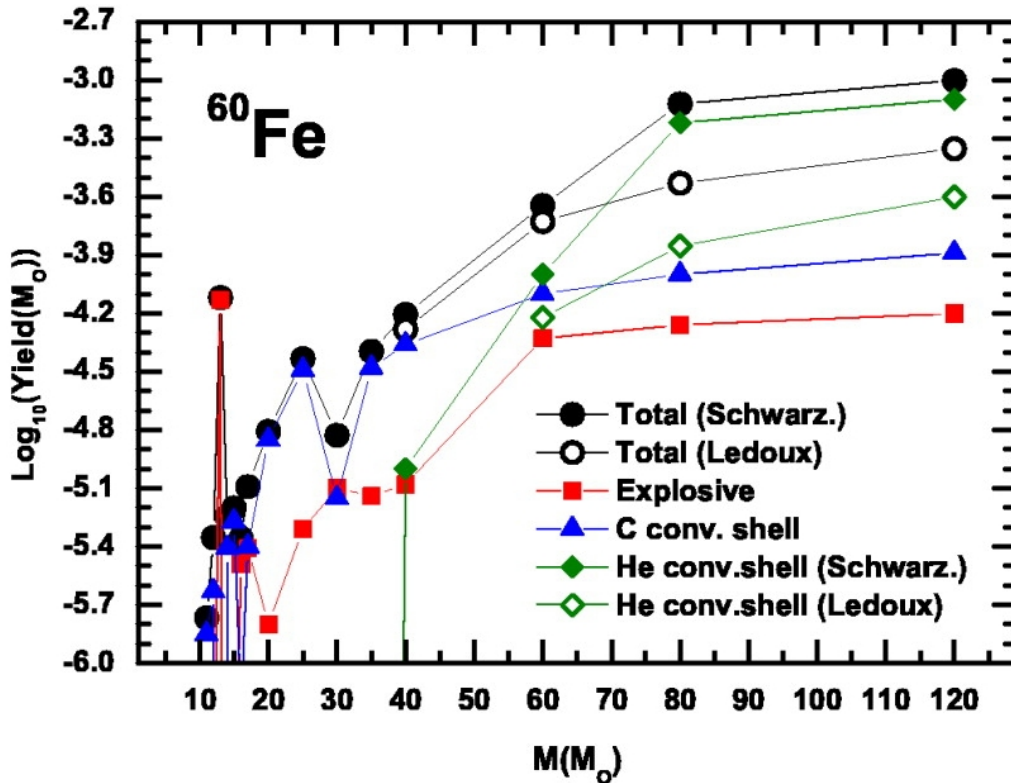
Figure 3.7: Contribution of the ^{60}Fe production from different stellar environments to the total nucleosynthesis yield (displayed in logarithmic scale in units of $M_\odot$) as a function of initial stellar mass (in units of $M_\odot$) (Limongi and Chieffi, 2006).

During the SN explosion, additional ^{60}Fe nucleosynthesis occurs roughly in the same region where ^{26}Al is produced. This is at the base or inside the C convective shell, where the temperature reaches values of the order of 2.2×10^9 K. The amount of ^{60}Fe produced depends mainly on the abundance of nuclei such as ^{20}Ne, ^{12}C, ^{23}Na, and ^{23}Ne. In lower mass stars in the range of 11-15 $M_\odot$, their abundances are low, therefore the contribution of explosive yields to the total yields are low (see Figure 3.7). However, "high mass stars" above 40 $M_\odot$ show a significant contribution from explosive burning to the production of ^{60}Fe.

An overview of various theoretical nucleosynthesis yield calculations between an initial stellar masses of 11-25 $M_\odot$ is given in Figure 3.8. These yields range from 1×10^{-6} to 3×10^{-4} $M_\odot$.
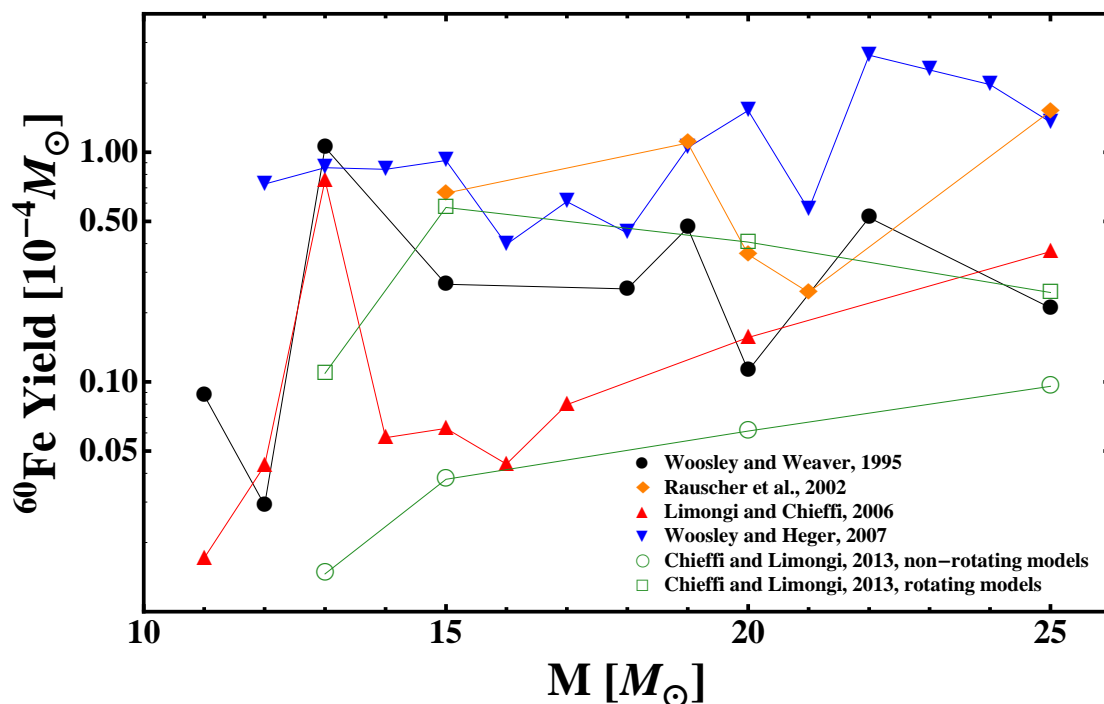
Figure 3.8: Comparison of theoretical ^{60}Fe nucleosynthesis yields (displayed in logarithmic scale in units of 10^{-4} M$_\odot$) from several research groups for stellar masses between 11 and 25 M$_\odot$.

3.1.3.2 Extraterrestrial Influx

It was suggested earlier in this work that no significant amounts of terrestrial and extraterrestrial ^{60}Fe would add to a potential SN signal in the sediment samples. However, there might be a possibility of extraterrestrial material of non-SN origin being deposited into deep-sea archives.

It is known, that ^{60}Fe is produced in asteroids or meteoroids by spallation reactions from cosmic rays on the nickel isotopes ^{62}Ni and ^{64}Ni (Knie et al., 1999b), with isotopic abundances of 3.63 % and 0.93 % (chart of nuclei, 8th edition, 2012). The reactions producing ^{60}Fe are mainly induced by GCRs; the contribution from SCRs is very low (Knie et al., 1999b). Reactions are primarily caused by secondary neutrons. Primary protons produce ^{60}Fe predominantly at the surface of an irradiated body. A comparable production rate arises further within the target from secondary protons (Merchel et al., 2000), see Figure 3.9.

Dust grains separated from surfaces of their parent bodies due to collisions in the asteroid belt might transport ^{60}Fe into terrestrial archives. While being transported through space, the dust grains are irradiated by cosmic rays. However, the sizes of IDPs or MMs are too small to build up a secondary neutron flux (Knie et al., 1999b).

Productions rates of ^{60}Fe in cosmic-ray exposed IDPs and MMs were calculated by Trappitsch and Leya (2013). They include recoil losses: produced particles gain a momentum
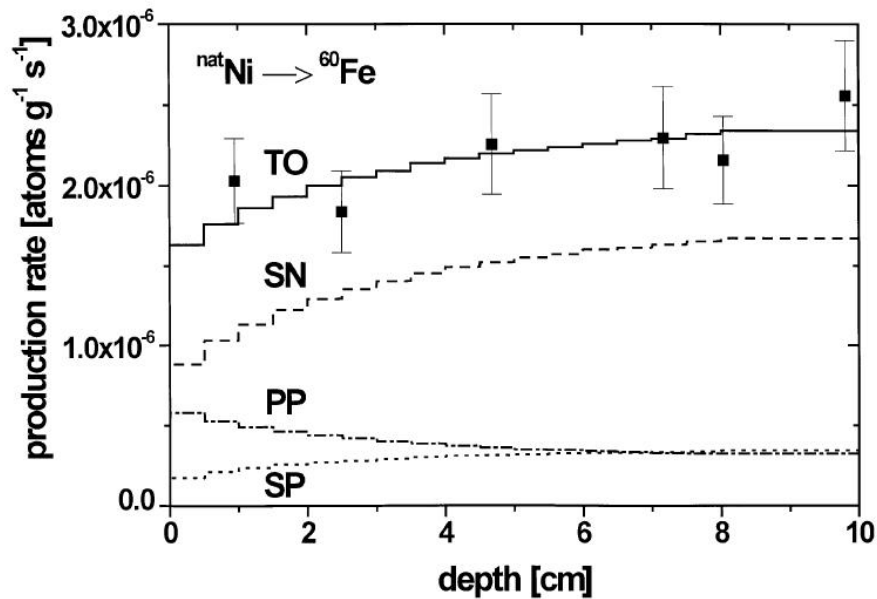
Figure 3.9: Measured production rates (squares) as a function of depth for an artificial meteoroid (Merchel et al., 2000). Different incident particles for the production of ^{60}Fe from ^{nat}Ni were used to fit the experimental results: primary protons (PP), secondary protons (SP), and secondary neutrons (here: SN), which sum up to the total production rate (TO).

after the collision between the incident cosmic ray particle and the target nucleus. Thus, freshly produced ^{60}Fe might leave the MM. For ^{60}Fe a production rate of 0.51 dpm kg^{-1} Ni is calculated Trappitsch and Leya (2013), a value similar to concentrations measured in meteorites by Knie et al. (1999b), which varied between 0.66 and 2.8 dpm kg^{-1} Ni. The input of extraterrestrial ^{60}Fe influx into deep-sea sediments will be further discussed in Chapter 5.6.5.

3.1.4 ^{10}Be

The half-life of ^{10}Be was recently determined with a value of 1.387±0.012 Myr (which is a weighted mean with standard error of Korschinek et al. (2010) and Chmeleff et al. (2010)).
In this work, ^{10}Be is measured to obtain a chronology of the *Eltanin* sediment cores via ^{10}Be/^{9}Be dating (section 2.3.3).

3.1.4.1 Production in Massive Stars

Light elements (z<6) are easily destroyed by proton capture at stellar temperatures (Reeves, 1994). As a result, no ^{10}Be ejected in a SN explosion. The most recently published yields from Chieffi and Limongi (2013) indicate values in the order of 10^{-60} M$_\odot$ of ^{10}Be.

3.1.4.2 Terrestrial and Extraterrestrial Production

(i) Cosmogenic Production

Spallation reactions, which produce cosmogenic ^{10}Be from secondary neutrons of galactic cosmic rays in the Earth's atmosphere, occur on the most abundant elements. These elements are predominantly nitrogen (with an abundance of 78 % in the atmosphere), with a lower contribution from oxygen (21 %). The average production rate of ^{10}Be was calculated to a value of $P_{10,atm} = 0.021$ ats cm^{-2} s^{-1} or $6.6{\times}10^5$ ats cm^{-2} yr^{-1} (Masarik and Beer, 2009). Assuming a wet bulk density of the sediment samples of $\rho = 1.35$ g cm^{-3} and an average accumulation rate of $S = 0.32$ cm kyr^{-1}, the concentration of ^{10}Be ats g^{-1} decreases with time as

$$C_{10}(t) = \frac{P_{10,atm}}{S \times \rho} e^{-\lambda_{10}t} = 1.52 \times 10^9 \ e^{-\lambda_{10}t} \text{ ats g}^{-1}. \tag{3.16}$$
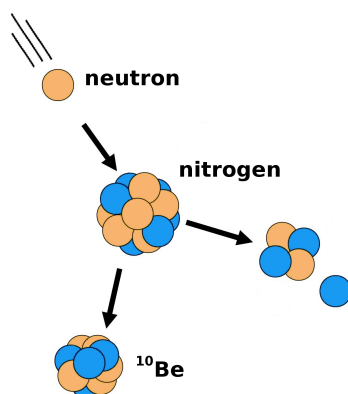
Figure 3.10: Spallation reaction of a secondary GCR neutron on nitrogen in the Earth's atmosphere producing ^{10}Be via ^{14}Ni(p,3p2n)^{10}Be (adapted from Silke Merchel).

(ii) Other Sources of ^{10}Be Input in Deep-Sea Sediments

A direct in-situ production of ^{10}Be from cosmic rays in the sediment is not possible due to shielding of 4000 m of ocean water. Trace amounts of ^{10}Be might be produced directly in the sediment samples by the ^{7}Li(α,p)^{10}Be, ^{9}Be(n,γ)^{10}Be, ^{10}B(n,p)^{10}Be, and ^{13}C(n,α)^{10}Be reactions (Sharma and Middleton, 1989). The α particles are generated in natural decay chains. Production rates of neutrons required for the neutron-induced reactions producing ^{10}Be, strongly depend on the composition of the samples (Feige et al., 1968). These are generated by (α,n) reactions on light nuclei such as ^{23}Na, ^{25,26}Mg and ^{27}Al. Sharma and Middleton (1989) calculated a value of in-situ produced ^{10}Be in pelagic clays of 4.8×10^2 ats g^{-1}. This value is three orders of magnitudes lower than the in-situ production of ^{26}Al. Given the 500 times higher atmospheric production of ^{10}Be compared to ^{26}Al, the radiogenic sources of ^{10}Be are negligible. The same argument is valid for the extraterrestrial input of ^{10}Be by IPDs and MMs.

3.2 Transport Mechanisms

The debris ejected from a stellar explosion will be transported through the ISM. Some of these dust particles may enter the heliosphere and spiral towards the sun, of which a fraction is deposited on Earth eventually. In which form the SN-produced radionuclides will finally settle on the sea floor (within dust grains or as other particles) is not known. Scenarios involving single ions as well as dust grains being transported into terrestrial archives are discussed in this section.

3.2.1 Transport from the Site of Stellar Explosion to Earth

The solar system is located within a large hot cavity in the local ISM, the Local Bubble (LB). This structure was presumably formed by a series of SNe, which exploded over a time period of roughly 14 Myr. Fuchs et al. (2006) suggested a total of 14-20 SNe, the last occurring a few 100 kyr ago.

The LB was presumably formed by a series of SN explosions occurring in a young stellar moving group passing the Solar System. The remaining members belong today to the subgroups Upper Centaurus Lupus (UCL), Lower Centaurus Crux (LCC), and Upper Scorpius (US) of the Scorpius-Centaurus association.

At time of formation of a stellar population, the stars have a certain mass distribution. This so-called initial mass function (IMF) is usually described by a power-law. The number of stars scales with their masses with $m^{-2.35}$ (Salpeter, 1955) (for stars more massive than 1 $M_{\odot}$). This means that the number of stars increases with decreasing masses. The stellar moving group, presumably responsible for the formation of the LB, lacks of stars with masses larger than ~8 $M_{\odot}$. This indicates, that these have already exploded as SNe. The kinematic development of the still existing stars was extrapolated in time to the past 30 Myr (Fuchs et al., 2006) (Figure 1.3) making it possible to estimate distances of SNe to the Solar System at any point in time during the past 30 Myr (Feige, 2010; Breitschwerdt et al., 2012). The explosion times can be inferred from a mass-age relation, as the stellar Main-Sequence life-time correlates with its mass. According to (Feige, 2010), the two closest explosions to the Solar System (between 90 and 100 pc) occurred at 2.3 (UCL) and 2.6 Myr BP (LCC).

3.2.1.1 SN Expansion Modeling

The explosion of a SN into a medium shaped by a previous explosion, as it is the case within the LB, and deposition of ^{60}Fe into the ferromanganese crust 237KD has been studied analytically by Feige (2010). In this work, the signal in the crust was assumed to be of multiple SNe origin. For each SN the expansion time needed to reach the Solar System from the location of the explosion was calculated. Usually, the Sedov-Taylor solution (Sedov, 1993) is applied for calculation of a SNR expansion into an ISM with a certain constant density ρ_{ISM}. Due to the inhomogeneous character of the ISM for the specific case of the LB, the Sedov-Taylor solution (Sedov, 1993) is not a suitable approximation for this problem. Instead, a modified model developed by Kahn (1998)

was used. It describes a second SN explosion into a medium with density $\rho = \Omega r^n$, with $n = 9/2$ and Ω a constant, which specifies the shape of the ISM after the first explosion, obtained by the Sedov equation. Then, the radius of the SNR with time t is derived with (Kahn, 1998)

$$r_{Kahn}(t) = \left(\frac{(n + 5)(2n + 7) \, E_{SN}}{6\pi \, \Omega} \right)^{\frac{1}{n+5}} t^{\frac{2}{n+5}}. \tag{3.17}$$

Here, r is the distance at time t of the expanding SN shell from the center of the explosion, and E_{SN} is the explosion energy, which is typically in the order of 10^{51} erg for a CCSN. With this model it was possible to calculate expansion times of explosions of the "missing" stars from the stellar moving group with distances obtained from trajectories of remaining stars. The most probable explosion distances from Earth between 2 and 3 Myr ago reside within 90-100 pc, yielding travel times of approximately 180-250 kyr of an expanding SN shell before reaching the solar system (Feige et al., to be published).

3.2.1.2 Dust in Supernova Remnants

In order to be deposited on Earth, the SN debris must first penetrate the heliosphere. Atomic ions arriving at the boundaries of the Solar System within the SN plasma, are to a large fraction repelled by the ram pressure of the solar wind and deflected by the interplanetary magnetic field. Condensation into dust grains within the SNR facilitates entering of long-lived radionuclides into the solar system due to their lower charge/mass ratio compared to atomic ions (Athanassiadou and Fields, 2011).

Dust particles are synthesized preferably in high gas-density environments such as atmospheres of AGB and SAGB-stars, Wolf-Rayet stars, and ejecta of novae and SNe (Cherchneff, 2014). Here, molecules (SiC, SiO, CO, AlO, FeS, etc.) and subsequently small clusters (such as silicates, carbon, metal oxides) are formed (Sarangi and Cherchneff, 2013a). These clusters with sizes less than one nm condense and form dust grains of variable chemical composition, most abundantly silicates, diamond, silicon carbide, metal oxides, pure metal and others (Ott and Hoppe, 2007; Cherchneff, 2014). Grain sizes of interstellar dust particles (ISDs) vary from the nm-range up to a few µm.
SN dust grains have been detected for instance by analyzing spectra of SNe in a wide wavelength range such as the mid- or far-infrared (e.g. Gomez (2013)). They are analyzed by space missions like *Pioneer 10* and *11, Galileo, Cassini*, and *Ulysses* (see e.g. Gruen et al. (1994); Altobelli et al. (2005), and references therein) or can directly be measured in the lab by extracting presolar dust grains from meteorites and IDPs, where the isotopic signature allows to differentiate between SN and other sources (Ott and Hoppe, 2007; Westphal et al., 2014).

However, formation of dust in SNRs is a young topic with unsolved questions, which are currently under investigation. Observations of high redshift galaxies (z>5, which corresponds to an age younger than one Gyr of the Universe) revealed large amounts of dust, which are difficult to explain without taking into account SNe as dust factories (e.g. Gomez (2013); Kotak (2014), and references therein). In contrast to AGB-stars,

which are long known to form dust in their stellar envelopes (e.g. Andersen (2007)), the harsh environments of SN ejecta were believed to prevent the production or efficiently destroy freshly condensed dust grains via collision and sputtering processes (Jones et al., 1994). Nonetheless, the observed dust in the early universe can not be explained by low mass AGB-stars, as their life-times (0.1-1 Gyr) were comparable to the age of the universe (Morgan and Edmunds, 2003). Including a contribution of dust from SNe helps to explain the dust budget (Rowlands et al., 2014).

Theoretical models of dust formation in SNRs indicate a high dust condensation efficiency. Dust yields of up to 1 $M_\odot$ are predicted by several studies as shown in Figure 3.11. Early observations of warm dust (> 60 K) for instance with the *Spitzer* and Gemini South telescopes could not confirm these predictions and found only low dust masses of 10^{-3}-10^{-4} $M_\odot$ in SNRs such as Cassiopeia A (Rho et al., 2008), the Crab Nebula (Temim et al., 2012), and SN1987A (Bouchet et al., 2004). Subsequent cold dust (<40 K) observations with *Herschel*, ALMA, and SCUBA reveal a much larger efficiency of dust formation that is consistent with theoretical models. Masses of cold dust observed in the above mentioned SNRs are now ranging between 0.1-1 $M_\odot$ (see Gomez (2013) and references therein).
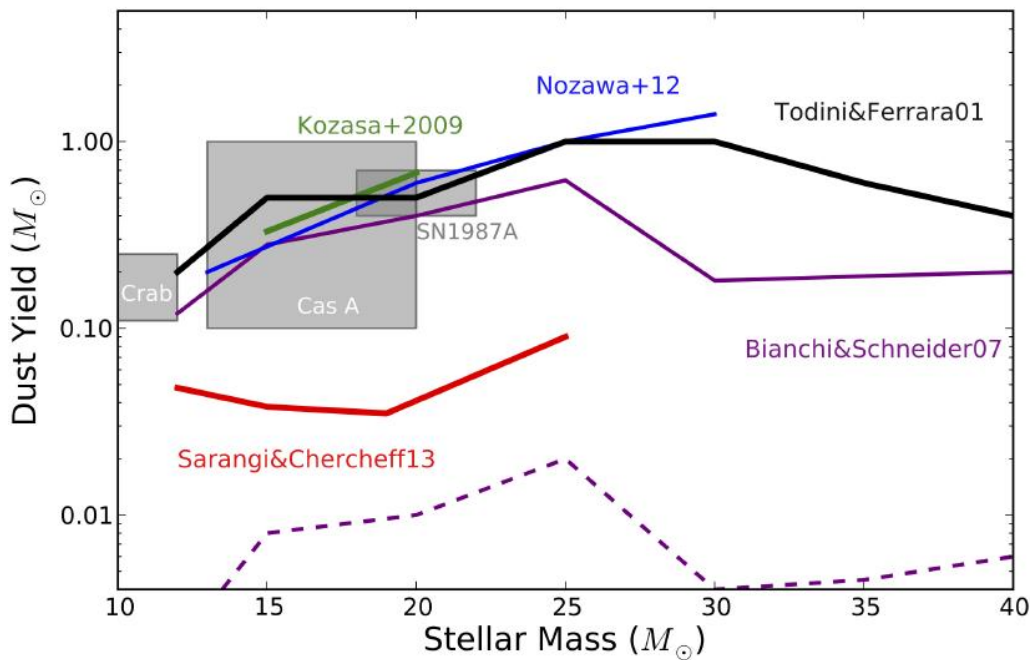
Figure 3.11: Theoretical models of dust masses formed in SNRs (Gomez 2013) in correlation with the initial stellar mass. A classical nucleation theory required for the formation of all types of dust is applied by Todini and Ferrara (2001); Bianchi and Schneider (2007), Kozasa et al. (2009), and Nozawa et al. (2012). Lower masses are predicted by Sarangi and Cherchneff (2013b) using a chemical kinetic theory approach. The dashed line includes destruction of dust grains by the reverse shock in the classical nucleation theory (Bianchi and Schneider, 2007); the gray boxes indicate observational dust yields for Cas A, the Crab Nebula, and SN1987A. Figure from Gomez (2013).

Figure 3.12 depicts observational data of dust masses found in SNRs collected by Gall et al. (2014). The mass fraction of SN dust is correlated with the time after the explosion and a build-up of dust is observable. Gall et al. (2014) analyzed the ejected material of SN2010jl at several stages of development. Although the total dust mass of this and other observed remnants is very low at young ages, an extrapolation to later ages yields high dust formation, which is comparable to SN1987A. Furthermore, it is suggested by Gomez (2013) that at the early stages of SNR evolution (within a few 100 days after the explosion) nearly all ejected metals are condensed into molecules and dust. This certainly includes all the elements of interest in this work: ^{26}Al, ^{53}Mn, and ^{60}Fe.
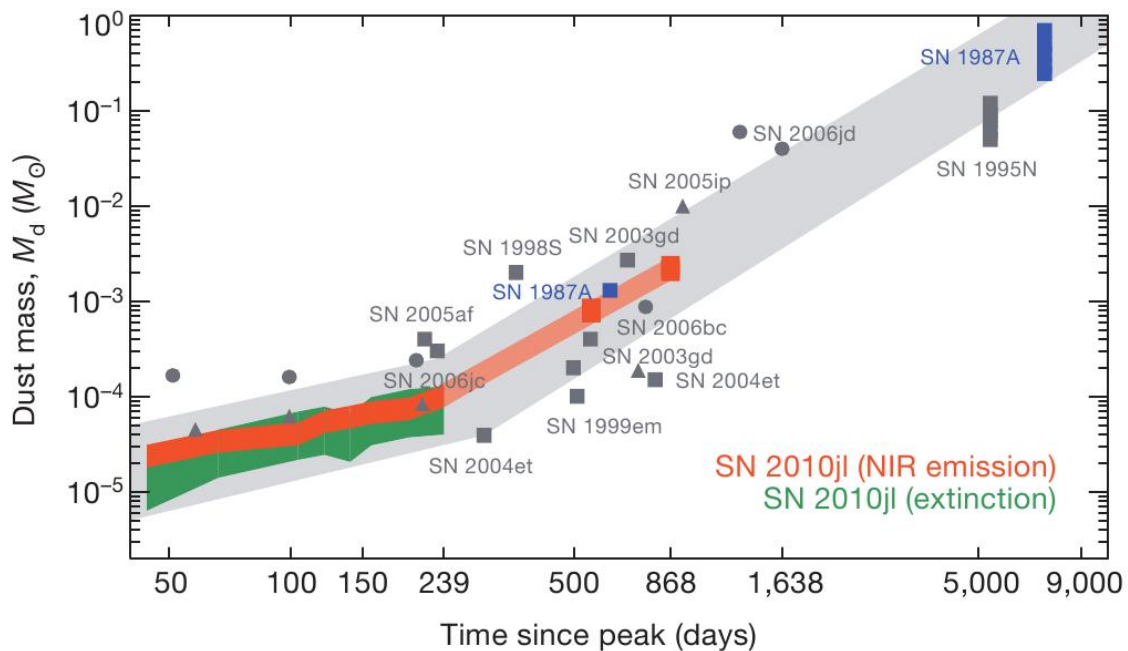
Figure 3.12: Formation of dust masses with time based on observational data (Gall et al., 2014). Based on the temporal evolution of SN2010lj from emission (red) and extinction (green) measurements the build-up of dust masses is predicted up to 9000 days (gray band).

The observed SNRs referred to above are all younger than 100 years and have not yet reached the stage where they enter the Sedov (or Kahn)-phase. Prior to this phase SNRs expand freely with r = v_{ej}t through the interstellar medium until the swept-up ISM mass equals the ejecta mass, causing the remnant to decelerate. This marks the end of the free-expansion phase. Thus, a reverse shock travels through the remnant towards the center of explosion, heating up the medium to very large temperatures and possibly destroying the freshly formed dust particles (Gomez, 2013).

Recent studies by Gall et al. (2014) and Gomez (2014) of SN2010jl provide evidence for the formation of large dust grains with sizes up to 4.2 µm in the SN ejecta. Such large grains are believed to survive the reverse shock (Silvia et al., 2010). Numerical simulations of a reverse shock passing through a clumpy ejecta medium demonstrate a high survival rate of grains larger than 0.1 µm. A mass fraction of 30 % is lost here,

whereas most of the grains with sizes <0.1 μm are destroyed. Gall et al. (2014) calculate a mass fraction of 80 % of grains larger than 0.1 μm in SN2010jl by applying the grain size distribution (with n the number of particles)

$$\frac{dn}{da} \sim a^{-\alpha}, \tag{3.18}$$

and convolving it with a volume term a^3, integrating over the radius a.

$$m_a \sim \int a^3 \, a^{-\alpha} \, da, \tag{3.19}$$

The total grain size range evaluated was between 0.001 and 4.2 μm with a the power-law slope $\alpha = 3.6$. Here, m_a is the dust mass. By combining the fraction of 70 % of particles larger than 0.1 μm that survive the reverse shock with the 80 % mass fraction of those grains, it is indicated that a total mass of more than 50 % of dust grains survive the reverse shock.

3.2.1.3 Entering the Solar System

Two scenarios, how dust particles might enter the inner Solar System, were theoretically modeled by Fields et al. (2008) and Athanassiadou and Fields (2011).
One scenario simulates the collision of the heliosphere with the SNR. Here, radionuclides might be deposited onto Earth directly as atomic ions, if the SN shell reaches a distance of 1 AU to the Sun. Fields et al. (2008) conclude, that for an ISM density of 0.1 cm^{-3} a remnant is able to penetrate the Solar System to a distance of a few AU to the sun for a SN distance of 20 pc. Direct deposition is only possible for a SN with a distance of <10 pc. However, these distances do not fit to the trajectories of stars presumably responsible for the formation of the LB and possibly for the deposition of SN-produced ^{60}Fe in a ferromanganese crust 2-3 Myr BP (discussed in section 3.2.1.1). Furthermore, a SN closer than 10 pc to the Solar System would have a hazardous impact on the Earth's biosphere (Gehrels et al., 2003) and no major extinction was observed 2-3 Myr ago.
In their second scenario, Athanassiadou and Fields (2011) study decoupling of charged dust grains from the SN ejecta when they collide with the heliosphere. Here, trajectories of grains with sizes between 0.1 and 0.7 μm were analyzed. Large distances of the SN explosion to the Solar System up to 100 pc are considered. Their results show, that grains with a radius of 0.2-0.7 μm move undisturbed after decoupling from the SN plasma. This indicates, that also ISDs larger than 0.7 μm enter the Solar System undeflected. The 0.1 μm particles are also able to enter the solar system, but are deflected within the solar system.

When entering the Solar System, ISDs differentiate kinematically from IDPs by their trajectories and velocities. They follow hyperbolical (or very eccentric elliptical) instead of elliptical orbits (like IDPs) due to their high relative speeds of up to 100 km s^{-1}. Like IDPs, they slow down due to the interactions with the solar wind, radiation pressure (Poynting-Robertson effect) and other mechanisms, such as deflection of the charged

dust particles by the interplanetary magnetic field and gravitational influences from the gas planets (Meisel et al., 2002).

Indeed, large grains have been detected entering our Solar System. Micrometeors were observed with the Arecibo radar as they entered the Earths atmosphere. By studying their kinematic behavior and tracing back these particles for 10 years, Meisel et al. (2002) identified 108 dust grains of interstellar origin. From their trace when entering due to deceleration and ablation, a grain size range of 0.3-11 μm of the interstellar particles was constrained. These values are in agreement with space missions confirming that ISDs with sizes larger than 0.3-0.4 μm are able to penetrate to the inner solar system (Altobelli et al., 2005).

3.2.2 Transport into Deep-Sea Sediments

Average entrance velocities of interstellar particles into the Earth's atmosphere are between 20-65 km s^{-1} (Meisel et al., 2002). As noted above, dust particles with sizes <20 μm and velocities of 20 km s^{-1} do not melt significantly when colliding with atmospheric particles (Love and Brownlee, 1991). It depends on the entrance velocity, whether a particle survives and reaches the Earth's surface. It is not clear how much grains smaller than 20μm are ablated and how the radionuclides originating from a SN are finally deposited in deep-sea archives. Either, the SN dust grains experience the climatic cycle, but stay rather unchanged when settling on the sea floor or, due to evaporation, SN-elements are released into the atmosphere.

If ^{26}Al is released due to ablation of a SN grain, it is quickly adsorbed onto atmospheric aerosol particles and will be deposited by wet and dry precipitation. Mn and Fe form nanoparticulate (oxyhydr)oxides, which can grow and transform to more stable particles over time. These are washed out from the atmosphere by rain or settle by gravitation (Howe et al., 2004; Raiswell, 2011).
Eventually all extraterrestrial radionuclides, which are transported into the ocean, are in particulate form, either still as preserved interstellar dust grain or as bound to terrestrial particles.

The residence time of dissolved Al in sea water is only short with 50-150 years (Orians and Bruland, 1986). Mn (in dissolved form and as MnCl$^+$) and Fe (as hydroxides) have comparable residence times of up to 100 years (Halbach (1986) and references therein). When transported in small particles (<5 μm) it still may take months to years for the "SN-radionuclides" to reach the sea floor (Robert, 2008). However, these settling times within the ocean are short compared to the expected temporal extension of a SN signal in a marine sediment (see the following section).

3.3 Exposure Time of the Solar System to a SNR[*]

Fields et al. (2005) estimated an exposure time of the solar system to a passing SN shell of 10 kyr. Bishop and Egli (2011) assumed a much larger extension of a SN signature in a deep-sea sediment between 250 and 750 kyr. A narrow peak was calculated by Feige et al. (2012), with a signal width of about 15 kyr. This value was obtained by using the Sedov equation to describe the expansion of a SNR into a thin LB medium with average density of $n = 5 \times 10^{-3}$ cm^{-3}. In the following, the equation from Kahn (1998), which describes a SNR expanding into a medium shaped by a previous SN, is applied to obtain a rough idea on the duration of a SNR encountering the Solar System.

First, the width d of the expanding SN shell at a certain radius r from the center of explosion is calculated. The correlation between these two parameters was estimated to $d/r \sim 1/12$ for a strong shock into a monoatomic gas (e.g. (Clarke and Carswell, 2007)) assuming that the entire ejected mass is concentrated in the SN shell (thin shell approximation). For an explosion distance to the Solar System of 100 pc the shell width becomes approximately $d = 8$ pc under this assumption.

After a SN explosion, a SNR travels freely through the interstellar medium. In this first phase, the SNR travels a distance of $\sim$25 pc in a low-density LB medium of $n = 5 \times 10^{-3}$ cm^{-3}. Subsequently, the remnant enters the second phase, here described with the model of Kahn (1998). The velocity of the expanding shell in the Kahn phase is calculated by derivation of equation (3.17)

$$\dot{r}_{Kahn}(t) = \left(\frac{2(2n+7)}{3\pi(n+5)} \frac{E}{\Omega} r_{Kahn}(t)^{-(n+3)} \right)^{\frac{1}{2}}. \qquad (3.20)$$

By substituting $r_{Kahn}(t)$ from equation (3.17), this equation becomes

$$\dot{r}_{Kahn}(t) = \frac{2}{(n+5)} \frac{r_{Kahn}(t)}{t}. \qquad (3.21)$$

For a travel time t between 180-250 kyr (section 3.2.1.1) and an travel distance r_{Kahn} of 65-75 pc in the Kahn phase, corresponding to 90-100 pc total travel distance, i.e. including the free expansion (the travel time in this phase is a few 1000 years only), the deposition time $t_{dep} = d/\dot{r}$ of SN ejecta material on Earth becomes approximately 100-130 kyr. This model suggests, that the remnant travels an order of magnitude slower when reaching the Solar System than calculated with the Sedov approximation. Instead of a velocity $\dot{r}_{Sedov} = 5\times10^7$ cm s^{-1} (Feige et al., 2012) a value of $\dot{r}_{Kahn} = 7\times10^6$ cm s^{-1} or 70 pc Myr^{-1} is obtained when the SN shell reaches the heliosphere. For this reason, the exposure time of the Solar System to the SNR for the model used above is an order of magnitude larger than in the previous estimation by Feige et al. (2012) and lies between the values proposed by Fields et al. (2005) and Bishop and Egli (2011).

---

[*]Parts of this section were published in Feige et al. (2012)

However, as discussed in Feige et al. (2012), these estimations, to deduce for the temporal extension of a SN signal in terrestrial archives, were carried out using simplified approximations. Various processes involved in the transport of SN radionuclides were not taken into account. For instance the assumption that all ejected SN mass is contained in a thin shell refers mostly to the ISM pushed away from the center of explosion by the expanding shock wave. The ejecta medium is accumulated in a very thin layer on the inner side of this shell making a signal very narrow. Diffuse interstellar medium containing SN-isotopes may form behind the shell leading to a temporal enlargement of the signal. A SNR expands into an inhomogeneous ISM with low-and high-density regions formed by previous SNe, stellar winds, etc. and the ejecta material expands as a clumpy medium rather than in a defined shell.

Processes that might also cause a broadening might occur within the Solar System: Some particles might enter the Earth's atmosphere soon after they have decoupled from the SNR, as others spiral inwards on strong elliptical trajectories. Furthermore, bioturbation within the sediment top layers smears out any short-term SN signal. The growth rate for the deep-sea sediments used in this work, was calculated to 0.32 cm kyr^{-1}. Mixing of the top 10 cm of a sediment corresponds to a time period of ~30 kyr being homogenized. A SN signal much broader than 30 kyr is distributed over a much large section than the mixing length of the sediment and will hardly be affected by such mixing processes. If a signal is shorter than 30 kyr, the SN radionuclides are distributed over the time scale of this mixing length and possibly beyond, as mixing occurs continuously in the sediment top layers. In addition, since the *Eltanin* sediment samples were taken approximately every 3-17 cm corresponding to 8-63 kyr, (section 2.3.2), a risk of missing a sharp signal (narrower than the gaps between samples) is present.

3.4 Expected SN Signal Intensities[*]

In the following, two approaches were used to evaluate the intensity of a possible SN signal from ^{26}Al, ^{53}Mn, and ^{60}Fe in deep-sea sediments. The first (relative) method applied in section 3.4.1 is by scaling from the ^{60}Fe fluence in the ferromanganese crust analyzed by Knie et al. (2004) to deduce an ^{60}Fe fluence in the deep-sea sediment cores. A ^{26}Al and ^{53}Mn fluence is then derived by using ^{60}Fe/^{26}Al and ^{60}Fe/^{53}Mn ratios from theoretical SN nucleosynthesis models.

The second (absolute) method (section 3.4.2) involves direct input of SN material into marine sediments. The SN signal intensity is calculated according to the procedure described in Feige (2010). Here, the distances of the SN explosions to the Solar System and travel times of the expanding SNRs were included in the model. Ejected yields of ^{26}Al, ^{53}Mn, and ^{60}Fe were taken from nucleosynthesis models (see section 3.1).

---

[*]Parts of this section were published in Feige et al. (2012)

3.4.1 Scaling from a SN Signal in a Ferromanganese Crust

The fluence $F_{60,crust}$ (the number of ^{60}Fe particles per cm^2 in the ferromanganese crust 237KD) was calculated from the measured ^{60}Fe/Fe ratio in the layer of 6-8 mm. This layer corresponds to the time range of 1.7-2.6 Myr, in which the SN signal was detected by Knie et al. (2004). The stable iron particle density n_{Fe} in that layer is calculated by

$$n_{Fe} = \frac{w\,N_A\rho}{A}, \tag{3.22}$$

where $N_A = 6.022\times10^{23}$ mol^{-1} is the Avogadro constant and A = 55.845 g mol^{-1} the molar mass. The weight fraction of iron in this layer is w = 15.27 wt% (Poutivtsev, 2007). One obtains a particle density of $n_{Fe} = 2.47\times10^{21}$ ats cm^{-3}. Knie et al. (2004) measured an average ^{60}Fe/Fe ratio of 1.9×10^{-15} in the respective layer. A background of $(^{60}$Fe/Fe$)_b = 2.4\times10^{-16}$ was determined from very old layers of the Fe-Mn crust, where any ^{60}Fe will have decayed to negligible concentrations. These layers originated from a depth of 20-46 mm below the crusts surface and corresponded to an age of 7-13 Myr. This background can be subtracted from the ^{60}Fe/Fe ratio in the layer of 6-8 mm to obtain the component originating from a possible SN. The resulting ^{60}Fe/Fe ratio was then converted to a particle density of ^{60}Fe by

$$n_{60} = ((^{60}\text{Fe/Fe}) - (^{60}\text{Fe/Fe})_b) \times n_{Fe} = 4.10 \times 10^6 \text{ ats cm}^{-3}. \tag{3.23}$$

As the considered layer of the manganese crust has a thickness of 2 mm, the fluence in that layer is then derived as

$$F_{60,crust} = n_{60} \times 0.2 \text{ cm} = 8.20 \times 10^5 \text{ ats cm}^{-2}. \tag{3.24}$$

This number represents the fluence value of ^{60}Fe deduced from the AMS measurement, which is only a fraction of the initially deposited amount of ^{60}Fe. Since the time of deposition, approximately half of the ^{60}Fe atoms in the crust have decayed. A mean age of $t_S = 2.2$ Myr (Feige et al., 2012) of the layer containing the signal is assumed. Using a half-life of $t_{1/2} = 2.62$ Myr (Rugel et al., 2009) the initial fluence (denoted by a subscript "HL" for **h**alf-**l**ife correction) of ^{60}Fe at the time of deposition is calculated with,

$$F_{60,crust,HL} = \frac{F_{60,crust}}{2^{-t_S/t_{1/2}}} = 1.47 \times 10^6 \text{ ats cm}^{-2}. \tag{3.25}$$

This value differs from the 2.9×10^6 ats cm^{-2} presented by Knie et al. (2004). The authors applied a previously established half-life of 1.51 Myr of ^{60}Fe (Kutschera et al., 1984) to calculate the initial fluence of ^{60}Fe in the crust. Furthermore, the dating of the crust was carried out using the previously accepted half-life of ^{10}Be, with 1.5 Myr, which has since changed to 1.39 Myr. Therefore, the age of the layer between 6 and 8 mm earlier corresponded to 2.4-3.2 Myr resulting in a value of $t_S = 2.8$ Myr. For the following calculations of the SN-signal intensities, the revised value of $t_S = 2.2$ Myr was used.

3.4.1.1 ^{60}Fe in Deep-Sea Sediments

When scaling the fluence $F_{60,crust,HL}$ to the SN signal of ^{60}Fe in the deep-sea sediment cores, the **u**ptake-efficiency U of iron particles into the ferromanganese crust and into sediments have to be taken into account. This factor is the fraction of the total amount of Fe available in the ocean, that is actually incorporated into the crust. Knie et al. (2004) suggested an uptake-factor of $U_{Fe} = 0.6$ %. This value was calculated by

$$\frac{U_{Fe}}{U_{Mn}} = \frac{C_{Fe,crust}}{C_{Fe,water}} \times \frac{C_{Mn,water}}{C_{Mn,crust}}. \tag{3.26}$$

Here, C, with the subscripts "Fe", "Mn", "crust", and "water", is the concentration of each element within the Fe-Mn crust and ocean water. These concentrations are known (see Knie et al. (2004)). The uptake factor for manganese (U_{Mn}) is calculated by comparing the ^{53}Mn flux measured by Knie et al. (2004) in the crust with other data of ^{53}Mn flux into arctic ice (Bibron et al., 1974) and deep-sea sediments (Imamura et al., 1979). For ice and sediment samples an uptake factor of 100 % was assumed.

Recent studies indicate, that the uptake-efficiency of 0.6 % in the crust is underestimated. Fitoussi et al. (2008) calculated an expected ratio of ^{60}Fe/Fe of 5×10^{-14} in their deep-sea sediment, assuming a deposition time of 10 kyr. They found no clear signal of a ^{60}Fe. One possible explanation suggested that the interstellar fluence calculated by Knie et al. (2004) might be overestimated due an underestimation of the uptake-factor. The second indication for such an overestimation of the ^{60}Fe fluence comes from ^{60}Fe measurements of lunar samples by Fimiani et al. (2014). A half-life corrected fluence value of 4×10^7 ^{60}Fe ats cm^{-2} is inferred by correcting for input of cosmogenic ^{60}Fe from GCRs in the lunar surface. This ^{60}Fe fluence measured on the Moon, which is higher than the fluence of 1.47×10^6 ats cm^{-2} in the crust, points to an uptake-efficiency of 3.7 % in the crust. Furthermore, new measurements of ^{53}Mn in snow and aerosol samples by Auer (2008) indicate an extraterrestrial influx of ^{53}Mn to Earth up to two orders of magnitudes lower than proposed by (Bibron et al., 1974) and (Imamura et al., 1979). Therefore, Korschinek, G. (private communication) suggest an uptake factor of 50-100 %.

The ^{60}Fe data obtained for the *Eltanin* deep-sea sediments in this work (chapter 2.2) will be compared to the data measured in the ferromanganese crust to recalculate the uptake-factor for the crust (section 5.6).

In the following analysis, fluences of ^{60}Fe into the *Eltanin* sediments with different uptake-efficiencies were calculated (table 3.1). Here, the relative method is used to derive this fluence: the signal is scaled from the fluence obtained in the ferromanganese crust. For an uptake factor of 100 %, the fluence in the sediments equals the value obtained for the crust (equation (3.25)). Again, $F_{60,sed,HL}$ is the half-life corrected value of the ^{60}Fe fluence in the deep-sea sediment cores and $F_{60,sed}$ the fluence after exponential decay, which would be measured today.

According to a SN signal width discussed in section 3.3, the signal is most likely larger than the time scale contained in one sample of the *Eltanin* cores. They, with a thickness of ~1 cm (Appendix B.2), cover approximately 3 kyr (for a sedimentation rate of

0.32 cm kyr^{-1}). For this reason the ^{60}Fe/Fe ratio can be estimated by integrating over a certain width of the signal taking into account the sediment accumulation rate. First, the amount of stable iron is calculated with equation (3.22), $n_{Fe,sed} = 2.80 \times 10^{19}$ ats cm^{-3}, using the density of the sediment of 1.35 g cm^{-3}. The fraction of leached authigenic iron from the sample is estimated as 0.2 wt% (Fitoussi and Raisbeck, 2007). Then the particle density of ^{60}Fe (ats cm^{-3}) is

$$n_{60,sed} = \frac{F_{60,sed}}{S\,d},\qquad(3.27)$$

where $S = 0.32$ cm kyr^{-1} is the sedimentation rate used for these estimations and d is the signal width in kyr. The ratio $n_{60,sed}/n_{Fe,sed}$ gives the expected ^{60}Fe/Fe ratio for a peak width d when assuming a rectangular shape of the signal.

Table 3.1 displays half-life corrected fluences expected in the deep-sea sediments. Four different uptake-efficiencies of ^{60}Fe into the ferromanganese crust are used. Corresponding fluences after radioactive decay for $t_S = 2.2$ Myr are calculated. Furthermore, time-integrated ^{60}Fe/Fe ratios (ats/ats kyr) are displayed. These are independent of the signal width, but scale with the stable authigenic Fe content estimated above of the deep-sea sediment,

$$\int \frac{^{60}Fe}{Fe}dt = \frac{n_{60,sed}}{n_{Fe,sed}}d.\qquad(3.28)$$

Table 3.1: Half-life corrected ^{60}Fe fluences and corresponding values after time $t_S = 2.2$ Myr in the deep sea sediment cores with different uptake-efficiencies U. $\int\,^{60}$Fe/Fe dt (kyr) is the integrated ratio over the duration of the entire signal.

U (%)	$F_{60,sed,HL}$ (ats cm^{-2})	$F_{60,sed}$ (ats cm^{-2})	$\int\,^{60}$Fe/Fe dt (kyr)
0.6	2.45×10^8	1.37×10^8	1.47×10^{-11}
4	3.67×10^7	2.05×10^7	2.20×10^{-12}
50	2.93×10^6	1.64×10^6	1.76×10^{-13}
100	1.47×10^6	8.20×10^5	8.80×10^{-14}

A gaussian shape of a SN peak is assumed. The corresponding gaussian distribution includes radioactive decay:

$$f(t, \mu, \sigma) = \frac{1}{\sigma k}e^{-\frac{1}{2}\left(\frac{t-\mu}{\sigma}\right)^2}\,e^{-\lambda t}.\qquad(3.29)$$

A mean value of $\mu = 2.2$ Myr is assumed, which corresponds to the mean age t_S of the layer between 6-8 mm in the crust. The parameter k depends on the area under the curve and is derived from the time-integrated ^{60}Fe/Fe ratios given in table 3.1, λ is the decay constant of ^{60}Fe. A range of standard deviations σ is applied for the signal width: 1, 0.8, 0.6, 0.4, 0.2, 0.1, 0.05, 0.01, and 0.005 kyr. These are expressed in terms of the **F**ull **W**idth **H**alf **M**aximum, where FWHM $= 2\sqrt{2\ln(2)}\,\sigma = 2.355\,\sigma$.

Results of ^{60}Fe/Fe ratios for the considered signal widths are displayed in Figure 3.13, Of course, the ^{60}Fe/Fe ratios shown here are based on stable iron content, which was assumed
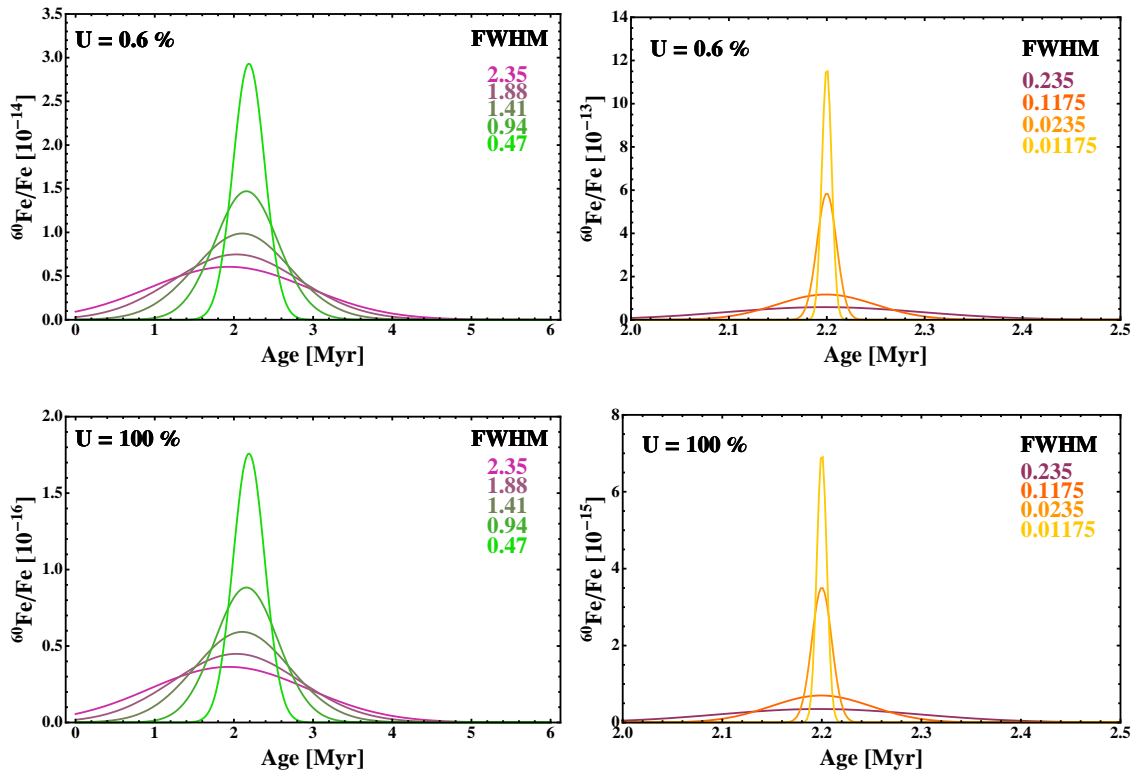
Figure 3.13: ^{60}Fe/Fe isotope ratios versus age in deep-sea sediment samples calculated for two different uptake-efficiencies of 0.6 and 100 %. A gaussian shape of the peak is assumed. Different signal widths (expressed as FWHM (Myr)) are considered.

to be $n_{Fe,sed} = 2.80 \times 10^{19}$ ats cm^{-3}. With a larger fraction of stable iron than considered in these calculations the signal will be diluted resulting in lower intensities of SN signatures. A lower amount of iron increases the chance of detecting SN-produced ^{60}Fe.

Figure 3.13 focuses on two scenarios for U: 0.6 % and 100 %. The left part of this figure contains very broad signals with FWHM values between 0.47 and 2.35 Myr. Here, the time range of 0-6 Myr is displayed. The right part of Figure 3.13 shows narrower peaks with FWHM between 12 and 235 kyr and the time is restricted to a region of 2-2.5 Myr. If the uptake-efficiency into the ferromanganese crust is 0.6 %, the expected signal in a deep sea sediment (with an uptake efficiency of 100 %) should be much larger than measured for the crust (indicated in the upper part of Figure 3.13). Even for the broadest signal considered here, the ^{60}Fe/Fe ratio is still in the order of 10^{-15}. The ratio for a signal width of 12 kyr results in ^{60}Fe/Fe intensities of 1.2×10^{-12}. An uptake-efficiency of 100 % in the crust yields ^{60}Fe/Fe ratios in a deep-sea sediment in the order of 10^{-16} (which is the AMS detection limit). In this case, only the most narrow signals with FWHM of 100 kyr or less (shown on the right part of Figure 3.13) have a chance to be detected.

3.4.1.2 ^{26}Al in Deep-Sea Sediments

In contrast to ^{60}Fe, there is a continuous terrestrial production of ^{26}Al, possibly overwhelming a ^{26}Al SN signal. The intensities of SNe input into the deep-sea sediments were determined for various signal widths, and compared to the terrestrial ^{26}Al production (section 3.1.1.2) as follows.

A SN signature of ^{26}Al is estimated by scaling the ^{60}Fe fluences determined above for sediment samples using ^{60}Fe/^{26}Al ratios from theoretical SN model calculations (see Figures 3.3 and 3.8). The yields of the two radionuclides ^{26}Al and ^{60}Fe are usually given in units of solar masses $M_\odot$, and thus have to be divided by the ratio of the mass numbers, 60/26, in order to compute atomic ratios. Various theoretical outcomes of different authors were considered, resulting in a wide range of possible ^{60}Fe/^{26}Al ratios, between 0.02 and 2 (Figure 3.14).
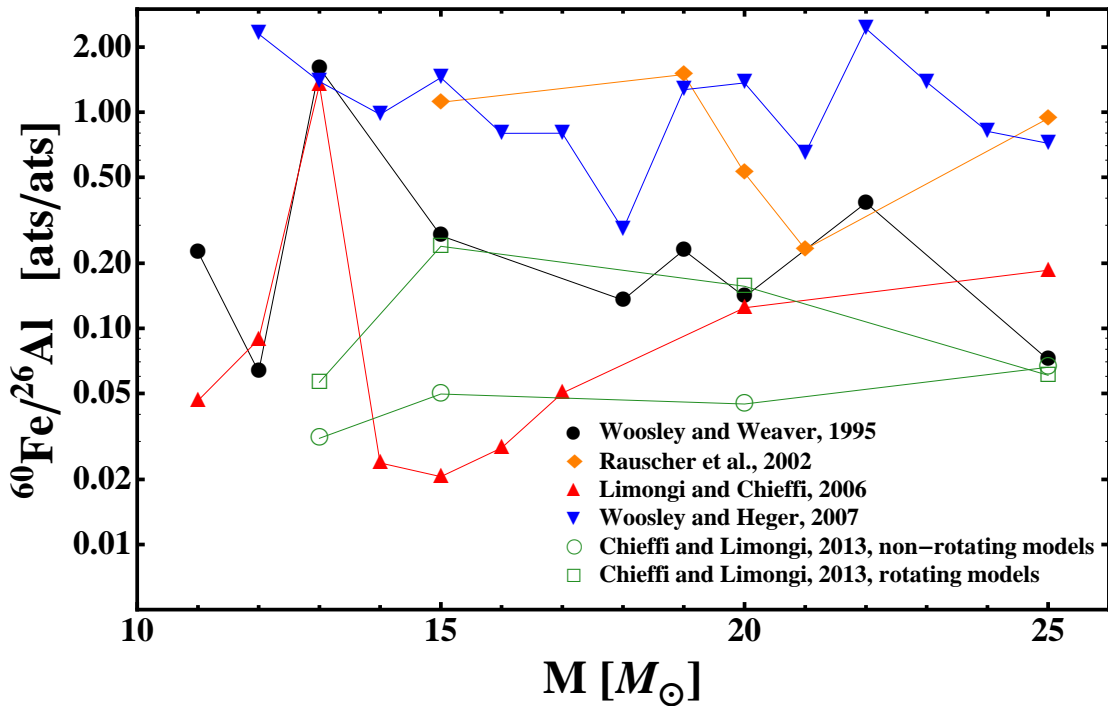
Figure 3.14: Comparison of theoretical ^{60}Fe/^{26}Al ratios (displayed in logarithmic scale in units of ats/ats) from several research groups for stellar masses between 11 and 25 $M_\odot$.

The fluence of ^{26}Al (ats cm^{-2}) was calculated by

$$F_{26,sed} = F_{60,sed,HL} \times \left(\frac{^{26}\text{Al}}{^{60}\text{Fe}}\right)_{th} \times 2^{-t_S/t_{1/2}}, \tag{3.30}$$

where again, a mean age of the signal of $t_S = 2.2$ Myr is assumed and $t_{1/2} = 0.717$ Myr is the half-life of ^{26}Al. Here, $(^{26}\text{Al}/^{60}\text{Fe})_{th}$ is the theoretical atomic ratio. Resulting decay-corrected fluences, corresponding to different uptake-efficiencies and ^{60}Fe/^{26}Al ratios, are

shown in table 3.2 below. Time integrated ^{26}Al/^{27}Al ratios (see table 3.3) are determined using an authigenic fraction of stable aluminium of 0.1 wt% (Fitoussi and Raisbeck, 2007), which translates into $n_{Al,sed} = 3.01 \times 10^{19}$ ats cm^{-3}.

Table 3.3 demonstrates that, in the combination of the highest values (i.e. U = 100 %, ^{60}Fe/^{26}Al = 2) results in the lowest ^{26}Al/^{27}Al ratios. For a narrow SN peak width of d = 10 kyr, the signal intensity becomes 9×10^{-16} assuming a rectangular shape of the peak. Detecting such a signal is challenging, as the detection limit of AMS for ^{26}Al is of the order of ^{26}Al/^{27}Al$\sim 10^{-16}$.

Table 3.2: ^{26}Al fluences $F_{26,sed}$ (ats cm^{-2}) expected into deep-sea sediment cores as measured today (i.e. correcting for exponential decay of initially deposited ^{26}Al) with t_S = 2.2 Myr for different uptake-factors U and ^{60}Fe/^{26}Al SN ratios.

$\frac{^{60}\text{Fe}}{^{26}\text{Al}}$	U (%)	$F_{26,sed}$ (ats cm^{-2})			
		0.6	4	50	100
0.02		1.46×10^{9}	2.19×10^{8}	1.75×10^{7}	8.75×10^{6}
0.1		2.92×10^{8}	4.37×10^{7}	3.50×10^{6}	1.75×10^{6}
0.5		5.83×10^{7}	8.75×10^{6}	7.00×10^{5}	3.50×10^{5}
2		1.46×10^{7}	2.19×10^{6}	1.75×10^{5}	8.75×10^{4}

Table 3.3: Time-integrated ^{26}Al/^{27}Al ratios (ats/ats $\times$ kyr) expected into deep-sea sediment cores as measured today (i.e. correcting for exponential decay of initially deposited ^{26}Al) with t_S = 2.2 Myr for different uptake-factors U and ^{60}Fe/^{26}Al SN ratios. Dividing this number by the width of the signal (kyr) gives the expected measured ratio for a signature of rectangular shape.

$\frac{^{60}\text{Fe}}{^{26}\text{Al}}$	U (%)	^{26}Al/^{27}Al ratios (ats/ats $\times$ kyr)			
		0.6	4	50	100
0.02		1.51×10^{-10}	2.27×10^{-11}	1.81×10^{-12}	9.07×10^{-13}
0.1		3.02×10^{-11}	4.54×10^{-12}	3.63×10^{-13}	1.81×10^{-13}
0.5		6.05×10^{-12}	9.07×10^{-13}	7.26×10^{-14}	3.63×10^{-14}
2		1.51×10^{-12}	2.27×10^{-13}	1.81×10^{-14}	9.07×10^{-15}

For further discussion, a gaussian distribution of the SN peak is assumed in deep-sea sediments. Figure 3.15 displays the calculated SN-produced ^{26}Al/^{27}Al ratios with different FWHM. Results calculated from the highest and lowest values of U $\times$ ^{60}Fe/^{26}Al SN ratios are shown. The lowest value is obtained from U = 0.6 % and ^{60}Fe/^{26}Al = 0.02, which corresponds to the highest ^{26}Al/^{27}Al signals. Vice versa, the upper limit of the product is determined by U = 100 % and ^{60}Fe/^{26}Al = 2, from which the lowest ^{26}Al signals are obtained. Detecting signatures for the latter scenario is challenging for small widths <100 kyr, as ratios of ^{26}Al/^{27}Al close to the AMS detection limit of 10^{-16} were obtained. A detection of signals with FWHM > 100 kyr is impossible (lower part of Figure 3.15). ^{26}Al/^{27}Al signals resulting from the combination of U = 0.6 % and ^{60}Fe/^{26}Al = 0.02 range

between 10^{-13} and 10^{-11}. Thus, signals with such high $^{26}Al/^{27}Al$ ratios are well above the AMS detection limit (Figure 3.15, upper part). Due to exponential decay of ^{26}Al, the maximum of the gaussian distributions, corresponding to the mean value of $\mu = 2.2$ Myr, shifts toward younger ages with increasing signal widths. This shifting occurred already for SN signals of ^{60}Fe (Figure 3.13). However, as the half-life of ^{26}Al is approximately three times shorter than that of ^{60}Fe this effect becomes more pronounced in the present calculations.
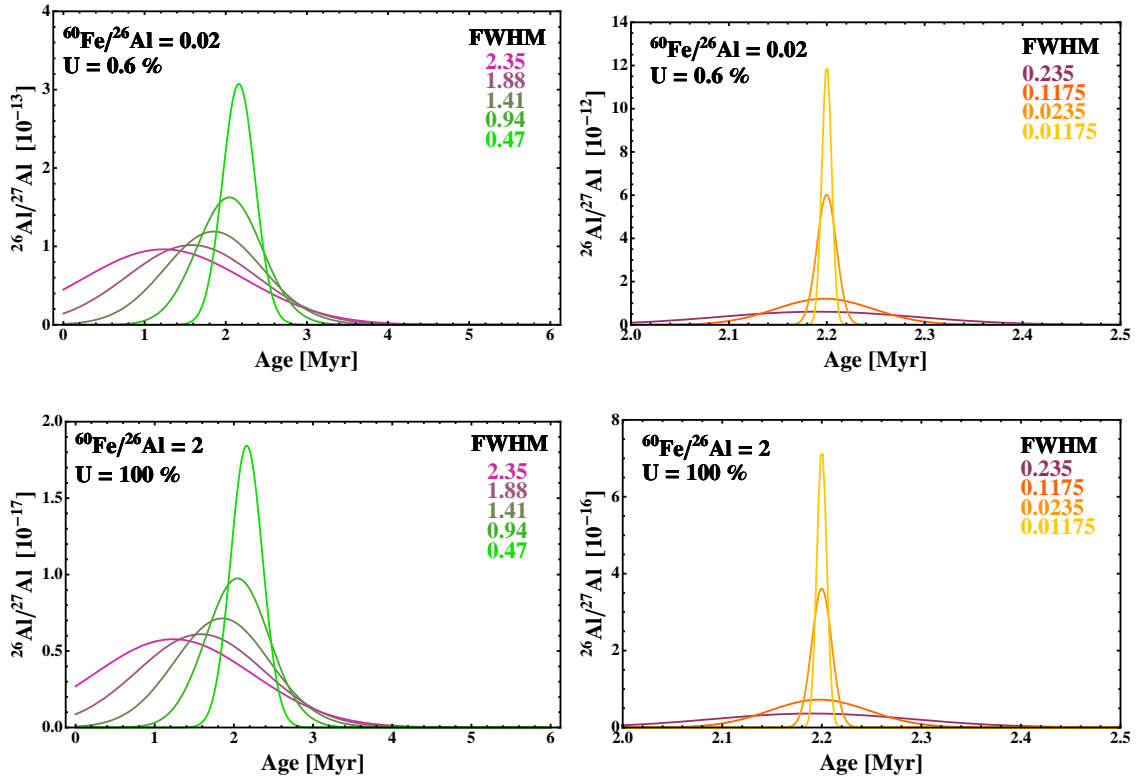
Figure 3.15: $^{26}Al/^{27}Al$ isotope ratios (ats/ats) versus age in deep-sea sediment samples calculated for the combined extreme values of uptake-efficiencies and theoretical $^{60}Fe/^{26}Al$ SN ratios. A gaussian shape of the signal is assumed, and different signal widths (expressed as the FWHM (Myr)) are considered.

In addition to a potential SN input of ^{26}Al into deep-sea sediments, there is continuous terrestrial ^{26}Al production, predominantly from atmospheric and in-situ production (section 3.1.1.2) forming a terrestrial background. The total ^{26}Al production from various sources of ^{26}Al in deep-sea sediments (calculated in section 3.1.1.2, Figure 3.4) is converted from ats g^{-1} into $^{26}Al/^{27}Al$ ratios. For this calculation, density of the sediment of 1.35 g cm^{-3} and the amount of stable aluminium estimated above was used. The potential ^{26}Al SN signals calculated above were then added to the resulting "terrestrial" $^{26}Al/^{27}Al$ ratios.

The results for a selection of combinations of U and $^{60}Fe/^{26}Al$ ratios are shown in Figure 3.16. For peak widths up to 0.47 Myr it is not possible to extract any signal for a

combination of U $\times$ ^{60}Fe/^{26}Al larger than 0.001. These SN signals are hidden within the terrestrial background of ^{26}Al assuming a measurement precision of 10 % in AMS. The lowest ^{26}Al/^{27}Al ratios displayed in that figure result from U = 4 % and ^{60}Fe/^{26}Al = 0.02. Here, the curve with FWHM = 0.47 Myr should start to raise above the background. The maximum of the broader curve with FWHM = 0.94 Myr lies about 20 % above the ^{26}Al background, but might be still hard to distinguish from the background due to its broadness. Maxima of narrow signals with FWHM = 11.7 kyr are already more than 10 % above the ^{26}Al background estimates with U $\times$ ^{60}Fe/^{26}Al > 0.1.
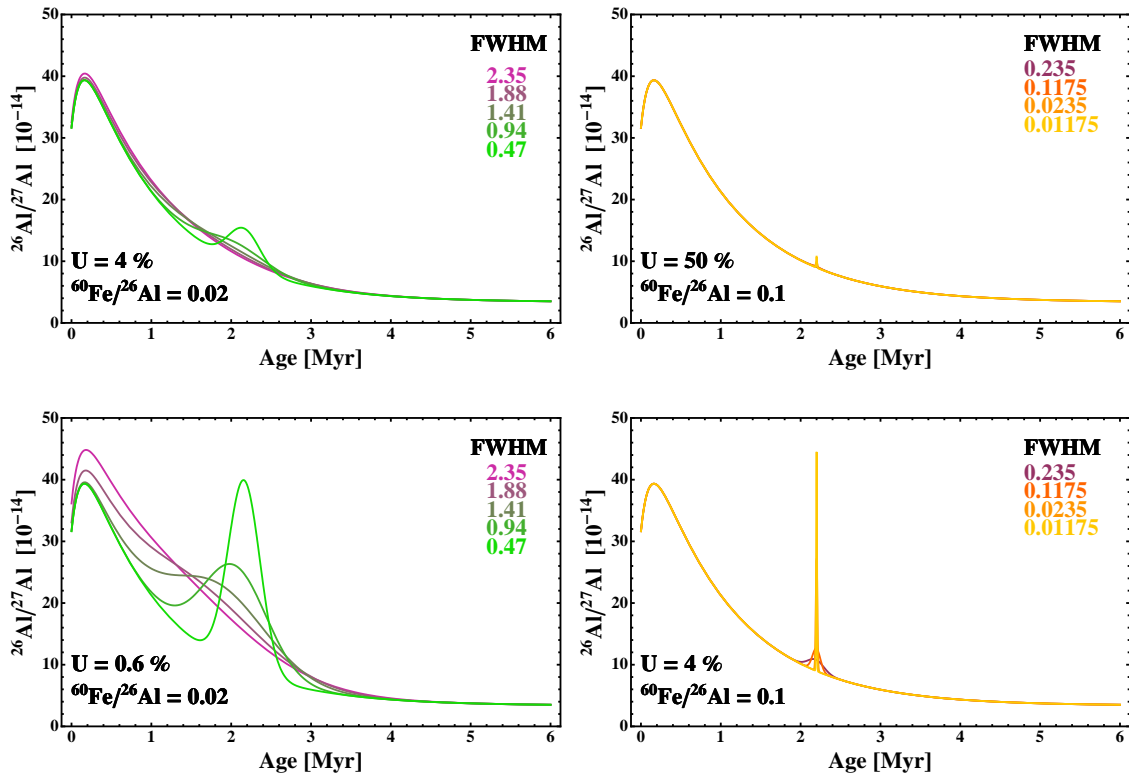
Figure 3.16: ^{26}Al/^{27}Al ratios (ats/ats) with varying FMHW (Myr) of SN signals added to a potential terrestrial background (section 3.1.1.2) versus age of sediments. A selection of combinations of uptake-efficiencies and modeled ^{60}Fe/^{26}Al SN ratios is displayed.

One problem with detecting very narrow signals is, that no continuous sampling over the whole time was available in this work and gaps of up to 60 kyr exist between sediment samples. If a narrow signal is located within a gap, it would be missed in the measurement. In addition, if the signature is deposited in just one sample, it has to be verified by repeated sampling and AMS measurements to not misjudge it as an outlier. If it indeed is confirmed to be an extraterrestrial signal, then the iron target of the same sample should also show an enhanced ^{60}Fe/Fe result. For this work, there are four sediment cores available. Thus, together they cover a range decreasing the gaps between samples and therefore the possibility to miss a potential SN signal.

3.4.1.3 ^{53}Mn in Deep-Sea Sediments

A SN signal of ^{53}Mn was estimated in the same way as done for ^{26}Al. First, intensities of SN signatures of ^{53}Mn/^{55}Mn ratios were determined. Subsequently, these peaks were added to a continuous background expected from meteoritic influx onto Earth.

The mass of ^{53}Mn ejected during a SN was obtained from nucleosynthesis calculations (Figure 3.6). Using these and the ^{60}Fe yields from Figure 3.8, ^{60}Fe/^{53}Mn atomic ratios were determined for different model computations (Figure 3.17). The values obtained here are again spread over a wide range, with ^{60}Fe/^{53}Mn values between 0.01 and 5.

The fluence of ^{53}Mn is

$$F_{53,sed} = F_{60,sed,HL} \times \left(\frac{^{53}Mn}{^{60}Fe}\right)_{th} \times 2^{-t_S/t_{1/2}}, \qquad (3.31)$$

where $F_{60,sed,HL}$ is the half-life corrected fluence of ^{60}Fe, $t_{1/2} = 3.7$ Myr is the half-life of ^{53}Mn and $t_S = 2.2$ Myr the assumed mean value of the peak position. $(^{53}Mn/^{60}Fe)_{th}$ ratios were taken from theoretical SN models. The results for $F_{53,sed}$, taking into account different uptake-factors U as well as different atomic ratios of ^{53}Mn/^{60}Fe, are given in table 3.4. The corresponding time-integrated ^{53}Mn/^{55}Mn ratios are displayed in table 3.5. Here, the concentration of stable authigenic ^{55}Mn within the deep-sea sediments was assumed to be 0.4 wt %. This number corresponds to 5.7×10^{19} Mn atoms in a sediment volume of 1 cm^3.

Figure 3.17: Comparison of theoretical ^{60}Fe/^{53}Mn ratios (displayed in logarithmic scale in units of ats/ats) from several research groups for stellar masses between 11 and 25 M$_\odot$.

Table 3.4: ^{53}Mn fluences $F_{53,sed}$ (ats cm^{-2}) expected into deep-sea sediment cores as measured today (i.e. correc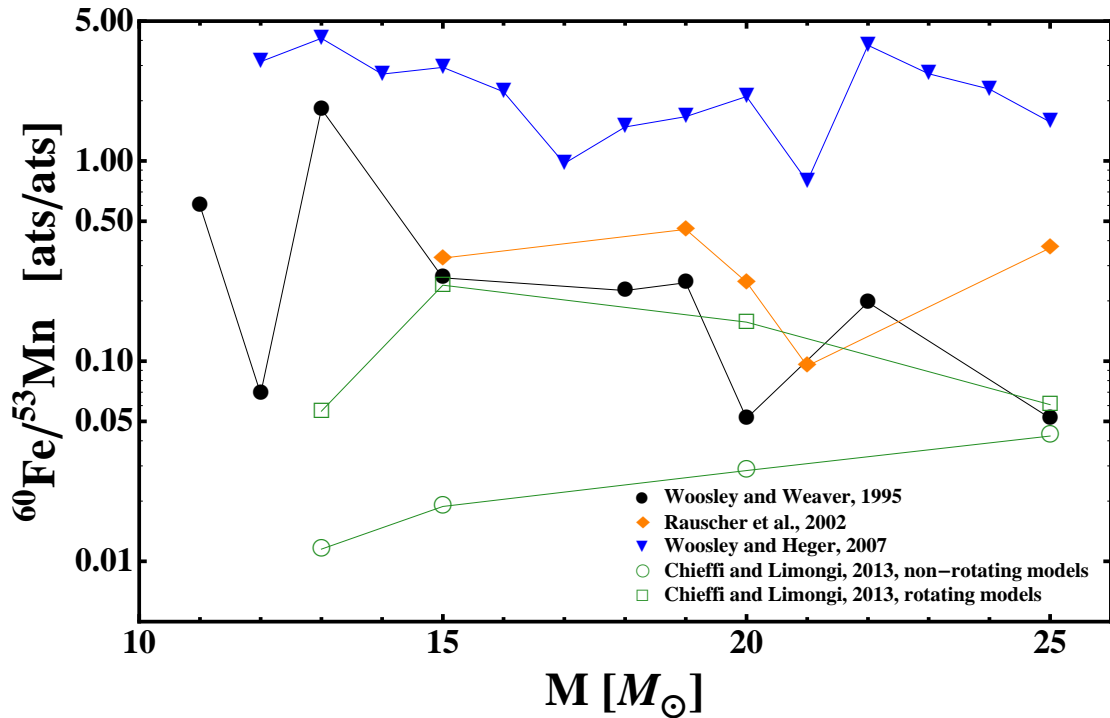ting for exponential decay of initially deposited ^{53}Mn) with t_S = 2.2 Myr for different uptake-factors U and ^{60}Fe/^{53}Mn SN ratios.

$\frac{^{60}Fe}{^{53}Mn}$		$F_{53,sed}$ (ats cm^{-2})			
	U (%)	0.6	4	50	100
0.01		1.62×10^{10}	2.43×10^{9}	1.94×10^{8}	9.72×10^{7}
0.08		2.02×10^{9}	3.04×10^{8}	2.43×10^{7}	1.21×10^{7}
0.7		2.31×10^{8}	3.47×10^{7}	2.78×10^{6}	1.39×10^{6}
5		3.24×10^{7}	4.86×10^{6}	3.89×10^{5}	1.94×10^{5}

Table 3.5: Time-integrated ^{53}Mn/^{55}Mn ratios (ats/ats × kyr) expected in deep-sea sediment cores present today (after exponential decay of initially deposited ^{53}Mn) with t_S = 2.2 Myr for different uptake-factors U and ^{60}Fe/^{53}Mn SN ratios.

$\frac{^{60}Fe}{^{53}Mn}$		^{53}Mn/^{55}Mn ratios (ats/ats × kyr)			
	U (%)	0.6	4	50	100
0.01		8.55×10^{-10}	1.28×10^{-10}	1.03×10^{-11}	5.13×10^{-12}
0.08		1.07×10^{-10}	1.60×10^{-11}	1.28×10^{-12}	6.41×10^{-13}
0.7		1.22×10^{-11}	1.83×10^{-12}	1.47×10^{-13}	7.33×10^{-14}
5		1.71×10^{-12}	2.57×10^{-13}	2.05×10^{-14}	1.03×10^{-14}

Assuming a gaussian distribution, intensities of ^{53}Mn/^{55}Mn ratios resulting from SN input into deep-sea sediments are plotted in Figure 3.18, for the highest and lowest values for the combination of uptake-factor × ^{60}Fe/^{53}Mn. For a high uptake-efficiency of 100 % and ^{60}Fe/^{53}Mn = 5, no data is above the AMS detection limit ($\sim10^{-14}$). The most narrow peak with a value of FWHM = 11.7 kyr is in the order of this detection limit for U × ^{60}Fe/^{53}Mn < 0.3. The combination of the lowest U and ^{60}Fe/^{53}Mn ratio results in ^{53}Mn/^{55}Mn ratios ranging from 10^{-13} to 10^{-11} depending on the width of the SN peak.

As pointed out in section 3.1.2.2, an extraterrestrial influx of ^{53}Mn onto Earth via dust particles and MMs was estimated to approximately 200 ats cm^{-2} yr^{-1} (Auer, 2008). With an accumulation rate of 0.32 cm kyr^{-1}, this flux value leads to a ^{53}Mn concentration of 6.25×10^{5} ats cm^{-3} in the deep-sea sediment samples. This can be converted into a ^{53}Mn/^{55}Mn ratio, and assuming a concentration of authigenic manganese of 0.4 wt%, one deduces values in the order of 10^{-14}. Assuming a constant influx of extraterrestrial material with time, this contribution is displayed as an exponential function in Figure 3.19 to which the ^{53}Mn SN signal is added.

A selection of ^{60}Fe/^{53}Mn and U values are plotted. Combinations with U×^{60}Fe/^{53}Mn > 0.1 do not yield a signal with maxima of >10 % above extraterrestrial influx for the broad peak range with FWHM ≥ 470 kyr. The most narrow peaks are always above the background, the lowest possible combination being shown in the upper right part of the
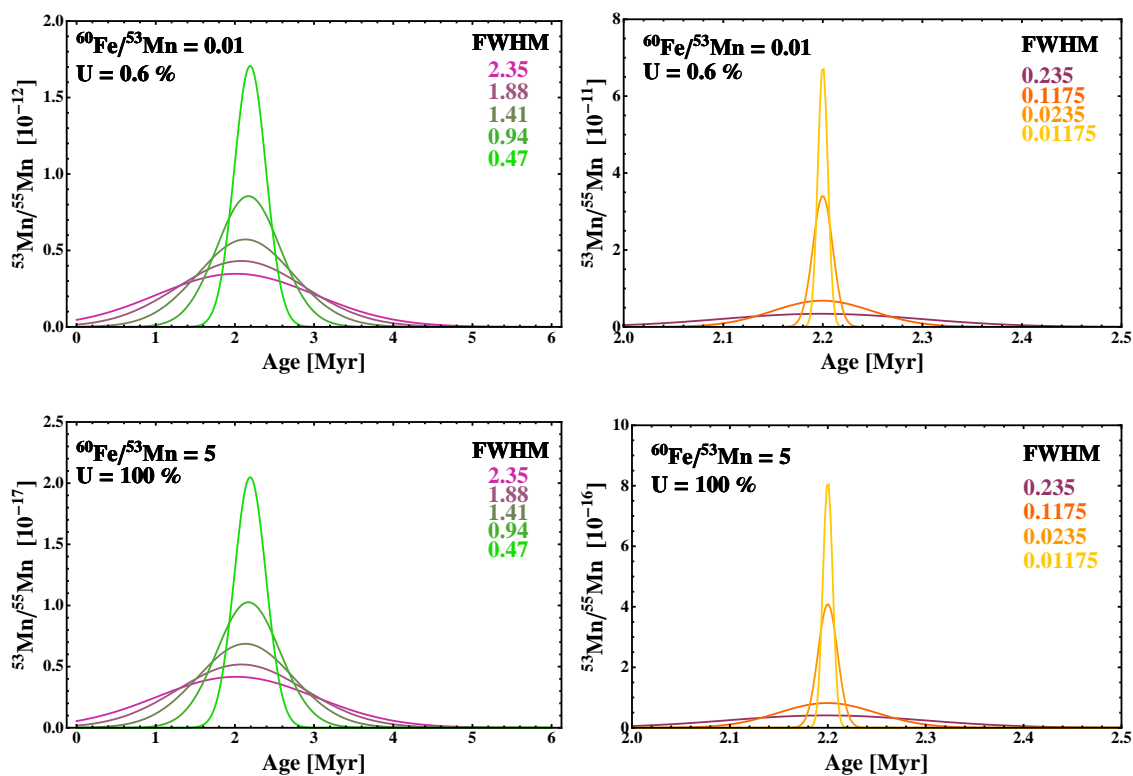
Figure 3.18: ^{53}Mn/^{55}Mn isotope ratios (ats/ats) versus age in deep-sea sediment samples calculated for the combined extreme values of uptake-efficiencies and theoretical ^{60}Fe/^{26}Al SN ratios. A gaussian shape of the signal is assumed, and different signal widths (expressed as the FWHM (Myr)) are considered.

figure. As discussed above, these peaks have widths of ~12 kyr and are easy to miss, because they might be located in a gap between two samples in this work.
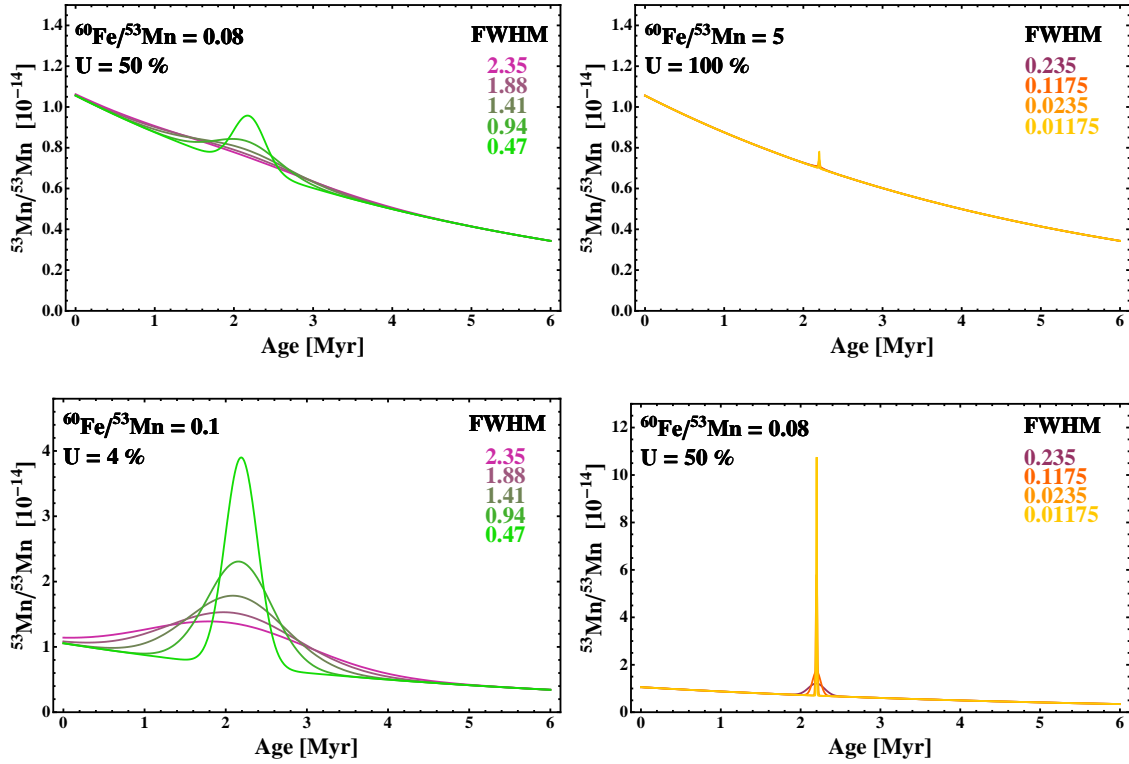
Figure 3.19: ^{53}Mn/^{27}Al ratios (ats/ats) with varying FMHW (Myr) of SN signals added to a potential background generated from meteoritic influx versus age of sediments. A selection of combinations of uptake-efficiencies and modeled ^{60}Fe/^{53}Mn SN ratios is displayed.

3.4.2 Absolute SN Input into a Deep-Sea Sediment

The fluence of a long-lived radionuclide expected in a deep-sea sediment from a close SN explosion is

$$F_{SN,sed} = \frac{1}{4} \frac{M_{ej}}{4\pi A m_p r^2} e^{-\lambda t_{SN}}. \tag{3.32}$$

Here, any losses occurring during transport from the SN site into the deep-sea sediments are ignored. Losses can occur for instance due to partial condensation of elements onto dust grains in the SNR, diffusion of grains out of the expanding SN shell, deflection of the grains from the interplanetary magnetic field and repulsion from the heliosphere. Also, an uptake of 100 % of the long-lived radionuclides into the marine sediments is assumed and thus represents an upper limit. M_{ej} is the ejected mass of a radionuclide in a SN explosion (Figures 3.3, 3.6, and 3.8). A is the mass number, m_p the proton mass, r the distance of the SN to the solar system, λ the decay constant, and t_{SN} the time that has passed since the star has exploded.

Fluence values for ^{26}Al, ^{53}Mn, and ^{60}Fe were calculated under these assumptions for three different explosion distances of 60, 90, and 120 pc (tables 3.6, 3.7, and 3.8). The SN nucleosynthesis yields are varied between the lower and upper limit of theoretical

calculations for stellar masses between 11 and 25 $M_\odot$. The explosion time t_{SN} is the sum of the estimated deposition time of t_S = 2.2 Myr BP of the radionuclides in the deep-sea sediments and the transport time t_{tr} of the isotope through the interstellar medium in the expanding SNR. The model developed by Kahn (1998) (introduced in section 3.2) is applied to evaluate the time the SN shell requires to arrive at the Solar System for an explosion distance d_{exp} to the Solar System.

Table 3.6: ^{60}Fe fluences $F_{60,sed}$ (ats cm^{-2}) expected into deep-sea sediment cores as measured today (i.e. correcting for exponential decay of initially deposited ^{60}Fe) with time t_{SN} from SNe with various distances d_{exp} and ejected yields M_{ej}.

d_{exp} (pc)	t_{SN} (Myr)	M_{ej} ($M_\odot$)	$F_{60,sed}$ (ats cm^{-2})		
			10^{-4}	2×10^{-5}	10^{-6}
60	2.25		6.53×10^8	1.31×10^8	6.53×10^6
90	2.38		2.80×10^8	5.60×10^7	2.80×10^6
120	2.60		1.49×10^8	2.97×10^7	1.49×10^6

Table 3.7: ^{26}Al fluences $F_{26,sed}$ (ats cm^{-2}) expected into deep-sea sediment cores as measured today (i.e. correcting for exponential decay of initially deposited ^{26}Al) with time t_{SN} from SNe with various distances d_{exp} and ejected yields M_{ej}.

d_{exp} (pc)	t_{SN} (Myr)	M_{ej} ($M_\odot$)	$F_{26,sed}$ (ats cm^{-2})		
			1.5×10^{-4}	2×10^{-5}	10^{-6}
60	2.25		2.02×10^8	2.69×10^7	1.34×10^7
90	2.38		7.90×10^7	1.05×10^7	5.27×10^6
120	2.60		3.59×10^7	4.79×10^6	2.40×10^6

Table 3.8: ^{53}Mn fluences $F_{53,sed}$ (ats cm^{-2}) expected in deep-sea sediment cores present today (after exponential decay of initially deposited ^{53}Mn) with time t_{SN} from SNe with various distances d_{exp} and ejected yields M_{ej}.

d_{exp} (pc)	t_{SN} (Myr)	M_{ej} ($M_\odot$)	$F_{53,sed}$ (ats cm^{-2})		
			3.5×10^{-4}	2×10^{-5}	10^{-5}
60	2.25		2.72×10^9	1.55×10^8	7.76×10^7
90	2.38		1.18×10^9	6.74×10^7	3.37×10^7
120	2.60		6.36×10^8	3.64×10^7	1.82×10^7

Applying this model (Kahn, 1998) for distances of d_{exp} = (60, 90, 120) pc yields travel times of t_{tr} = (50, 180, 400) kyr. Free expansion of the SN shell is assumed to occur in a medium with LB particle density of n = 5×10^{-3} ats cm^{-3} (e.g. Snowden et al. (1990)). The velocity of ejected material is 3×10^8cm s^{-1} for an ejected SN mass in the order of

10 $M_\odot$. This results in a travel time of 6 kyr, which is a much lower value than the transport time resulting from the model of Kahn (1998) and can therefore be neglected.

Results for SN fluences in deep-sea sediments of ^{60}Fe, ^{26}Al, and ^{53}Mn are displayed in tables 3.6, 3.7, and 3.8. These absolute numbers can be compared to the relative fluences obtained from scaling from the ferromanganese crust signal.

The upper limit of ^{60}Fe (obtained for d_{exp} = 60 pc and M_{ej} = 10^{-4} $M_\odot$) in the sediment from absolute SN input is higher than values estimated from scaling. The lower limit (for d_{exp} = 120 pc and M_{ej} = 10^{-6} $M_\odot$) is still twice as high as the scaled fluence with a crust uptake-efficiency 100 %. Conversion to ^{60}Fe/Fe ratios results in SN signals in the order of 10^{-15} for signal widths narrower than 200 kyr.

The upper limit the ^{26}Al fluence in table 3.7 is comparable to the scaled values with U = 4% and a ^{60}Fe/^{26}Al ratio of 0.02, which is plotted in the upper left part of Figure 3.16. Therefore, SN signals with FWHM < 470 kyr rise above the terrestrial background. ^{26}Al/^{27}Al ratios corresponding to the lowest fluence of 2.40×10^6 ats cm^2 (d_{exp} = 120 pc, M_{ej} = 10^{-6} $M_\odot$) are only above the AMS detection limit for the smallest signal width of 11.7 kyr.

The lowest ratios of ^{53}Mn/^{55}Mn from the fluence value of 1.82×10^7 ats cm^2 (d_{exp} = 120 pc, M_{ej} = 10^{-5} $M_\odot$) obtained from absolute SN yields are comparable to the scaled ratio for U = 50 % and a ^{60}Fe/^{53}Mn ratio of 0.08. This was shown in Figure 3.19 (upper left part). Therefore, signals narrower than 470 kyr are well distinguished from the extraterrestrial background. However, the ^{53}Mn/^{55}Mn ratios shown in this plot lie within the AMS detection limit of 10^{-14}. All other fluence are higher than 1.82×10^7 ats cm^2, and therefore are above the detection limit for signal widths smaller than 470 kyr.

4 Experimental Procedures[*]

This chapter describes the chemical procedures to separate Al, Be, Mn, and Fe from deep-sea sediment samples. During sample preparation, a first suppression of isobars, that might introduce interfering background in the subsequent AMS measurements, is achieved.

AMS facilities involved for detection of trace amounts of radioactive isotopes and further suppression of isobars with the respective AMS facilities are discussed. This is followed by a brief introduction to the measurement procedures used for stable element concentration analysis.

First chemistry tests are described. The chemical procedure had to be adapted to obtain a high yield.

4.1 Methods for the Chemical Extraction of Selected Elements

The sample preparation was carried out at the chemistry laboratory at the **H**elmholtz-**Z**entrum **D**resden-**R**ossendorf (HZDR). All chemicals used were of pro analysis quality. Deionised water (18 MΩ) was used in all steps and is in the following referred to as H_2O.

A leaching procedure described by Bourlès et al. (1989) and Fitoussi and Raisbeck (2007) was adapted for this work. The chemical separation of Al, Be, Fe, and Mn from the leachate follows Merchel and Herpers (1999). These techniques were applied to sediment samples weighing 1 g or less. First tests, however, showed that using 1 g of sediment only as starting mass was not sufficient to extract enough Al and Fe for a quantitative AMS measurement (see section 4.4.1). Consequentially, 3 g of material were taken for sample preparation. For these larger sample masses the procedures had to be adapted in order to leach more efficiently, and to adjust for higher concentrations of elements like Ca, Na, and K. A scheme of the separation technique is presented in Figure 4.1.

In one chemistry batch seven samples were processed simultaneously. Furthermore, a processing blank was added to each batch and prepared in the same manner, starting with the leaching procedure. Altogether, 16 batches were processed.

---

[*]Parts of this chapter are published in Feige et al. (2013)

Figure 4.1: Scheme of the separation technique for Be, Al, Mn, and Fe from 3 g of deep-sea sediment samples (adapted from Merchel and Herpers (1999)) for producing BeO, Al_2O_3, MnO_2, and Fe_2O_3 targets for AMS measurements.

4.1.1 Leaching

This technique was designed to extract the authigenic fraction, which includes the isotopes of interest, from the detrital material. The goal was to separate as much as possible of the elements adsorbed to the mineral phases of the samples. These authigenic elements represent the soluble phase in the ocean water. Dissolving the whole sediment sample material would lead to a full extraction of the stable elements from the detrital component as well, i.e. would dilute a possible SN signal.

Before starting the leaching procedure, the whole sample was suspended in H_2O, mixed and dried overnight. The goal was to homogenize the material of which an aliquot of roughly 3 g was taken. This sample (representative for the whole initial sample) was used for the chemical extraction of Al, Be, Fe, and Mn. To each sample 60 ml of 0.04 M $NH_2OH \cdot HCl$ in 25% (V/V) acetic acid was added in steps of 15 + 15 + 30 ml to account for CO_2 release, since the sediment contained a high amount of $CaCO_3$.

The samples were leached for 1 hour at $(90\pm5)°C$, then for 7 hours at $(95\pm5)°C$ in a sand bath with magnetic stirrers (Stirring Drybath) and subsequently washed three times with 8 ml of 0.04 M $NH_2OH \cdot HCl$ in 25% (V/V) acetic acid. After separating the leachate from the undissolved residue by centrifuging, an aliquot ($\sim$3 ml) was taken from the solution (in total 84 ml) for stable isotope determination by inductively coupled plasma mass spectrometry (ICP-MS). About 600 μg of stable ^{9}Be-carrier was then added to each leachate (including the blank), since the natural amount of stable Be in the sediment was too low to allow for further processing. The leachate was then evaporated to dryness; 5 ml HNO_{3c} was added and evaporated to dryness three times to remove acetates and ammonia, and to oxidise Fe^{2+} to Fe^{3+}.

4.1.2 Precipitation with NH_{3aq} and Extraction of Manganese

The residue was dissolved in 3 ml 7.1 M HCl, centrifuged, and the solution transferred into another centrifuge tube to remove unsolvable material, which might have blocked the column during ion exchange.

Adding NH_{3aq} resulted in the immediate precipitation of beryllium, aluminium and iron hydroxides at pH 8-9. The solution containing manganese, which slowly precipitated as $MnO(OH)_2$, was quickly separated from the precipitates of Al, Be and Fe by centrifuging to avoid losing already precipitated material of Mn.

With a supply of O_2 from air, manganese was slowly oxidised from Mn^{2+} to Mn^{4+} resulting in a delayed precipitation of $MnO(OH)_2$.

After leaving it for a few days at rest, manganese was reprecipitated to achieve purification of the sample by suppressing the interfering isobaric content of ^{53}Cr: after centrifugation and disposal of the solution, 5 ml HNO_3, 5 ml H_2O and 0.5 ml H_2O_2 was added. This lead to a reduction of Mn^{4+} to Mn^{2+} and, thus, dissolution of $MnO(OH)_2$. The solution was heated to 175 °C, Mn^{2+} oxidated again to Mn^{4+} with $KClO_3$ and reprecipitated to $MnO(OH)_2$ at this temperature. Washing three times with H_2O and drying at 90°C re-

sulted in targets of MnO_2.

For AMS measurements, the resulting material (oxide form of powder) was mixed with a metal powder to improve the thermal and electrical conductivity. This is important for the sputtering process, as it increases the efficiency of ions being extracted from the targets in the ion source in AMS. Furthermore, it makes the target easier to handle during sample pressing as adding a metal powder decreases electrostatic charging of the targets. For this reason MnO_2 targets were mixed with Ag (1:1 by volume).

4.1.3 Anion Exchange and Extration of Iron

A column (height 20 cm, diameter 1 cm) was filled with the anion exchange material DOWEX 1x8, 100-200 mesh. This was washed with 20 ml H_2O and conditioned with 20 ml of 10.2 M HCl, where Cl^--ions bound to the resin. The hydroxides were dissolved in 1.5 ml 10.2 M HCl and applied to the columns. Iron was then present as chloro-complex $[FeCl_4]^-$. This replaced Cl^- and stayed in the column as Al^{3+} and Be^{2+} were eluted with 18 ml 10.2 M HCl.

The $[FeCl_4]^-$-complex was destroyed with 25 ml H_2O and Fe^{3+} was eluted. In this step the nickel content, containing the stable isobar of ^{60}Fe, i.e. ^{60}Ni, which was already reduced in a previous step by precipitation, was further suppressed.

FeO(OH) was precipitated with NH_{3aq} and dried at 90°C to obtain Fe_2O_3. Samples from batches 15 and 16 were additionally ignited for 2 hours at 800°C. Like MnO_2, Fe_2O_3 was mixed with Ag (1:1 by volume) for the AMS measurements.

4.1.4 Cation Exchange and Extraction of Aluminium and Beryllium

The cation exchange step was performed with DOWEX 50Wx8, 100-200 mesh (height 20 cm, diameter 1 cm), also washed with 20 ml H_2O and conditioned with 20 ml of 1 M HCl. Here, the H^+-ions bound to the resin.

Hydroxides of Al and Be were precipitated with NH_{3aq}, redissolved in 1.5 ml 1 M HCl and applied to the ion exchange column. The positively charged Al^{3+}- and Be^{2+}-ions replaced H^+ and stayed in the column, while 40 ml of eluate (1 M HCl), containing the interfering isobar of ^{10}Be, ^{10}B, was discarded. Be^{3+} was collected with the next 115 ml eluate (1 M HCl) as it was in turn replaced by the H^+-ions. Al^{2+} still stayed in the column, and was collected afterwards with 50 ml of an acid with higher concentration (4.5 M HCl).

The two solutions were heated in order to reduce their volume. Then $Be(OH)_2 \cdot H_2O$ and $Al(OH)_3 \cdot xH_2O$ were precipitated with NH_{3aq}. The precipitates were washed three times with aqueous ammonia (pH 8-9), then dried and ignited for 2 hours at 900°C to produce BeO and Al_2O_3. BeO was mixed with niobium in a mass ratio of BeO/Nb = 1:6, Al_2O_3 with Cu in a mass ratio 1:1 (in the first three chemistry batches it was mixed with Ag, 1:1 in mass ratio) for the AMS measurement.

4.2 Accelerator Mass Spectrometry

The sample material produced with the chemical method described above, was analyzed with AMS. With AMS one is able to quantify the expected low trace amounts of analyzed radioisotopes in deep-sea sediments. Ratios of a radionuclide to its stable isotope were determined, which here were in the order of 10^{-10} for $^{10}Be/^9Be$. The ratio was determined by the amount of ^9Be carrier added to the sample. The isotope ratios for Al, Mn, and Fe were expected between 10^{-13} and 10^{-16}.

AMS measurements were carried out at different facilities by the local AMS staff[*]. ^{26}Al and ^{10}Be were measured at the **V**ienna **E**nvironmental **R**esearch **A**ccelerator (VERA)-facility in Vienna, Austria. Comparative ^{10}Be measurements were performed at the **Dre**sden-**AMS** (DREAMS)-facility at HZDR in Dresden, Germany. The heavier nuclides ^{53}Mn and ^{60}Fe were measured at the **H**eavy **I**on **A**ccelerator **F**acility (HIAF) at the Australian National University (ANU) in Canberra, Australia. Test measurements of two ^{60}Fe targets were additionally performed at the tandem accelerator at the Maier-Leibnitz-Laboratory of the Technische Universität München in Garching, Germany.

The basic principle of an AMS facility is described in the following: negative ions are produced in a Cs sputter source. These are preaccelerated and subsequently pass two mass spectrometers connected with a tandem accelerator. A scheme of the setup of VERA, the Vienna Environmental Research Accelerator, is given in Figure 4.2. The mass spectrometers consist of a combination of electrostatic analyzers and magnets, which sort the atoms and molecules by their energy and mass (momentum) over charge ratio. The tandem accelerator consists of a positively charged terminal and a foil or gas stripper in the center. As the negatively charged atoms or molecules pass through the tube, they are accelerated towards the terminal center and interact with the stripper gas. Some outer electrons are stripped off and molecules, which may have the same mass as the isotope of interest and, therefore, passed through the first mass spectrometer, break up. The now positively charged ions are accelerated further due to repulsion from the positive high voltage. These high-energy ions pass the second mass spectrometer and the molecule debris are filtered from the beam (Kutschera et al., 1997). With an ionization chamber or a semiconductor detector the selected radionuclides are counted. Currents of the stable isobars are measured in Faraday cups.

---

[*]AMS measurements at VERA were carried out by Peter Steier, Alfred Priller, Anton Wallner, Martin Martschini and Johannes Lachner. At the DREAMS facility, Silke Merchel, Georg Rugel, Stefan Pavetich as well as the local operator team was responsible for measurements. Measurements at HIAF were performed by Anton Wallner, Steve Tims, and Keith Fifield. At TUM, AMS measurement were carried out by Peter Ludwig, Leticia Fimiani, Gunther Korschinek, and Thomas Faestermann.
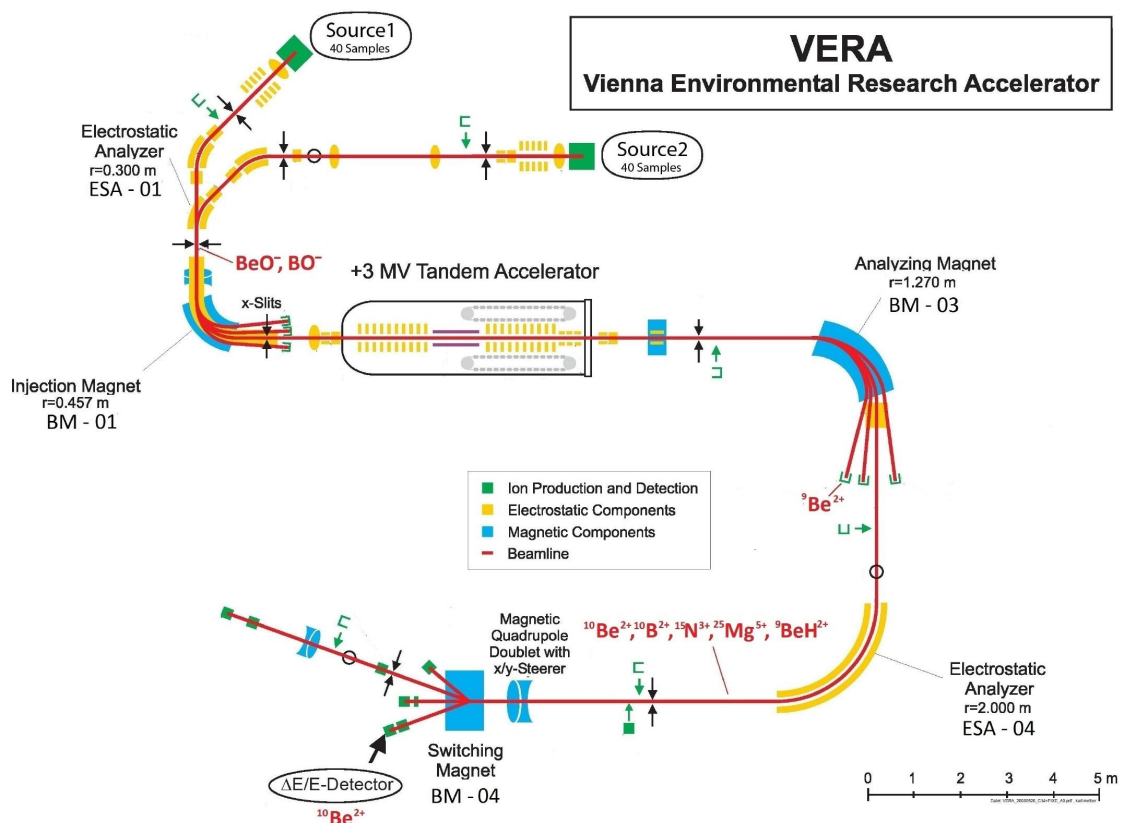
Figure 4.2: Schematic setup of the Vienna Environmental Research Accelerator for the example of a ^{10}Be measurement (courtesy of VERA staff). BeO$^-$ (and oxides of the isobar, BO$^-$) are selected by the low-energy mass spectrometer. Atomic and molecular ions with the same mass over charge ratio as ^{10}Be^{2+} (such as ^{10}B^{2+}, ^{15}Ni^{3+}, ^{25}Mg^{5+}, and ^{9}BeH$^+$) might pass through the high-energy mass spectrometer located behind the tandem accelerator. These are separated from ^{10}Be^{2+} in the SiN foil stack placed in front the particle detector due to their different energy loss compared to ^{10}Be^{2+}. Further separation is achieved in the ionization chamber itself.

4.2.1 Isobar Suppression

Not all atomic stable isobars will be filtered by the AMS setup described above and will thus be detected in the same manner with a particle detector. As they are much more abundant in nature than the corresponding radionuclide, stable isobars would cause a high background or a detector dead time and have to be suppressed by additional filters in the setup. The specific techniques of isobaric suppression at the various AMS facilities utilized in this work are explained below.

4.2.1.1 VERA

The isotopic ratios of ^{26}Al/^{27}Al and ^{10}Be/^{9}Be were determined with the VERA-laboratory, a 3 MV tandem accelerator facility at the University of Vienna, Austria (Steier et al., 2005). Al$^-$ and BeO$^-$-ions were selected for passage through the terminal. The stable

isobar of ^{26}Al, ^{26}Mg, does not form negative ions and, therefore, no isobaric suppression was necessary for this isotope.

^{10}Be has the stable isobar ^{10}B and BeO$^-$ as well of BO$^-$ forms negative ions. Here the suppression of ^{10}B is based upon the principle of energy loss in matter. A stack of 13 SiN foils with a total thickness of 8 μm was placed directly in front of the particle detector, a split-anode ionization chamber. A large fraction of the intense ^{10}B^{2+} beam is stopped in the foil stack, while most ^{10}Be^{2+} ions, due to their lower nuclear charge and thus lower energy loss, enter the detector. Further separation of the remaining stable isobars from the radionulide is achieved in the ionization chamber itself (Steier et al., manuscript in preparation, Schmidt (2013)).

4.2.1.2 DREAMS

Comparative measurements for the ^{10}Be/^{9}Be results obtained from the VERA-facility in deep-sea sediment samples (section 5.1.1) were carried out at the HZDR, Germany. The DREAMS laboratory operates a 6 MV tandem accelerator. Suppression of ^{10}B works slightly different to the VERA setup. Instead of placing the absorber foils directly in front of the detector, one 1 μm thick silicon nitride foil is placed between the high-energy 90° analyzing magnet and a 35° electrostatic analyzer (Akhmadaliev et al., 2013). ^{10}B^{2+} was separated from ^{10}Be^{2+} utilizing their different energy loss in the SiN foil and by a subsequent electrostatic analyzer, which separates ions by their E/q ratio. ^{10}Be was counted with a four-anode gas ionization chamber filled with isobutane.

4.2.1.3 HIAF

The radionuclides ^{53}Mn and ^{60}Fe have higher mass numbers than ^{10}Be and ^{26}Al. The relative differences of atomic numbers between the radionulide and its stable isobar is $z_{rel} = (z_1-z_2)/z_1$ (where z is the nuclear charge and $z_1 > z_2$). For ^{53}Mn (z=25) and ^{53}Cr (z=24), $z_{rel} = 0.04$, for ^{60}Fe (z=26) and ^{60}Ni (z=28), $z_{rel} = 0.07$. These values are much lower than for ^{10}Be (z=4) and ^{10}B (z=5), with $z_{rel} = 0.25$. Therefore, the heavier nuclides can not be separated as easily as ^{10}Be from ^{10}Be. For this reason, acceleration to very high energies in the order of 150 MeV was combined with a gas-filled magnet to achieve sufficient suppression of the interfering isobar (e.g. Paul et al. (1989); Poutivtsev et al. (2010), Knie et al. (1997)). Interaction of the particles with the gas atoms in the magnet lead to an average charge state, which depends on the atomic number. As a result the radionuclide and its stable isobar are deflected differently and take separate trajectories in the magnet.

To achieve the required energy for efficient isobar suppression for ^{53}Mn and ^{60}Fe, AMS facilities with terminal voltages above 10 MV are required. The HIAF at the Australian National University (ANU) in Canberra is capable of reaching terminal voltages of 14.5-15.5 MV (Fifield et al., 2010). At their facility, the ^{53}Mn and ^{60}Fe samples were measured. Two ^{60}Fe targets were analyzed at the 14 MV tandem accelerator at the Maier-Leibnitz-Laboratory of the Technische Universität München in Garching, Germany.

4.3 Methods for Stable Isotope Measurements

Because a ^{9}Be carrier is added to each sample after leaching, the ratios measured with AMS do not represent the oceanic ^{10}Be/^{9}Be ratios. Therefore, measurements of the stable isotope content were needed to quantify the amount of natural ^{9}Be atoms and to calculate the natural isotopic ratios. The method used here allowed to measure stable Be, but also other elements such as Mg, Al, Ca, Mn, Fe, and Ni (ICP-MS (**I**nductively **C**oupled **P**lasma **M**ass **S**pectrometry)).

Independent measurements verifying the ICP-MS results for stable Fe and Ni were obtained by GF-AAS (**G**raphite **F**urnace - **A**tomic **A**bsorption **S**pectrometry) for chemistry batches 1-5 (Fe) and batches 10-14 (Fe and Ni). The Mg and Ca results from ICP-MS were checked via F (**F**lame)-AAS. These measurements were carried out by Aline Ritter and Sabrina Gurlit at the HZDR. Be was also quantified with GF-AAS at CEREGE (Aix-Marseille-University, France) by Valéry Guillou. Basic principles of the two techniques are briefly described in the following (for further reading see e.g. Broekaert (2005); Welz and Sperling (1997)).

4.3.1 ICP-MS

The sample is introduced to the ICP ion source as an aerosol by nebulizing the sample, which is dissolved in a liquid. Subsequently the fine aerosol droplets pass through an argon-plasma with typical temperatures of 6000-10 000 K, where they are first evaporated, then the individual atoms are positively ionized. These ions pass from a region of atmospheric pressure to an intermediate vacuum, and subsequently into a low-pressure region with less than 10^{-5} mbar, that is confined by two cones: the sampler and the skimmer. Holes in the cones sample the center fraction of the ion beam which is then focused by a setup of ion optics. In a mass spectrometer consisting of a magnet and an electrostatic analyzer a mass-over-charge ratio is selected for measurement and subsequently the atom is counted.

Concentrations lower than ng/mL can be quantitatively determined with this method. However, molecular interference can not be prevented and stable isobars not separated. Therefore this technique (as well as AAS) is suitable for elements without stable isobars and that are abundant enough to neglect isobaric molecules.

4.3.2 AAS

With AAS absorption spectra from an optical light source of sample elements are determined. In this work, two methods were applied to extract atoms from the solution containing the dissolved sample: GF (**G**raphite **F**urnace)-AAS and F (**F**lame)-AAS.

In GF-AAS the dissolved sample is heated in a graphite furnace until complete atomization at temperatures between 1000 and 3000 K. In a F-AAS facility the liquid containing the sample is nebulized and converted to a burner by mixing the aerosol droplets with a burning gas and an oxidant. When encountering the flame, temperatures of 2000-3000 K can be achieved to atomize the fine droplets. A radiation source is lead through the volume

of atomic sample elements. The amount of light absorbed correlates with the concentration of the measured element. The attenuation of the light intensity is detected with a photomultiplier. Usually the detection limit is in the order of ng/mL.

4.4 Chemistry Yields

To extract quantitatively and with high chemical yields the full set of the radionuclides ^{10}Be, ^{26}Al, ^{53}Mn, and ^{60}Fe requires a long and challenging preparation procedure. During this work, 85 samples were chemically prepared, some of them multiple times: seven sediment samples and an additional processing blank per batch. Altogether, 16 batches were prepared and are referred to as batch 1-16. Appendix B.2 contains tables with the sample numbers with and corresponding batches. The extraction procedure for the elements of interest (Al, Be, Mn, and Fe) from the marine sediments, applying the procedure described in chapter 4.1, required up to 2 weeks per batch. It was possible to simultaneously parallel two batches, therefore, the total time for chemical processing added up to approximately half a year.

4.4.1 Batch 1: a Test for the Extraction Procedure

The first batch was prepared in January 2012. It contained 4 samples and one blank and served as a first test to determine the chemical yield of each element from a sediment sample of 1 g. The procedure was slightly different to that described in chapter 4.1. Leaching of this batch was done according to Bourlès et al. (1989), using 20 ml of 0.04 M NH$_2$OH·HCl in 25% (V/V) acetic acid. The next steps were performed as explained in chapter 4.1 until the precipitation with NH$_{3aq}$ (chapter 4.1.2). Instead of separating manganese by slow precipitation, it was collected during anion exchange, i.e. after evaporation of the leaching solution to dryness 1.5 ml 10.2 M HCl was added and applied to the column. Between elution of Al^{3+} and Be^{2+} with 18 ml 10.2 M HCl and Fe with 25 ml H$_2$O, Mn was collected by dissolving the [MnCl$_3$]$^-$ complex, which was slightly bound to the resin, with 100 ml 7.1 M HCl. It was then reprecipitated and and dried as described in chapter 4.1.2.

The amount of sample material (oxides of Al, Be, Mn, and Fe produced for an AMS measurement) extracted from 1 g sample weight in this first test was much lower than expected. To quantify the efficiency of the chemical extraction procedure, the chemical yield is determined. It is defined as the fraction of sample material retrieved during sample preparation relative to the total amount available after leaching

$$\text{chemical yield} = \frac{\text{weight of oxides retrieved}}{\text{total amount (oxides)}} \times 100. \tag{4.1}$$

The elements are retrieved as oxides, therefore the mass of the total amount available is converted to oxides as well. The total amount of Al, Mn, and Fe was calculated from an aliquot measured by ICP-MS and AAS from an aliquot taken after leaching. The concentration of these elements in the leachate corresponds to 100 %. The total concentration

of stable Be in the final AMS sample was dominated by the carrier added. Natural ^{9}Be in the sediments is negligible compared to the amount of carrier added. For all elements extracted from the test samples the starting weight, the total amount and the final weight of recovered oxides, and the chemical yields are listed in table 4.1.

Table 4.1: Chemistry batch 1: starting weights of the sediment samples, weights of total amounts after leaching (obtained from amount of carrier added (Be) and from ICP-MS measurements (other elements)) and extracted oxides of desired elements and their chemical yields are listed for sample numbers 10, 34, 40, 68, and the processing blank.

Sample Number	10	34	40	68	processing blank
Starting Weight (g)	0.95	0.99	1.02	1.00	
BeO carrier (mg)	0.84	0.84	0.84	0.84	0.84
BeO extracted (mg)	0.67	0.80	0.53	0.46	0.08
BeO chemistry yield (%)	80	95	63	55	9
Al_2O_3 leached (mg)	1.59	2.09	1.87	1.13	
Al_2O_3 extracted (mg)	0.66	1.29	0.79	0.17	
Al_2O_3 chemistry yield (%)	45	66	45	16	
MnO_2 leached (mg)	4.12	0.98	6.88	5.15	
MnO_2 extracted (mg)	3.15	0.05	4.47	3.92	
MnO_2 chemistry yield (%)	82	5	70	82	
Fe_2O_3 leached (mg)	1.51	0.87	1.50	0.99	
Fe_2O_3 extracted (mg)	1.00	0.37	0.99	0.51	
Fe_2O_3 chemistry yield (%)	71	46	71	55	

Low yields of beryllium are not a problem, because due to high ^{10}Be/^{9}Be ratios, only little target material needs to be sputtered during an AMS measurement. A carrier of 300 µg of stable ^{9}Be was added during the first batch, which leads to lower AMS measurement ratios of ^{10}Be/^{9}Be than the expected natural ratio of $\sim 10^{-7}$. The measured ^{10}Be/^{9}Be ratios are still in the order of $\sim 10^{-11}$. The chemical yield of extracted BeO was between 55 and 95 % corresponding to masses between 0.46 and 0.80 mg of BeO. However, for the processing blank, only 9 % of the originally available material was extracted. In later batches the average yields were higher (section 4.4.2); an indication for improved performance of the chemical procedure after the first test batch. The AMS sample material of batch 1 was only measured at the DREAMS facility, not at VERA. For comparative measurement results of both laboratories the amount of carrier was doubled in the subsequent chemistry batches and the BeO was shared between the two facilities.

All other isotopes were expected to have ratios in the order of 10^{-13} (^{26}Al/^{27}Al surface samples) to $\lesssim 10^{-15}$ for ^{60}Fe/Fe. Therefore, long measurement times i.e. several hours were required per target. This is only possible if enough target material is available. Batch 1 yielded Al_2O_3 masses between 16 % (number 68) of originally 1.13 mg available and 66 % (number 34) of a higher sample of mass 2.09 mg available for chemistry (table 4.1). A correlation between the leached amount and the chemical yield was observed for Al.

This effect will be further analyzed in the following section.

All Al_2O_3 targets were measured at the VERA facility. Target number 68 did not give a useful current (<2 nA) and no ^{26}Al count was obtained during this measurement (as expected). For the other three samples, up to 18 ^{26}Al events were detected with statistical uncertainties ranging between 25 and 40 %. Al^- current were ≤200 nA and resulting $^{26}Al/^{27}Al$ ratios were in the order of 10^{-14}.

Since $^{60}Fe/Fe$ ratios were expected in the same order of magnitude as $^{26}Al/^{27}Al$ or even less (Figure 3.13), the amount of AMS target material obtained from 1 g sediment was not sufficient for a quantitative measurement. For this reason, and to increase the chemical yield for all elements especially for Al, 3 g of sediment material was used in the subsequent chemistry batches and all samples were chemically processed according to chapter 4.1.

The manganese samples in batch 1 were tested for their stable ^{53}Cr content (the isobar of ^{53}Mn). These tests were performed at the Maier-Leibnitz-Laboratory at the Technical University of Munich. Ratios of $^{53}Cr/^{55}Mn$ of $1\text{-}2\times10^{-6}$ were obtained in all samples, which was close to a measured blank (sample with low Cr-concentration), with $^{53}Cr/^{55}Mn$ = 7.6×10^{-7}.

However, this low Cr-background was achieved by chemical separation of manganese during anion exchange and subsequent re-precipitation. As the procedure was later adapted to 3 g of sample material, Mn was slowly precipitated before the anion exchange step and loaded onto the column. Indeed, it was reprecipitated with $KClO_3$, but test measurements at HIAF, already at an advanced state of this work, showed that chromium suppression with this adapted method was less efficient and compromises the ^{53}Mn measurements.

4.4.2 Sample Statistics Including Subsequent Batches

In the course of this work 13 additional batches of a set of 71 samples provided by the ARF were prepared. These did not include samples from the sediments top surface, corresponding to the present time. Such samples are required to obtain a chronology of the sediment cores using ^{26}Al and ^{10}Be measurements. Surface samples became available from the ARF in 2013. These were prepared as batch 15 and 16 together with additional samples expected to cover ages of 2, 3-5, and 25 Myr.

ICP-MS measurements of aliquots, taken after leaching were carried out at HZDR. The intrinsic amount of stable Be was quantified with ICP-MS. In addition, concentrations of leached Mg, Al, Ca, Mn, Fe, and Ni were determined. The accuracy of ICP-MS was reported to range within 5-10 % (Be, Fe), 3-5 % (Al, Ca, Ni), and 1-3 % (Mg, Mn) (Aline Ritter, private communication, 2013). If supplementary GF-AAS measurements were performed for Fe and Ni, the uncertainty in the stable contents decreased to 1-3 %.

In the course of this work, problems of ICP-MS measurements of Be due to its low natural abundance in combination with the applied leaching solution became evident. Therefore, one additional batch of eleven 1 g samples (marked with the letter 'L' in the tables of Ap-

pendix B.2) and one processing blank was leached. The aliquots were split and its stable Be content was measured at HZDR with ICP-MS, as well as at CEREGE (Aix-Marseille-University, France) with GF-AAS for comparison. Details to problems concerning ICP-MS measurements of ^{9}Be and results of comparative measurements are discussed in section 5.1.2.
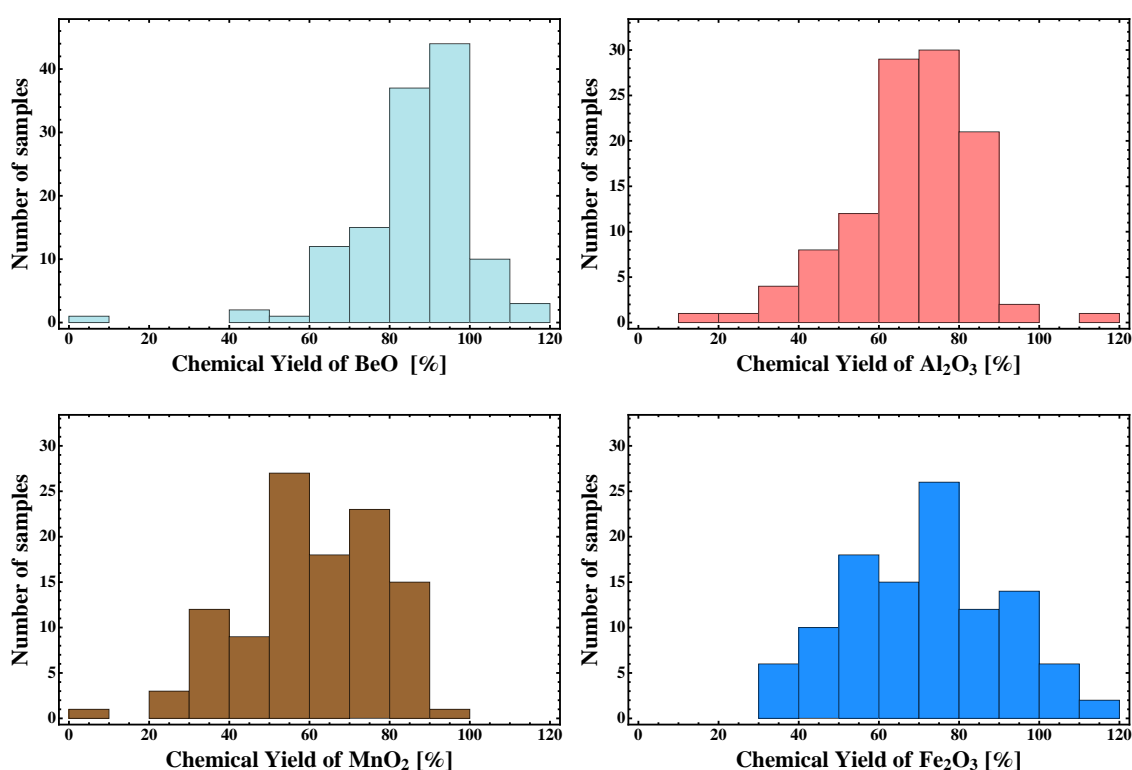

Figure 4.3: Distribution of the chemical yields from sample processing. Leached elemental concentrations were measured with ICP-MS for Al, Mn, and Fe. In case of Be the "initial amount" is dominated by the carrier added.

Chemical yields were calculated for all samples prepared in batches 1-16. Figure 4.3 depicts the yields for BeO, Al_2O_3, MnO_2, and Fe_2O_3 as histograms for all sediment and Be blank samples. As mentioned above, the lowest yields observed were for samples of batch 1 and they differ significantly from the mean. On average 86 % of BeO, 68 % Al_2O_3, 61 % MnO_2, and 72 % Fe_2O_3 were recovered during the chemical procedure. It is evident, that some samples yield more than "100 %", indicating other elements present in the final AMS targets, e.g. titanium in beryllium targets and chromium in aluminium targets. Other elements might be also present in samples with yields lower than 100 %, indicating that the yields calculated can be considered as upper limits. On average 1.4 mg of BeO, 3.0 mg of Al_2O_3, 11.8 mg of MnO_2, and 5.5 mg of Fe_2O_3 were available for the AMS measurements. The variability of element concentrations within the deep-sea sediment cores is discussed in more detail in section 5.5.

Figure 4.4 displays the correlation between the total amount of stable elements measured
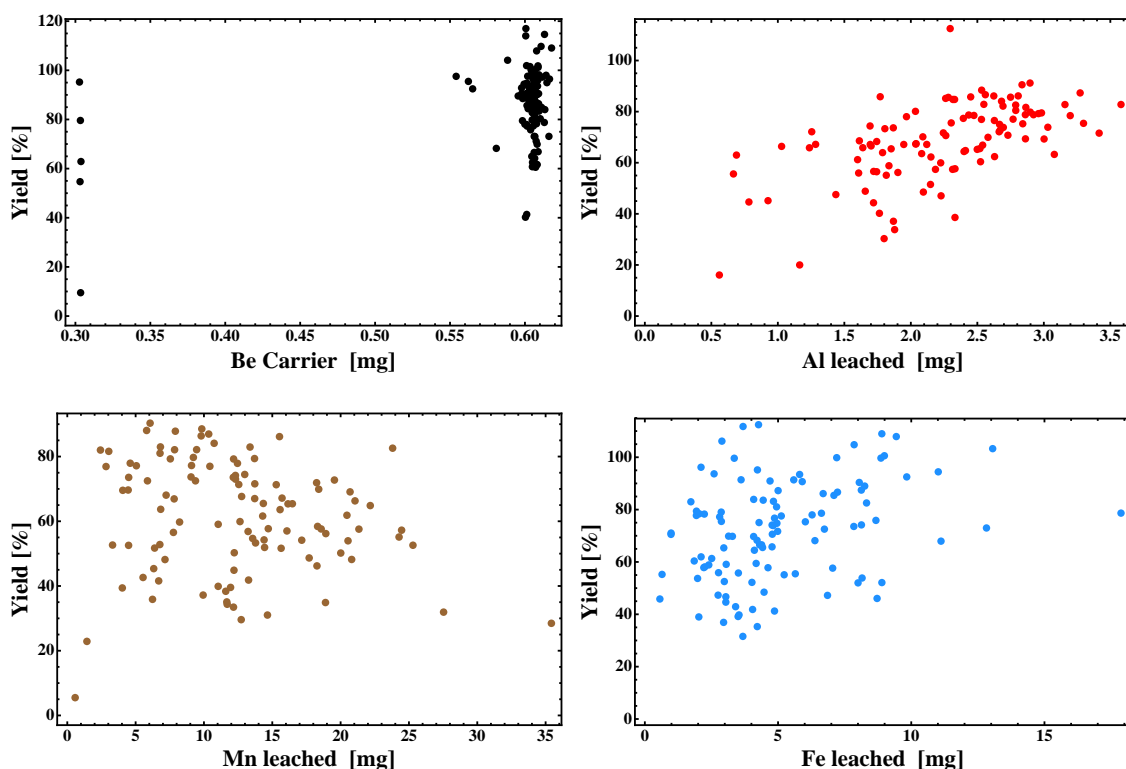
Figure 4.4: Absolute amount of target material extracted as oxides during chemical preparation per sample of 16 batches displayed as histograms.

within the leachates and the chemical yield. It was already mentioned above, that samples in batch 1, with a lower initial mass, resulted in a lower chemical yield. For Al, a clear correlation is visible, for Fe a correlation is not clear. Mn does not show any correlation between yield and leached amount. The amount of Mn is high compared to Fe and especially to Al, indicating this correlation becomes significant for lower amounts of leached element concentrations (<4 mg).

As a Be-carrier had to be added to make extraction of the trace amounts of natural beryllium possible, a processing blank is available for Be samples. The processing blank is needed to quantify a possible cross contamination of the samples by ^{10}Be due to their high ^{10}Be/^{9}Be ratios. One processing blank was produced for Fe. If no processing blanks were available, machine blanks were measured, which consist of commercially available Al_2O_3, Fe_2O_3, and MnO_2.

^{26}Al and ^{10}Be were measured at the VERA (^{10}Be, ^{26}Al) and DREAMS (^{10}Be) facilities (sections 5.1 and 5.2). ^{60}Fe had not been measured before at the HIAF facility of the Australian National University and first test measurements were carried out towards the end of 2012. Since then ^{60}Fe data of the deep-sea sediments were collected during several beam times for 43 samples and results are given in section 5.3. Measurements of ^{60}Fe had priority over ^{53}Mn (a SN-signal will be rather visible in background-free ^{60}Fe than in ^{53}Mn, where a large background component from meteoric influx is expected). First measurements of ^{53}Mn at HIAF are discussed in section 5.3.

5 Results and Discussion

Long-lived radionuclides in deep-sea sediments provide useful information for applications in astrophysics as well as geophysics. The primary goal of in this thesis was the detection of a SN signal. However, before the outcome is discussed, several other topics concerning details of measurement procedures, dating of the deep-sea sediments, and geological applications, are addressed.

First, beryllium measurements are presented (section 5.1). Results for $^{10}Be/^9Be$ obtained from the two facilities VERA and DREAMS are compared (section 5.1.1). To determine the abundance of stable ^9Be in the sediment samples before a carrier is added, ICP-MS measurements were carried out. The results of ICP-MS measurements of stable Be were not consistent with each other. Possible reasons for offsets between the data of different measurement series and their correction is discussed in section 5.1.2. Results of ^{26}Al measurements at VERA are presented in section 5.2. The measurement efficiency for ^{26}Al at VERA is examined and compared to results obtained in earlier studies (e.g. Auer et al. (2007)). Subsequently, results for ^{53}Mn and ^{60}Fe measurements at HIAF are presented (section 5.3). Dating procedures using isotopic ratios of $^{26}Al/^{27}Al$ and $^{10}Be/^9Be$ are applied to the deep-sea *Eltanin* samples in section 5.4. Subsequently the possibility of using the $^{26}Al/^{10}Be$ ratio as a dating tool is discussed in section 5.5. Data for ^{26}Al and ^{60}Fe are discussed with respect to potentially one or more SN explosions in section 5.6. An uptake factor for the ferromanganese crust signal (Knie et al., 2004) is recalculated by comparison of the ^{60}Fe fluence in terrestrial and lunar samples.

5.1 Measurements of ^{10}Be at DREAMS and VERA

^{10}Be, was measured at two AMS-facilities. After chemical sample preparation, the resulting BeO was mixed with niobium in a mass ratio of BeO/Nb = 1:6, and material then split into two sputter samples. One sputter sample was measured at the DREAMS-facility at the HZDR in Germany, the other one at the VERA facility at the University of Vienna.

5.1.1 Comparison of the VERA and DREAMS Data for ^{10}Be

At the DREAMS facility, BeO^- was injected into the 6 MV tandem accelerator. The currents of $^9BeO^-$ were between 2 and 7 µA. After passage of the stripper gas in the terminal of the accelerator, the 2^+ charge state at a terminal voltage of 4.5 MV was selected, which resulted in energies of 10.7 MeV for $^{10}Be^{2+}$. The charge state 4^+ was selected after

passing a SiN absorber foil that was used for suppression of boron (Akhmadaliev et al., 2013).

The DREAMS in-house standard SMD-Be-12, with a $^{10}Be/^9Be$ value of (1.70 ± 0.03) $\times10^{-12}$ (Akhmadaliev et al., 2013), was used for normalization. The ratios of the sediment samples were all in the order of 10^{-11}. $^{10}Be/^9Be$ ratios for processing blanks were between 1.5×10^{-15} and 7.5×10^{-14}. The beam times were spread over a time period of two years. Each sample was measured only once (see table 5.1). The results of these measurement series are displayed in Figure 5.1.

Table 5.1: Beam-times for $^{10}Be/^9Be$ measurements at DREAMS. Numbers in the first column represent the chemistry batches.

Batches	Beam Time
1	February 2012
2 - 5	August 2012
6	September 2012
7 - 9	January 2013
10 - 11	February 2013
12 - 14	June 2013
15	December 2013
16	February 2014

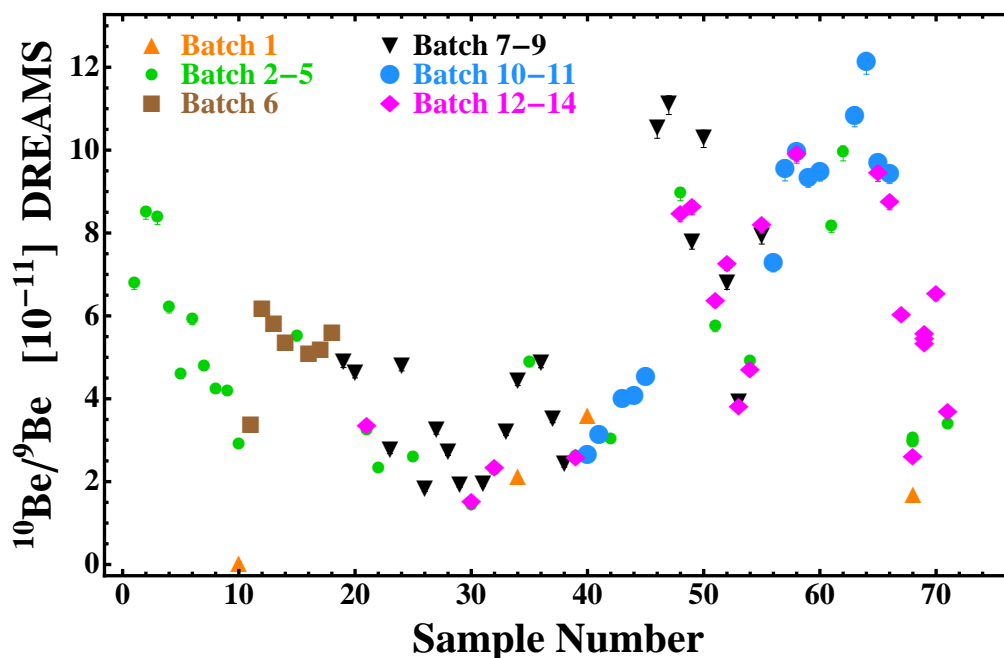**Figure 5.1:** $^{10}Be/^9Be$ results of DREAMS measurements identified by the beam-times listed in table 5.1. Each sample was measured during one beam-time.

At VERA, a BeO$^-$ beam is produced with typical currents of 1 μA for ^{9}BeO$^-$. The beam is injected into the tandem accelerator, which operates with a terminal voltage of 3 MV for Be measurements. A charge state of ^{10}Be^{2+} is used, resulting in a particle energy of 7.18 MeV. A SiN foil stack placed directly in front of the ionization chamber allows for a sufficient suppression of ^{10}B^{2+} (Schmidt (2013), Steier et al., manuscript in preparation). This specific setup is relatively new and differs from a previous setup, where a degrader foil was mounted in the beam line similarly to the setup at DREAMS. The degrader foil method causes scattering of the beam, which has to be refocused by additional quadrupole lenses (Akhmadaliev et al., 2013). Losses of ^{10}B^{2+} due to scattering are minimized using the new setup at VERA.

Some of the *Eltanin* samples were measured multiple times for ^{10}Be to test the reproducibility of this new measurement setup. Beam-times were carried out between June 2012 and December 2013 (see table 5.2). The results of these beam-times are plotted in Figure 5.2. Blank levels ranged between 1.8 and 6.7×10^{-15} in all measurement series.

Name	Batches	Beam Time
SiN05	2, 3	June 2012
Be1101	2, 3	June 2012
ELT03	4, 5, 6	December 2012
ELT04	4, 5, 7, 8, 9	February 2013
ELT05	10, 11, 12	June 2013
ELT06	2, 3, 13, 14	September 2013
ELT07	6, 7, 15, 16	December 2013

Table 5.2: Beam-times for ^{10}Be/^{9}Be measurements at VERA. Each measurement series was given a name as listed in the first column. Chemistry batches analyzed during a beam-time are shown in the second column. Some samples were measured multiple times as indicated by repeatedly listed batches.

During the measurements with the newly installed SiN foil stack, systematic offsets were observed between data sets of different measurement series. Some reasons for these possible systematic errors are listed below:

- The first tests with this new approach were carried out with an insufficient stripper gas pressure (~0.5 μg cm^{-2}) for a charge state ^{10}Be^{2+}. This pressure was not high enough to completely destroy molecular ^{9}BeH^{2+}. These followed ^{10}Be^{2+} on the same beam trajectory and enter the SiN foil stack that is placed in front of the detector. The molecule ^{9}BeH^{2+} breaks up in the foil stack. The fragments enter the ionization chamber with very low energies (in the order of 100 keV), which was below the electronic threshold used for the data acquisition, but still caused a hidden dead time in the data acquisition, i.e. the effective time (life-time), where the detector electronics were active, was overrated. Thus, the ^{10}Be count rate was underestimated. This was later corrected by normalizing to the fixed pulser count rate.

- The measurement results were then evaluated by normalizing to a standard value, for each turn (i.e. each sample placed in the sample wheel is measured one time)
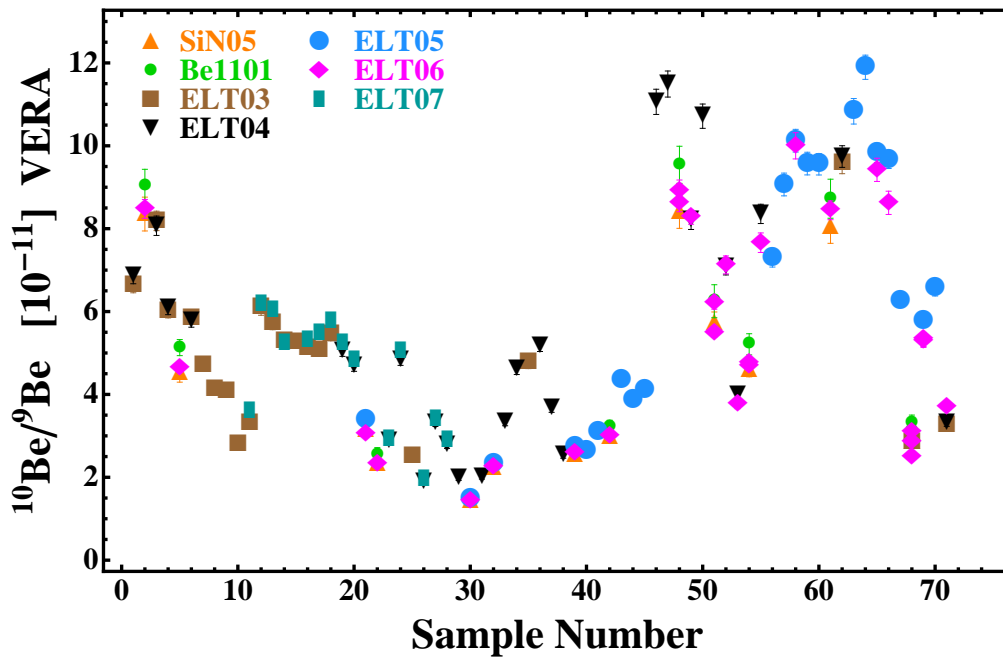
Figure 5.2: Beam-times performed at VERA, identified by the measurement series given in table 5.2. Some samples were measured repeatedly in several measurement series to test for systematical errors.

of the sample wheel separately. Typically three turns were collected, before a re-tuning of the instrument was carried out. Data from at least three retunings were combined to obtain final results. Frequent tuning was required to reduce systematic uncertainties caused by the limited experience with the new SiN-foil stack method. A possible offset between tunings is averaged out and the measurement results converge against a mean value. Data from runs with low particle transmission and of larger scatter in the standards, were rejected.

- Three different standards were used for normalization of the ^{10}Be/^{9}Be data: the Dresden in-house standard material SMD-Be-12 (see above), the S555 standard of ETH-Zurich, and the VERA in-house standard Be1-ATI. S555, with a nominal value of ^{10}Be/^{9}Be = (9.55±0.24)×10^{-11} (Kubik and Christl, 2010), was recalibrated taking into account the new half-life of ^{10}Be of (1.387±0.012) Myr (Chmeleff et al., 2010; Korschinek et al., 2010). The revised ratio of ^{10}Be/^{9}Be becomes then (8.71±0.24)×10^{-11} and the standard was renamed to S555 N (Christl et al., 2013). Be1-ATI is a BeO standard material with a calculated value of (1.72±0.05)×10^{-12}. However, this number was based on the old S555 standard value.

The measured data showed systematic offsets of up to 10 % between the two measurement series ELT03 and ELT04 indicating incorrect standard values. For a direct comparison of the VERA results with the DREAMS data, both standards, Be1-ATI and S555, were later normalized to the DREAMS standard SMD-Be-12. The two measurement series were then corrected for the nominal values: ELT03 yielded ratios of (1.797±0.088)×10^{-12} for Be1-ATI and (8.71±0.39)×10^{-11} for S555, and

ELT04 resulted in $(1.947\pm0.100)\times10^{-12}$ and $(8.85\pm0.18)\times10^{-11}$ for Be1-ATI and S555, respectively. Weighted averages produce

$$\text{Be1} - \text{ATI}: \quad (1.86 \pm 0.07) \times 10^{-12},$$
$$\text{S555}: \quad (8.83 \pm 0.16) \times 10^{-11}.$$

The new value for Be1-ATI is higher than the previous one, exactly reflecting the change of the half-life of ^{10}Be. S555 N agrees with Christl et al. (2013) within the uncertainty. These standards were then renamed to Be1-ATI-nSMD and S555-nSMD for further usage.

Renormalization cleared the systematic offset between ELT03 and ELT04. The reproducibility of ^{10}Be/^{9}Be ratios between different measurement series was calculated from samples produced in the two batches 4 and 5, as these were measured in the two beam-times. Ratios of individual data points were reproduced with a relative uncertainty of 1.7 %. This number was added quadratically as a systematic contribution to the total uncertainty to all measured Be-data of VERA according to equation (E.5) in the Appendix.

A comparison of DREAMS and VERA data is shown in Figure 5.3 including the first set of 71 samples prepared in batch 2-14. The upper panel gives the background-corrected ^{10}Be/^{9}Be ratios normalized to the SMD-Be-12 standard. Multiple data points of a few samples (e.g. samples 49, 48, 51, and 52) indicate a repeated measurement, if the sample material was chemically prepared a second time. The amount of Be-carrier added in the chemical procedure determines the ^{10}Be/^{9}Be ratio, therefore, different ratios for the same sample were obtained.
The lower part of Figure 5.3 visualizes the same data, where ^{10}Be/^{9}Be ratios from DREAMS versus VERA are plotted. A solid line indicates a ratio of one between the two data sets. 61 % of the data points follow this line within 1 σ. This number is close to the value expected from statistics (68 %).

The clarification of the initial problems with the new SiN-foil stack method and the standards used delayed the final evaluation of the ^{10}Be/^{9}Be VERA data. Therefore, only the data obtained with the DREAMS facility was used for further evaluation.
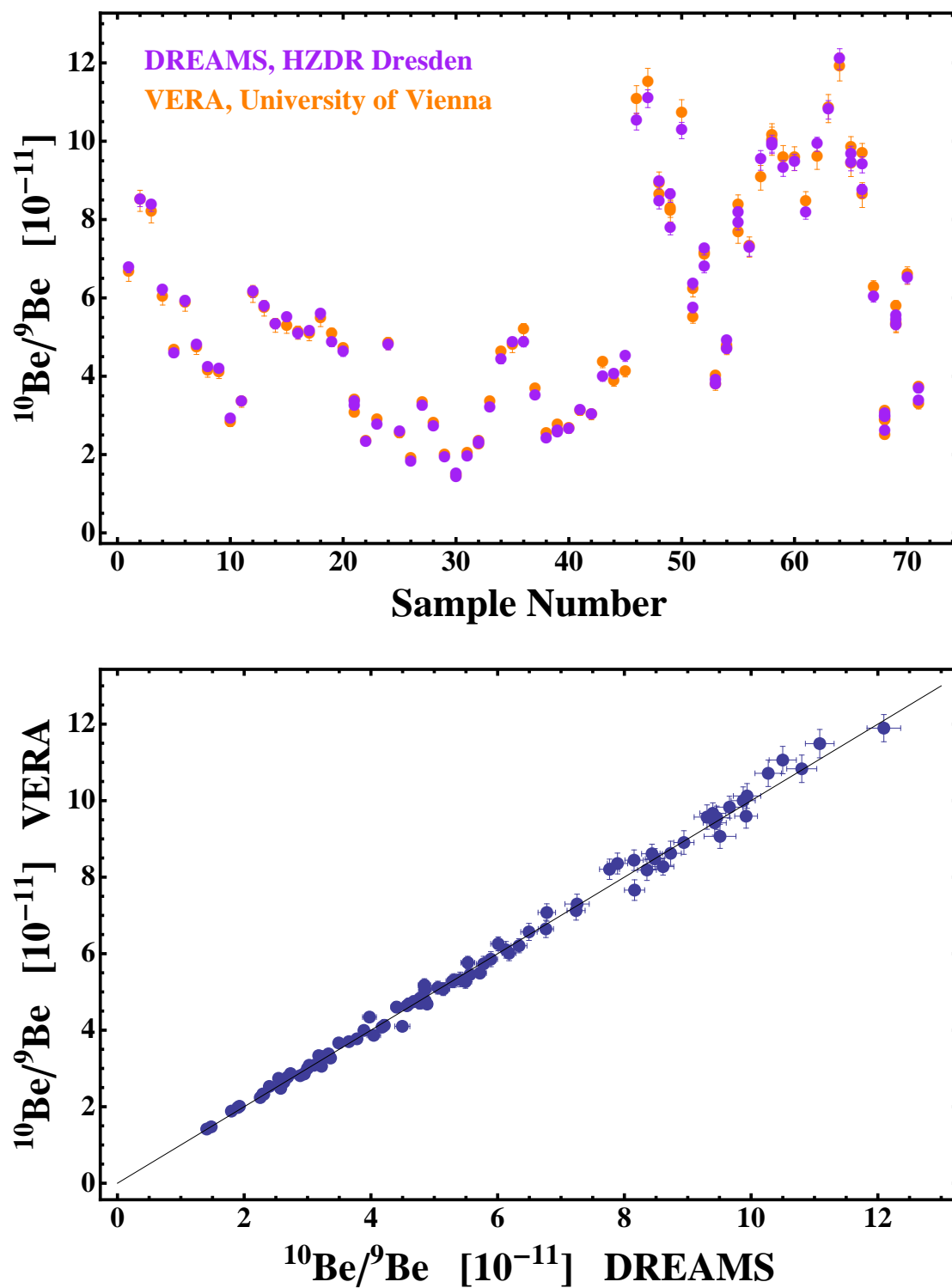
Figure 5.3: **Upper part:** Direct comparison of ^{10}Be/^{9}Be ratios obtain from DREAMS and VERA measurements versus sample number. **Lower Part:** The same results represented in a VERA versus DREAMS plot. The data points follow a solid line with unity slope.

5.1.2 ICP-MS Measurements of Stable ^{9}Be

Before adding a carrier of stable ^{9}Be to the leachate, an aliquot (referred to as a fraction f_A (%) of the total leachate) was taken for the determination of the content of initial (referred to as natural) ^{9}Be as well as other stable element contents in a sediment sample. This number was required to calculate the natural $(^{10}Be/^9Be)_{nat}$ ratio from the measured AMS ratio $(^{10}Be/^9Be)_{AMS}$ in a sample:

ICP-MS measurements yielded the ^{9}Be concentration (μg ml^{-1}) in the aliquot taken: This concentration was converted to ^{9}Be atoms present in the initial sample that was leached (n_9^S). Because the remaining fraction ($\sim$96 %) used for AMS was reduced by the amount of the aliquot, the fraction f_A was subtracted from the initial sample mass and a carrier was added to the residual solution,

$$n_{9,chem}^{S+C} = n_9^S(1 - f_A) + n_9^C. \tag{5.1}$$

Here, n_9^C is the ^{9}Be content (ats) of the carrier, and $n_{9,chem}^{S+C}$ refers to the sum of natural and carrier ^{9}Be ats in solution used for further chemistry. The BeO target produced from this solution was measured with AMS. The amount of ^{10}Be ats in the initial sample mass is calculated by multiplying the AMS ratio $(^{10}Be/^9Be)_{AMS}$ with the n_9^C and correcting for the fraction f_A of aliquot taken,

$$n_{10}^S = \frac{\left(\frac{^{10}Be}{^9Be}\right)_{AMS} \times n_{9,chem}^{S+C}}{1 - f_A}. \tag{5.2}$$

The initial $(^{10}Be/^9Be)_{nat}$ ratio within the deep-sea sediment sample was calculated by

$$\left(\frac{^{10}Be}{^9Be}\right)_{nat} = \frac{n_{10}^S}{n_9^S}. \tag{5.3}$$

The ICP-MS measurements introduced an additional source of uncertainty. The precision of an AMS measurement depends mainly on the counting statistics, the uncertainty of the standard used (1.8 % for SMD-Be-12) as well as on systematic uncertainties (1.7 %). 1 % counting statistics was achieved easily due to the high $^{10}Be/^9Be$ ratios in the samples. ICP-MS adds to the AMS uncertainties by 3-5 % for Be (A. Ritter, private communication (2013)).

5.1.2.1 Systematic Offsets Between ICP-MS Measurement Series

The batches 1, 2-5, 6-9, and 10-14 were analyzed in different ICP-MS measurement series, respectively, distributed over 14 months (February 2012 - March 2013). The calculated intrinsic $^{10}Be/^9Be$ ratios in the sediment samples after ICP-MS measurements are displayed in the upper parts of Figures F.1 and F.2 in the Appendix. It seems the ratios of batch 2-5 and 6-9 are in agreement with each other. Batch 1 and 10-14 also seem to agree.

However, between those measurement series an offset of a factor of ~1.5 was observed.

When this systematic deviation became apparent, no aliquots from batches 1-9 were available anymore. However, measurements for samples from batch 10-14 could be repeated. The results of the second measurement (green diamonds in Figure 5.4) are in agreement (within ~5 %) with those of the first measurement (orange squares), corroborating the reliability of the first set of data for batch 10-14. For further clarification, another 11 samples that were leached during all 14 batches were selected for measurement. For those samples sediment material was still available. These samples are labeled with the letter 'L' (Appendix B.2). 1 g sample material was leached according to the procedure described in section 4.1. The leachate was measured with two facilities: ICP-MS was performed at HZDR and comparative GF-AAS measurements were carried out at CEREGE (Aix-Marseille-University, France). The results are shown as blue triangles (HZDR New Leaching) and brown squares (CEREGE New Leaching) in Figure 5.4. The concentrations measured at these two facilities were in agreement with each other (±5 %), and with those obtained initially for batch 10-14.
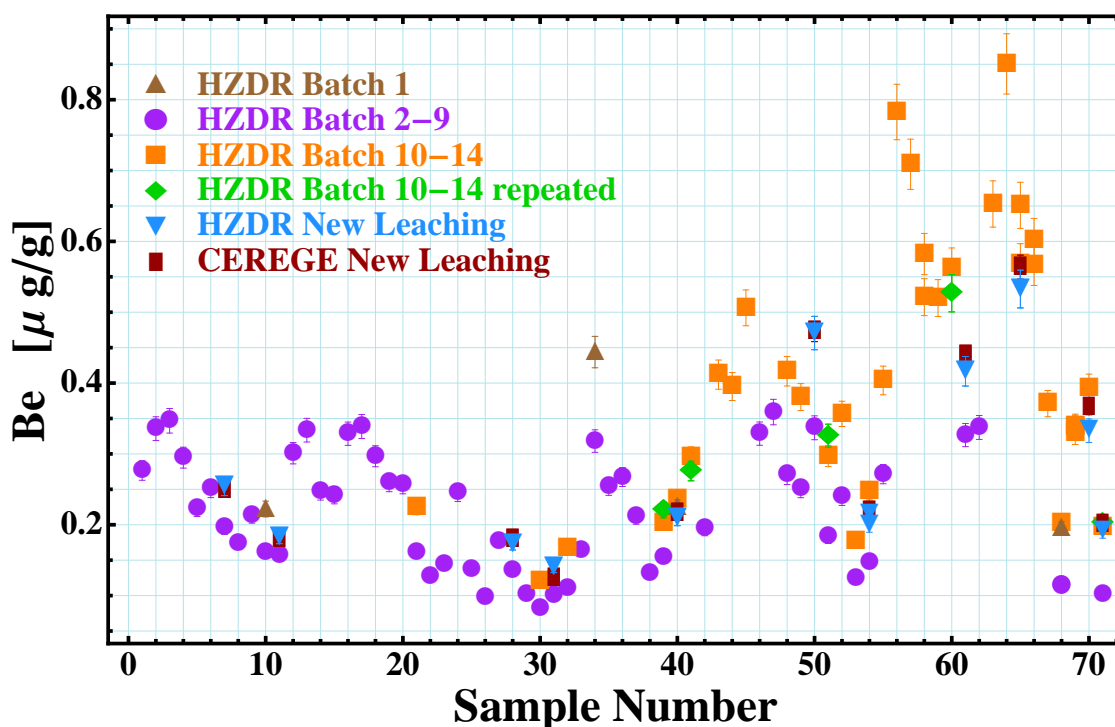
Figure 5.4: Concentrations of stable beryllium (μg per g sample material) versus sample number for different ICP-MS measurement series. Some HZDR ICP-MS results were compared to data obtained from independent GF-AAS measurements at CEREGE (Aix-Marseille-University, France).

Because the ^{9}Be data obtained for batch 10-14 was found to be consistent, data of batch 2-9 were then normalized to batch 10-14. Natural ^{9}Be concentrations (μg per g starting sample material) of samples chemically prepared from the same initial sample material

in batches 2-9 as well as in batches 10-14 are plotted in the top left part of Figure 5.5. The results differ by a factor of ~1.5. The top right part of that figure displays a plot of batch 2-9 versus batch 10-14 ^{9}Be concentrations. The result should be located on a line with unity slope. However, a systematic deviation from that line was observed. Ratios of the measured ^{9}Be concentrations for batch 10-14 and 2-9 are shown in lower left part of Figure 5.5. Possible explanations for the offset in the measurements suggest a time-dependent change of measured ^{9}Be concentrations (discussed in the following section). The aliquot concentrations were analyzed chronologically with the sediment identification number, therefore the data is fitted in correlation with the sample number. The resulting linear function is displayed in the figure.

With this correlation the data of batch 2-9 was corrected. The resulting ^{9}Be concentrations are again shown in a 1:1 plot of batch 2-9 versus batch 10-14 in the bottom right part of Figure 5.5. The corrected data agree with the unity line, as expected. The uncertainties of the corrected ^{9}Be concentrations of batch 2-9 values now exceed 10 %, as the error of the correction function adds to the ICP-MS data. The data before and after normalization can be viewed in Figures F.1 and F.2 in the Appendix.

In Figure 5.6 the final results of the natural ^{10}Be/^{9}Be ratios of the deep-sea sediment samples from the DREAMS measurement (E45-21 and E49-53) are plotted. The figure shows the results for all samples measured within the depth range of 100-700 cm, where most samples were available. Average ^{10}Be/^{9}Be values and their uncertainties of repeatedly measured samples are calculated with equations (E.2) and (E.3) in the Appendix.

The uncertainties are dominated by the systematic contributions from the ICP-MS measurements and the corrections made above. The ^{10}Be/^{9}Be ratios do not decrease smoothly with depth. Instead, fluctuations are observed. Whether these originate from offsets between batches caused by the chemical treatment and during the AMS measurement procedures or from natural fluctuations is discussed in section 5.5.3.

ICP-MS measurement results for ^{9}Be for batches 15 and 16 were measured only in a single measurement series at HZDR. They were not discussed yet. These batches include surface samples, whose ^{10}Be/^{9}Be ratios were later required for normalization in the dating procedure. The ^{10}Be/^{9}Be value of the sediment's top surface, represents the present oceanic ratio, and is used for absolute dating via equation (2.1). Therefore, the ICP-MS results obtained from these samples are particularly important. However, Figure 5.6 indicates, that the ^{10}Be/^{9}Be values of batch 16 are high compared to the batches 2-14. The implication for ^{10}Be/^{9}Be dating from such an offset for batch 15 and 16 will be discussed in section 5.4.1.

Possible explanations causing systematic offsets in the ICP-MS data and suggestions for improvements in future measurements are discussed in the following.
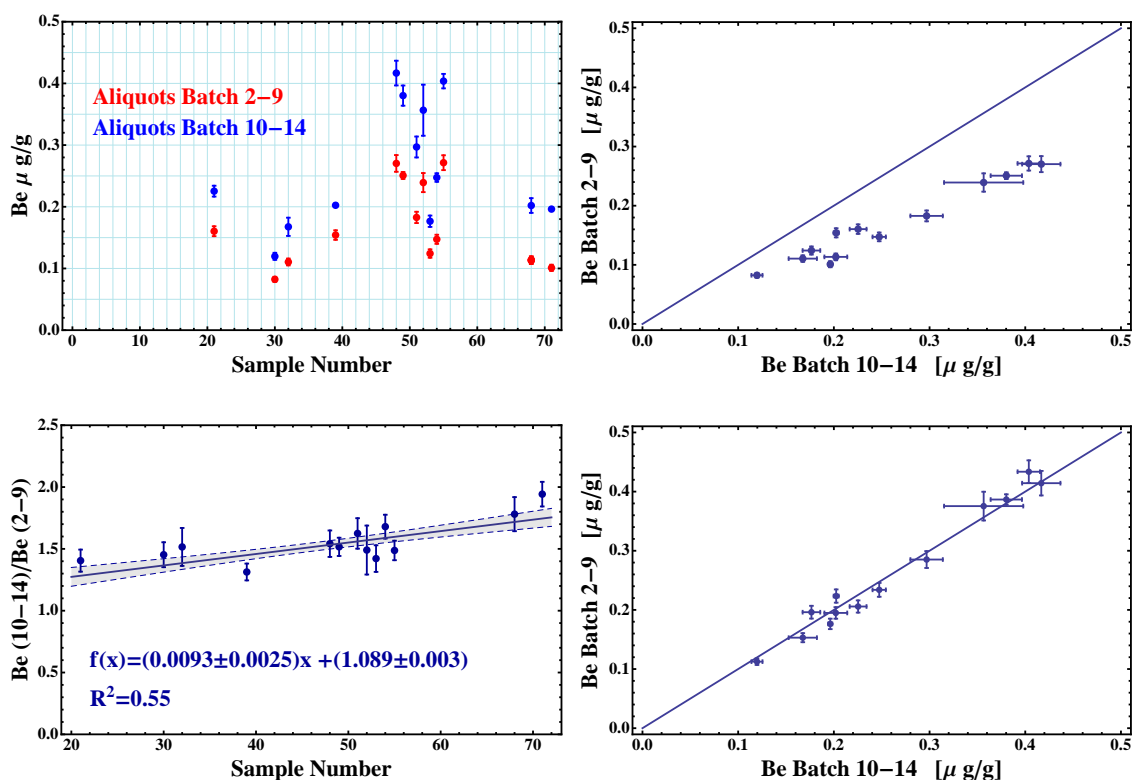
Figure 5.5: Top left: Concentrations of [9]Be of samples chemically prepared from the same initial sample material in batches 2-9 and 10-14. **Top right:** A direct comparison of studied concentrations of batch 2-9 versus 10-14. The solid 1:1 line indicates the expected concentrations if measurement results would agree with each other. **Bottom left:** The correction function obtained from [9]Be ratios of batch 10-14 to 2-9 versus sample number. **Bottom right:** Corrected [9]Be concentration of batch 2-9, which fit the solid unity line, when compared to batch 10-14 values.

5.1.2.2 Possible Reasons for Systematic Offsets and Potential Improvements in Future ICP-MS Measurements of [9]Be

An offset between [9]Be-data of different ICP-MS measurements at HZDR were observed. A possible explanation for such an offset could be a change in the rhodium concentration during the measurement. Rh is used to normalize the data. Another, probably more crucial influence on the measurement outcome is the solution, in which the sample is dissolved. The leaching solution is a mixture of acetic acid and hydroxylammonium. This type of sample solution was not tested in the ion source of the ICP-MS at HZDR prior to this measurement. The carbon from acetic acid might influence the behavior of beryllium in the ICP source and could lead to an interference in the measurement (Grindlay et al., 2013). Each aliquot introduced an additional amount of carbon into the ion-source, which might lead to larger systematic offsets with increasing time of a measurement. For this reason, a time-dependent change in the measured [9]Be data might have been present. This, and the very low concentrations of [9]Be in the sediment samples might have been the cause for the observed large offsets in the measurement results.
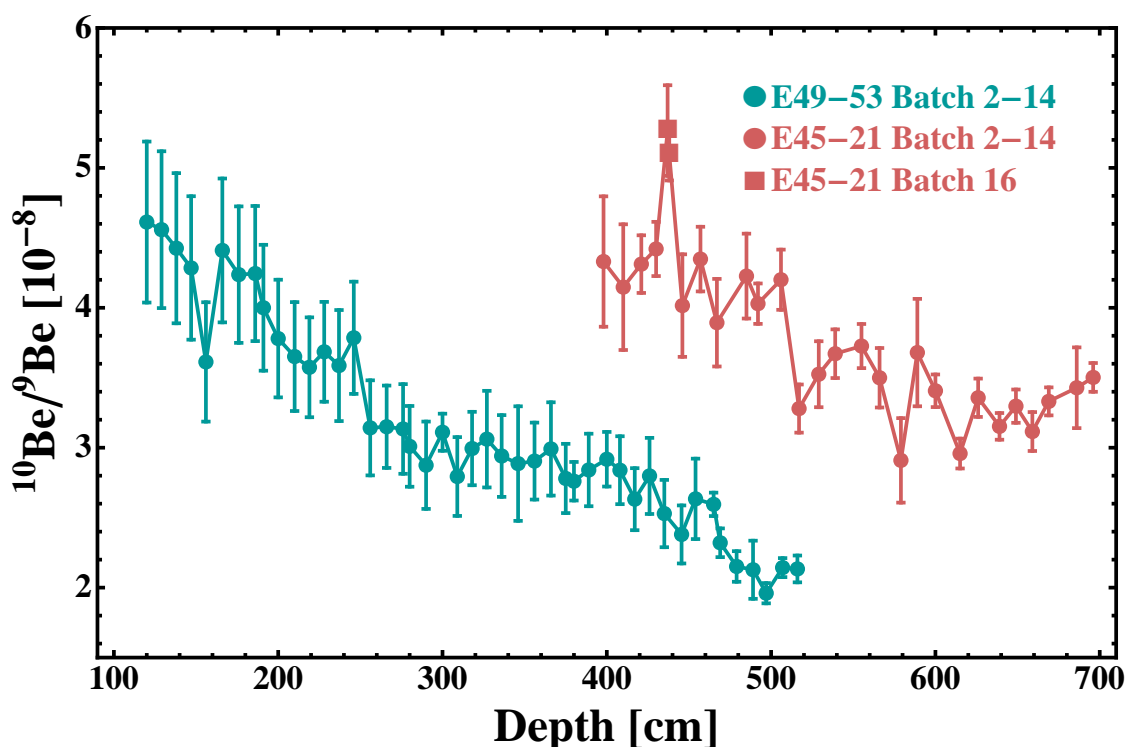
Figure 5.6: Intrinsic ^{10}Be/^{9}Be ratios (DREAMS) versus depth for the two deep-sea sediment cores E-45-21 (red) and E49-53 (green). The error bars reflect mainly systematic uncertainties originating from the correction of ICP-MS results of batch 2-9 samples.

This problem might be solved by evaporating the leaching solution to dryness and then use a different acid to re-dissolve the sample. Commonly, HNO$_3$ is used as a sample solution for ICP-MS. However, if NH$_2$OH·HCl in acetic acid is used, a blank consisting of a different acid should be measured between each sample to reduce the carbon content in the ICP ion source (A. Ritter, privat communication, 2014).

Furthermore, GF-AAS can be used instead of ICP-MS. This technique was applied at CEREGE, France (by Valéry Guillou) for some samples. Here, the standard addition and double beam correction methods were used to calibrate the spectrometer, which reduces possible measurement offsets.

5.2 Results of ^{26}Al Measurements at VERA[*]

The ^{26}Al/^{27}Al isotope ratios of the *Eltanin* samples were determined with the AMS facility VERA, Vienna. As pointed out by Auer et al. (2007), the ionization efficiencies of Al do not change largely when mixing the sample with the conductor powder with Ag or Cu. Measurement efficiencies are highest for a conductor/Al$_2$O$_3$ mass ratio of 1:1. The efficiency decreases with increasing conductor/Al$_2$O$_3$ ratio.

---

[*]Parts of this section are based on Feige et al. (2013)

The target material of the first batch was mixed with silver in the mass ratio $Ag:Al_2O_3 =$ 2:1. For batches 2-4, where higher masses of Al_2O_3 targets were obtained, the amount of Ag added was decreased to 1:1 mixing ratios. Targets of the subsequent batches were mixed with Cu in the mass ratio 1:1.

At the VERA facility, an Al^- beam is used at the low energy side of the accelerator. The stable isobar of ^{26}Al, ^{26}Mg, does not form negative ions and is therefore suppressed in the ion source. Typical currents of $^{27}Al^-$ were in the order of 200-300 nA for the deep-sea sediment samples. A charge state of 3^+ was chosen at the high-energy side of the spectrometer. This results in energies of 11.27 MeV of $^{26}Al^{3+}$ ions for a terminal voltage of 2.8 MV including the 70 keV injection energy. ^{26}Al was counted with a semiconductor detector.

$^{26}Al/^{27}Al$ isotopic ratios for the sediment samples were of $\sim 10^{-14}$. This is six orders of magnitudes lower than the $^{10}Be/^9Be$ ratios. The production rate of ^{26}Al in the Earth's atmosphere is three orders of magnitudes lower than for ^{10}Be. Due to the lower half-life of ^{26}Al compared to ^{10}Be, the ratios of $^{26}Al/^{27}Al$ are reduced more for the 2-3 Myr old *Eltanin* samples (see section 2.3.2). These ages correspond to approximately 3-4 half-lifes of ^{26}Al. Furthermore, stable aluminium is highly abundant in deep-sea clay sediments. The stable aluminium content was reduced by leaching rather than dissolving the whole material during the chemical processing.

Due to the low $^{26}Al/^{27}Al$ ratios of $\sim 10^{-14}$ in the sediment samples, a longer measurement time was required in order to detect sufficient numbers of ^{26}Al atoms. To obtain a statistical uncertainty of <10 %, each sample was sputtered for several hours and measured in several measurement series until complete exhaustion.

The data was normalized to the standard material AW-V-2 and AW-V-3 with $^{26}Al/^{27}Al$ values of $(2.71\pm0.02)\times10^{12}$ and $(3.65\pm0.05)\times10^{12}$, respectively (Wallner, A. et al., 2000). Processing blanks were not produced during the chemical procedure. Instead commercially available Al_2O_3 powder was measured as machine blank. The measured $^{26}Al/^{27}Al$ isotope ratios of blanks were between 2×10^{-16} and 1×10^{-15}.

The $^{26}Al/^{27}Al$ ratios of batches 1-14 and 16 are displayed in Figure 5.7 for the two sediment cores E45-21 and E49-53. The two samples of batch 16 of core E45-21 are shown as red squares. These were additionally measured to study in more detail a possible higher ratio around $\sim$440 cm, suggested by one sediment sample. The uncertainties are dominated by counting statistics. Results of replicated and repeatedly measured samples were averaged. Some ratios are as accurate as 3 %; only a few targets missed an accuracy of better than 10 %.
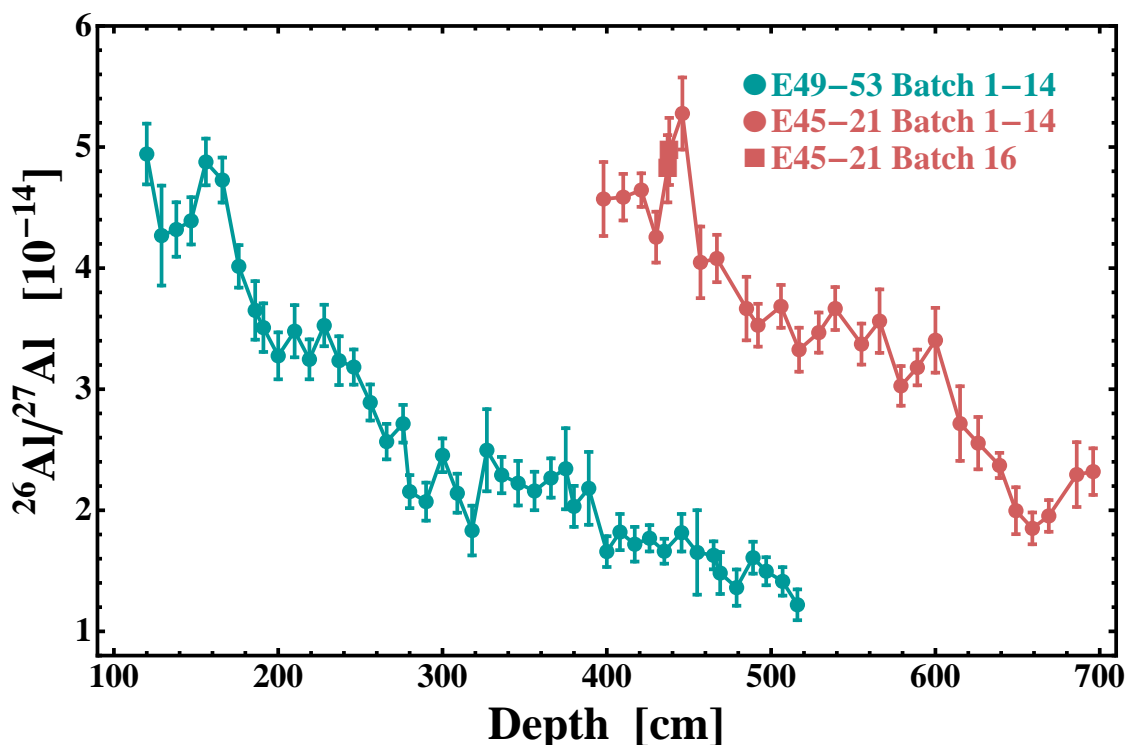
Figure 5.7: ^{26}Al/^{27}Al isotope ratios (measured at VERA) versus depth of two deep-sea sediment cores E45-21 (red, circles: batch 2-14, squares: batch 16) and E49-53 (green). All individual measurements were combined and averaged data are plotted.

5.2.1 Measurement Efficiency of ^{26}Al at VERA

The AMS efficiency of ^{26}Al-measurements at VERA has been extensively studied by Auer et al. (2007). Not only the influence of the conductor material, but also other criteria such as the composition of the target, the target geometry and the energy of the Cs-beam are affecting the detection efficiency. In general the ionization efficiency for producing ^{27}Al$^-$ from a Al$_2$O$_3$ target in a Cs sputter source is about 0.2 % (Middleton, 1990). As mentioned above, copper and silver as conductor material gave comparable currents. The geometry of the sample holder plays a role as the AMS efficiency increases with decreasing sample surface depth. Furthermore, Auer et al. (2007) found, that varying the energy of the Cs-beam does not significantly influence the efficiency.

Different matrices might influence the measurement efficiency. Therefore, the efficiency was determined for the deep-sea sediment samples in this work. Al$_2$O$_3$ was used as target material, copper as conductor, except for the first four batches (see above). Between 2 and 7 mg of Al$_2$O$_3$-Cu powder was pressed into the Cu sample holder. The AMS efficiency was determined by calculating the ratio of ^{27}Al atoms obtained from the current measured on the high energy side of the AMS facility to the number of ^{27}Al atoms in the target

holder (Auer, 2008)

$$\epsilon_{AMS} = \frac{N_{Al}(he)}{N_{Al}(target)}. \tag{5.4}$$

Typical high-energy currents for $^{27}Al^{3+}$ were in the order of 100 nA. To determine the AMS efficiency, the targets were sputtered until complete exhaustion and yielded an average value of $\epsilon_{AMS} = (2.7\pm0.7)\times10^{-4}$. In general, higher efficiencies were obtained by Auer et al. (2007) reaching up to almost 1×10^{-3}. The efficiency obtained in this work is situated below Auer's value, similar to the value of 5×10^{-4} from Arazi et al. (2006), but significantly higher than 5×10^{-5} reported in (Pavicevic et al., 2004).

The overall efficiency of ^{26}Al was calculated by also considering potential losses between the ion source and ^{26}Al detection with the particle detector. The average transmission was 45 % from source to detector, which is mainly determined by the charge state yield of Al^{3+} ions in the gas stripper. Additional sputtering without ^{26}Al counting accounted for another ~40 % of efficiency reduction. These occur due to sputtering of the target material without actual data collection, i.e. during accelerator tuning procedures (the sediment sample targets were used for a short retuning on individual samples) and ^{27}Al currents measurements, while the target is sputtered. Auer (2008) neglected such effects for the efficiency calculations. Taking these losses into account leads to an overall yield of $(0.98\pm0.26)\times10^{-3}$.

5.3 HIAF results of ^{53}Mn and ^{60}Fe

The two heavier radionuclides ^{53}Mn and ^{60}Fe were measured at the **H**eavy **I**on **A**ccelerator **F**acility (HIAF), ANU, Canberra, Australia. These two isotopes have stable isobars, which can only be separated with high-energy facilities and additional equipment complementing the usual AMS setup, such as a gas-filled magnet (chapter 4.2). Partial suppression is already achieved with suitable chemical procedures (chapter 4.1).

5.3.1 ^{53}Mn

Measurement procedures of ^{53}Mn at the ANU were already established some years ago (Gladkis et al., 2007). Average currents for $^{55}MnO^-$ of 0.5 μA were measured. After the passage through gas and foil strippers and destruction of molecules a charge state of Mn^{11+} was chosen. The positive $^{53}Mn^{11+}$ ions are accelerated with terminal voltages of e.g. 14.4 MV to energies of 170 MeV, selected with the analyzing magnet, then pass a switching magnet and a Wien filter. After passage through the gas-filled magnet, ^{53}Mn and ^{53}Cr beams with a FWHM of ~2 cm are separated by 3.4 cm. A large fraction of the ^{53}Cr-ions is blocked by a metal plate and ^{53}Mn is counted in a gas-ionization chamber.

For the *Eltanin* sediment samples, low isotopic ratios of $^{53}Mn/^{55}Mn$ in the order of 10^{-14}-10^{-13} were expected (see chapter 3.4). For such low ratios, it is of utmost importance, that ^{53}Cr is suppressed. Tests of samples prepared in batch 1 were performed at the

Maier-Leibnitz Laboratory at the TU Munich. Ratios of ^{53}Cr/^{55}Mn of 1-2×10^{-6} were measured for all samples, which was similar to a known sample of low Cr-concentration, with ^{53}Cr/^{55}Mn = 7.6×10^{-7}. However, in batch 1 the MnO$_2$ was extracted with a different chemical procedure (section 4.4.1) than in the subsequent batches. For batches 2-16, the chemical procedure was adapted to higher sample volumes and the separation technique for Mn was changed (section 4.1).

First tests investigating the Cr-background of Mn-samples from the deep-sea sediments (batch 2-16) were performed in late 2013 at HIAF. It was shown, that chromium was not as efficiently suppressed during chemical separation and compromises the ^{53}Mn AMS results. After these AMS tests it is evident, that another reprecipitation with KClO$_3$ or an anion-exchange has to be performed to achieve sufficient suppression of ^{53}Cr. This will be a subject to future projects.

5.3.2 ^{60}Fe

Measuring ^{60}Fe at HIAF has just been started during the course of this work. The measurement principle is the same as for ^{53}Mn. Here, FeO$^-$-ions were selected for injection into the tandem accelerator with terminal voltages of 13.5-14.5 MV. Low energy currents of FeO$^-$ ranged between 0.7 and 3 μA. During the passage of the gas and foil stripper, a charge state of 11$^+$ was chosen, resulting in energies of 160-170 MeV at the high-energy side of the accelerator. ^{60}Fe^{11+} and it's stable isobar ^{60}Ni followed the same trajectories in the beam line and were separated by the gas-filled magnet followed by an ionization-chamber.

So far, ^{60}Fe/Fe ratios of 29 targets were measured and more than 200 ^{60}Fe counts were detected resulting in an average of ~10 counts per target. ^{60}Ni count rates were in the order of 100 s^{-1}. The ratios of most of the samples range in the order of 10^{-15} and therefore long measurement times of several hours per target were required. The ^{60}Fe/Fe blank level measured here is (0.4±0.2)×10^{-16}.

The measured ^{60}Fe/Fe ratios versus depth of the sediment samples are shown in Figure 5.8. Samples of all four sediment cores used in this work were analyzed. Two Fe-targets of E45-21 were also measured at the Maier-Leibnitz-Laboratory at the TUM (Germany), where no ^{60}Fe event was detected due to a short measurement time.
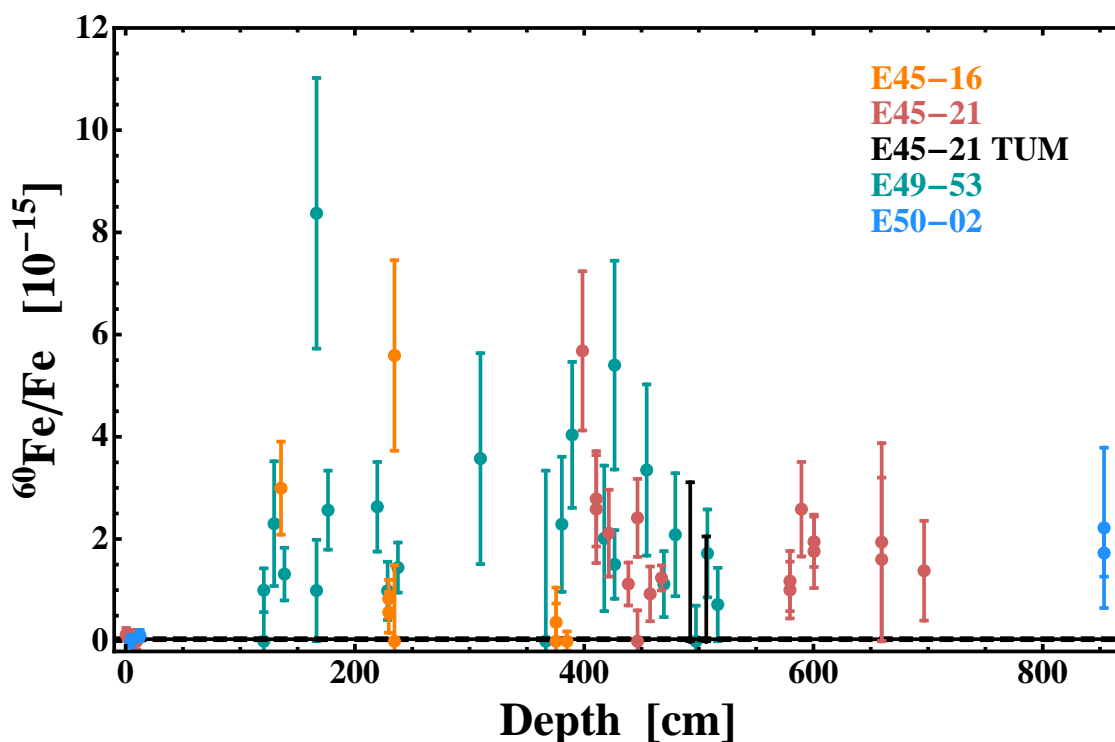
Figure 5.8: ^{60}Fe/Fe versus depth below sea floor of targets from from deep-sea sediment cores measured at HIAF, Australia. Two samples of E45-21 were measured at TUM, Germany.

5.4 Dating Procedures for the *Eltanin* Sediment Cores

The paleomagnetic ages for *Eltanin* cores E45-21 and E49-53 were adopted from Allison and Ledbetter (1982) as shown in chapter 2.3.2. The deduced averaged sedimentation rate changes between magnetic reversals. Average sediment accumulation rates over the time range of 1.7-3.2 Myr weighted by the length of the polarity zones were calculated and yielded 3.67 mm kyr^{-1} and 2.71 mm kyr^{-1} for E45-21 and E49-53, respectively. However, fluctuations in the sedimentation rate within polarity zones can not be resolved by this technique.

5.4.1 Age Models for E45-21 and 49-53

The aim of radioisotopic dating was to obtain ages between magnetic reversals and to verify that these are in agreement with the paleomagnetic ages. Furthermore, a comparison between both, ^{10}Be/^{9}Be and ^{26}Al/^{27}Al dating was possible.

Variations in the measured isotopic ratios were observed in the measured ^{26}Al/^{27}Al and ^{10}Be/^{9}Be isotope ratios. They might originate from statistical scattering. However, systematic offsets e.g. between batches or measurement series might add to scattering of the measured data (discussed later in section 5.5.3). When producing an age model, it is clear

that the chronology of samples versus depth has to be maintained. Individual isotopic ratios of single targets are therefore not suitable for dating, as the chronology might not be maintained for short term scales. An age model is obtained by grouping sets of data points together.

A χ^2-test has been performed to group data points yielding similar isotopic ratios. Figures 5.9 and 5.10 display the groupings of ^{10}Be/^{9}Be and ^{26}Al/^{27}Al ratios from samples of E49-53 and E45-21. The grouped data-sets are color coded and separated by vertical lines. Results that did not pass the test (because their measured isotope ratios differed significantly from the mean value of the grouped data) were marked as outliers with different colors.

For each group, a weighted mean isotopic ratio is calculated. The exponential decay function (2.1) is applied to calculate corresponding mean ages. The ^{26}Al/^{27}Al and ^{10}Be/^{9}Be ratios of the surface samples (recent ages) represent the values for t=0. Surface samples were available for cores E45-21 and E50-02 (processed in batch 16). Individual isotopic ratios of each surface sample are listed in table G.1 in the Appendix. The mean ratios were for $(^{26}$Al/^{27}Al$)_{t=0} = (2.56\pm0.11) \times 10^{-13}$ and for $(^{10}$Be/^{9}Be$)_{t=0} = (1.30\pm0.09) \times 10^{-7}$. This can be compared to literature values of $\sim 2\times10^{-13}$ for aluminium (Sharma et al. (1987a) in manganese nodules) and $(1.0\pm0.4)\times10^{-7}$ for beryllium (Bourlès et al., 1989). They do not differ significantly from the results obtained in this work.

The mean ages of each group generated with this method are listed in tables G.2 and G.3 (Appendix). The results indicate, that ages obtained from the ^{10}Be/^{9}Be data are systematically higher than those from the ^{26}Al/^{27}Al data.

Subsequently, a stratigraphy throughout the two cores could be obtained. The calculated mean ages and paleomagnetic ages, adopted from chapter 2.3.2, were correlated with the respective depth in the cores. Then, a linear regression was performed. Several sources of uncertainties were considered: the most obvious are measurement uncertainties of ^{26}Al/^{27}Al and ^{10}Be/^{9}Be. Furthermore, half-life uncertainties needed to be taken into account. As paleomagnetic ages were obtained from reading the depths of magnetic reversals from Figure 2.9, an uncertainty of 10 cm was added for each magnetic reversal. This translates into a time range of 36.9 kyr for E49-53 with an average sedimentation rate of 2.71 mm kyr^{-1} and to 27.3 kyr for E45-21 with a sediment accumulation rate of 3.67 mm kyr^{-1}.
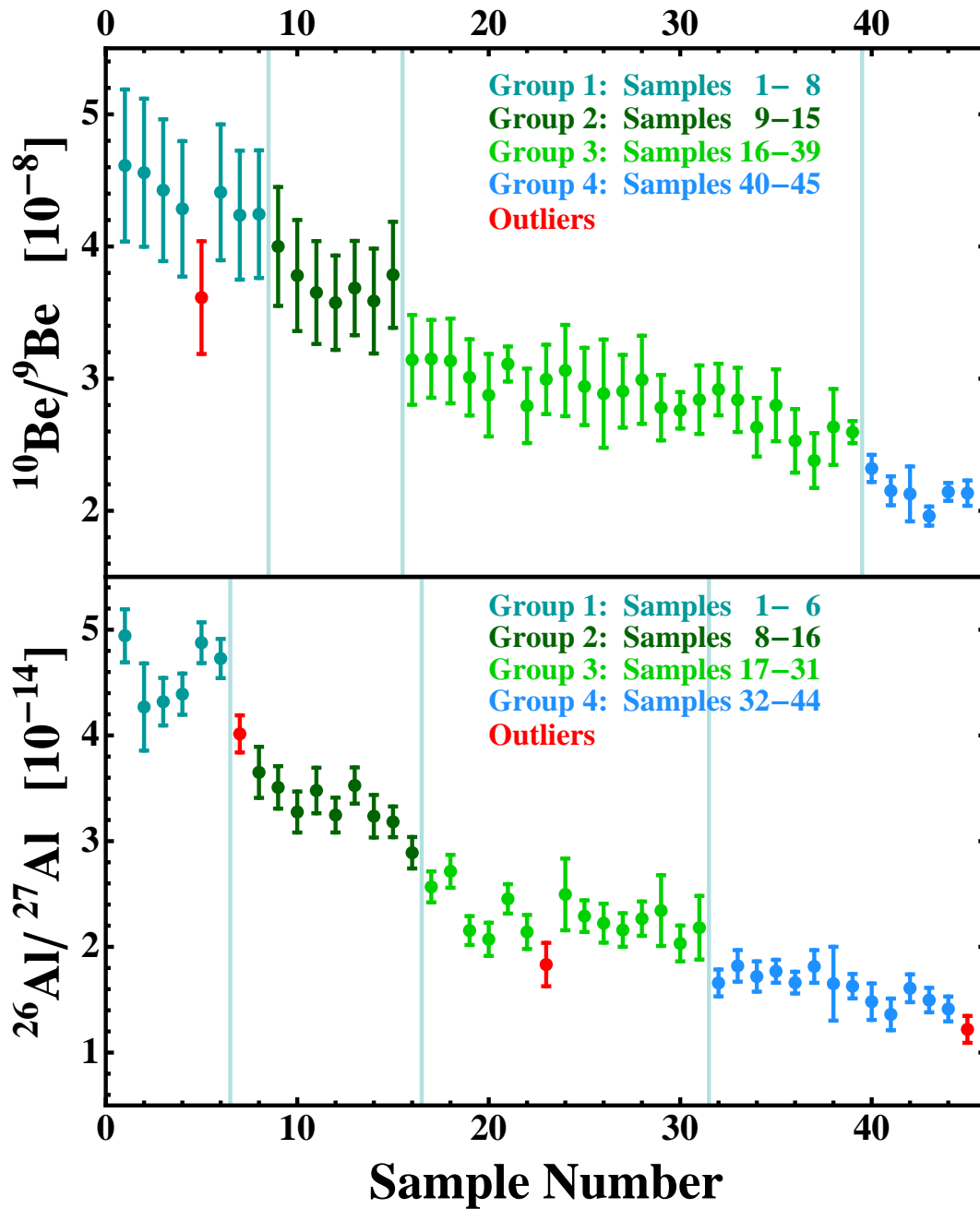
Figure 5.9: ^{10}Be/^{9}Be (upper part) and ^{26}Al/^{27}Al isotope ratios (lower part) of core E49-53 grouped by data points yielding similar results. Results that did not pass the χ^2-test (i.e. their ratios differed significantly from the mean value of the grouped data), which was applied to obtain the group data sets, were marked as outliers with different colors. Note: the ^{10}Be/^{9}Be uncertainties include the systematic uncertainties from corrections made in section 5.1.2.
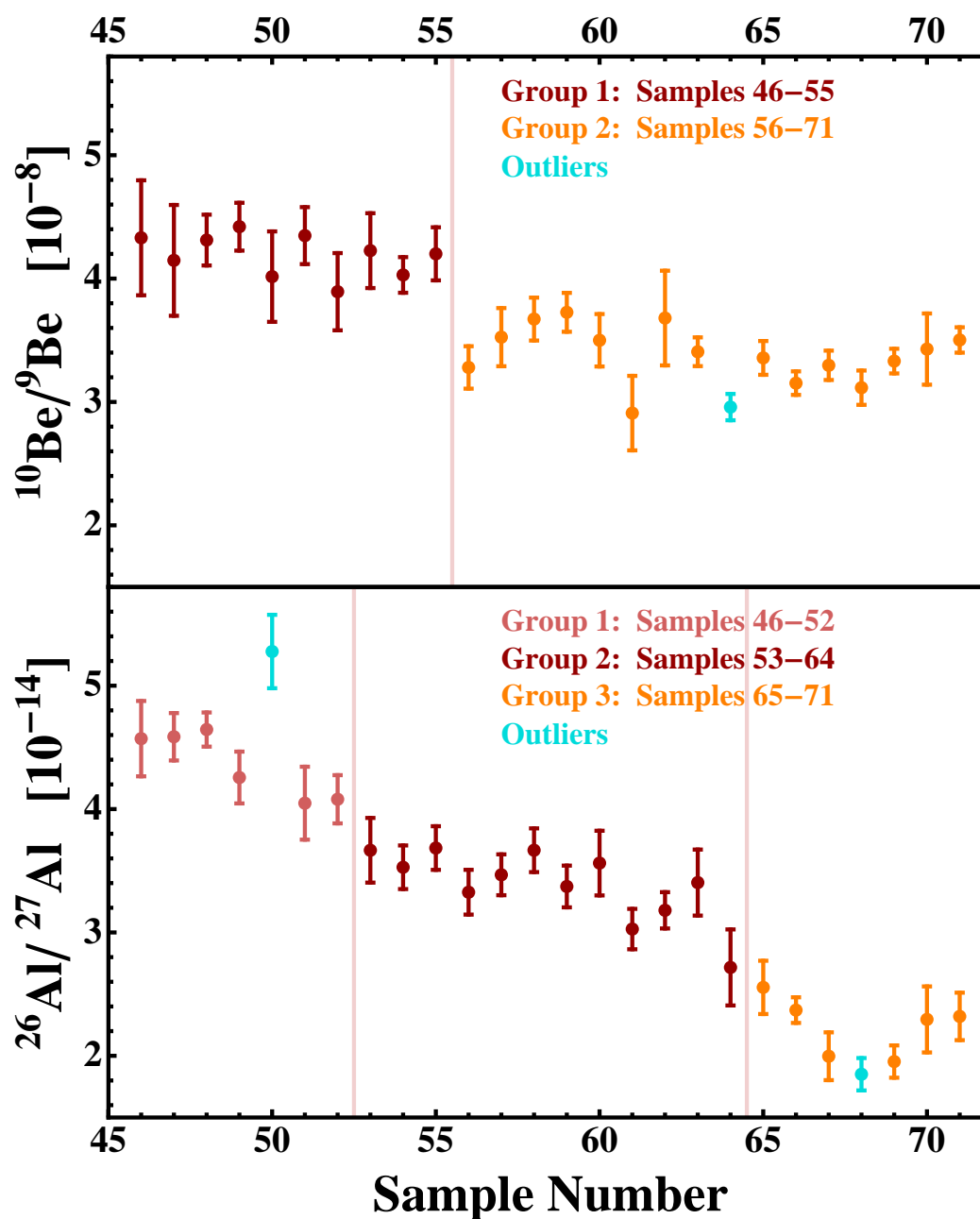
Figure 5.10: ^{10}Be/^{9}Be (upper part) and ^{26}Al/^{27}Al isotope ratios (lower part) of core E45-21 grouped by data points yielding similar results. Results that did not pass the χ^2-test, which was applied to obtain the group data sets, were marked as outliers with different colors.

5.4.1.1 Dating the Cores with ^{26}Al/^{27}Al Ratios

The results of the ^{26}Al/^{27}Al mean values obtained from the grouping and the magnetostratigraphic tie points of E49-53 and E45-21 are fitted linearly (Figure 5.11). Here, the depth of the initial groupings is indicated by vertical lines. Especially for E49-53 the calculated mean ratios are in very good agreement with the paleomagnetic ages. The sedimentation rate seems constant within the depth analyzed here. This results in values of (2.79±0.06) mm kyr^{-1} for E49-53 and (3.73±0.18) mm kyr^{-1} for E45-21. They fit perfectly to the age estimations obtained solely by magnetostratigraphy.

Figure 5.11: Linear regressions performed on the combination of magnetostratigraphic tie points and mean ^{26}Al/^{27}Al ratios obtained for the grouped data sets shown in figures 5.9 and 5.10 of E49-53 and E45-21.

Ages were then assigned to each individual sample. Uncertainties, which were assumed to be constant, were added quadratically: Mixing of sediment material due to bioturbational activity smears the location of magnetic reversal over its mixing length of ~10 cm. With the sedimentation rates obtained above, the mixing length translates into time periods of 27.9 kyr and 37.9 kyr for E49-53 and E45-21, respectively. In addition, the not precisely known isotope ratios for t=0, required for absolute dating, will add to the uncertainty of individual data points. For this reason, the age uncertainty for absolute ages ranges between 4 and 5 % depending on the age of the samples, or ~ ±100 kyr. The individual results of the ^{26}Al/^{27}Al dating method can be viewed in tables G.4 and G.5 in the Appendix.

The ^{10}Be/^{9}Be and ^{26}Al/^{27}Al ratios measured in samples from E45-21 and E49-53 were shown with depth in Figures 5.6 and 5.7. With the ^{26}Al/^{27}Al age model obtained above, the depth profiles were converted into an age profile. The results are shown in the upper parts of Figures 5.14 and 5.15. The absolute age uncertainty is shown as horizontal error bars. The depth chronology has to be maintained here, a significant shift in time would affect all samples.

5.4.1.2 Dating the Cores with ^{10}Be/^{9}Be Ratios

The same procedure was carried out for dating the sediment cores E45-21 and E49-53 using ^{10}Be/^{9}Be ratios. A ^{10}Be/^{9}Be age-depth diagram is shown in Figure G.1 in the Appendix. The isotopic ages differ from magnetostratigraphic ages (and therefore also from ^{26}Al/^{27}Al ages) by 20-50 %. A possible explanation for this difference might be a systematic error in the ICP-MS data in the surface samples (t=0), which would affect all samples of batches 15 and 16.

The ^{26}Al/^{27}Al age model thus was used to normalize these ^{10}Be/^{9}Be ratios. Applying ages deduced via ^{26}Al/^{27}Al dating, the ^{10}Be/^{9}Be ratios were then corrected for the half-life of ^{10}Be to estimate initial values at the time of deposition (t=0). This is illustrated in Figure 5.12. Subsequently, a weighted mean of $(1.057\pm0.064)\times10^{-7}$ was calculated from the decay-corrected ^{10}Be/^{9}Be ratios, and used as initial ratio at t=0 for the ^{10}Be/^{9}Be dating procedure. The ratio of this new surface value to the old value of $(1.30\pm0.09)\times10^{-7}$ was used to normalize incorrect ^{10}Be/^{9}Be ratios of additional samples from batches 15 and 16.
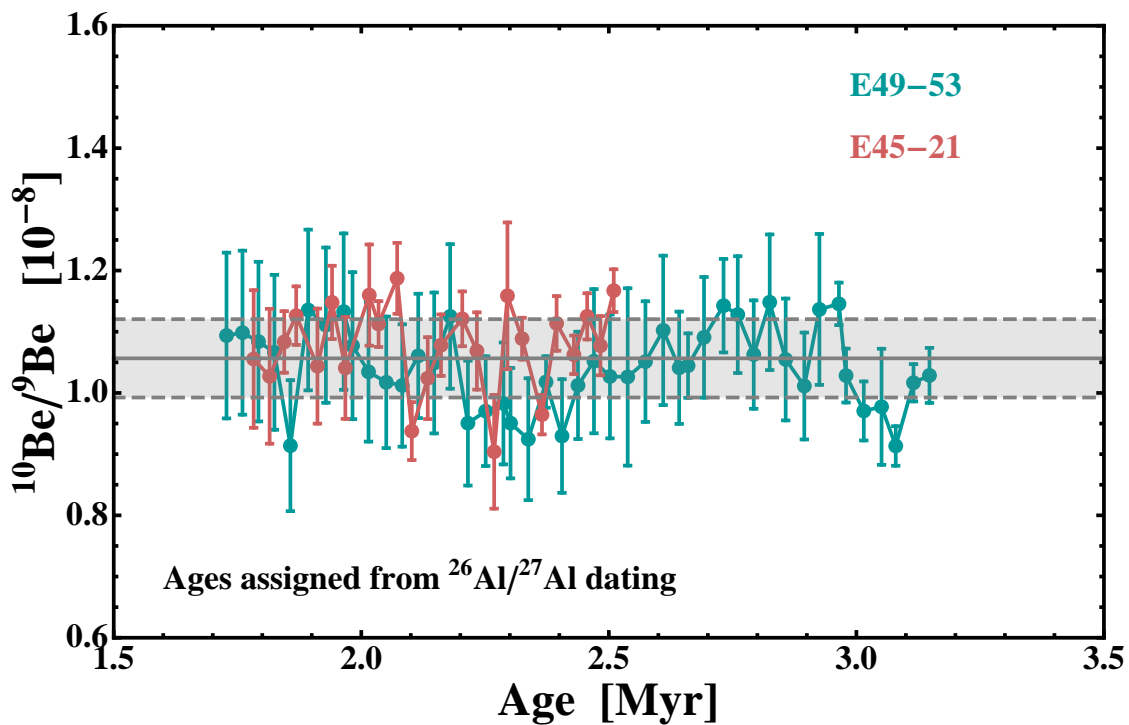
Figure 5.12: Decay corrected ^{10}Be/^{9}Be data using ages assigned from "^{26}Al/^{27}Al dating". A value of ^{10}Be/^{9}Be $= (1.057\pm0.064)\times10^{-7}$ was calculated for surface samples (t=0).

This new surface ratio was used for the ^{10}Be/^{9}Be age model with the method explained above for ^{26}Al/^{27}Al. The new age-depth diagram with a linear regression function is plotted in Figure 5.13. Here, the average sedimentation rates were found to be (2.75 ± 0.08) mm kyr^{-1} for E49-53 and (3.75 ± 0.13) mm kyr^{-1} for E45-21.
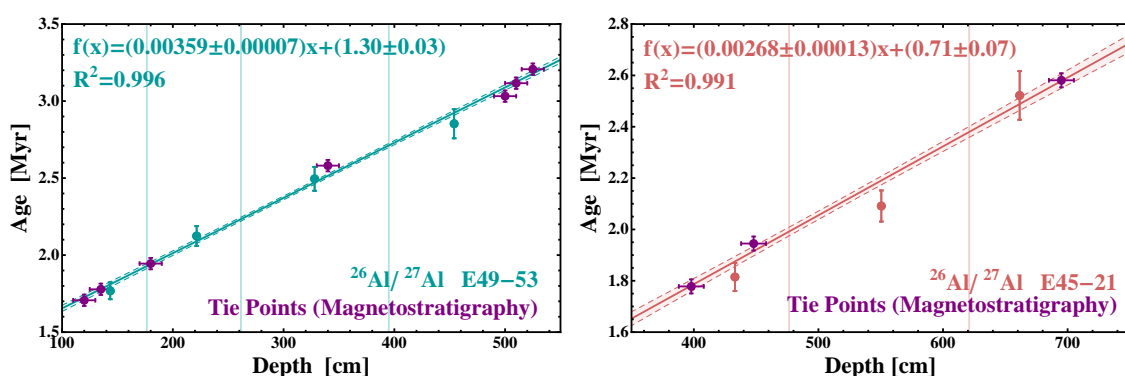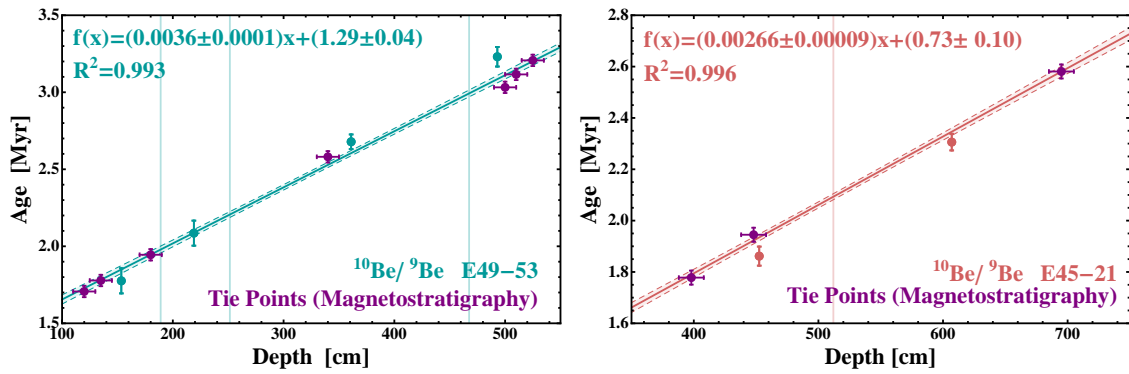
Figure 5.13: Linear regressions performed on the combination of magnetostratigraphic tie points and mean ^{10}Be/^{9}Be ratios obtained for the grouping of data sets shown in figures 5.9 and 5.10 of E49-53 and E45-21. Ages of the mean ^{10}Be/^{9}Be ratios were calculated using the surface ratio ^{10}Be/^{9}Be = $(1.057\pm0.064)\times10^{-7}$ obtained from ^{26}Al/^{27}Al age dating. The resulting linear regression functions are displayed in each graph.
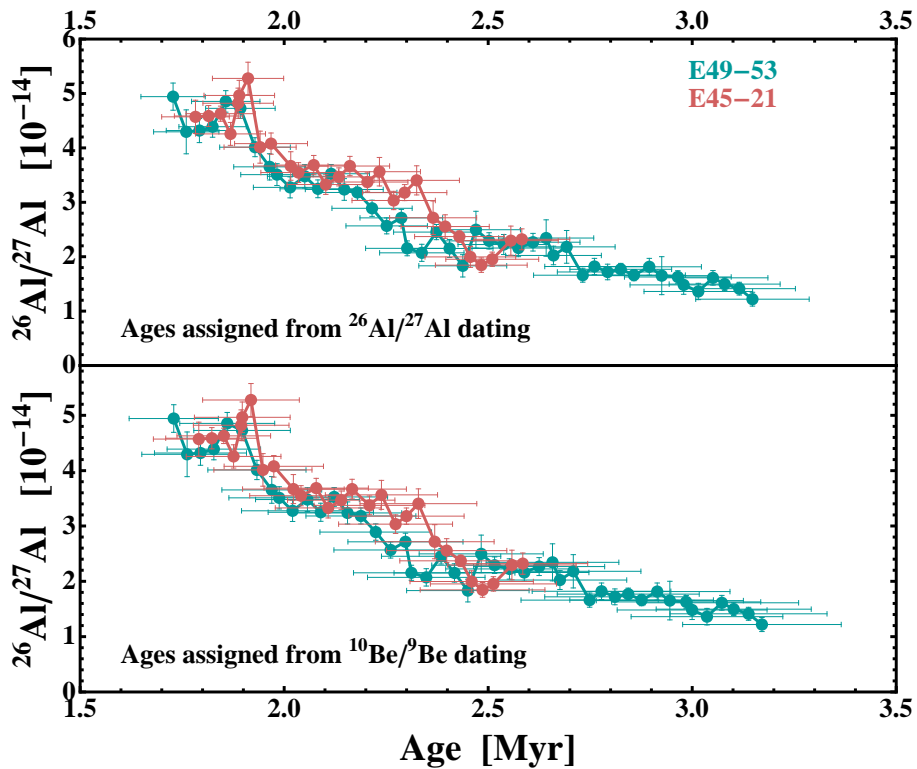
Figure 5.14: Ages assigned to ^{26}Al/^{27}Al isotopic ratios (which were shown in Figure 5.7) for the two *Eltanin* sediment cores E49-53 and E45-21. Two age models are applied to this data: the ^{26}Al/^{27}Al age model (upper part) and the ^{10}Be/^{9}Be age model (lower part). The two methods differ by absolute ages and the age uncertainties. Samples dated with the ^{10}Be/^{9}Be dating method are systematically shifted by ~10 kyr towards older ages compared to the ^{26}Al/^{27}Al ages. On average, the ^{10}Be/^{9}Be dating has a 25 % larger uncertainty as the ^{26}Al/^{27}Al age model.
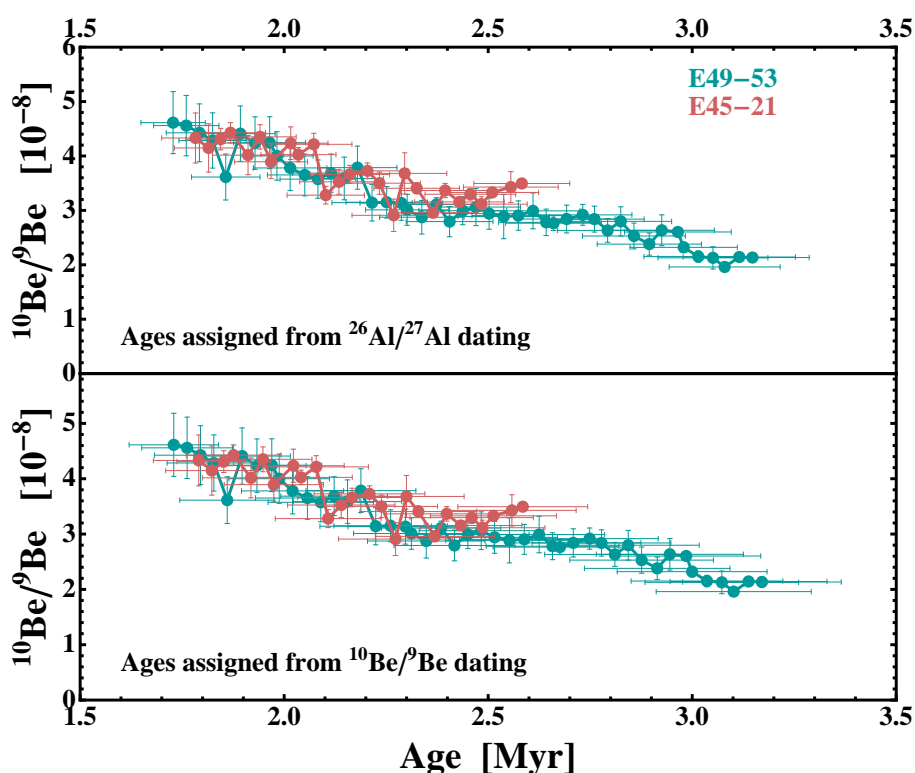
Figure 5.15: Ages assigned to ^{10}Be/^{9}Be isotopic ratios (which were shown in Figure 5.6) for the two *Eltanin* sediment cores E49-53 and E45-21. Two age models are applied to this data: the ^{26}Al/^{27}Al age model (upper part) and the ^{10}Be/^{9}Be age model (lower part).

The ^{10}Be/^{9}Be age model was applied to the measured ^{10}Be/^{9}Be and ^{26}Al/^{27}Al ratios of the individual samples and these ages were compared to the ages obtained with the ^{26}Al/^{27}Al dating method in Figures 5.14 and 5.15. As the ^{10}Be age model is based on ^{26}Al results, the two models have to agree with each other. With values of ~6 %, the age uncertainties of the ^{10}Be/^{9}Be age model correspond to ±150 kyr. Tables G.4 and G.5 (Appendix) summarize the dating results of the two age models for each sample of the *Eltanin* cores E45-21 and E49-53.

Advantages and disadvantages of dating with each radioisotope was discussed in chapter 2.3.3. Through the course of this work it became clear that the ^{26}Al/^{27}Al ratios are better suited for dating, because of the various corrections required for the ^{10}Be/^{9}Be ratios (ICP-MS limitation).
However, due to its shorter half-life, dating with ^{26}Al does not reach back in time as far as ^{10}Be. Furthermore, according to the calculations made in chapter 3.1.1.2 (see Figure 3.4) in-situ production could become important for ages >2 Myr. Given that the ^{26}Al/^{27}Al data do agree well with paleomagnetic dating suggests that the amount of in-situ produced ^{26}Al was overestimated in chapter 3.1.1.2. The ^{26}Al/^{27}Al ages obtained for the *Eltanin* cores E45-21 and E49-53 will be used in this work.

5.4.2 Dating of Samples from E45-16 and E50-02

Paleomagnetic ages are not available for E45-16 and E50-02. Only a few samples were provided for these two cores, not sufficient to produce age models for these cores as performed for E45-21 and E49-53. Therefore, the samples were dated individually using equation (2.1) and the initial ratios $(^{26}Al/^{27}Al)_{t=0} = (2.56\pm0.11) \times 10^{-13}$ and $(^{10}Be/^{9}Be)_{t=0} = (1.057\pm0.064)\times10^{-7}$. The resulting ages are listed in table 5.3. For comparison, ages provided by ARF are shown.

Table 5.3: Assigned Ages for E45-16 and E50-02 samples with $^{26}Al/^{27}Al$ and $^{10}Be/^{9}Be$ dating.

Number	Core	Depth	Al Age (Myr)	Be Age (Myr)	ARF Age [Myr]
72	45-16	130	2.79 ± 0.19	2.83 ± 0.26	~2
73	45-16	135	2.65 ± 0.32	2.83 ± 0.19	~2
74	45-16	229	2.94 ± 0.19	3.37 ± 0.19	~4.5
75	45-16	234	2.88 ± 0.17	3.52 ± 0.19	~4.5
76	45-16	375	3.65 ± 0.42	7.33 ± 0.20	~25
77	45-16	385	4.33 ± 0.67	8.63 ± 0.20	~25
79	50-02	847	2.23 ± 0.10	2.53 ± 0.19	3-5

The stratigraphy by Kennett and Watkins (1976) indicated there are no samples of E45-16 between 0.4 and ~23 Myr. However, Radioisotopic dating agrees with the ages roughly estimated by the ARF for samples 72 to 75. Sample 76 and 77 do not agree with the ARF ages and yield much younger ages using isotopic dating. In addition, according to Figure 2.8, for marine sediment core E50-02 no material should exist for ages older than ~2.3 Myr. The ARF assumed an age of 3-5 Myr for sample 79. However, radioisotopic dating is consistent with the stratigraphy shown by Kennett and Watkins (1976) and Allison and Ledbetter (1982). With ages between 2.2 (Al) and 2.5 Myr (Be), this sample was measured younger than suggested by the ARF.

In general, ages derived from the $^{26}Al/^{27}Al$ and $^{10}Be/^{9}Be$ data agree with each other within their uncertainties, except for samples number 75, 76, and 77. It is not clear, whether all corrections of the ICP-MS results (batches 15 and 16) finally produce correct $^{10}Be/^{9}Be$ ratios. The method used in section 5.1.2 to corrected for systematic errors of batches 2-14, took into account the time-dependent "drift" of measure $^{10}Be/^{9}Be$ ratios. In batches 15 and 16, all $^{10}Be/^{9}Be$ ratios were corrected with the same factor. Therefore, and because ^{10}Be dating correlates with ^{26}Al dating, the stratigraphy obtained from $^{26}Al/^{27}Al$ was applied for all samples.

Whether the lower ages of samples 76 and 77 from $^{26}Al/^{27}Al$ dating compared to $^{10}Be/^{9}Be$ dating are due to in-situ production of ^{26}Al is not known. More samples older than 3 Myr have to be measured and compared with ^{10}Be dating to answer this question.

5.5 ^{26}Al/^{10}Be Ratios and Sediment Composition

Ratios of ^{26}Al/^{10}Be were determined in aerosol, antarctic ice and firn samples by Auer et al. (2009) and were suggested as chronology tool. However, the determination of ^{26}Al/^{10}Be ratios in deep-sea sediments encounters difficulties due to the different behavior of aluminium and beryllium during deposition. Such fractionation effects have been observed, e.g. by Raisbeck and Yiou (1984); Sharma et al. (1987a) and Wang et al. (1996). A strong correlation of fractionation with the $CaCO_3$ content in the sediment samples was found and will be further explored in this work.

5.5.1 ^{26}Al/^{27}Al and ^{10}Be/^{9}Be Results with Assigned Ages

The ^{10}Be/^{9}Be results of all samples measured with the DREAMS facility are displayed in Figure 5.16. Part 5.16(a) shows the ratio of samples of the four sediment cores measured within the time range of 1.7-3.2 Myr. Results of *Eltanin* cores 45-21 and 49-53 are joined to allow a better visibility of a general trend, although it is not clear how the ratios develop between the individual data points.

The distribution of ^{10}Be/^{9}Be over time agrees with the exponential decay function using the surface value of $(1.057\pm0.064) \times 10^{-7}$ as initial ratio (Figures 5.16(a) and 5.16(c)). The measured ratios were also corrected for the ^{10}Be radioactive decay to calculate the ratios at the time of deposition (Figures 5.16(b) and 5.16(d)). These data are plotted with the measured surface ratio shown as solid line. The uncertainty of the ^{10}Be half-life has been added to the error of the initial value.
The ^{26}Al/^{27}Al dating method was used to obtain ages. For E45-16 and E50-02, ^{10}Be/^{9}Be ratios of the four samples with ages $\geq$2.9 Myr significantly disagree with the value expected from the surface ratio at t=0 (see also table 5.3).

The ^{26}Al/^{27}Al results are displayed in Figure 5.17. The exponential decay function was calculated with an initial value of $(2.56\pm0.11) \times 10^{-13}$. The uncertainty of the ^{26}Al half-life was added to the error of the initial value, leading to a broadening of the uncertainty band towards higher ages. All data for E45-16 and E50-02 (except surface samples) are lying directly on this curve, as the exponential decay function was used to date those samples.

(a) ^{10}Be/^{9}Be ratios versus age

(b) ^{10}Be/^{9}Be corrected for half-life

(c) full time range, not half-life corrected

(d) full time range, corrected for half-life
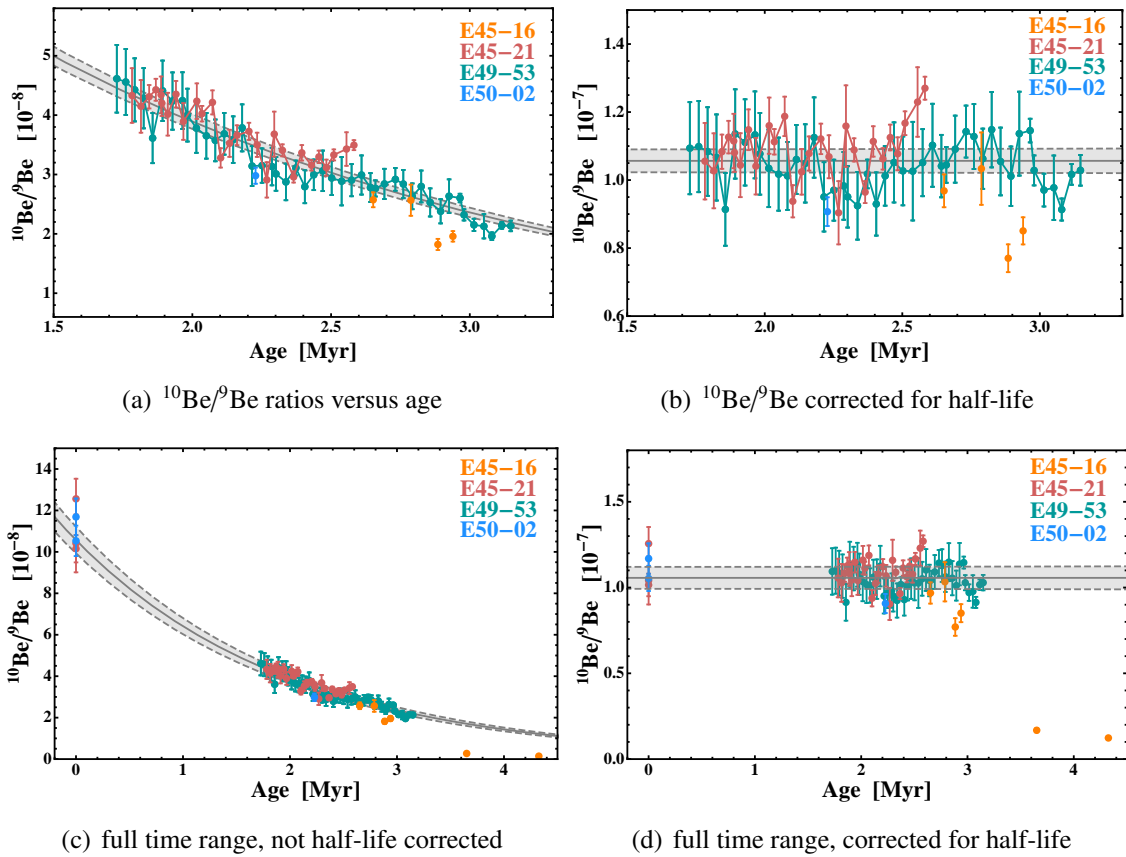
Figure 5.16: ^{10}Be/^{9}Be ratios (measured by DREAMS) displayed in the time range of 1.5-3.5 Myr (upper part) and 0-4.5 Myr (lower part) of targets from all cores measured. Ages were obtained with the ^{26}Al/^{27}Al dating procedure. **Left:** Data are shown with the exponential decay function using a mean surface ratio of $(1.057\pm0.033)\times10^{-7}$. **Right**: Decay-corrected ^{10}Be/^{9}Be data corresponding to initial ratios of each sample at time of deposition. The mean value corresponds again to the surface ratio.

(a) ^{26}Al/^{27}Al versus age

(b) ^{26}Al/^{27}Al corrected for half-life

(c) full time range, not half-life corrected

(d) full time range, corrected for half-life
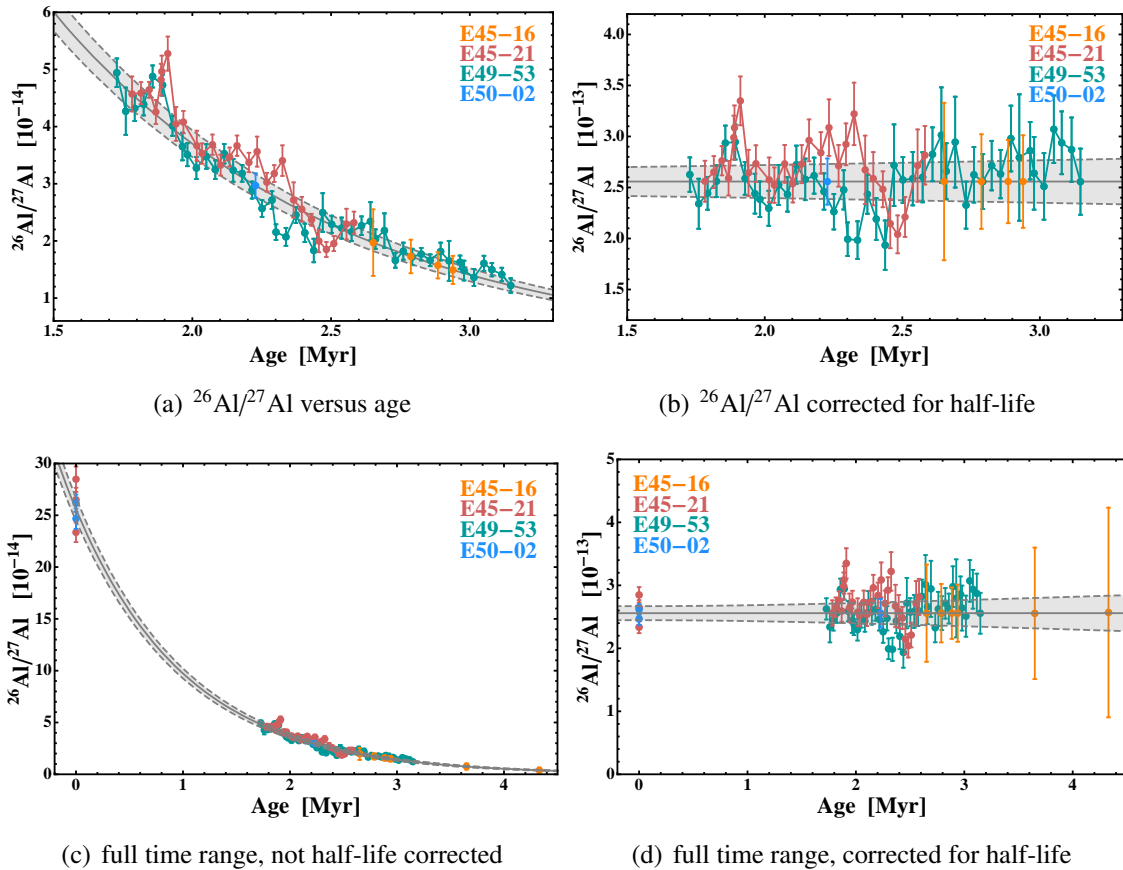
Figure 5.17: ^{26}Al/^{27}Al ratios displayed in the time range of 1.5-3.5 Myr (upper part) and 0-4.5 Myr (lower part) of targets from all cores measured. Ages were obtained with the ^{26}Al/^{27}Al dating procedure. **Left:** Data are shown with the exponential decay function using a mean surface ratio of $(2.56\pm0.11)\times10^{-13}$. **Right**: Decay-corrected ^{26}Al/^{27}Al data corresponding to initial ratios of each sample at time of deposition. The mean value corresponds again to the surface ratio.

5.5.2 Measured ^{26}Al/^{27}Al Ratios vs Theoretical ^{26}Al Production

In chapter 3.1.1.2, the contributions to the total amount of ^{26}Al from different sources were quantified, such as atmospheric production, extraterrestrial influx and in-situ production from the ^{23}Na(α,n) ^{26}Al reaction were quantified. Using an average concentration of 2×10^{19} ats g^{-1} of stable aluminium, the calculated production of ^{26}Al from all these sources were converted into ^{26}Al/^{27}Al ratios and are shown in Figure 5.18 (left) together with measured AMS data.

It is obvious, that the formation of radiogenic ^{26}Al from in-situ production seems overestimated. The measurement results were fitted by an exponential decay curve (Figure 5.17(c)). Possible reasons for a lower ^{26}Al in-situ content were given earlier (section 3.1.1.2).
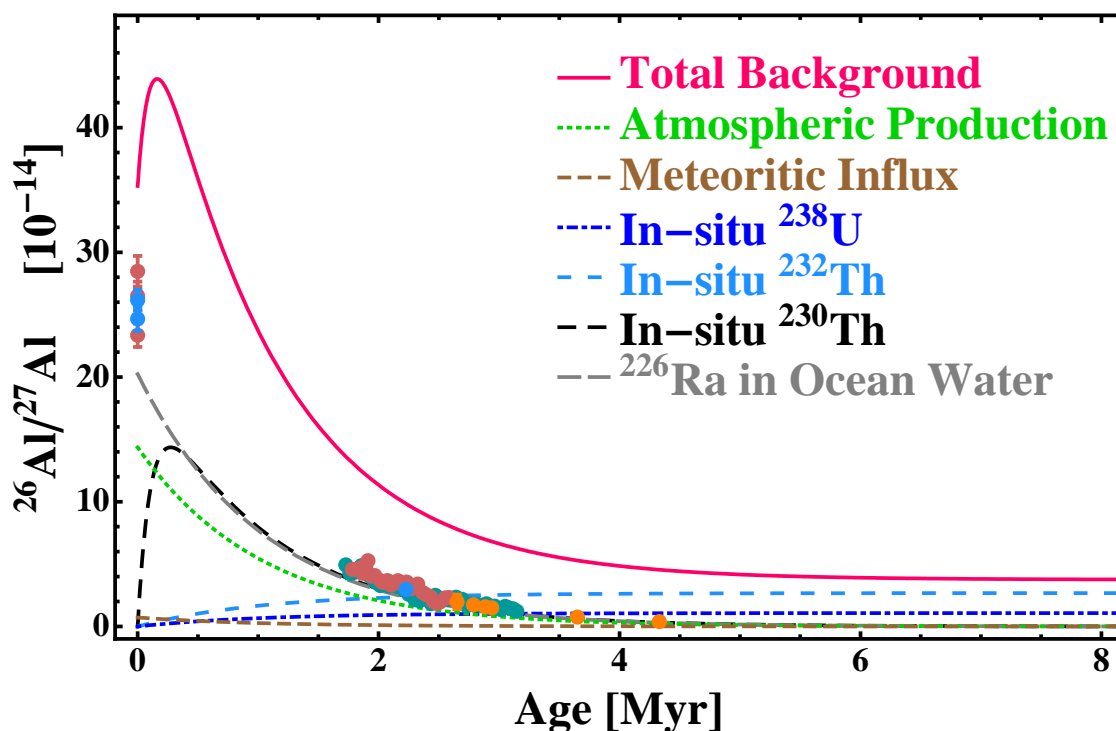
Figure 5.18: Sources for ^{26}Al input in deep-sea sediments as calculated in chapter 3.1.1.2 and displayed as ^{26}Al/^{27}Al ratios. The measured ^{26}Al/^{27}Al data is compared with the theoretical ratios.

Although the atmospheric production seems underestimated here, it is possibly the major contributor to the production of ^{26}Al that is measured in the deep-sea sediments (Wang et al., 1996). In chapter 3.1.1.2, absolute concentrations of ^{26}Al in deep-sea sediments were calculated. This approach might be problematic. First, it was pointed out in chapter 2.3.3, that aluminium is quickly scavenged and not distributed homogeneously in the ocean. Second, dilution effects for instance by $CaCO_3$ lead to lower concentrations than expected (see section 5.5.5).

5.5.3 Fluctuations of ^{10}Be/^{9}Be and ^{26}Al/^{27}Al Ratios

Considering the data presented in Figures 5.6 and 5.7, short term fluctuations in the ^{10}Be/^{9}Be and ^{26}Al/^{27}Al were observed. The uncertainty of the ^{10}Be/^{9}Be ratios is dominated by systematic contributions. However, particularly for *Eltanin* core E45-21, the ^{10}Be/^{9}Be data suggest real fluctuations. It is not clear, whether they originate from oceanographic mechanisms or from chemistry and measurements. This will be discussed below.

5.5.3.1 Effects of Chemistry and Measurements on Short-Term Fluctuations

To investigate potential systematic due to unknown effects from chemical preparation of the samples, the ^{10}Be/^{9}Be and ^{26}Al/^{27}Al ratios are plotted in Figure 5.19 and labeled by the chemistry batches (listed in the tables displayed in Appendix B.2) .
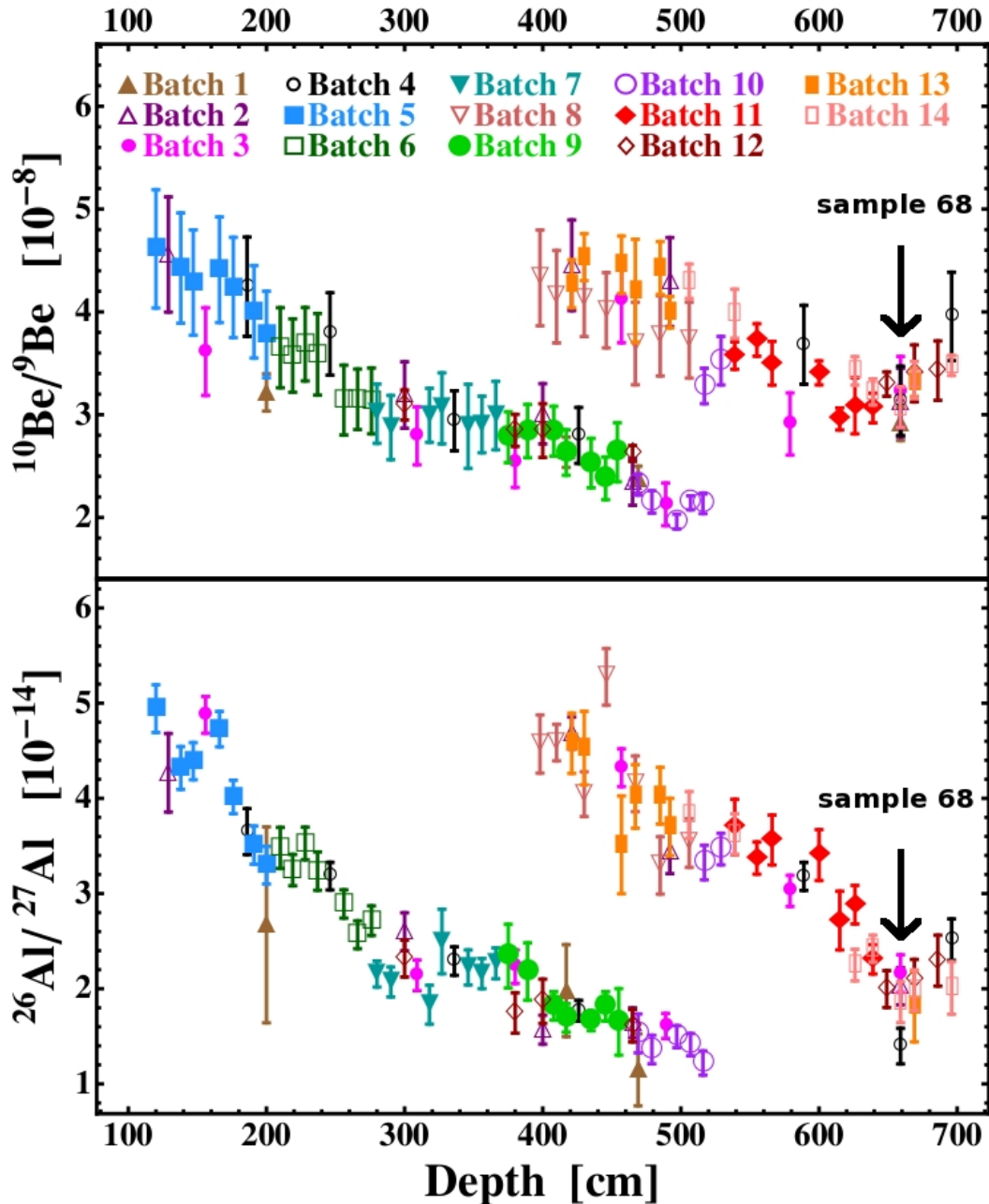
Figure 5.19: ^{10}Be/^{9}Be (DREAMS) and ^{26}Al/^{27}Al (VERA) ratios versus depth. Each batch is coded by a different color/symbol to uncover possible systematic differences between samples prepared in different batches.

Here, isotopic ratios versus sample depth are shown. As noted in chapter 4.1 each batch consisted of seven samples, which were processed simultaneously. If conditions change between batches, systematic deviations might occur between samples. To check the reproducibility, one large sample (number 68) was split and chemically processed five times. The ^{10}Be/^{9}Be and ^{26}Al/^{27}Al ratios of sample 68 (indicated with an error in Figure 5.19) agree well within their uncertainties. However, the ^{10}Be/^{9}Be results of batch 8 seem to be systematically lower than results of batch 13 and is probably caused by the normalization procedure using ICP-MS data of ^{9}Be. As the systematic uncertainties of these data points are large, the results still agree with each other.
The ^{26}Al targets were not measured during one AMS beam time, as a sample requires sputtering for several hours. Furthermore, multiple AMS sputter targets were obtained for some of the samples prepared. For ^{26}Al/^{27}Al ratios, no systematic offset between chemistry batches, and also not for different AMS measurement series was observed.

Systematic offsets in ^{10}Be for the DREAMS data are explored in Figure 5.20. This figure differs from Figure 5.1, as the data were already normalized with the ICP-MS ^{9}Be data. Each target was measured during a single beam-time, giving in total six different measurement series (table 5.1).
The ^{10}Be/^{9}Be ratios of E49-53 show no discrepancies between the measurement series. In case of E45-21, a deviation between the batches 7-9 and 12-14 is observed. Again, these are batches, showing offsets between each other in the ICP-MS ^{9}Be data. Therefore, fluctuations between samples from batch 7-9 and 12-14 are dominated by a systematic offset.
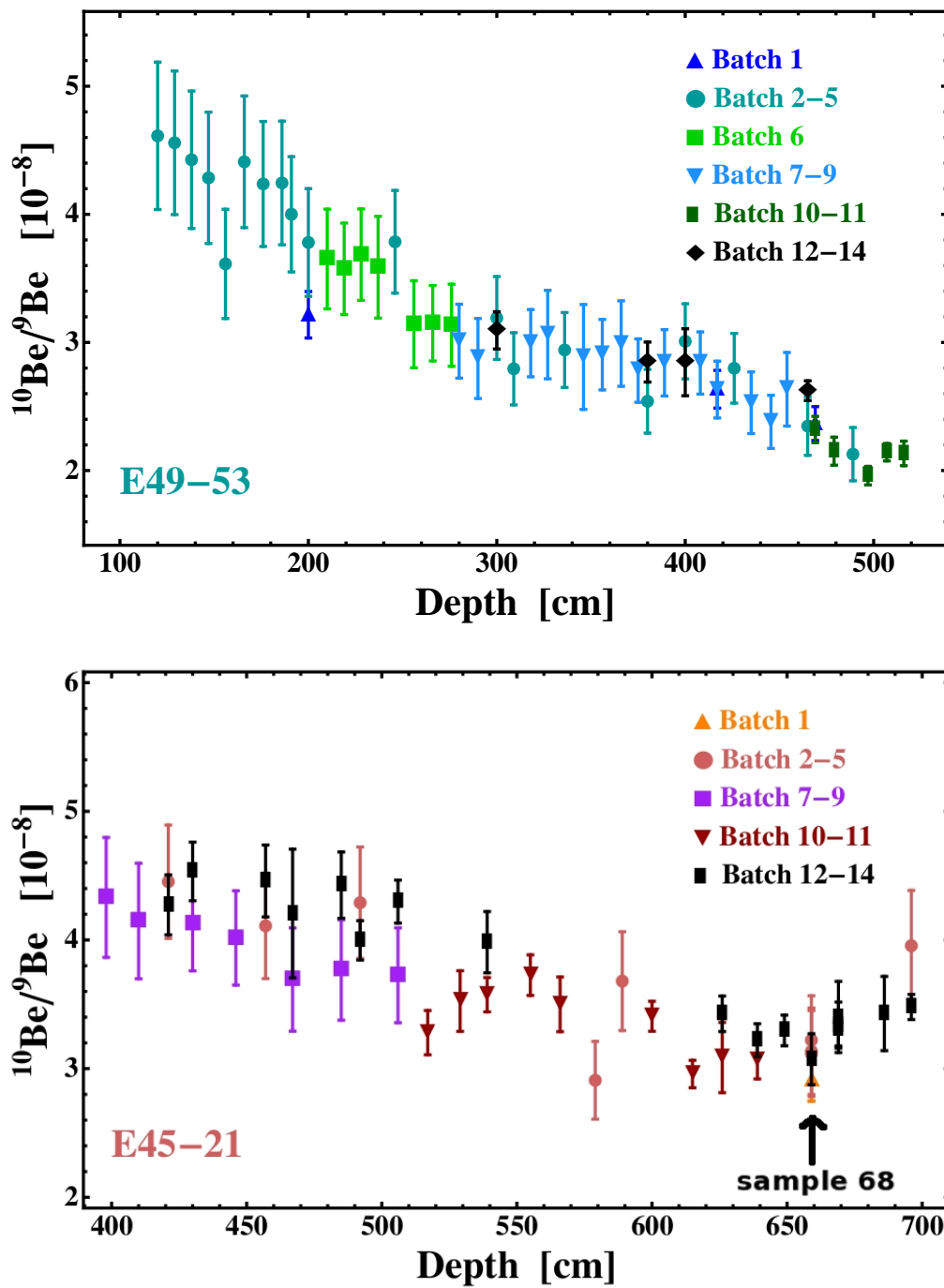
Figure 5.20: ^{10}Be/^{9}Be ratios (DREAMS) versus depth for sediments E49-53 (upper part) and E45-21 (lower part). Beam-Times carried out at the DREAMS facility are coded by a different colors/symbols to uncover possible systematical differences between samples studied in different measurement series.

5.5.3.2 Statistical Analysis of Short- and Long-Term Fluctuations

Variations of the ^{26}Al/^{27}Al and ^{10}Be/^{9}Be isotope ratios might be caused by oceanic mechanisms. On one hand there could be short term ($\sim 10^4$ years) changes of soluble aluminum and beryllium in deep-sea water (Bourlès et al., 1989). In addition, enhanced bottom-water velocities may lead to a change in sediment grain size and therefore a decrease in sedimentation rate (Allison and Ledbetter, 1982). A sudden change in accumulation rate or even a hiatus should be distinguishable by an abrupt shift in both, the aluminum and beryllium data.

Events such as a magnetic reversal at around 2 Myr and 2.6 Myr might be observed in higher ^{10}Be/^{9}Be ratios as the ^{10}Be production is increased due to an enhanced cosmic ray flux onto Earth. However, distances of 3-17 cm (corresponding to 8-63 kyr) (section 2.3.2) between the samples are not sufficiently small for temporarily resolving such an increase of ^{10}Be. Furthermore, the sedimentation rates are too low for detecting a magnetic instability. A magnetic reversal in ^{10}Be is only extending over a few 10 kyr (e.g. Lachner (2013)), which is in the same order as the mixing length (10 cm, corresponding to $\sim$30 kyr). ^{26}Al is produced 10^3 times less in the Earths atmosphere than ^{10}Be. A change of the ^{26}Al concentration in a deep-sea sediment sample due to a magnetic instability is expected to be less pronounced than that of ^{10}Be.

Figure 5.21 shows the fluctuations of the ^{26}Al/^{27}Al and ^{10}Be/^{9}Be data in the two *Eltanin* cores E45-21 and E49-53. The data is decay-corrected with the corresponding half-lifes of ^{10}Be and ^{26}Al. The two ratios of ^{26}Al/^{27}Al and ^{10}Be/^{9}Be follow a very similar pattern, indicating, that at least some of the fluctuations in the data are caused from changing conditions of the ocean. Larger discrepancies between the aluminum and beryllium data are observable in layers deeper than 2.4 Myr of E45-21. In addition a possible small increase of the ^{26}Al/^{27}Al ratio is suggested around 1.9 Myr in the two cores, which is not visible in the ^{10}Be/^{9}Be data.

The scatter of the ^{26}Al/^{27}Al and ^{10}Be/^{9}Be ratios around their mean value was analyzed statistically. First, the mean is subtracted from the isotope ratio of each data point. Because the surface ratio (t=0) for the ^{10}Be/^{9}Be data was obtained by calculating a mean from the decay-corrected data (Figure 5.12), its mean ratio is equal to the surface ratio. The mean value was calculated to $(^{10}$Be/^{9}Be$)_{mean} = (1.057 \pm 0.064) \times 10^{-7}$ (see above, section 5.4.1). Decay-correction of the ^{26}Al/^{27}Al data yields a very similar mean value of $(^{26}$Al/^{27}Al$)_{mean} = (2.59 \pm 0.11) \times 10^{-13}$ to the surface value of $(^{26}$Al/^{27}Al$)_{surface} = (2.56 \pm 0.11) \times 10^{-13}$. Subsequently, each value is weighted with its standard deviation. This was done for both, the ^{26}Al/^{27}Al and ^{10}Be/^{9}Be ratios of the two cores and the data is displayed in Figure 5.22. Here, the deviation of each value from the mean is plotted in units of the standard deviation. In general, a larger scattering around the mean value is observed in the ^{26}Al/^{27}Al data, however, with a similar pattern in both cores.

This scattering is displayed as histograms with different bin widths, and was fitted with a gaussian distribution. Figure 5.23 shows histograms with bin widths of 0.5 σ. Histograms
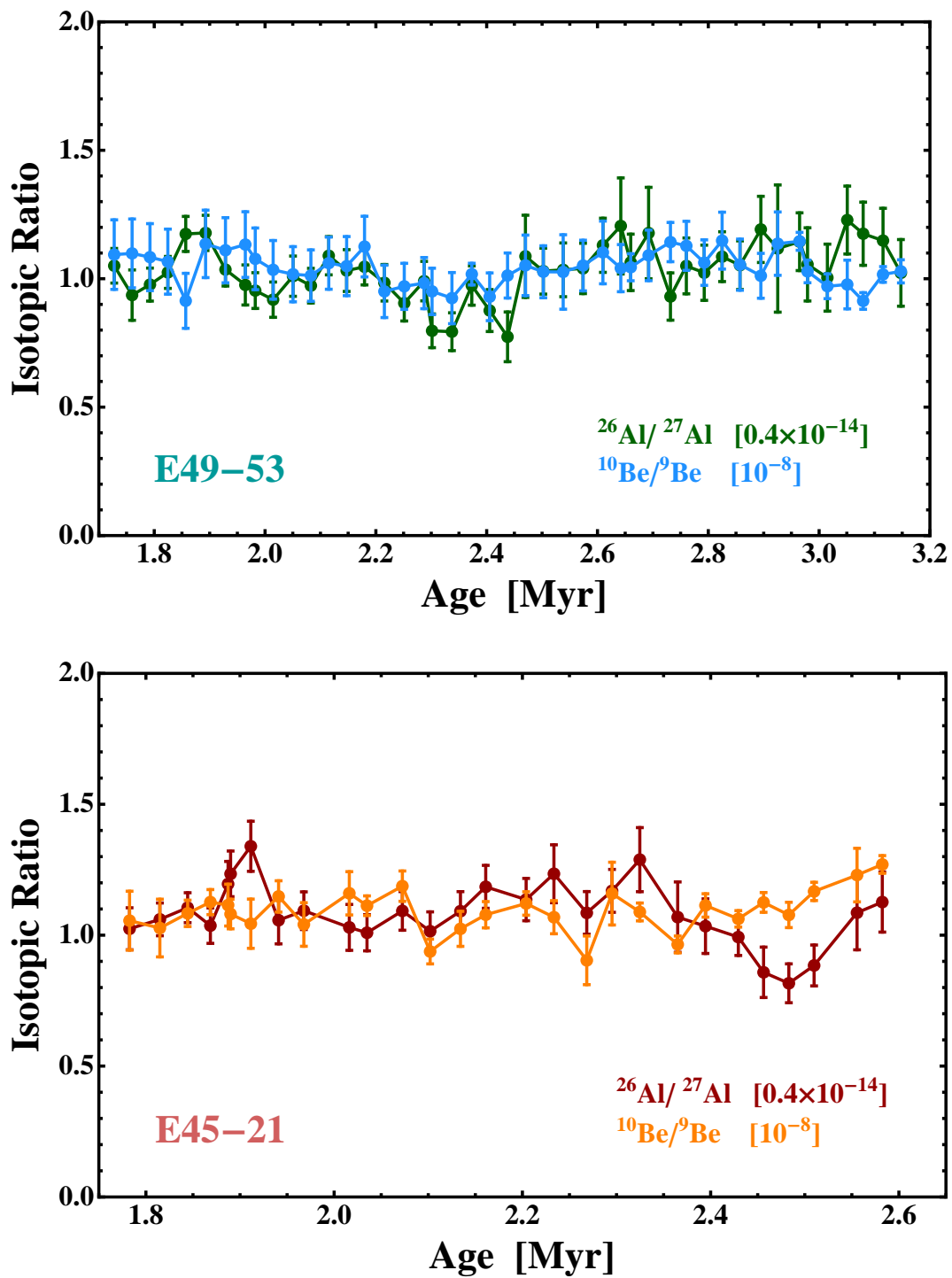
Figure 5.21: Isotopic ratios of ^{10}Be/^{9}Be and ^{26}Al/^{27}Al vs age for cores E49-53 and E45-21. The ^{10}Be/^{9}Be is multiplied with 10^{-8} and the ^{26}Al/^{27}Al data with a factor of 0.4×10^{-14} for comparison. The data is decay-corrected with the corresponding half-life values.
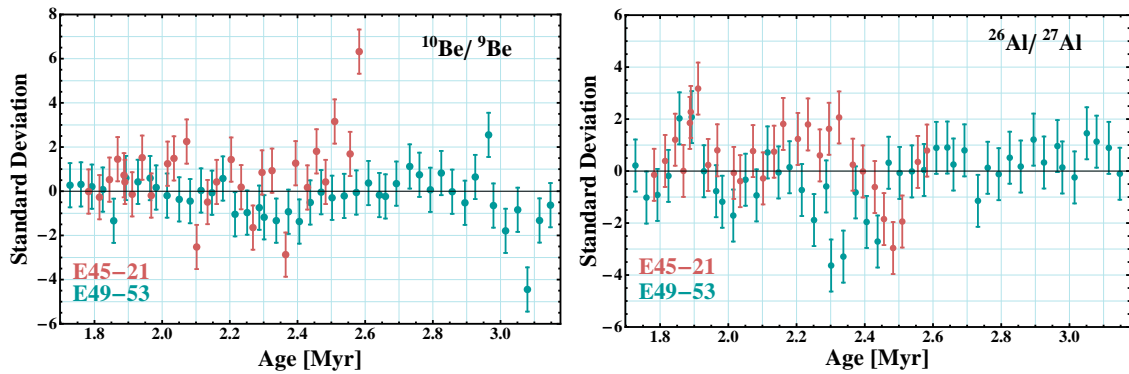
Figure 5.22: Deviations of decay-corrected isotopic ratios from their mean values for E45-21 (red) and E49-53 (green) versus time. The data were normalized to their individual standard deviations.

with varying bin widths are also displayed in Figures H.1 and H.2 in the Appendix. The two upper figures represent the combined data of the two cores E45-21 and E49-53. The data set of the ^{10}Be/^{9}Be ratios for both cores can be well reproduced by a gaussian distribution and does not change for different bin widths. The same applies to the ^{26}Al/^{27}Al ratios.

In the middle and lower part of Figure 5.23, as well as in the figures H.3-H.6 of the Appendix, the data sets were split into the two cores E45-21 and E49-53. Is is observed, that the distribution of ^{26}Al/^{27}Al and ^{10}Be/^{9}Be ratios within the histogram of E45-21 are shifted compared to the mean value of the gaussian distribution. The reason is, that the mean value calculated from the whole data set might not exactly be identical to the mean values for the individual cores.

Fluctuations of ^{26}Al/^{27}Al ratios, as well as for ^{10}Be/^{9}Be ratios occur in positive and negative directions and it is assumed that changing conditions of the oceanic environment are responsible. If a SN signal were visible in the ^{26}Al/^{27}Al data, ratios should differ significantly from the mean value in the positive direction. However, this is not observed in the ^{26}Al/^{27}Al data.

For a better visualization of the general trend of the ^{26}Al/^{27}Al and ^{10}Be/^{9}Be data with time, running means of the half-life corrected data were calculated. Figure 5.24 shows moving averages of ^{26}Al/^{27}Al and ^{10}Be/^{9}Be isotope ratios, where n=5 successive data points were combined and weighted averages were calculated. Running means of two to eight data points are also displayed in Appendix H.2. The mean ratios are shown as a gray band, moving averages of E45-21 as red and of E49-53 as green bands with mean values indicated as a solid line.

For subsets with higher n the short term fluctuations become smoothed out. In general the ratios of ^{26}Al/^{27}Al and ^{10}Be/^{9}Be decrease to a minimum about 2.4 Myr, and then start to increase again towards higher ages. This trend is significant for core E49-53, however, for E45-21 the running means of the ^{10}Be/^{9}Be data are within the uncertainty band of the mean value. The ^{26}Al/^{27}Al data for E45-21 fluctuate stronger around the mean value. A
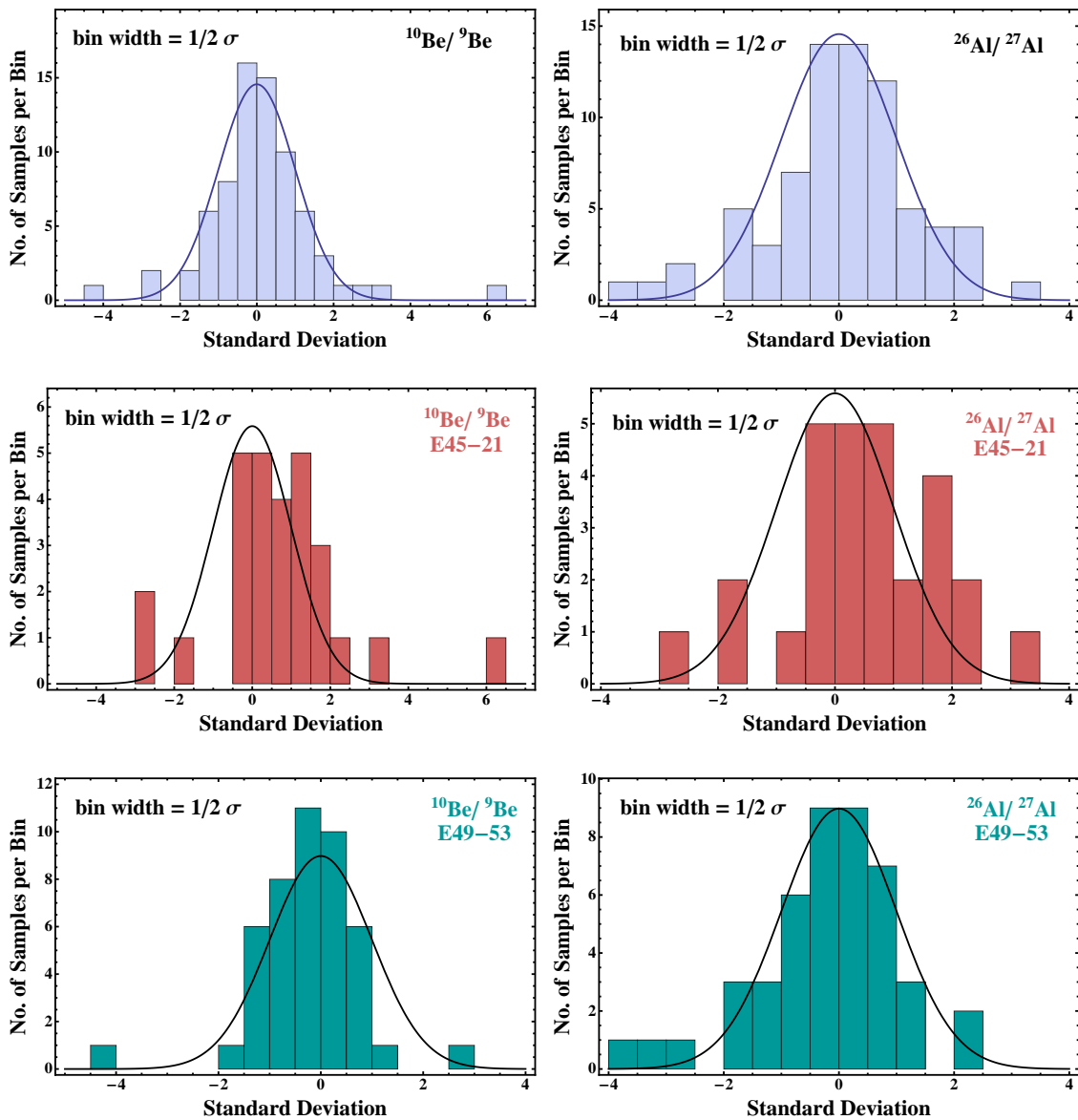
Figure 5.23: Fluctuations of ^{10}Be/^{9}Be (left) and ^{26}Al/^{27}Al ratios (right) displayed as histograms in terms of standard deviations with bin width of 0.5 σ. **Upper part:** Data of E45-21 and E49-53 combined. **Middle:** Isotopic ratios of E45-21. **Lower Part:** Isotopic ratios of E49-53.

maximum of ^{26}Al/^{27}Al in E45-21 is observed for 2.3 Myr.

Similar to what was inferred from the histograms (Figure 5.23), a time offset between E45-21 and E49-53 is observed in Figure 5.24. The ^{26}Al/^{27}Al data suggests a time offset of 100 kyr at 2 Myr, increasing to 200 kyr for higher ages. This points to variations of the sedimentation rate with time. Such variations were ignored in the age models, because average sedimentation rates were used for the whole time range investigated. However, the time offsets between the two cores are still within the uncertainties of the ^{26}Al/^{27}Al age model (compare tables G.4 and G.5 in the Appendix).
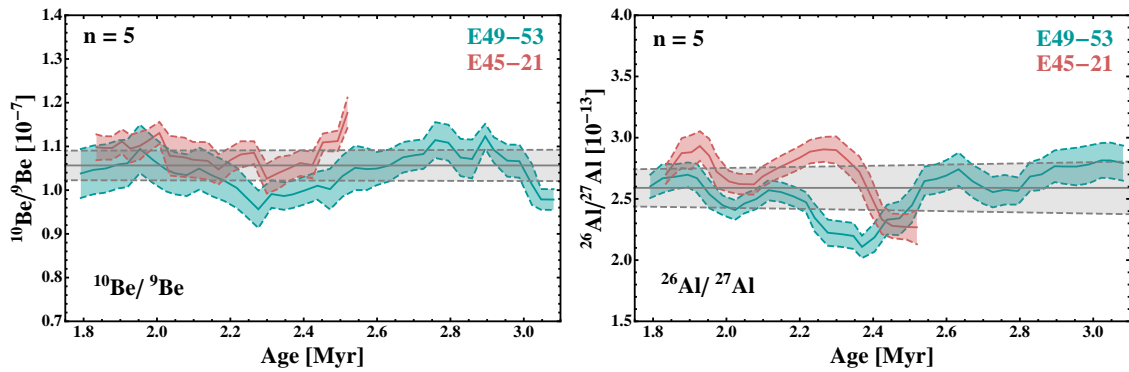
Figure 5.24: Running means calculated from weighted averages of subsets of n=5 data points of the two half-life corrected isotopic ratios $^{26}Al/^{27}Al$ and $^{10}Be/^{9}Be$ in E45-21 and E49-53.

5.5.4 Absolute Concentrations of Elements and Fractionation Effects

Absolute concentrations of stable beryllium and aluminium were measured with ICP-MS. The ^{9}Be concentrations from ICP-MS measurements were corrected according to the procedure used in section 5.1.2. These, and the ^{27}Al concentrations were multiplied with the $^{10}Be/^{9}Be$ and $^{26}Al/^{27}Al$ isotope ratios of a sample, respectively, to determine the absolute concentrations of ^{26}Al and ^{10}Be.

The results are displayed in Figure 5.25. The upper part shows absolute concentrations of stable ^{9}Be and ^{27}Al in each sample (ats g^{-1}). The data for the corresponding radionuclides are plotted in the lower part of this figure and were corrected for exponential decay. It is obvious, that the concentrations of the two elements (radionuclides and stable isotopes) seem similar throughout the cores. The reason is dilution by $CaCO_3$, as will be discussed in the following section. It will be shown, that from these changes in the concentrations of beryllium and aluminium, a stronger correlation between $CaCO_3$ with beryllium than with aluminium can be inferred. The core which contains less $CaCO_3$, E45-21, has a higher Be-content than E49-53 with the higher $CaCO_3$ content, whereas the aluminum content of the two cores does not differ strongly.

The absolute concentrations of aluminium and beryllium were used to calculate Al/Be ratios. The individual ratios of $^{26}Al/^{10}Be$ and $^{27}Al/^{9}Be$ for each sample are plotted in Figure 5.26. The atmospheric value of $^{26}Al/^{10}Be = (1.89\pm0.05)\times10^{-3}$ (Auer et al., 2009) is indicated by a solid blue line with the uncertainty shown as dashed lines.

Mean values of the $^{26}Al/^{10}Be$ of the two cores yield

$$(^{26}Al/^{10}Be)_{E45-21} = (1.63 \pm 0.11) \times 10^{-3},$$
$$(^{26}Al/^{10}Be)_{E49-53} = (2.37 \pm 0.11) \times 10^{-3}. \tag{5.5}$$

The radioisotopic ratios are in the order of the atmospheric value measured by Auer et al. (2009). The individual data points are scattered around the atmospheric value. By comparison with the $^{27}Al/^{9}Be$ data, a similar profile is observed. Here, fractionation effects
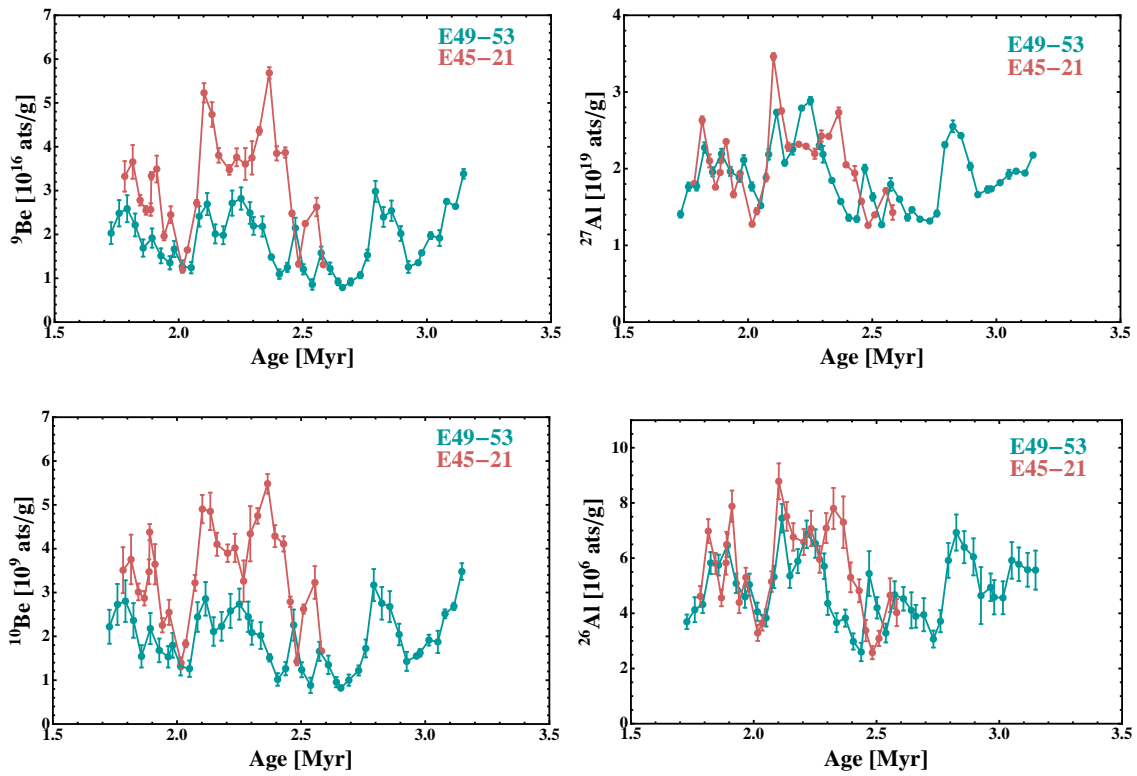
Figure 5.25: Absolute concentrations of ^{9}Be and ^{27}Al and their long-lived isotopes ^{10}Be and ^{26}Al in the two deep-sea sediment cores E45-21 (red) and E49-53 (green). Radioisotopic concentrations have been corrected for decay. The ages are based in the ^{26}Al/^{27}Al dating method.
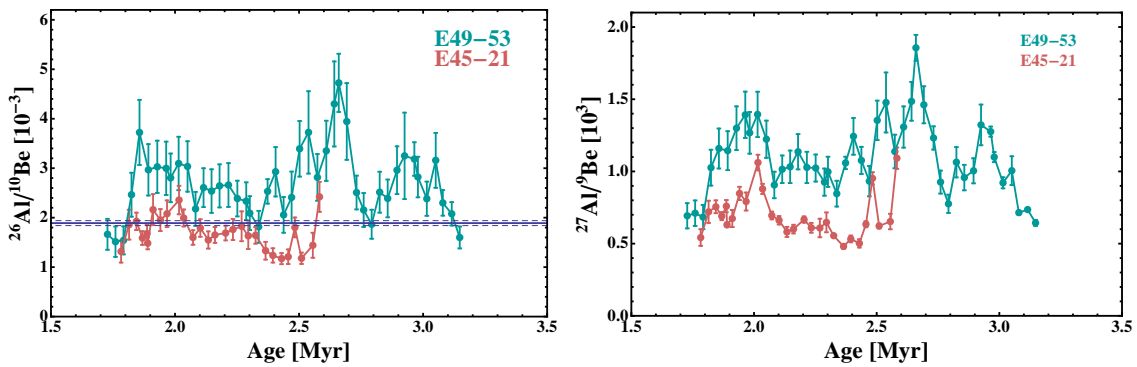
Figure 5.26: Half-life corrected ^{26}Al/^{10}Be and stable ^{27}Al/^{9}Be ratios determined for core E45-21 (red) and E49-53 (green). The blue line indicates the atmospheric ratio published by Auer et al. (2009).

between Al and Be due to the $CaCO_3$ content influence the Al/Be ratios, and will be examined in the following.

5.5.5 CaCO$_3$ as Dilutant and Correction of ^{26}Al/^{10}Be Ratios

As described in chapter 4.1, the leaching solution was applied to 3 g sediment material. Instantly, a large amount of CO$_2$ is released: CaCO$_3$ was dissolved by HCl and acetic acid, before the actual leaching procedure starts. Ca, however, remains in the solution. After leaching and isolation of the residue from the leached solution the residue is dried and weighted to estimate the percentage leached. It was found, that a fraction of 5-50 % of the total sample material remains as unleached leftover. The 50-95 % "lost" from the original sample material correspond largely to the amount of CaCO$_3$ dissolved. A small fraction correspond to other elements leached from the sample. The fraction of 50-95 % is referred to as mass "loss".

The correlation between the CaCO$_3$ content of the sample and mass loss is illustrated in Figure 5.27. Here, the concentration of Ca is shown in units of 10^{21} ats g^{-1}. The mass of material lost from the original sample is given in percentage. In order to scale the mass loss to the Ca concentration, the mass loss of E49-53 and E45-21 was divided by a factor of 18 and 20, respectively. A correlation between mass loss and Ca content becomes evident. If 1 g of sediment sample would consist only of CaCO$_3$, a concentration of 6.02×10^{21} Ca atoms would be measured. It appears, that the sediment samples predominantly consist of CaCO$_3$, particularly E49-53.

Various elements in the leached solution were quantified with ICP-MS. Due to their high concentrations of Mg, Al, Ca, Mn, Fe, Ni in the samples (in contrast to Be), no systematical offsets occurred between measurements. Figure 5.28 displays the concentrations of these elements in each sample in E45-21 and E49-53. An inverse correlation between Ca and all other measured elements is observed. It was pointed out by several research groups (e.g. Bourlès et al. (1989) and Henken-Mellies et al. (1990)), that CaCO$_3$ is acting as dilutant for beryllium. Only minor amounts are transported in the CaCO$_3$ mineral fraction; the same is indicated for the other elements examined. This dilution from CaCO$_3$ can be avoided by first dissolving the carbonates during the chemical procedure. A specific amount of sample material can then be taken from the undissolved residuum for further separation of elements.

As mentioned above, the ratios of stable ^{27}Al/^{9}Be show a similar pattern over time as the ^{26}Al/^{10}Be ratios throughout the sediment cores (Figure 5.26). In Figure 5.29 the two ratios are plotted for E45-21 and E49-53. Ratios of ^{26}Al/^{10}Be are the order of $\sim 10^{-3}$, and ^{27}Al/^{9}Be $\sim 10^3$.

Due to the different origin of radionuclides and stable nuclides, variations in their distribution within the sediment cores would be expected. However, when scaling with the curve of material loss from CaCO$_3$ dissolution and leaching, the Ca-content is again reflected in the distribution of the Al/Be ratios. This hints to fractionation effects between these two elements and a correlation of the fractionation with the sediment's carbonate content. In general, if the CaCO$_3$ content is high, less Al and Be is present in the sample due to dilution. However, high Al/Be ratios are accompanied with a high CaCO$_3$ content,
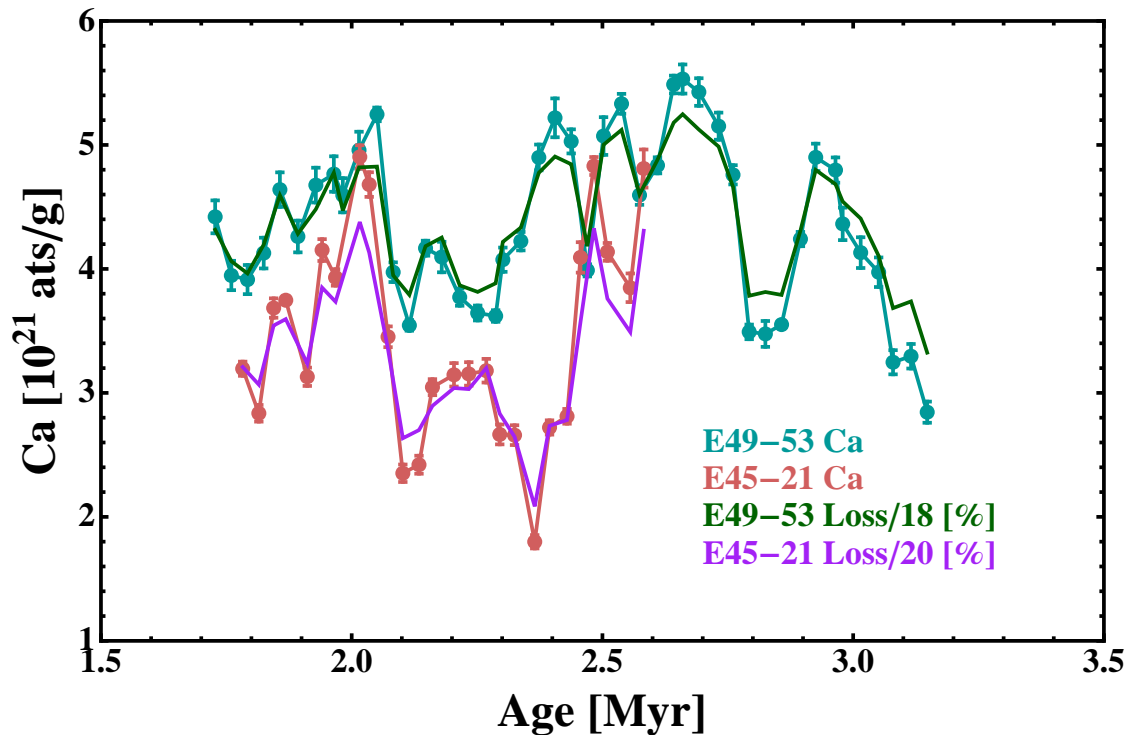
Figure 5.27: Number of Ca ats g^{-1} in E45-21 and E49-53 vs age of samples. The mass of dissolved and leached material is referred to as "loss". The percentage of loss was scaled with a factor of 18 and 20 for E49-53 and E45-21 to match the Ca pattern, respectively.

indicating that more Al relative to Be is present. Vice versa, for a low CaCO$_3$ the ratio of Al/Be is lower, therefore, a proportionally lower amount of Al compared to Be is present in the sediment sample.

The reason is illustrated in Figure 5.30, where concentrations of ^{10}Be and ^{26}Al are plotted against the Ca content. A linear dependence is fitted for both cases to obtain the amount of ^{10}Be and ^{26}Al atoms for a sample containing no CaCO$_3$. This procedure is usually applied to correct for the dilution effect. One data point had very low Ca of ~1.4×10^{21}Ca ats g^{-1} and was considered as an outlier and therefore not included in the regression. Henken-Mellies et al. (1990), who analyzed the correlation of beryllium and CaCO$_3$, found that the CaCO$_3$ fraction transports only scarce amounts of ^{10}Be with less than 1×10^8 ats g^{-1}. The non-CaCO$_3$ fraction contains on average 4.5×10^9 ats g^{-1}. Here, the result is similar: 100 % CaCO$_3$, translating to 6.02 × 10^{21} Ca atoms, contain no ^{10}Be in E45-21 (the regression line crosses this value at (-0.3±0.5)×10^8 ats g^{-1}) and (4.4±0.4)×10^8 ats g^{-1} in E49-53. On the other hand, the non-CaCO$_3$ fraction carries (8.0±0.2)×10^9 ats g^{-1} and (5.6±0.2)×10^9 ats g^{-1} in E45-21 and E49-53, respectively.

The same procedure was applied for ^{26}Al, which shows a larger scatter against Ca. In contrast to ^{10}Be, a higher amount was transported within the carbonate-phases, thus leading to a fractionation between the two isotopes. For E45-21 the ^{26}Al concentration amounts
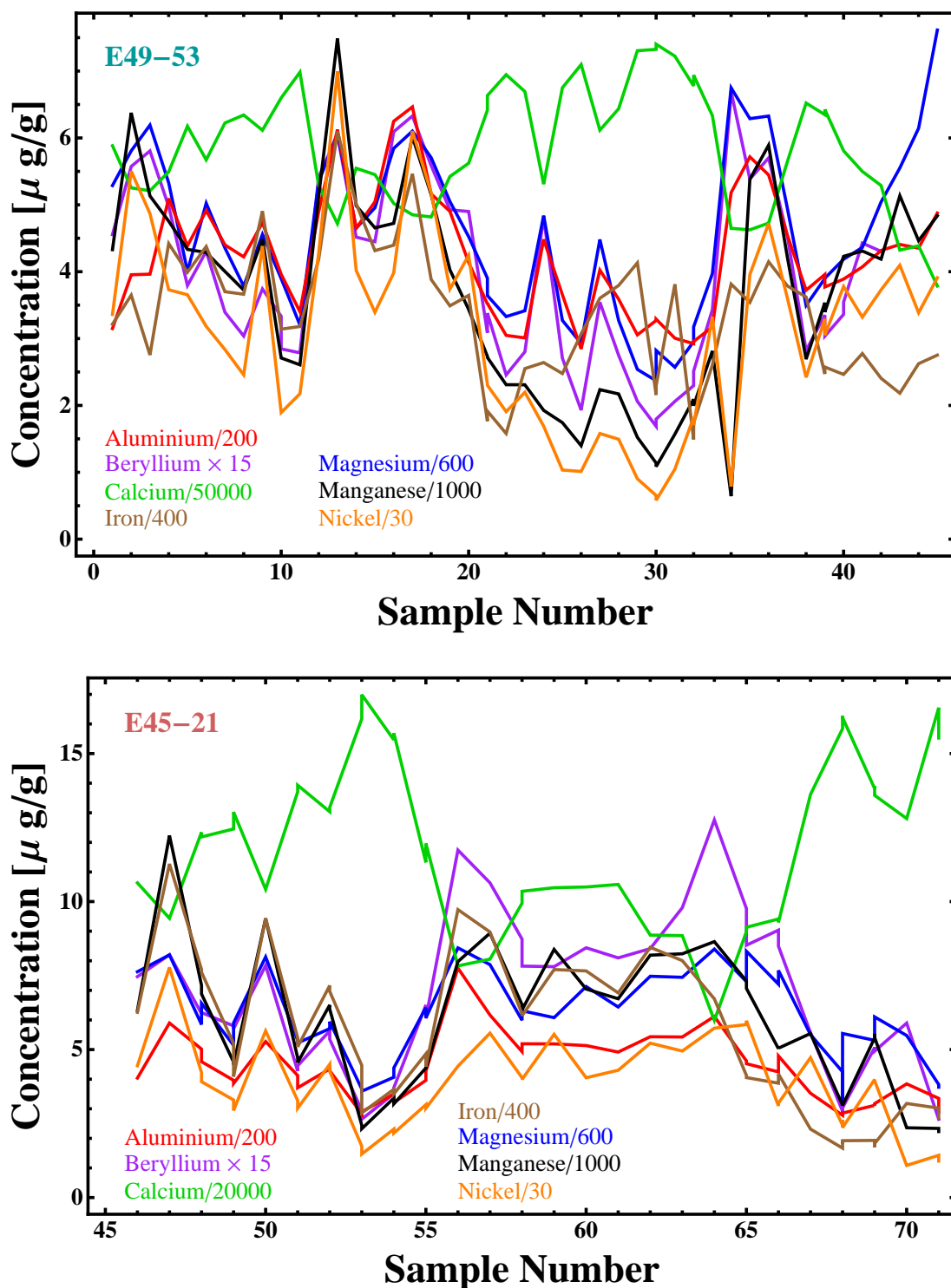
Figure 5.28: Concentrations of Al, Be, Ca, Fe, Mg, Mn, and Ni in µg/g multiplied/divided by a factor to emphasize the inverse behavior of Ca to all other elements. Note, that for a better representation Ca in samples of E49-53 is divided by 50 000, in E45-21 only by 20 000 due to lower $CaCO_3$ contents.
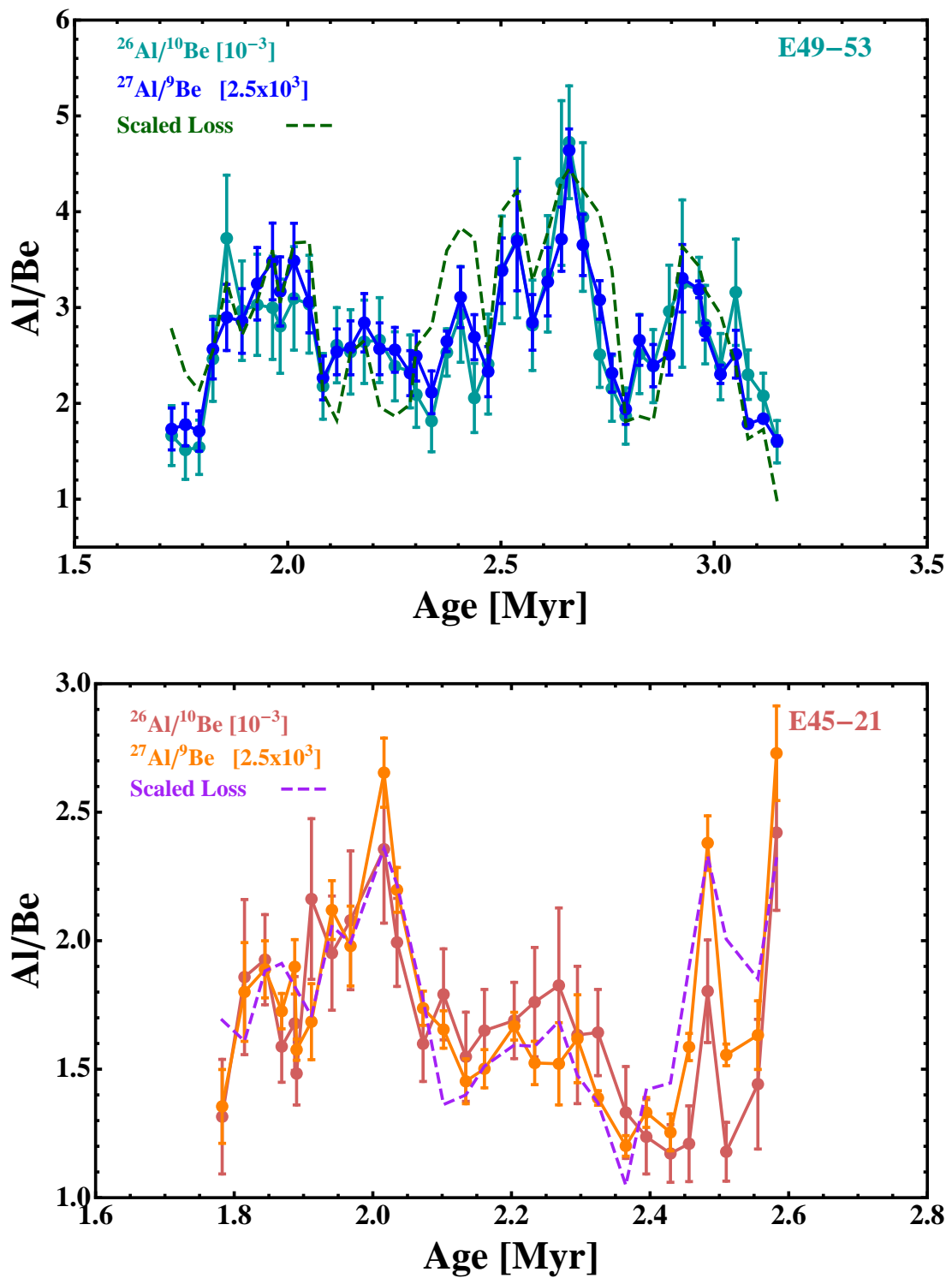
Figure 5.29: ^{26}Al/^{10}Be as well as ^{27}Al/^{9}Be ratios of E49-53 (upper figure) and E45-21 (lower figure). In addition sample mass lost during the leaching procedure is displayed and scaled for comparison of the curve's shape with the obtained ratios.
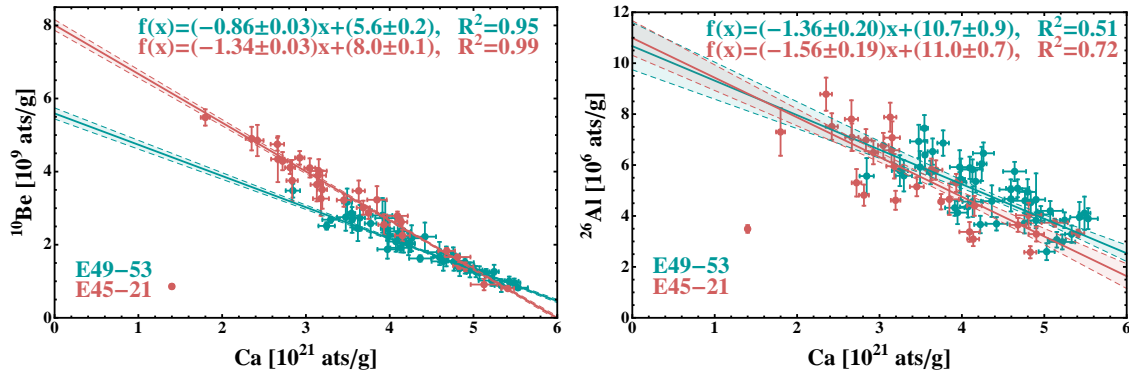
Figure 5.30: Concentrations of ^{10}Be and ^{26}Al versus Ca of *Eltanin* cores E45-21 (red) and E49-53 (green). A clear correlation is regressed linearly. In each graph corresponding functions are displayed for the two cores.

to $(1.6\pm0.5)\times10^6$ ats g^{-1} compared to $(11.0\pm0.7)\times10^6$ ats g^{-1} in the non-CaCO$_3$ mineral phases. A similar result is obtained in E49-53: $(2.5\pm0.3)\times10^6$ ats g^{-1} are in the carbonate, $(10.7\pm0.9)\times10^6$ ats g^{-1} in the non-CaCO$_3$ fraction.

The values of the non-carbonate fraction can now be used to obtain a revised ratio of ^{26}Al/^{10}Be for the two *Eltanin* cores E45-21 and E49-53, corrected for fractionation effects from CaCO$_3$ dilution and transport. For the two cores this yields

$$(^{26}\text{Al}/^{10}\text{Be})_{\text{E45-21,corr}} = (1.37 \pm 0.09) \times 10^{-3},$$
$$(^{26}\text{Al}/^{10}\text{Be})_{\text{E49-53,corr}} = (1.91 \pm 0.17) \times 10^{-3}. \tag{5.6}$$

The uncertainties were estimated by a gaussian error propagation for the standard deviation given for the non-carbonate fraction. The newly obtained ^{26}Al/^{10}Be ratios are lower than the original yields deduced earlier via equation (5.5) as the dilution effect of CaCO$_3$ has a larger influence on beryllium. Therefore, with no CaCO$_3$, the amount of Be increases more than of Al and consequently leading to lower ^{26}Al/^{10}Be isotopic ratios. The effect is stronger in E49-53, as it contains more CaCO$_3$. The ratio of this core is 19.4 % lower than the uncorrected ratio, for E45-21 it is 15.6 %.

The Ca-corrected ^{26}Al/^{10}Be ratios are still in the order of the atmospheric ratios measured by Auer et al. (2009). For the various input sources for ^{26}Al into deep-sea sediments discussed in chapter 3.1.1.2 this implies, that the major fraction is of atmospheric origin and in-situ production is negligible for all samples measured in this work.

It must be noted, that these ratios are an estimation, as the CaCO$_3$ is most likely not the only source leading to variations of Al and Be. Fractionation can occur anywhere in the geochemical pathway from the atmosphere into the marine sediment (Wang et al., 1996). However, the results seem to agree fairly well with earlier studies such as Auer et al. (2009) and Sharma et al. (1987a). The latter measured a ^{26}Al/^{10}Be ratio of approximately

2×10^{-3} in the top layer of a manganese nodule and a much higher ratio of 38×10^{-3} in marine phillipsite of a sediment core from the South Pacific. Additional measurements of manganese nodules with ^{26}Al/^{10}Be yielded much lower ratios of $(2-4)\times10^{-4}$ and corals were between 2.7 and 13.5×10^{-4} (Bourlès et al., 1984).

One has to be aware of the fractionation between Al and Be in correlation with the $CaCO_3$ content, when using the ^{26}Al/^{10}Be ratios as dating tool for deep-sea sediments. Other fractionation effects, like scavenging efficiency of particles of different size and composition, might may also influence this ratio. To make sure to correct for dilution and other effects, it is best to apply the stable isotope as normalization parameter and therefore use isotopic ratios for dating (e.g. Bourlès et al. (1989)).

5.6 Discussion of an ^{60}Fe and ^{26}Al SN Signal

Finally the measured ^{60}Fe data in the sediment samples will be analyzed with respect to a possible SN origin. A comparison to the ^{26}Al data will be made and compared to nucleosynthesis models with different ^{60}Fe/^{26}Al ratios.

5.6.1 An Extraterrestrial ^{60}Fe Signal in Deep-Sea Sediments

The ^{26}Al/^{27}Al age model was applied to the ^{60}Fe/Fe data shown in Figure 5.8. The result is displayed in Figure 5.31. Clearly, an ^{60}Fe signal is detected in the measured time period of 1.73-3.15 Myr in all four different deep-sea sediment cores. This peak exceeds the time range of the 6-8 mm layer in the ferromanganese crust (Knie et al., 2004), which corresponds to a time range of 1.7-2.6 Myr (Feige et al., 2012).

Samples prepared in batches 2-14 were measured first. These included material from E45-21 and E49-53 in the time range between 1.7 and 3.2 Myr. ^{60}Fe was detected in all of these targets. In the course of this work, ^{60}Fe measurements were just developed at the HIAF facility at the ANU. Therefore, it had to be verified, that indeed ^{60}Fe was measured at such low isotope ratios, and isobaric background (^{60}Ni, molecules) does not interfere. Furthermore, it is possible that a constant influx of ^{60}Fe in the sediments was observed instead of a single SN signal. This background could originate possibly from extraterrestrial influx of MMs. For this reason old samples, where ^{60}Fe should already have decayed, and very young samples of the sediment's top layers (corresponding to the present time) were analyzed. Indeed, surface targets did not yield any ^{60}Fe events, nor did the slightly older samples with assigned ages of 3.7 and 4.3 Myr. Therefore, a temporarily enhanced extraterrestrial ^{60}Fe influx on Earth was observed. Measurement errors as well as a constant background source can therefore be excluded. How broad the ^{60}Fe signal really is towards younger ages, can not be deduced from the available data, as no samples were examined between 0 and 1.73 Myr.

Further evaluation will not include the two data points obtained from test measurements at TU Munich, as measurement times were too short.
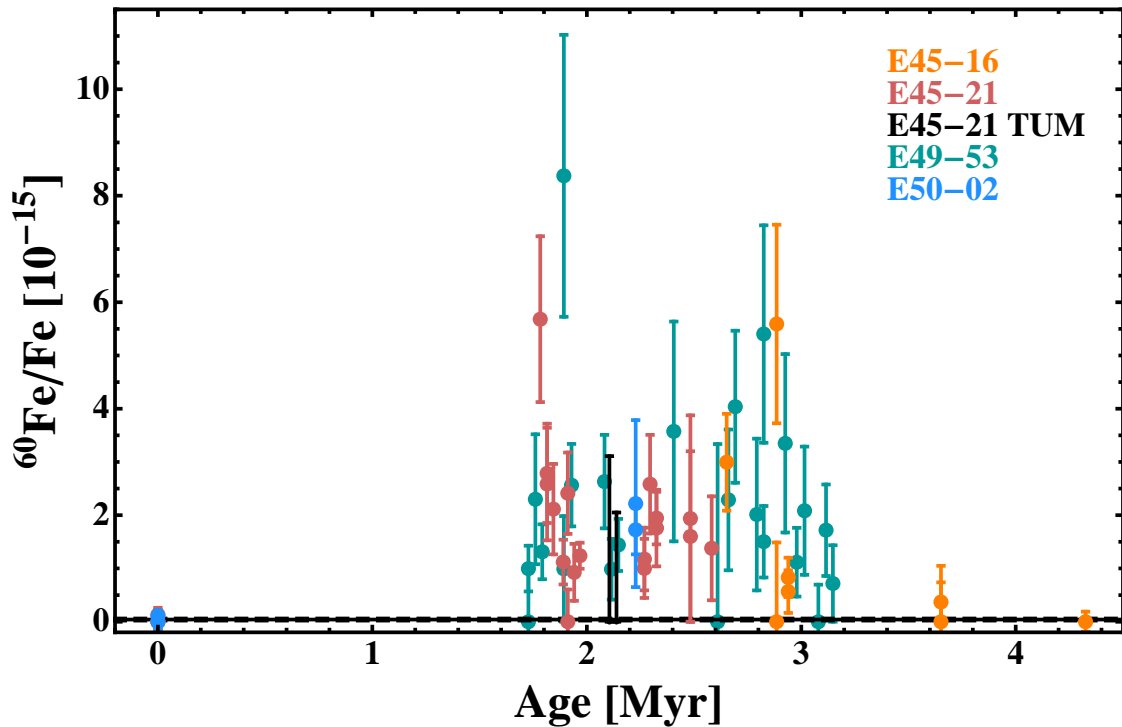
Figure 5.31: ^{60}Fe/Fe isotope ratios measured in samples from four deep-sea sediment cores using ages deduced from ^{26}Al/^{27}Al data. The ratios are not corrected for background and radioactive decay. All samples were measured at the HIAF facility (ANU, Canberra, Australia), with exception of two data (points displayed in black color), which were obtained from AMS measurements at TU Munich (Germany). The dashed black line indicates the background level from measurements at HIAF with ^{60}Fe/Fe = (0.4±0.2)×10^{-16}.

5.6.2 Recalculation of an Uptake-Factor in the Ferromanganese Crust

All matter that enters the ocean is eventually deposited on the ocean's floor. Of course, there are scavenging effects that might lead to enrichment of elements in regions of high particle flux. However, the uptake-efficiency of a deep-sea sediment is assumed to be 100 % for further estimations. A ferromanganese crust forms in locations with low sedimentation rates by precipitation mainly of Mn and Fe as oxides, which is a very slow process (Gall et al., 2013). This leads to very low growth rates in the order of mm Myr^{-1}. The ferromanganese crust 237KD with manganese and iron concentrations of ~20 and ~15 %, respectively (Poutivtsev, 2007), has a growth rate of 2.37 mm Myr^{-1} in the relevant time period (<6 Myr) and it was originally assumed to incorporate only a fraction of 0.6 % of iron (Knie et al., 2004).

For validation of the uptake-efficiency of this crust, the ratio of fluences in each archive is evaluated. A half-life corrected fluence of $F_{60,crust,HL}$ = (1.47±0.35)×10^6 ats cm^{-2} in the ferromanganese crust for the layer of 6-8 mm depth was calculated in chapter 3.4.1.
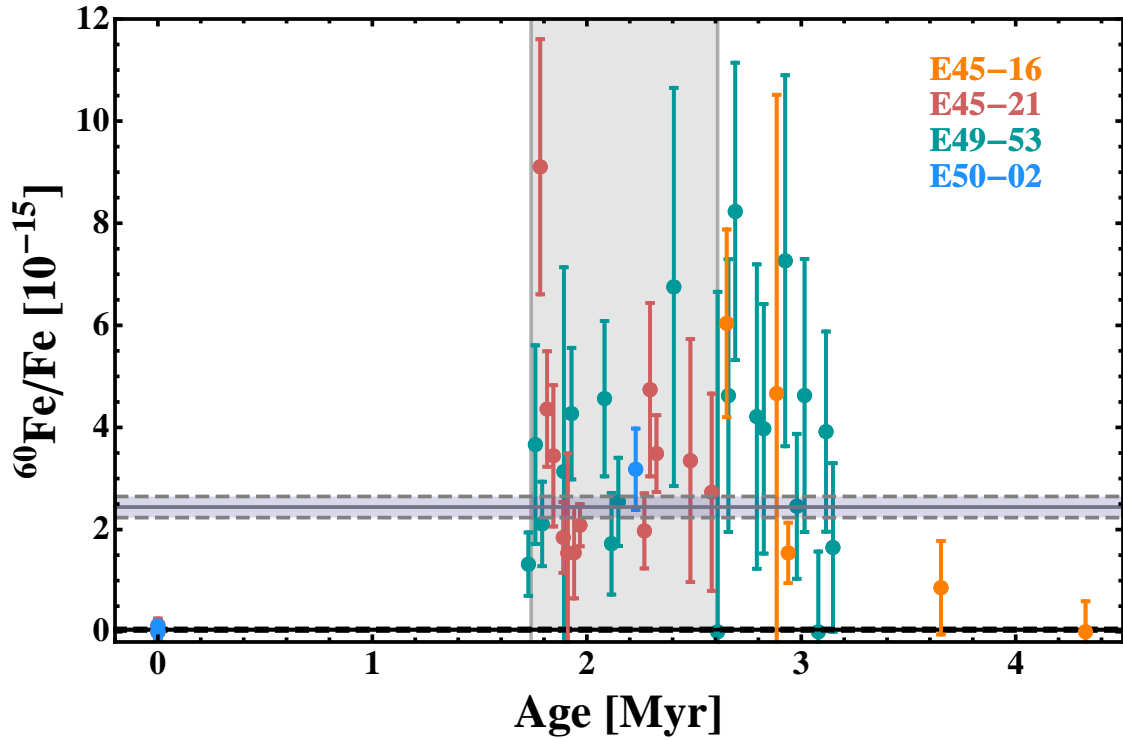
Figure 5.32: Half-life corrected ^{60}Fe/Fe ratios versus age of four marine sediment cores. Values of repeatedly measured targets are averaged (compare with Figure 5.31). A mean of ratios in the peak area yields $(2.44\pm0.21)\times10^{-15}$ and is displayed as the gray ribbon. Two vertical lines filled with gray color indicate the peak region between 6-8 mm in the ferromanganese crust measured by Knie et al. (2004).

Following Knie et al. (2004) the uncertainty consists of the measurement uncertainty (~20 %), the error of the crust's density (5 %), uncertainty of ^{10}Be dating (10 %) and the half-life of ^{60}Fe.

The new results of ^{60}Fe/Fe in the marine sediments were corrected for decay, and are plotted in Figure 5.32. The peak region of 1.74-2.61 Myr in the crust is marked by a gray vertical band. The mean background-corrected value of the signal in the sediments is ^{60}Fe/Fe = $(2.37\pm0.20) \times 10^{-15}$. Calculating individual means of the two cores gives $(2.40\pm0.32) \times 10^{-15}$ and $(2.36\pm0.33) \times 10^{-15}$ for E45-21 and E49-53, respectively.

The ^{60}Fe fluence corrected for the exponential decay of ^{60}Fe (index "HL" for **h**alf-**l**ife) in the sediment is obtained with

$$F_{60,sed,HL} = \overline{C_{Fe}\left(\frac{^{60}Fe}{Fe}\right)} \, \rho_{sed} \, S \, d. \tag{5.7}$$

The mean of the product of ^{60}Fe/Fe (from AMS measurements) and the concentration C_{Fe} of stable Fe (measured with ICP-MS) in each sample considered here gives the concentration of ^{60}Fe (ats g^{-1}). This results in an average concentration $C_{60} = (4.0\pm0.5)\times10^4$ ats g^{-1}. A dry sediment density of $\rho_{sed} = 1.16$ g cm^{-3}, a sediment accumulation rate of S = 0.33 cm kyr^{-1}, and a signal width d = 870 kyr corresponding to the layer of 6-8 mm in the fer-

romanganese crust was used for the comparison with the crust data. Then, the fluence becomes $F_{60,sed,HL} = (1.42\pm0.37)\times10^7$ ats cm^{-2}. The fluence integrated over the whole signal width of d = 1.42 Myr results in a higher value of $F^{tot}_{60,sed,HL} = (2.32\pm0.60)\times10^7$ ats cm^{-2}. The error is composed of the uncertainty in the AMS and ICP-MS measurements and the error of the ^{60}Fe half-life. Further uncertainties originate from the signal width of the ferromanganese crust (10 %, only used for the calculation of $F_{60,sed,HL}$), the accumulation rate of the sediment (8 %) and its density. The latter is the density of the dry material, as the concentrations were determined from weights of samples after drying. Therefore, the assumed wet bulk density estimated in chapter 2.2.1, 1.35 g ($\pm$10 %), was multiplied with the fraction that was left after drying, which is (86$\pm$1) %.

Finally, the uptake-efficiency of the ferromanganese crust 237KD is calculated by determining the ratio of fluences in the crust and the sediments. This yields

$$U_{Fe,crust} = \frac{F_{60,crust,HL}}{F_{60,sed,HL}} \times 100 = (10.3 \pm 3.6) \text{ \%}. \tag{5.8}$$

Fitoussi et al. (2008) suggested an overestimation of the uptake-factor derived from Knie et al. (2004) as one possibility for the "missing" ^{60}Fe signal in an Atlantic ocean sediment. The result obtained here shows that the uptake-efficiency of the crust is $\sim1/10^{th}$ of that of a deep-sea sediment. However, it is not clear, whether indeed 100 % of material entering the Earth are deposited in a deep-sea sediment.

Comparing the fluence deduced from the total measured signal time range of 1.42 Myr with the interstellar fluence of 4×10^7 ats cm^{-2} obtained from lunar samples (Fimiani et al., 2014) results in an uptake-efficiency of the sediment:

$$U_{Fe,sed} = \frac{F^{tot}_{60,sed,HL}}{F_{60,Moon,HL}} \times 100 \geq (58 \pm 15) \text{ \%}. \tag{5.9}$$

The uncertainty arises only from the fluence in the marine sediments as no error was given for the lunar ^{60}Fe fluence by Fimiani et al. (2014). Here, it is indicated that more than half the amount of ^{60}Fe deposited on the lunar surface reaches the Earth and enters the ocean to settle onto the sediment surface. Of course, this value serves as a lower limit, since the full dimension of the peak is not identified yet. Therefore, the ^{60}Fe fluence into the marine sediments might be higher.

5.6.3 Exploring the Shape and Origin of the ^{60}Fe Peak

The obviously large temporal extension of the peak in the *Eltanin* sediment cores is surprising. Nonetheless, it fits to Fitoussi et al. (2008), where a sharp signal was excluded. The average ^{60}Fe/Fe ratio of the marginal signal in a deep-sea sediment found by Fitoussi et al. (2008) was only 3×10^{-16}, an order of magnitude lower than the ^{60}Fe signature detected here. A possible explanation is the 10 times lower sedimentation rate of the Indian Ocean samples analyzed here. The Atlantic Ocean sediments used in Fitoussi et al. (2008) had an accumulation rate of 3 cm kyr^{-1}, the sediments here showed an average

rate of 0.33 cm kyr^{-1}. The chemical leaching method for iron was almost identical in both studies, only the amount of material used for chemistry differs and was compensated by an equally modified amount of leaching solution. Perhaps a dilution effect occurred due to the dissolution of the relatively higher fraction of stable Fe to ^{60}Fe in faster-growing sediments.

For identification of a general trend in the ^{60}Fe data, running means were calculated over the peak area. Such moving averages were calculated for half-life corrected ^{60}Fe/Fe ratios for combined data points of n=2 to n=15. Results for n=5 and n=10 are displayed in Figure 5.33. The plot with n=5 includes the ratios of all measured samples. The full set for all n computed is shown in Appendix I (Figure I.1 and I.2).
For low values of n, one significant peak within the time period of the signal showed up, lying between 2.4-2.8 Myr. Another marginal enhancement is observed at 1.8-1.9 Myr, which is not significant with respect to the counting statistics obtained for each sample and disappears completely for n>10. It seems a relatively sharp increase in the ^{60}Fe/Fe ratio starting less than 3 Myr ago with a slow decrease towards younger ages over 700-800 kyr is visible. Such a time profile of an ^{60}Fe peak in terrestrial archives was suggested by Fry et al. (2014).
These results are compared with running means performed by Fitoussi et al. (2008) (Figure 5.33, lower part). In this paper, a similar, but only marginal general trend is observed with a running mean over data points contained in a time range of 800 kyr. Again, a maximum at 2.6-2.7 Myr is indicated.

Unfortunately the shape of the full signal can not be completely determined due to a lack of samples outside of the peak region towards younger ages. However, it can be compared to the signal found in the ferromanganese crust. Due to similar ^{60}Fe/Fe ratios measured in the two archives no normalization was performed. Figure 5.34 shows mean values of combined data points of each core: each 4 adjacent samples of E49-53 and 3 of E45-21, respectively, were used to calculated mean values. The three data points of E45-16 within the peak area as well as the two samples located at higher ages of 3.7 and 4.3 Myr were combined. Of E50-02 only one sample was measured in the peak area. The data obtained matches very well the ^{60}Fe/Fe result in the ferromanganese crust from Knie et al. (2004) and Fitoussi et al. (2008). The crust sample measured by Fitoussi et al. (2008) with a mean width of ~1.3 Myr indicates that the signal is extended towards younger ages. However, the measurement of ^{60}Fe/Fe were performed at the same crust as used by Knie et al. (2004). It is possible, that the ages obtained by Fitoussi et al. (2008) of the crust layers are shifted towards younger ages. Due to the very small layers of 2 mm, a systematic time shift may have occurred in the dating procedure. To study the true extension of the signal, samples from the "missing" time ranges should be analyzed in the future.

The question remains why is this peak is extended to a width of more than 1.4 Myr. From the sediment data in Figure 5.33 it seems that most of the ^{60}Fe arrived between 2.4 and 2.8 Myr. The estimated fluence of $(2.32\pm0.60)\times10^7$ ats cm^{-2} is compatible with values listed in table 3.6 in chapter 3.4.2 for the ejection of 10^{-5} M$_\odot$ ^{60}Fe of a single SN at a
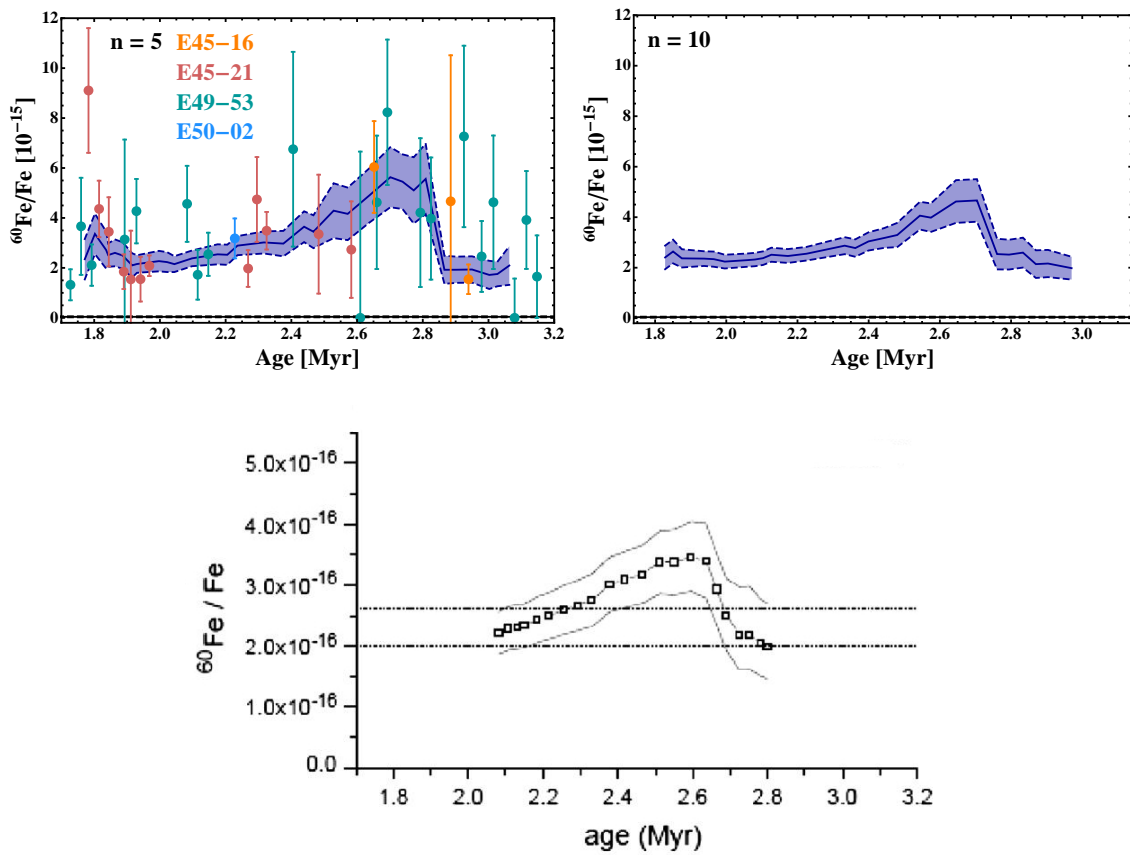
Figure 5.33: Top: Moving averages of combined ^{60}Fe/Fe data points with n=5 and n=10 (number of data points combined) in the peak area. In addition the individual measured ^{60}Fe/Fe results for each sample are shown in the left figure. **Bottom:** Running means over a 800 kyr time interval of an Atlantic Ocean sediment published by Fitoussi et al. (2008), which seems to indicates a similar trend as the signal found in the *Eltanin* sediments from the Indian Ocean used in this work.

distance of 90 pc. But, as indicated by Fitoussi et al. (2008), and as calculated in section 3.3, a signal of one SN should be much narrower. In the SN input calculations losses for instance due to the transport in dust grains into the solar system, diffusion from the expanding SN shell as well as the possibility of clumpy ejecta were not included.

The findings in this work seem to corroborate the theory of multiple SNe producing a broad signal as demonstrated by Feige (2010). The stellar moving group believed to have formed the LB approached the solar system within the last 14 Myr and the closest trajectory had its least distant point around 2.2 Myr ago. In Feige (2010) not only the peak, but the whole shape of the ^{60}Fe/Fe signal in the crust was modeled. Still, the time intervals between individual explosions are on average around 0.5-1 Myr. The exposure time of the Earth to an arriving SN shell was calculated to be of ~100 kyr. With the time resolution obtained in the analyzed sediments it should be possible to resolve individual SNe. This does not seem to be the case. However, processes leading to a broadening of a signal such as material being ejected in clumps rather then in a homogeneous shell around the explosion were discussed in section 3.3.
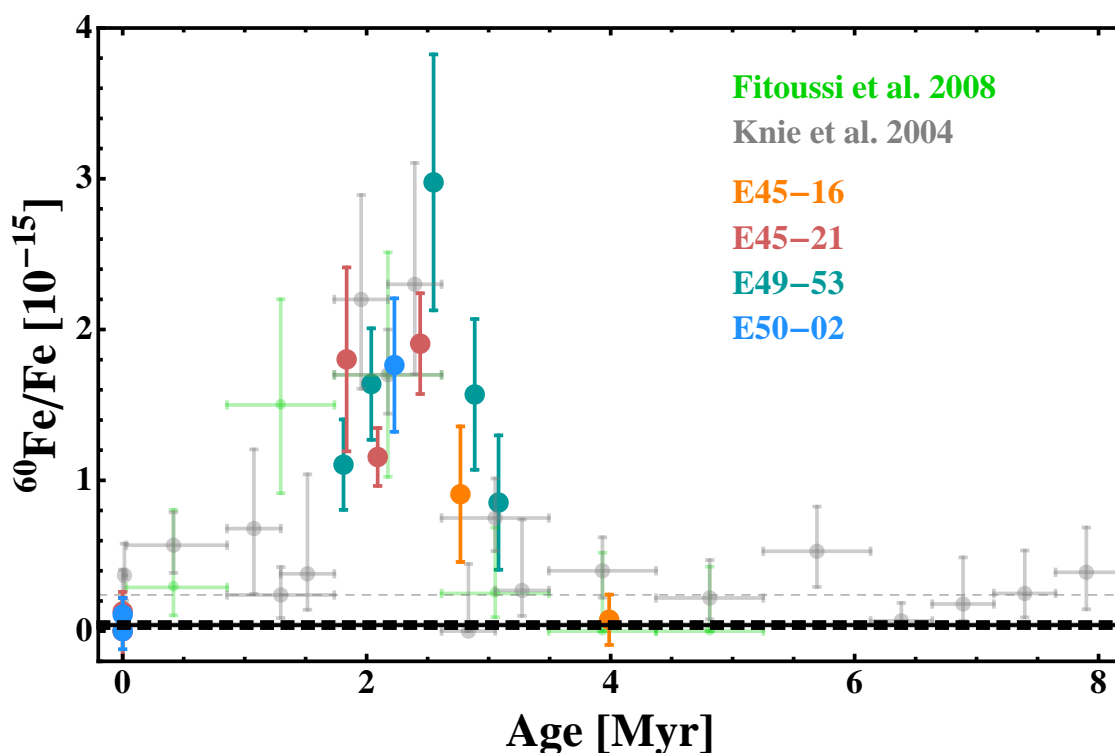
Figure 5.34: Comparison of the data obtained from the *Eltanin* deep-sea sediment samples with ferromanganese crust measurements from Knie et al. (2004) and Fitoussi et al. (2008). Data points of sediment samples were combined: each 4 adjacent samples of E49-53 and 3 of E45-21, respectively. Three data points of E45-16 within the peak area as well as the two samples located at higher ages of 3.7 and 4.3 Myr were combined. One sample of E50-02 was measured in the peak area.

An alternative solution would be the shell of the LB overrunning the solar system at 2-3 Myr ago. This could explain a broad peak as the LB shell consists of accumulated multi-SN ejecta and swept-up ISM. As SN activity within the LB was still ongoing until about 0.5 Myr ago (Fuchs et al., 2006), one or more single SNR should have followed at younger ages leaving a smaller signature than the LB shell.

5.6.4 Search for the ^{26}Al Signal and Constraints on ^{60}Fe/^{26}Al Nucleosynthesis Models

Figures 5.22 and 5.23 (section 5.5) evaluated long-term fluctuations of ^{26}Al/^{27}Al around the mean value. Moving averages showed fluctuations, which are partly reflected in the ^{10}Be/^{9}Be data. Small maxima of ^{26}Al seem to occur at roughly 1.9 Myr (E45-21 and E49-53) and 2.3 Myr (E45-21). The local ^{60}Fe maximum within the total range of the signal was located between 2.4 and 2.8 Myr (Figure 5.33). This does not coincide with the maxima found in the ^{26}Al data. For further conclusions the total influx of ^{60}Fe from a SN into the deep-sea sediments is compared to a possible influx of ^{26}Al.

To estimate the possibility of observing an enhancement in the ^{26}Al/^{27}Al ratio due to an extraterrestrial SN input, different stellar ^{60}Fe/^{26}Al ratios were used. Although the shape of the ^{60}Fe/Fe signal seems asymmetric (a faster increase than decrease of the ^{60}Fe/Fe ratio towards younger ages), it is approximated by a gaussian shape for simplification. Figure 5.35 displays again the data measured in the ferromanganese crust and the combined sediment data from Figure 5.34. Furthermore, some gaussian distributions are plotted with different widths, all having the same area under the curve. The mean value of the gaussian distribution was set to 2.5 Myr. The curves' maximum shifts towards younger ages when exponential decay of ^{60}Fe is included for the calculation of the gaussian distribution (equation (3.29)).

In order to translate the input of ^{60}Fe to a corresponding SN input of ^{26}Al, three cases of stellar ^{60}Fe/^{26}Al ratios were considered. In chapter 3 it was indicated, that these ratios might vary between 0.02 and 2. Here the values 1, 0.5, and 0.1 are used. The resulting gaussian function is added to an exponential decay function with an initial value of ^{26}Al/^{27}Al = 2.56×10^{-13}, as inferred in section 5.5. The results are illustrated in Figure 5.36. On the left the total measured range of 0-4.5 Myr is displayed, FWHM between 0.117 and 2.35 Myr were plotted. The right part shows a zoom into the major sampling section. Here, only FWHM are displayed with maxima between 20-30 % above the background.
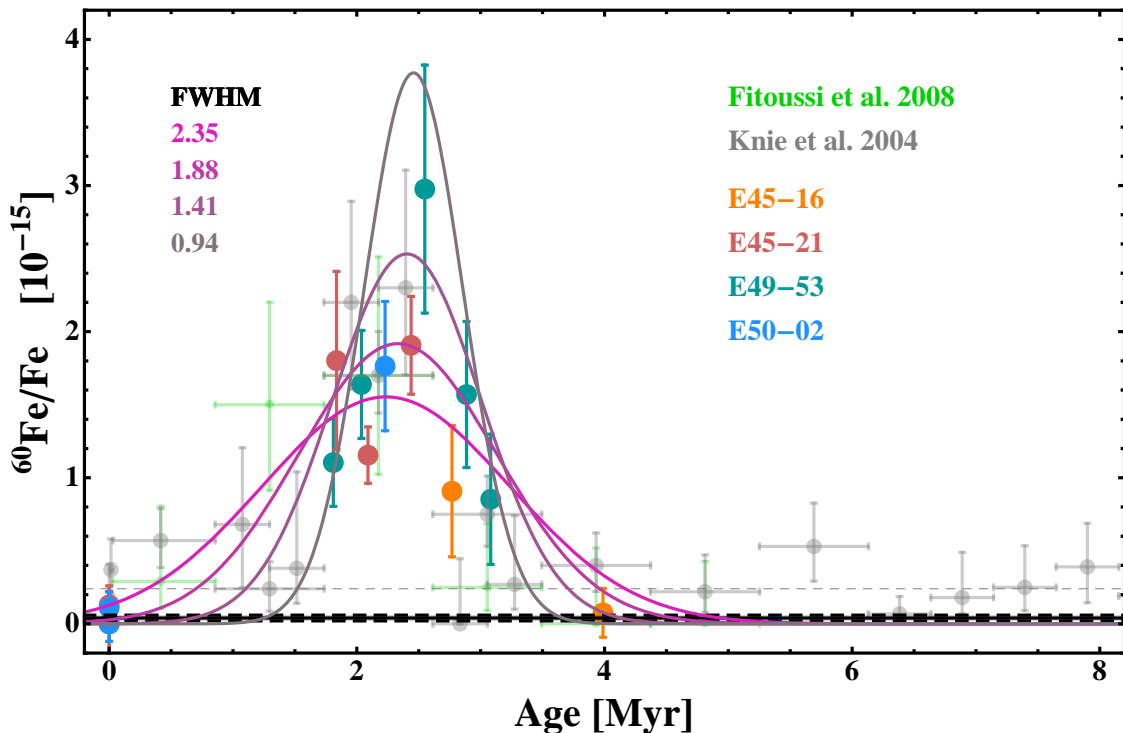
Figure 5.35: Same figure as 5.34 with gaussian distributions of different FWHM. The integration over the gaussian distribution yields the estimated total fluence of 2.32×10^7 ats cm^{-2}.
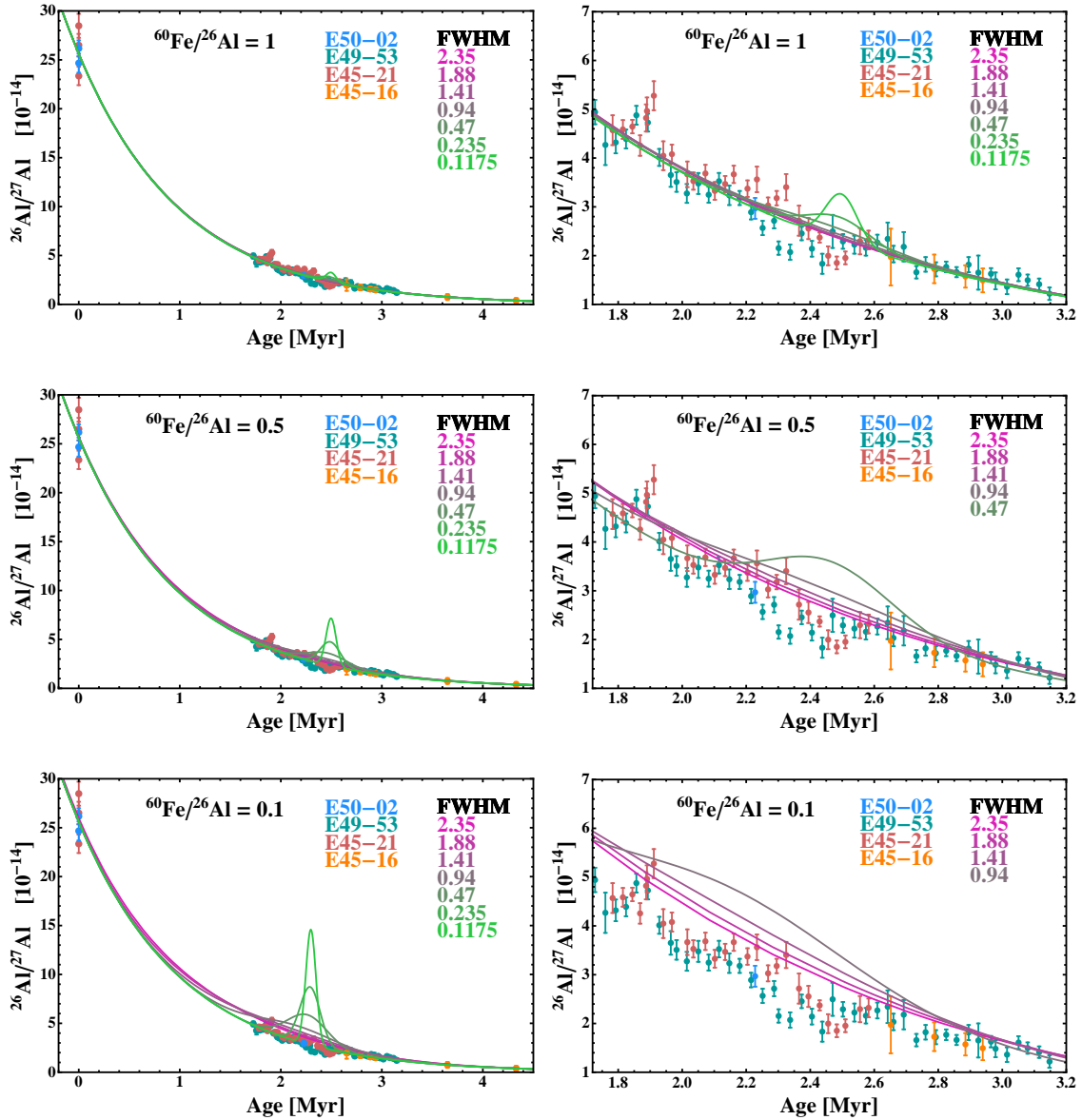
Figure 5.36: The area under the gaussian curves fitting the ^{60}Fe/Fe data in Figure 5.35 is translated to an ^{26}Al/^{27}Al signal, which is added to terrestrial background. ^{60}Fe/^{26}Al ratios of 1, 0.5, and 0.1 from nucleosynthesis models are used for conversion. The left part displayed the whole analyzed time range of 0-4.5 Myr. The right part zooms into the region of 1.7-3.2 Myr.

The upper plots with a ratio of ^{60}Fe/^{26}Al=1 display the lowest possible influx of ^{26}Al of the three cases considered. The left part indicates almost no change of the exponential decay curve due to an additional SN source. An increase might be observed in signals narrower than FWHM=117 kyr, which is the highest signal shown in Figure 5.36 (upper part) and just disappears within the scattering of the ^{26}Al/^{27}Al data. The maximum of the signal with FWHM=117 kyr is ~30 % above the background.

The middle part of Figure 5.36 displays results for ^{60}Fe/^{26}Al=0.5. Here, signals with

widths narrower than 470 kyr would be visible above the background. Its maximum exceeds the background by almost 40 %. However, from Figure 5.35 it is inferred that the total width should be at least around one Myr, possibly more, to reproduce the ^{60}Fe signal. If the signal is spread over a large time range of one Myr, the ^{26}Al signal is observed rather as an offset of the data to the atmospheric ratio in the time range between 1.7 and 3.2 Myr (compare with the left part of Figure 5.36, where a larger time region of 0-4.5 Myr is shown). For a signal with a FWHM of 0.94 Myr, an offset of roughly 8 % at 2.5 Myr is indicated to the expected exponential decay function from atmospheric production of ^{26}Al. Such an offset could not be observed in the measured data.

For an even smaller ratio of ^{60}Fe/^{26}Al=0.1 (lower part of Figure 5.35) this offset becomes larger with ~17 % at 2.5 Myr. It is obvious, that the modeled curves do not represent the data set within the peak range although the surface ratios are in agreement with the model.

Two conclusions are drawn from these considerations. First, constraints on nucleosynthesis ratios of ^{60}Fe/^{26}Al in massive stars can be inferred. A broad peak is observed in the ^{60}Fe distribution, a peak of the same width would be expected in the ^{26}Al data. However, with ratios of ^{60}Fe/^{26}Al of 0.5 and 0.1 the ^{26}Al/^{27}Al data can not be represented with the model, whereas the ratio 1 is compatible with the measured curve. These results suggest, that the ejected ratio of ^{60}Fe/^{26}Al in SN explosions is higher than 0.5. An isotopic ratio of ^{60}Fe/^{26}Al is converted to a γ-ray flux ratio by

$$\left(\frac{^{60}\text{Fe}}{^{26}\text{Al}}\right)_{\gamma} = \left(\frac{^{60}\text{Fe}}{^{26}\text{Al}}\right) \times \frac{t_{1/2,26}}{t_{1/2,60}}, \qquad (5.10)$$

where $t_{1/2,26}$ and $t_{1/2,60}$ are the half-lifes of ^{26}Al and ^{60}Fe, respectively. For ^{60}Fe/^{26}Al = 0.5, a γ-ray flux ratio of $(^{60}$Fe/^{26}Al$)_{\gamma}$ = 0.14 is calculated, for ^{60}Fe/^{26}Al = 1, $(^{60}$Fe/^{26}Al$)_{\gamma}$ = 0.28. The obtained flux ratio agrees with observational data of ^{26}Al and ^{60}Fe present in the ISM, with $(^{60}$Fe/^{26}Al$)_{\gamma,\text{obs}}$ = (0.15±0.05) (Wang, 2008) for an iotopic SN ratio of ^{60}Fe/^{26}Al = 0.5 and higher. An isotope ratio of ^{60}Fe/^{26}Al = 1 might be too high to represent the measured flux ratio. The γ-ray flux ratio of ^{60}Fe/^{26}Al obtained from observations includes not only ^{26}Al and ^{60}Fe ejected in SNe explosion, but also the contribution from lower mass stars. AGB- and SAGB-stars are producers of ^{26}Al and ^{60}Fe. Theoretical isotope ratios were calculated to ^{60}Fe/^{26}Al $\geq$ 1 (e.g. Lugaro and Karakas (2008); Doherty et al. (2014)), which is also higher than the observed γ-ray flux ratio. However, as pointed out by Diehl et al. (2011), there are uncertainties in the γ-ray telescope analysis as well as in the nuclear physics involved for nucleosynthesis calculations.

The second conclusion can be drawn by concentrating on the upper part of Figure 5.36. It was already mentioned, the only signature visible would be a narrow signal with FWHM $\leq$117 kyr. However, as the signal is expected to be broader from the ^{60}Fe/Fe data, a possible SN input of ^{26}Al is hidden within the large background.

5.6.5 ^{60}Fe and Micrometeorites

A alternative explanation contrasting the assumption of the ^{60}Fe signal due to a nearby SN was presented by Basu et al. (2007) and Stuart and Lee (2012). They state, that ^{60}Fe may have been transported to Earth by MMs, which are not of interstellar origin. In chapter 3.1.3.2 it was pointed out, that there might be a chance of constant extraterrestrial influx from debris of asteroid surfaces. ^{60}Fe might be produced and transported in interplanetary IDPs and MMs. In these targets ^{60}Fe is produced on ^{62}Ni and ^{64}Ni by cosmic rays (Knie et al., 1999b).

Leaching experiments performed by S. Merchel (private communication) on iron and stony meteorites with 0.04 M $NH_2OH \cdot HCl$ in 25% (V/V) acetic acid indicate that the iron meteorite is fully dissolved. Of the stony meteorite a residue of negligible fraction is left over. Assuming all Ni dissolved in the sediment samples originates from MM and IDP input, the amount of expected ^{60}Fe can be estimated in a simple calculation:
On average, the dissolved amount of Ni was (40.4±3.6) µg per g sample material in the *Eltanin* sediment samples, excluding surface and old samples (determined with ICP-MS measurements). A theoretical amount of ^{60}Fe produced in IDPs and MMs was published by Trappitsch and Leya (2013) with a value of 0.51 dpm kg^{-1} Ni. Then the concentration of ^{60}Fe in a sediment sample is

$$C_{60} = \frac{0.51 \times 40.4}{10^9 \lambda_{60}} = 40\,778 \text{ ats g}^{-1}. \tag{5.11}$$

The decay constant is given in units of minutes, which yields $\lambda_{60} = 5.05 \times 10^{-13}$ min^{-1}, the factor 10^9 converts µg to kg. This result is close to the measured weighted average value of $(40\pm5) \times 10^{-3}$ ats g^{-1} calculated in section 5.6.2 and agrees with a MM origin of ^{60}Fe.

Two reasons still argue against interplanetary MM and IDP input. First, it is unlikely that the total amount of nickel dissolved is of extraterrestrial origin. The leaching method applied always dissolved a detrital component. This is demonstrated when comparing the ^{60}Fe/Fe isotope ratios obtained in this work to the low measured ratios in the sediment samples from Fitoussi et al. (2008). As discussed earlier, the growth rate was 10 times larger in the Atlantic sediments, which yielded 10 times ^{60}Fe/Fe lower ratios.
Secondly, if the ^{60}Fe influx originated from interplanetary particles, one would expect a continuous background and not a temporally limited enhancement. However, at the surface and in the 3.6 and 4.3 Myr old samples no significant enhancement was observed. The Ni content in these samples, with (34.7±3.1) µg/g, agrees with the samples from the time range of the ^{60}Fe signal. This Ni concentration corresponds to a concentration of $(35\pm3) \times 10^{-3}$ ats g^{-1} ^{60}Fe produced via cosmic rays in MMs. As no ^{60}Fe was detected in the samples outside the time region of the ^{60}Fe peak, it is indicated that MMs and IDPs do not seem to deposit a detectable amount of ^{60}Fe on Earth.

Another explanation for an enhancement of ^{60}Fe could be an impact of a larger object, where, due to ablation when entering the Earths atmosphere, ^{60}Fe is released and buried on the Earths surface. In fact, there was an impact (2.51±0.07) Myr ago of an asteroid with the suitable name *Eltanin* (e.g. Goff et al. (2012)). An object with the size of 1-2 km fell into the Pacific Ocean SSW of Chile (Shuvalov and Gersonde, 2014). The possibility of depositing long-lived radionuclides by impacts was pointed out by Overholt and Melott (2013). However, it seems that the time of the impact is too early and there is no obvious reason why fractions of this object should be deposited over a time range of more than 1 Myr rather than within a few kyr as expected from the residence and mixing time scales of radionuclides in atmosphere and ocean.

Nevertheless, the SN and the MM theories do not necessarily have to exclude each other. As was pointed out in chapter 3.2, the SN radionuclides are most likely to arrive on Earth incorporated into dust grains. A fraction of the grains will be ablated when entering the Earths atmosphere releasing also the long-lived isotopes ^{26}Al, ^{53}Mn, and ^{60}Fe. The other fraction will be deposited almost unaltered as interstellar dust or MM grains amongst their interplanetary counterparts, waiting for their history to be unraveled.

6 Conclusions

In this final sections a summary of this work including the results and their interpretation is presented. This is followed by a brief overview of impacts of nearby SN explosions for the Earth's history.

6.1 Summary

This interdisciplinary work explored the deposition of extraterrestrial material, most likely due to a SN in the solar vicinity, into deep-sea sediments. A hint to recent SN activity is the existence of a superbubble in which the solar system is embedded. This large cavity in the local ISM, called the Local Bubble, was presumably produced by multiple SN explosions in a stellar moving group passing the solar system close enough to leave traces on Earth (Breitschwerdt et al., 2012) and possibly on the Moon (Fimiani et al., 2014).

For this work, deep-sea sediments allowing for a high time resolution were chosen for the detection of SN-produced radionuclides. A measurement of ^{60}Fe in a ferromanganese crust (Knie et al., 2004) indicated, that a nearby SN to the Solar System might have occurred approximately 2-3 Myr ago. More than 100 samples of four marine sediments from the Indian Ocean including not only the time period of the ^{60}Fe signal found in the ferromanganese crust, but also surface samples (corresponding to the present time) and older samples of 3.6 and 4.5 Myr, were analyzed. The search for ^{60}Fe was complemented by two other interesting long-lived radionuclides generated in massive stars, ^{26}Al and ^{53}Mn. All these radionuclides have half-lifes in the order of Myr, which coincides with the age of the signal in the crust and are therefore suitable candidate isotopes. In addition, ^{10}Be was extracted to serve as a dating tool. All samples were already pre-dated with magnetostratigraphy and partly with biostratigraphy.

The transport of radionuclides to Earth was discussed. It was concluded, that incorporation in dust grains within an expanding SN shell is the most likely scenario to overcome the ram pressure of the heliosphere. Estimations were made to infer intensities of expected signals of the analyzed radionuclides using different nucleosynthesis models and signal width. In addition, possible background production interfering with a SN signal was explored with special focus on ^{26}Al, as a variety of background sources contributed to a signal for this radionuclide. It became clear, that particularly broad signals (FHWM $\geq \sim$500 kyr) of ^{26}Al and ^{53}Mn might be hard to detect within a high terrestrial and extraterrestrial background.

The samples were chemically prepared using a leaching solution to extract largely authigenic matter, for example soluble iron-(oxyhydr)oxides or particles attached onto dust or

141

aerosol particles in order to decrease the dilution effect from stable isotopes. First tests of the chemical procedure showed, that the originally chosen amount of initial sample material of 1 g did not yield sufficient target material. For this reason the initial sample mass was increased to 3 g and the chemical method had to be adapted accordingly. The radionuclides extracted from the deep-sea sediment samples were measured at three different AMS facilities: ^{26}Al at VERA (Vienna) and ^{10}Be at VERA and DREAMS (Dresden). The heavier nuclides ^{53}Mn and ^{60}Fe, requiring higher particle energies to separate interfering stable isobars, were measured at the HIAF facility (ANU, Canberra). Two ^{60}Fe targets were analyzed at the AMS facility of the TUM. Concentrations of stable isotopes were measured with ICP-MS and AAS at HZDR, Dresden, and CEREGE, France.

The results are summarized below:

^{10}Be was analyzed at two different facilities, the Vienna Environmental Research Accelerator (VERA) and the Dresden AMS (DREAMS) laboratory (chapter 5.1). Beryllium targets were split into two to obtain comparable measurement ratios of ^{10}Be/^{9}Be. The data are in good agreement with each other (61 % of data coincided within 1 σ).

The ^{10}Be/^{9}Be ratios measured with AMS include the amount of carrier that was added to the samples during the chemical procedure. To calculate the intrinsic ^{10}Be/^{9}Be ratio (corresponding to the natural amount of ^{9}Be) in the deep-sea sediment samples, the ^{9}Be content was measured independently via ICP-MS. Complications arising in these ^{9}Be isotope measurements were discussed and several large corrections had to be made to correct some systematic deviations between measurement batches.

The measurement efficiency for ^{26}Al from the deep-sea sediment samples at VERA was examined. The efficiencies were found lower than previous measurements by Auer et al. (2007), but fit to the values reported by Arazi et al. (2006) (chapter 5.2).

^{53}Mn/^{55}Mn test measurements were performed during this work. The stable isobar to ^{53}Mn, ^{53}Cr, was not suppressed sufficiently during the chemical preparation procedure. Therefore, the stable isobar interfered with the low amounts of ^{53}Mn during the AMS measurements at HIAF, Canberra. The chromium content within these samples will have to be reduced in additional chemistry steps. This will be subject for future projects. Successful measurements were carried out for ^{60}Fe at the HIAF facility (chapter 5.3).

Dating of the marine sediment was carried out using the two radionuclides ^{10}Be and ^{26}Al, and linked to the magnetostratigraphic chronology. ^{10}Be/^{9}Be surface ratios suffered from wrong ICP-MS measurements. Dating with ^{26}Al resulted in lower uncertainties and was applied to all sediment samples. In fact, this is the first time that such a detailed profile of ^{26}Al/^{27}Al in deep-sea sediment cores was measured with typical uncertainties of 5-10 %. For the sediments used in this work, ^{26}Al seems to be a suitable dating tool (chapter 5.4). Subsequently, the possibility of using the ^{26}Al/^{10}Be ratio as a dating tool was addressed (chapter 5.5). It is known that normalization to the stable isotope such as ^{10}Be/^{9}Be and ^{26}Al/^{27}Al accounts for fractionation effects, therefore, these ratios are used for dating. This is not the case for radioisotopic ratios. Fractionation depends e.g. on the sediment composition and was verified by a strong correlation with the carbonate content in the *Eltanin* samples. Nevertheless, an estimation of ^{26}Al/^{10}Be was calculated and found to be comparable to the atmospheric value reported in Auer et al. (2009). This suggests,

that most of the ^{26}Al measured within the deep-sea sediment originates from atmospheric production. An additional contribution from in-situ production was not detected in this work. Sediment samples with higher age, where ^{26}Al is expected to have decayed, should be measured in the future to investigate the amount of in-situ produced ^{26}Al.

Finally, results for ^{26}Al and ^{60}Fe in the deep-sea sediments were evaluated in a SN context (chapter 5.6). A clear signal of ^{60}Fe was observed throughout the sediment sections between 1.7 and 3.1 Myr for all *Eltanin* samples. An ^{60}Fe fluence was derived and the uptake factor of ^{60}Fe into the ferromanganese crust 237KD was recalculated with a value of ~10 %. It differs from the previous value of 0.6 % (Knie et al., 2004) by more than an order of magnitude. The shape of the ^{60}Fe distribution in the sediments seems to indicate that the influx of ^{60}Fe started to increase sharply at ~3 Myr, than decreased towards younger ages over 700-800 kyr, with a maximum between 2.4 and 2.8 Myr. The large width of the signal can not be explained by an individual SN, rather pointing towards an accumulation of SNe, either as a sequence of multiple SNe reaching the Earth successively or in form of one large shell carrying debris of multiple SNe; the LB shell.

As expected for a low-intensity broad extraterrestrial signal of ^{26}Al, this is hidden within a large terrestrial background. Limits of the ^{26}Al/^{60}Fe ratio ejected in a SN were studied and the results reveal a ratio higher than 0.5 in order to reproduce the measured ^{26}Al/^{27}Al profile. This isotope ratio translates into a γ-ray flux ratio of $(^{60}\text{Fe}/^{26}\text{Al})_\gamma \geq 0.14$.

MMs as carrier of radionuclides are a possible explanation if they arrive in a defined time range only. A recent input from IDPs and MMs can be excluded as no ^{60}Fe is determined in surface samples. However, it is likely that the SN-produced radionuclides are transported to Earth within dust grains. These might survive their journey from the site of the SN and be deposited as interstellar dust in terrestrial archives.

Although the signal detected in the ferromanganese crust (Knie et al., 2004) is finally confirmed and resolved, there is still potential for further exploration of this subject. The extension of the ^{60}Fe peak in time should be constrained in more detail. In this work, no sediment samples between recent age (from the sediment's surface) and 1.7 Myr were measured. The link to the LB is still not clear, as the question remains whether the whole superbubble shell or individual SNe caused a signature. Another issue is of course the role of dust and MMs and how long-lived radionuclides are deposited eventually. These and many other questions remain still unsolved and should be further investigated in the future.

6.2 Impact on the Earths History

Whether a nearby SN can be detected by effects other than depositions of long-lived radionuclides is an unsolved question. Of course, the degree of an impact depends on the distance of the explosion to the solar system. Gehrels et al. (2003) state, that a SN occurring less than 8 pc would reduce the amount of ozone in the Earth's atmosphere by a factor of two due to interactions of incident γ- and cosmic rays. This would double the UV flux, that reaches the Earth's surface, which is a threshold for causing serious

biological damage. A similar critical distance for serious destruction of the biosphere is given by Beech (2011) with a distance of 10 pc.

However, the SN explosions presumably originated from a stellar moving group that now belongs to the Sco-Cen association (Fuchs et al., 2006). Their distances at 2-3 Myr, with approximately 90-100 pc, were far off the Solar System. SN sites further away than 15-30 pc seem to cause essentially no radiation damage on the Earth's biosphere (Beech, 2011). Benítez et al. (2002) suggested a SN might have been as close as 40 pc. According to this study a minor extinction could have happened, where mostly the marine ecosystem is affected. The amount of phytoplankton might be reduced, propagating to the upper species in the food chain such as zooplankton, foraminifera, and mollusks.

Gehrels et al. (2003) proposed that at a distance of 40 pc only a few percent of the atmospheres' ozone would be destroyed. Nevertheless, the authors did not draw any conclusions about the impact of cumulative SNe. However, the center of the stellar moving group, that presumably formed the LB, was located around 90-100 pc (Benítez et al., 2002) from the Solar System. This is more than twice the distance of 40 pc. Therefore it is not clear, whether the cosmic ray flux from one or more SN might have influenced the biosphere.

Extinctions of organisms were observed at the transition of the Plio- to Pleistocene, between 2.6 and 2.9 Myr, as well as 1.6-1.9 Myr ago (deMenocal, 2011). Surprisingly this coincides with the large enhancement of ^{60}Fe at 2.4-2.8 Myr within the global peak region, as well as with the marginal increase at 1.8-1.9 Myr. A decline of mollusks diversity was then seen in tropical areas, where the solar angle is high (e.g. Petuch (1995)). The transition coincides with a magnetic field change at the Matuyama-Gauss boundary, roughly 2.6 Myr ago, which would facilitate an enhanced cosmic rays flux to enter the atmosphere and damage the ozone layer.

A more spectacular assumption is that a change of climate due to enhanced cosmic rays flux could have influenced the developments in mankind (e.g. Knie et al. (2004)). Indeed, at 2.9 Myr the *Australopithecus afarensis* "Lucy" became extinct, at 2.7 Myr the australopiths (*Paranthropus spp.*) emerged and the species Homo evolved some time after 2.6 Myr. The second time period mentioned, 1.6-1.9 Myr, includes further evolution of the human species to *Homo erectus* and development of stone tools (deMenocal, 2011).

APPENDIX A Positions of Selected Sediment Cores

Figure A.1: Locations of deep-sea sediments that were analyzed for isotope anomalies, recovered by the research vessel *Eltanin*. They are located approximately 1000 km southwest of Australia. Courtesy of Google Maps (maps.google.com).

APPENDIX B Core Descriptions

B.1 Sediment Classifications

Table B.1: Characteristics of *Eltanin* cores in depths of samples available as described by Frakes (1971) (E45-16 and E45-21) and Frakes (1973) (E49-53 and E50-02). Lithology such as mud and ooze is listed first, followed by composition such as content of foraminfera or radiolaria ordered by relative abundance. If separated by a dash, such as foraminifera-radiolaria an equal amount of the two are indicated.

Cruise	Depth (cm)	Lithology and Composition
E45-16	3-132	mud, radiolaria, foraminifers
E45-16	132-204	mud, foraminifers, radiolaria
E45-16	204-245	mud, radiolaria-foraminifers
E45-16	245-345	mud
E45-16	345-362	mud, sandy
E45-16	362-398	mud, ashy-foraminfers
E45-21	0-27	ooze, foraminifera, radiolaria
E45-21	200-508	mud, foraminifera, radiolaria
E45-21	508-630	mud, foraminifera-radiolaria, diatoms, spicules
E45-21	630-774	mud, foraminifera, radiolaria, diatoms
E49-53	100-220	ooze, foraminifera, spines
E49-53	220-280	ooze, foraminifera, muddy, spines
E49-53	280-328	ooze, foraminifera, spines
E49-53	328-410	ooze, foraminifera, nannofossils, spines, spicules
E49-53	410-420	ooze, foraminifera, muddy
E49.53	420-444	ooze, foraminifera, muddy, spines
E49-53	444-496	ooze, foraminifera, muddy, spines
E49-53	496-593	mud and ooze, foraminifera
E50-02	0-16	mud, foraminifera
E50-02	847-879	mud, radiolaria

B.2 Further Information on the *Eltanin* Sediment Samples

The tables below contain information on samples of *Eltanin* cores 45-16, 45-21, 49-53, and 50-02. The data is sorted by depth below sediment surface. The top and bottom positions of samples below the sea floor are listed. All samples were chemically prepared with exceptions of numbers 86 and 88 (E45-21) and numbers 78 and 80 (E50-02).

Table B.2: *Eltanin* samples of core E45-16 sorted by depth below sediment surface (top and bottom). All samples were chemically prepared. The column "Batch" refers to the chemistry batch. The comments contain age information provided by the ARF.

Cruise	Number	Batch	Top (cm)	Bottom (cm)	ARF Age
E45-16	72	15	130	131	~2 Myr
E45-16	73	15	135	136	~2 Myr
E45-16	74	15	229	230	~4.5 Myr
E45-16	75	15	234	235	~4.5 Myr
E45-16	76	15	375	376	~25 Myr
E45-16	77	15	385	386	~25 Myr

Table B.3: *Eltanin* samples of core E45-21 sorted by depth below sediment surface (top and bottom). All samples were chemically prepared with the exception of numbers 86 and 88. The column "Batch" refers to the chemistry batch. The comments contain information provided by ARF. "MN" denotes **M**anganese **N**odule.

Cruise	Number	Batch	Top (cm)	Bottom (cm)	Comment (ARF)
E45-21	85	16	0	1	surface
E45-21	83	16	6	7	surface
E45-21	84	16	9	10	surface
E45-21	86	16	9	10	surface, MN
E45-21	46	8	398	399	
E45-21	47	8	410	411	
E45-21	48	2, 13	421	422	
E45-21	49	8,13	430	431	
E45-21	89	16	437	438	archive
E45-21	87	16	438	439	
E45-21	88		439	440	archive, 420-430 cm
E45-21	50	8	446	447	
E45-21	51	3, 13	457	458	
E45-21	52	8, 13	467	468	
E45-21	53	8, 13	485	486	
E45-21	54	2, 13	492	493	
E45-21	55	8, 14	506	507	
E45-21	56	10	517	518	
E45-21	57	10	529	530	
E45-21	58	11, 14	539	540	
E45-21	59	11	555	556	
E45-21	60	11	566	567	
E45-21	61	3	579	580	
E45-21	62	4	589	590	
E45-21	63	11	600	601	
E45-21	64	11	615	616	
E45-21	65	11, 14	626	627	
E45-21	66	11, 14	639	640	
E45-21	67	12	649	650	
E45-21	68	1, 2, 3, 4, 14	659	660	
E45-21	69	12, 13, 14	669	670	
E45-21	70	12	686	687	
E45-21	71	4, 14	696	697	

Table B.4: *Eltanin* samples of core E49-53 sorted by depth below sediment surface (top and bottom). All samples were chemically prepared. The column "Batch" refers to the chemistry batch.

Cruise	Number	Batch	Top (cm)	Bottom (cm)
E49-53	1	5	120	121
E49-53	2	2	129	130
E49-53	3	5	138	139
E49-53	4	5	147	148
E49-53	5	3	156	157
E49-53	6	5	166	167
E49-53	7	5, L	176	177
E49-53	8	4	186	187
E49-53	9	5	191	192
E49-53	10	1, 5	200	201
E49-53	11	6, L	210	211
E49-53	12	6	219	220
E49-53	13	6	228	229
E49-53	14	6	237	238
E49-53	15	4	246	247
E49-53	16	6	256	257
E49-53	17	6	266	267
E49-53	18	6	276	277
E49-53	19	7	280	281
E49-53	20	7	290	291
E49-53	21	2, 12	300	301
E49-53	22	3	309	310
E49-53	23	7	318	319
E49-53	24	7	327	328
E49-53	25	4	336	337
E49-53	26	7	346	347
E49-53	27	7	356	357
E49-53	28	7	366	367
E49-53	29	9	375	376
E49-53	30	3, 12	380	381
E49-53	31	9	389	390
E49-53	32	2, 12	400	401
E49-53	33	9	408	409
E49-53	34	1, 9	417	418
E49-53	35	4	426	427
E49-53	36	9	435	436
E49-53	37	9	445.5	446.5
E49-53	38	9	454	455
E49-53	39	2, 12	465	466
E49-53	40	1, 10	469	470
E49-53	41	10	479	480
E49-53	42	3	489	490
E49-53	43	10	497	498
E49-53	44	10	507	508
E49-53	45	10	516	517

Table B.5: *Eltanin* samples of core E50-02 sorted by depth below sediment surface (top and bottom). All samples, except numbers 78 and 80, were chemically prepared. The column "Batch" refers to the chemistry batch. The comments contain age information provided by ARF.

Cruise	Number	Batch	Top (cm)	Bottom (cm)	Comment (ARF)
E50-02	81	16	4	5	surface sample
E50-02	80		9	10	surface sample
E50-02	82	16	12	13	surface sample
E50-02	79	15	847	848	~3-5 Myr
E50-02	78		853	854	~3-5 Myr

APPENDIX C α-Energies and Cross Sections

C.1 α-Energies of the Radium- and Thorium Decay Series

Table C.1: Energies of α-particles produced by radioactive decays in the radium decay series of the corresponding mother isotopes and probability fraction of ^{26}Al produced via the ^{23}Na$(\alpha,n)^{26}$Al reaction with α's of corresponding energies. Weighted mean energies were calculated from radioactive decays with more than one α intensity.

Isotope	E_α [MeV]	$p(\alpha)$ [%]
^{238}U	4.198	0.4
^{234}U	4.759	1.6
^{230}Th	4.664	1.4
^{226}Ra	4.773	1.7
^{222}Rn	5.489	5.6
^{218}Po	6.002	11.1
^{214}Po	7.687	51.9
^{210}Po	5.304	4.3

Table C.2: Energies of α-particles produced by radioactive decays in the thorium decay series of the corresponding mother isotopes and probability fraction of ^{26}Al produced via the ^{23}Na$(\alpha,n)^{26}$Al reaction with α's of corresponding energies. To include branching ratios the probability fraction of ^{212}Bi and ^{212}Po are weighted by 64.06 % and 35.94 %, respectively.

Isotope	E_α [MeV]	$p(\alpha)$ [%]
^{232}Th	3.997	0.3
^{228}Th	5.404	5.0
^{224}Ra	5.673	7.3
^{220}Rn	6.288	15.4
^{216}Po	6.778	25.2
^{212}Bi	6.062	7.6
^{212}Po	8.785	34.7

Table C.3: Energies of α-particles produced by radioactive decays in the ^{230}Th decay chain (part of the radium series) of the corresponding mother isotopes and probability fraction of ^{26}Al produced via the ^{23}Na(α,n)^{26}Al reaction with α's of corresponding energies. Weighted mean energies were calculated from radioactive decays with more than one α intensity.

Isotope	E_α [MeV]	$p(\alpha)$ [%]
^{230}Th	4.664	1.8
^{226}Ra	4.773	2.3
^{222}Rn	5.489	7.4
^{218}Po	6.002	14.6
^{214}Po	7.687	68.3
^{210}Po	5.304	5.6

C.2 Production Cross Sections for the ^{23}Na(α,n)^{26}Al Reaction

Table C.4: Cross sections σ for the production of ^{26}Al in mbarn from the ^{23}Na(α,n)^{26}Al reaction for different α energies. The data was published in Norman et al. (1982).

E_α [MeV]	σ [mbarn]	E_α [MeV]	σ [mbarn]
3.75	2.5	6.75	169
4.25	15.1	7.25	215
4.75	33.2	7.75	254
5.25	55.7	8.25	264
5.75	82.2	8.75	279
6.25	128	9.25	286

APPENDIX D SRIM Simulations

D.1 Energy Loss of α-Particles in the Sample Material

```
===============================================================
             SRIM version ---> SRIM-2013.00
             Calc. date   ---> September 14. 2014
===============================================================

Disk File Name = SRIM Outputs\Helium in Al-Si-Ca- C- H- O_1.35.txt

Ion = Helium [2] . Mass = 4.003 amu

Target Density =   1.3500E+00 g/cm3 = 4.7995E+22 atoms/cm3
====== Target  Composition ========
   Atom   Atom   Atomic     Mass
   Name   Numb   Percent   Percent
   ----   ----   -------   -------
    Al     13    007.14    011.37
    Si     14    007.14    011.84
    Ca     20    007.14    016.90
    C       6    007.14    005.06
    H       1    014.29    000.85
    O       8    057.15    053.98
==================================
Bragg Correction = 0.00%
Stopping Units =  MeV / mm
See bottom of Table for other Stopping units
```

Ion Energy	dE/dx Elec.	dE/dx Nuclear	Projected Range	Longitudinal Straggling	Lateral Straggling
1.00 MeV	2.065E+02	2.680E-01	5.78 um	3362 A	4413 A
1.10 MeV	2.021E+02	2.474E-01	6.26 um	3465 A	4526 A
1.20 MeV	1.973E+02	2.300E-01	6.76 um	3569 A	4638 A
1.30 MeV	1.925E+02	2.150E-01	7.27 um	3674 A	4750 A
1.40 MeV	1.876E+02	2.020E-01	7.80 um	3780 A	4862 A
1.50 MeV	1.829E+02	1.905E-01	8.34 um	3888 A	4974 A
1.60 MeV	1.782E+02	1.804E-01	8.89 um	3998 A	5088 A
1.70 MeV	1.737E+02	1.713E-01	9.45 um	4110 A	5203 A
1.80 MeV	1.694E+02	1.632E-01	10.03 um	4224 A	5320 A
2.00 MeV	1.613E+02	1.492E-01	11.24 um	4619 A	5560 A
2.25 MeV	1.521E+02	1.349E-01	12.83 um	5214 A	5874 A
2.50 MeV	1.439E+02	1.232E-01	14.52 um	5809 A	6204 A
2.75 MeV	1.365E+02	1.135E-01	16.30 um	6407 A	6552 A
3.00 MeV	1.299E+02	1.054E-01	18.17 um	7010 A	6918 A
3.25 MeV	1.239E+02	9.832E-02	20.14 um	7621 A	7302 A
3.50 MeV	1.185E+02	9.222E-02	22.20 um	8238 A	7706 A
3.75 MeV	1.136E+02	8.688E-02	24.35 um	8864 A	8128 A
4.00 MeV	1.092E+02	8.215E-02	26.59 um	9498 A	8569 A
4.50 MeV	1.013E+02	7.416E-02	31.33 um	1.18 um	9508 A
5.00 MeV	9.469E+01	6.766E-02	36.43 um	1.40 um	1.05 um
5.50 MeV	8.895E+01	6.227E-02	41.87 um	1.61 um	1.16 um
6.00 MeV	8.394E+01	5.771E-02	47.65 um	1.82 um	1.28 um
6.50 MeV	7.954E+01	5.381E-02	53.76 um	2.03 um	1.40 um
7.00 MeV	7.564E+01	5.042E-02	60.19 um	2.25 um	1.53 um

8.00 MeV	6.899E+01	4.485E−02	74.02 um	3.01 um	1.80 um
9.00 MeV	6.397E+01	4.043E−02	89.05 um	3.72 um	2.10 um
10.00 MeV	5.916E+01	3.685E−02	105.29 um	4.40 um	2.42 um

```
-------------------------------------------------------------
Multiply Stopping by          for Stopping Units
-------------------           ------------------
 1.0000E−01                    eV / Angstrom
 1.0000E+00                    keV / micron
 1.0000E+00                    MeV / mm
 7.4077E−03                    keV / (ug/cm2)
 7.4077E−03                    MeV / (mg/cm2)
 7.4077E+00                    keV / (mg/cm2)
 2.0836E−01                    eV / (1E15 atoms/cm2)
 1.8175E−02                    L.S.S. reduced units
=============================================================
```
(C) 1984.1989.1992.1998.2008 by J.P. Biersack and J.F. Ziegler

D.2 Energy Loss of α-Particles in Water

```
===================================================================
             SRIM version ---> SRIM−2013.00
             Calc. date   ---> Januar 20. 2014
===================================================================
```

Disk File Name = SRIM Outputs\Helium in H– O.txt

Ion = Helium [2] . Mass = 4.003 amu

Target Density = 1.0000E+00 g/cm3 = 1.0029E+23 atoms/cm3

```
======= Target  Composition ========
   Atom   Atom   Atomic    Mass
   Name   Numb   Percent   Percent
   ----   ----   -------   -------
     H      1    066.67    011.19
     O      8    033.33    088.81
====================================
```
Bragg Correction = 2.00%
Stopping Units = MeV / mm
See bottom of Table for other Stopping units

Ion Energy	dE/dx Elec.	dE/dx Nuclear	Projected Range	Longitudinal Straggling	Lateral Straggling
1.00 MeV	2.227E+02	2.824E−01	5.49 um	2556 A	3258 A
1.10 MeV	2.163E+02	2.604E−01	5.95 um	2654 A	3326 A
1.20 MeV	2.096E+02	2.418E−01	6.42 um	2753 A	3394 A
1.30 MeV	2.031E+02	2.258E−01	6.90 um	2855 A	3462 A
1.40 MeV	1.967E+02	2.119E−01	7.40 um	2958 A	3531 A
1.50 MeV	1.906E+02	1.997E−01	7.91 um	3065 A	3601 A
1.60 MeV	1.847E+02	1.890E−01	8.45 um	3174 A	3673 A
1.70 MeV	1.792E+02	1.794E−01	8.99 um	3285 A	3745 A
1.80 MeV	1.739E+02	1.707E−01	9.56 um	3400 A	3820 A
2.00 MeV	1.643E+02	1.559E−01	10.74 um	3823 A	3975 A
2.25 MeV	1.536E+02	1.408E−01	12.31 um	4464 A	4181 A
2.50 MeV	1.442E+02	1.285E−01	13.99 um	5097 A	4401 A
2.75 MeV	1.360E+02	1.183E−01	15.77 um	5728 A	4637 A
3.00 MeV	1.287E+02	1.096E−01	17.66 um	6362 A	4889 A
3.25 MeV	1.223E+02	1.022E−01	19.65 um	7001 A	5157 A
3.50 MeV	1.164E+02	9.583E−02	21.74 um	7646 A	5441 A
3.75 MeV	1.112E+02	9.022E−02	23.94 um	8298 A	5742 A
4.00 MeV	1.065E+02	8.526E−02	26.23 um	8959 A	6059 A
4.50 MeV	9.824E+01	7.689E−02	31.11 um	1.14 um	6742 A

```
  5.00 MeV   9.130E+01   7.009E−02    36.39 um    1.37 um    7487 A
  5.50 MeV   8.536E+01   6.445E−02    42.05 um    1.60 um    8294 A
  6.00 MeV   8.023E+01   5.969E−02    48.08 um    1.82 um    9160 A
  6.50 MeV   7.573E+01   5.562E−02    54.49 um    2.04 um    1.01 um
  7.00 MeV   7.176E+01   5.209E−02    61.27 um    2.27 um    1.11 um
  8.00 MeV   6.505E+01   4.628E−02    75.89 um    3.09 um    1.32 um
  9.00 MeV   6.079E+01   4.169E−02    91.78 um    3.84 um    1.55 um
 10.00 MeV   5.641E+01   3.796E−02   108.85 um    4.55 um    1.80 um
-------------------------------------------------------------
Multiply Stopping by        for Stopping Units
-------------------         ------------------
 1.0000E−01                 eV / Angstrom
 1.0000E+00                 keV / micron
 1.0000E+00                 MeV / mm
 1.0000E−02                 keV / (ug/cm2)
 1.0000E−02                 MeV / (mg/cm2)
 1.0000E+01                 keV / (mg/cm2)
 9.9709E−02                 eV / (1E15 atoms/cm2)
 8.6356E−03                 L.S.S. reduced units
=============================================================
```
(C) 1984.1989.1992.1998.2008 by J.P. Biersack and J.F. Ziegler

APPENDIX E Estimation of Uncertainties

Counting atoms in a sample with AMS is a statistical process, therefore a true value can only be estimated and uncertainties are introduced. In one measurement run i a certain number x_i of atoms are detected in a target. To analyzed the precision of a measurement a Poisson or Gaussian distribution is assumed and the standard deviation of each measurement value is

$$\sigma_i = \sqrt{x_i}. \tag{E.1}$$

A weighted mean $\bar{x}$ is calculated with

$$\bar{x} = \frac{\sum_{i=1}^{n} \frac{x_i}{\sigma_i^2}}{\sum_{i=1}^{n} \frac{1}{\sigma_i^2}}. \tag{E.2}$$

Two types of standard deviations of the weighted mean, the inner and outer standard deviation, are defined as (e.g. L'Annunziata (2012))

$$\sigma_{in} = \sqrt{\frac{1}{\sum_{i=1}^{n} \frac{1}{\sigma_i^2}}}$$

$$\sigma_{out} = \sqrt{\frac{\sum_{i=1}^{n} \frac{(x_i - \bar{x})^2}{\sigma_i^2}}{(n-1) \sum_{i=1}^{n} \frac{1}{\sigma_i^2}}} \tag{E.3}$$

The greatest of the two values is used to estimate the standard deviation. For equal σ_i the two equations reduce to a common expression for the standard deviation of the mean value

$$\bar{\sigma} = \frac{\sigma_i}{\sqrt{n}}. \tag{E.4}$$

If the ratio of σ_{out}/σ_{in} differs significantly from unity, systematic errors are present between measurements. The relative statistical and other relative uncertainties $\sigma_{rel,j}$ contributing to the total measurement precision are added quadratically according to the gaussian error propagation

$$\sigma_{rel,tot} = \sqrt{\sum_{j} \sigma_{rel,j}^2}, \tag{E.5}$$

where $\sigma_{rel,tot}$ is the total measurement precision taking into account j different sources of uncertainty.

APPENDIX F Systematic Offsets of ICP-MS Results

Figure F.1: Intrinsic (natural) ^{10}Be/^{9}Be ratios of sediment samples of E49-53. **Upper part:** Application of the original ICP-MS ^{9}Be measurement data to convert the AMS results to ^{10}Be/^{9}Be ratios. Four different ICP-MS measurement series are color-coded. **Lower part:** Results after normalization of batch 2-9 data to batch 10-14 using ICP-MS results of repeatedly measured samples.

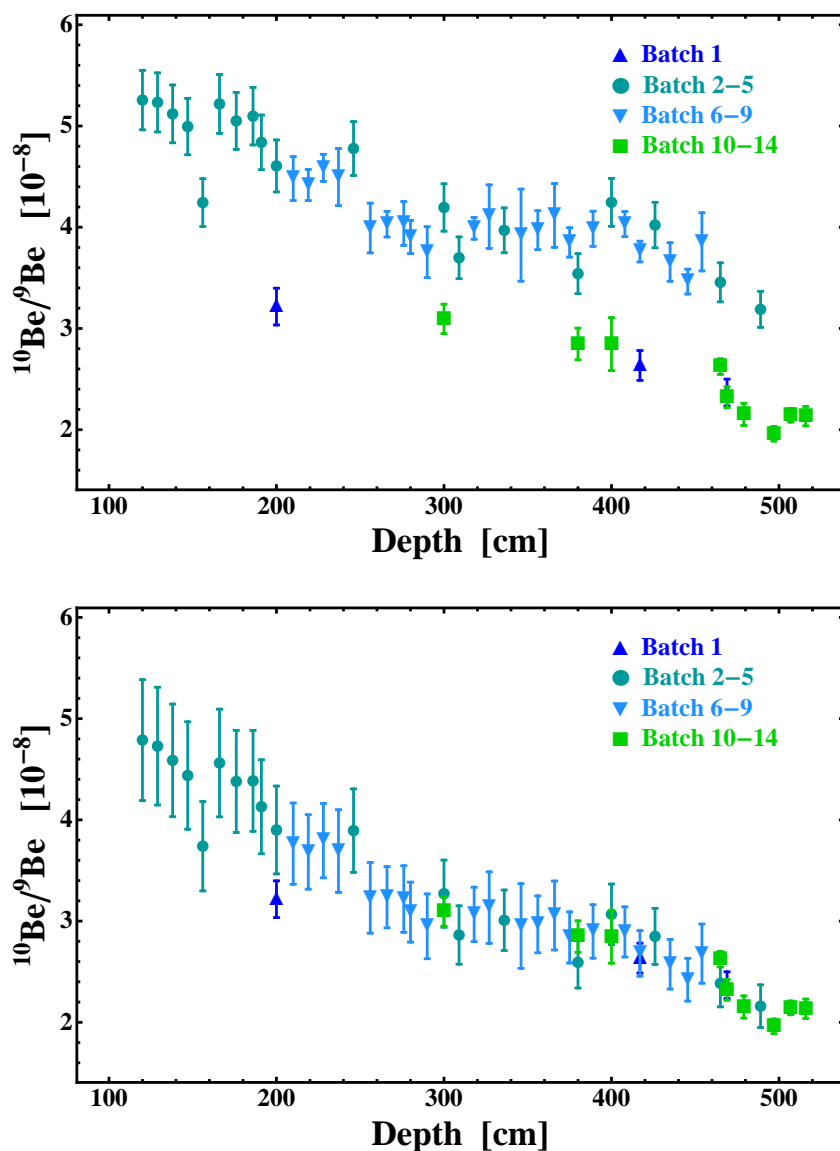**Figure F.2:** Intrinsic (natural) ^{10}Be/^{9}Be ratios of sediment samples of E45-21. **Upper part:** Application of the original ICP-MS ^{9}Be measurement data to convert the AMS results to ^{10}Be/^{9}Be ratios. Four different ICP-MS measurement series are color-coded. **Lower part:** Results after normalization of batch 2-9 data to batch 10-14 using ICP-MS results of repeatedly measured samples.
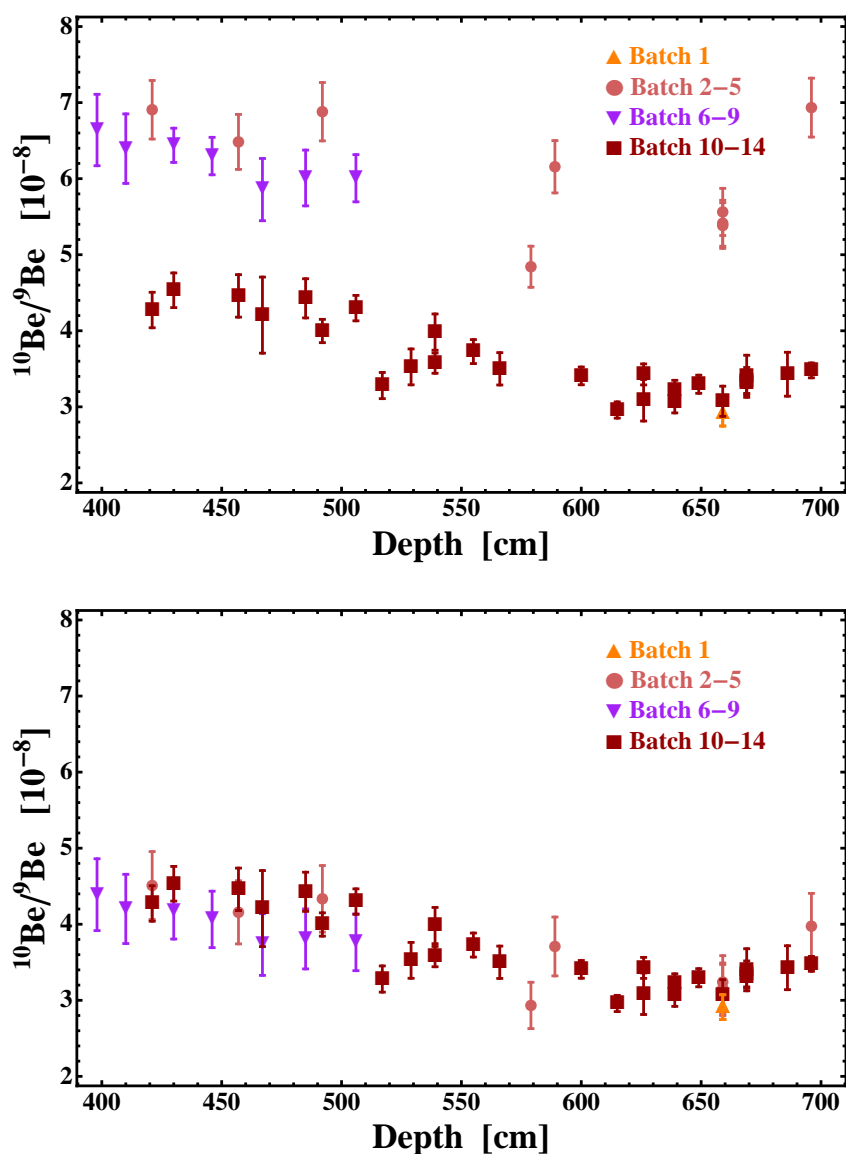
APPENDIX G Dating of the *Eltanin* Cores

G.1 Surface Ratios

Table G.1: AMS measurement ratios of surface samples corresponding to an age of t=0 Myr. ^{26}Al/^{27}Al yields a weigthed mean of $(2.56\pm0.15)\times10^{-13}$, ^{10}Be/^{9}Be = $(1.30\pm0.08)\times10^{-7}$.

Cruise	Number	Depth (cm)	^{26}Al/^{27}Al (10^{-13})	^{10}Be/^{9}Be (10^{-7})
E50-02	81	4 - 5	2.62 ± 0.08	1.42 ± 0.07
E50-02	82	12 - 13	2.47 ± 0.10	1.28 ± 0.05
E45-21	83	6 - 7	2.65 ± 0.11	1.23 ± 0.04
E45-21	84	9 - 10	2.85 ± 0.12	1.52 ± 0.08
E45-21	85	0 - 1	2.34 ± 0.09	1.26 ± 0.15

G.2 Mean Ages of Grouped Data

Table G.2: Grouping of data sets and corresponding mean ^{26}Al/^{27}Al and ^{10}Be/^{9}Be ratios of core E49-53. From these mean values, ages were calculated.

Group	^{26}Al/^{27}Al (10^{-14})	Age (Myr)	Group	^{10}Be/^{9}Be (10^{-8})	Age (Myr)
1 - 6	4.63 ± 0.09	1.768	1 - 8	4.38 ± 0.20	2.182
8 - 16	3.28 ± 0.06	2.124	9 - 15	3.75 ± 0.14	2.491
17 - 31	2.29 ± 0.05	2.495	16 - 39	2.79 ± 0.04	3.085
32 - 45	1.62 ± 0.04	2.853	40 - 45	2.12 ± 0.04	3.637

Table G.3: Grouping of data sets and corresponding mean ^{26}Al/^{27}Al and ^{10}Be/^{9}Be ratios of core E45-21. From these mean values, ages were calculated.

Group	^{26}Al/^{27}Al (10^{-14})	Age (Myr)	Group	^{10}Be/^{9}Be (10^{-8})	Age (Myr)
46 - 52	4.42 ± 0.08	1.815	46 - 55	4.17 ± 0.08	2.268
53 - 64	3.39 ± 0.05	2.091	56 - 71	3.36 ± 0.04	2.712
65 - 71	2.23 ± 0.06	2.522			

G.3 Uncorrected Be-Age-Depth Diagrams

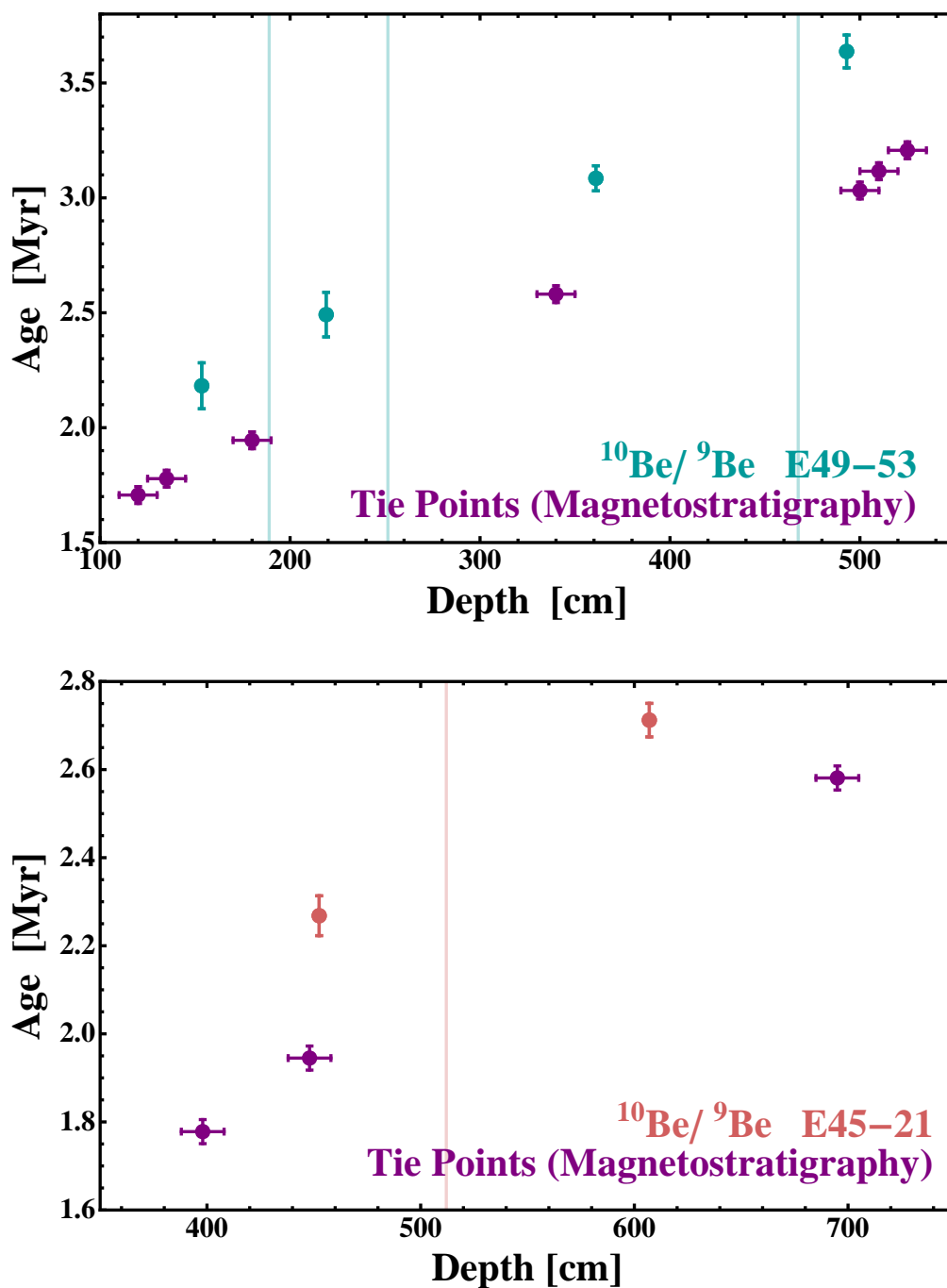**Figure G.1:** Combination of magnetostratigraphic tie points and mean ^{10}Be/^{9}Be ratios obtained for the grouping of data sets shown in figures 5.9 and 5.10 of E49-53 and E45-21. Due to a systematical error in stable ICP-MS ^{9}Be concentrations affecting the surface samples (prepared in batches 15 and 16), the mean ^{10}Be/^{9}Be ratios are not in agreement with paleomagnetic dating.

G.4 Ages of Samples from E45-21 and E49-53

Table G.4: Assigned ages to all samples prepared of E45-21. Models are developed with the ^{26}Al/^{27}Al (Al-Age) and the ^{10}Be/^{9}Be (Be-age) dating methods.

Number	Depth	Al-age (Myr)	Unc (%)	Be-Age (Myr)	Unc (%)
46	398	1.783 ± 0.083	4.65	1.791 ± 0.111	6.21
47	410	1.815 ± 0.084	4.62	1.823 ± 0.113	6.20
48	421	1.844 ± 0.085	4.60	1.852 ± 0.115	6.19
49	430	1.869 ± 0.086	4.59	1.876 ± 0.116	6.19
50	446	1.911 ± 0.087	4.56	1.919 ± 0.118	6.18
51	457	1.941 ± 0.088	4.55	1.948 ± 0.120	6.17
52	467	1.968 ± 0.089	4.54	1.975 ± 0.122	6.16
53	485	2.016 ± 0.091	4.53	2.023 ± 0.125	6.16
54	492	2.035 ± 0.092	4.52	2.041 ± 0.126	6.16
55	506	2.072 ± 0.094	4.51	2.079 ± 0.128	6.15
56	517	2.102 ± 0.095	4.51	2.108 ± 0.130	6.15
57	529	2.134 ± 0.096	4.50	2.140 ± 0.132	6.15
58	539	2.161 ± 0.097	4.50	2.166 ± 0.133	6.14
59	555	2.204 ± 0.099	4.50	2.209 ± 0.136	6.14
60	566	2.233 ± 0.101	4.50	2.238 ± 0.137	6.14
61	579	2.268 ± 0.102	4.50	2.273 ± 0.140	6.14
62	589	2.295 ± 0.103	4.50	2.300 ± 0.141	6.14
63	600	2.325 ± 0.105	4.51	2.329 ± 0.143	6.14
64	615	2.365 ± 0.107	4.51	2.369 ± 0.146	6.14
65	626	2.395 ± 0.108	4.51	2.398 ± 0.147	6.14
66	639	2.429 ± 0.110	4.52	2.433 ± 0.149	6.14
67	649	2.456 ± 0.111	4.52	2.460 ± 0.151	6.15
68	659	2.483 ± 0.112	4.53	2.486 ± 0.153	6.15
69	669	2.510 ± 0.114	4.53	2.513 ± 0.154	6.15
70	686	2.556 ± 0.116	4.54	2.558 ± 0.157	6.15
71	696	2.582 ± 0.117	4.55	2.585 ± 0.159	6.15
87	438	1.890 ± 0.086	4.58	1.897 ± 0.117	6.18
89	437	1.887 ± 0.086	4.58	1.895 ± 0.117	6.18

Table G.5: Assigned ages to all samples prepared of E49-53. Models are developed with the ^{26}Al/^{27}Al (Al-Age) and the ^{10}Be/^{9}Be (Be-age) dating methods.

Number	Depth	Al Age (Myr)	Unc (%)	Be Age (Myr)	Unc (%)
1	120	1.728 ± 0.079	4.56	1.729 ± 0.109	6.32
2	129	1.760 ± 0.080	4.55	1.762 ± 0.111	6.30
3	138	1.792 ± 0.081	4.53	1.795 ± 0.113	6.28
4	147	1.825 ± 0.082	4.52	1.828 ± 0.115	6.27
5	156	1.857 ± 0.084	4.51	1.860 ± 0.116	6.25
6	166	1.893 ± 0.085	4.50	1.897 ± 0.118	6.23
7	176	1.929 ± 0.087	4.49	1.933 ± 0.120	6.22
8	186	1.964 ± 0.088	4.48	1.970 ± 0.122	6.21
9	191	1.982 ± 0.089	4.48	1.988 ± 0.123	6.20
10	200	2.015 ± 0.090	4.47	2.021 ± 0.125	6.19
11	210	2.050 ± 0.091	4.46	2.057 ± 0.127	6.18
12	219	2.083 ± 0.093	4.46	2.090 ± 0.129	6.17
13	228	2.115 ± 0.094	4.45	2.123 ± 0.131	6.17
14	237	2.147 ± 0.095	4.45	2.155 ± 0.133	6.16
15	246	2.180 ± 0.097	4.44	2.188 ± 0.135	6.15
16	256	2.215 ± 0.098	4.44	2.224 ± 0.137	6.15
17	266	2.251 ± 0.100	4.43	2.261 ± 0.139	6.14
18	276	2.287 ± 0.101	4.43	2.297 ± 0.141	6.14
19	280	2.301 ± 0.102	4.43	2.312 ± 0.142	6.14
20	290	2.337 ± 0.103	4.42	2.348 ± 0.144	6.13
21	300	2.373 ± 0.105	4.42	2.385 ± 0.146	6.13
22	309	2.405 ± 0.106	4.42	2.417 ± 0.148	6.13
23	318	2.438 ± 0.108	4.42	2.450 ± 0.150	6.12
24	327	2.470 ± 0.109	4.42	2.483 ± 0.152	6.12
25	336	2.502 ± 0.110	4.42	2.516 ± 0.154	6.12
26	346	2.538 ± 0.112	4.41	2.552 ± 0.156	6.12
27	356	2.574 ± 0.114	4.41	2.588 ± 0.158	6.12
28	366	2.610 ± 0.115	4.41	2.625 ± 0.161	6.12
29	375	2.642 ± 0.117	4.41	2.658 ± 0.163	6.12
30	380	2.660 ± 0.117	4.41	2.676 ± 0.164	6.12
31	389	2.692 ± 0.119	4.41	2.709 ± 0.166	6.12
32	400	2.732 ± 0.120	4.41	2.749 ± 0.168	6.12
33	408	2.760 ± 0.122	4.41	2.778 ± 0.170	6.12
34	417	2.793 ± 0.123	4.41	2.810 ± 0.172	6.12
35	426	2.825 ± 0.125	4.41	2.843 ± 0.174	6.12
36	435	2.857 ± 0.126	4.41	2.876 ± 0.176	6.12
37	445.5	2.895 ± 0.128	4.41	2.914 ± 0.178	6.12
38	455	2.925 ± 0.129	4.41	2.945 ± 0.180	6.12
39	465	2.965 ± 0.131	4.41	2.985 ± 0.183	6.12
40	469	2.979 ± 0.131	4.41	3.000 ± 0.184	6.12
41	479	3.015 ± 0.133	4.41	3.036 ± 0.186	6.12
42	489	3.051 ± 0.135	4.41	3.073 ± 0.188	6.12
43	497	3.079 ± 0.136	4.41	3.102 ± 0.190	6.12
44	507	3.115 ± 0.138	4.42	3.138 ± 0.192	6.13
45	516	3.148 ± 0.139	4.42	3.171 ± 0.194	6.13

APPENDIX H Further Studies of ^{26}Al and ^{10}Be

H.1 Fluctuation Histograms

Scattering of Combined ^{10}Be/^{9}Be Ratios from E45-21 and E49-53

Figure H.1: Fluctuations of ^{10}Be/^{9}Be displayed as histograms in terms of standard deviations with bin widths varying from 1-1/6 σ. Here, the combined data sets of E45-21 and E49-53 were taken into account.

Scattering of Combined ^{26}Al/^{27}Al Ratios from E45-21 and E49-53

Figure H.2: Fluctuations of ^{26}Al/^{27}Al displayed as histograms in terms of standard deviations with bin widths varying from 1-1/6 σ. Here, the combined data sets of E45-21 and E49-53 were taken into account.

Scattering of ^{10}Be/^{9}Be Ratios (E45-21)
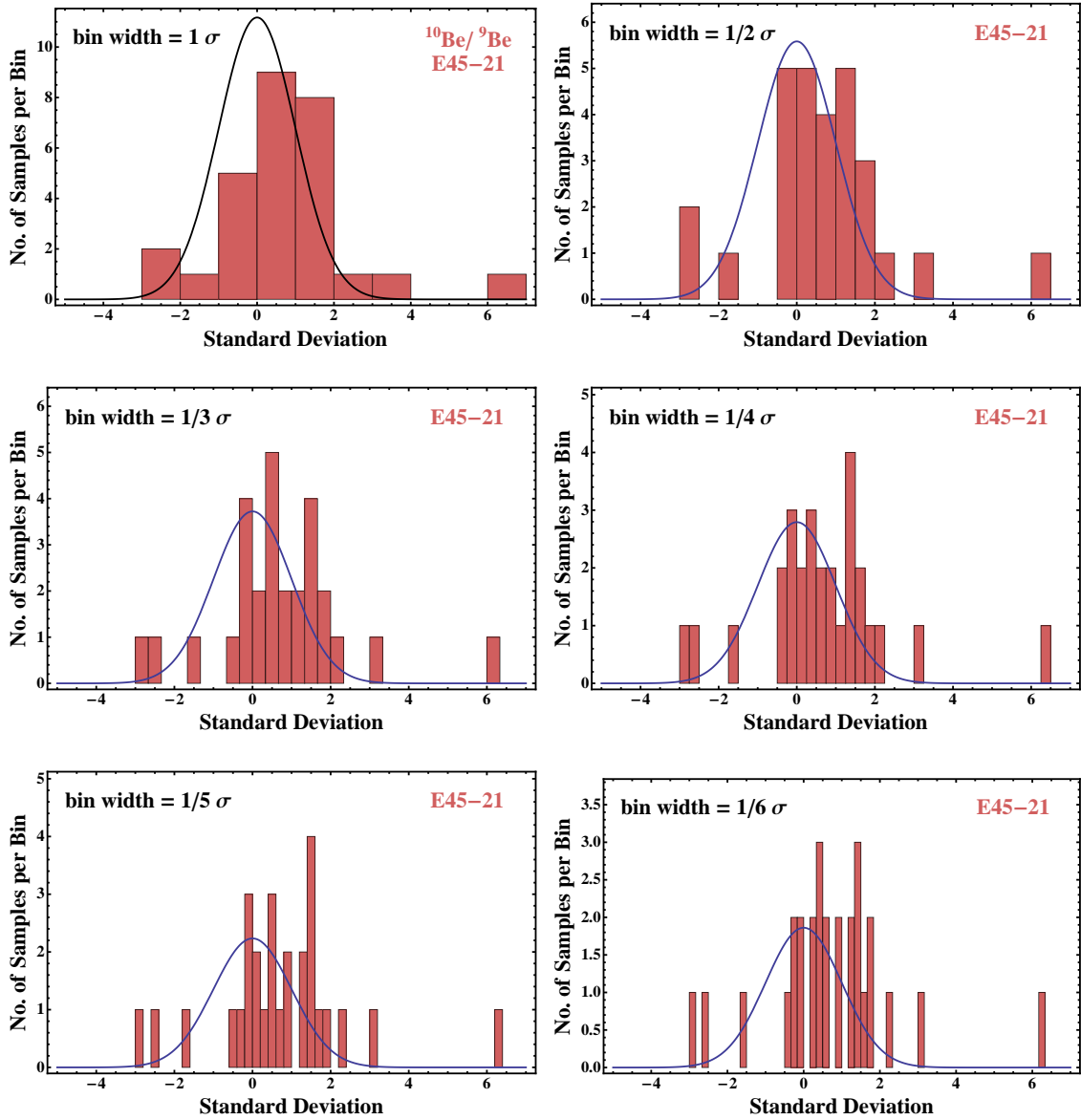
Figure H.3: Fluctuations of ^{10}Be/^{9}Be displayed as histograms in terms of standard deviations with bin widths varying from 1-1/6 σ. Here, only the data set of E45-21 was taken into account.

Scattering of ^{26}Al/^{27}Al Ratios (E45-21)
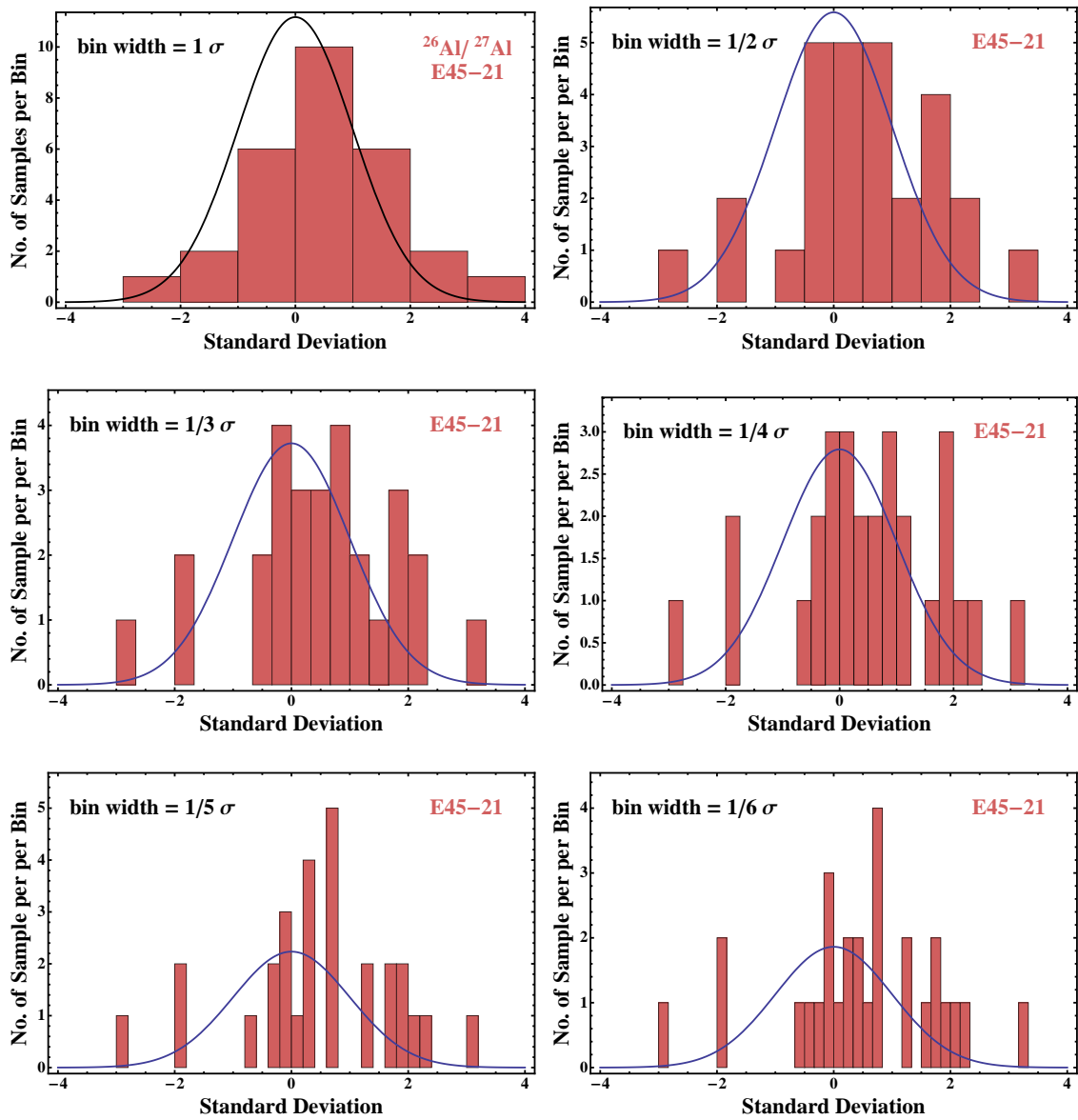
Figure H.4: Fluctuations of ^{26}Al/^{27}Al displayed as histograms in terms of standard deviations with bin widths varying from 1-1/6 σ. Here, only the data set of E45-21 was taken into account.

Scattering of ^{10}Be/^{9}Be Ratios (E49-53)
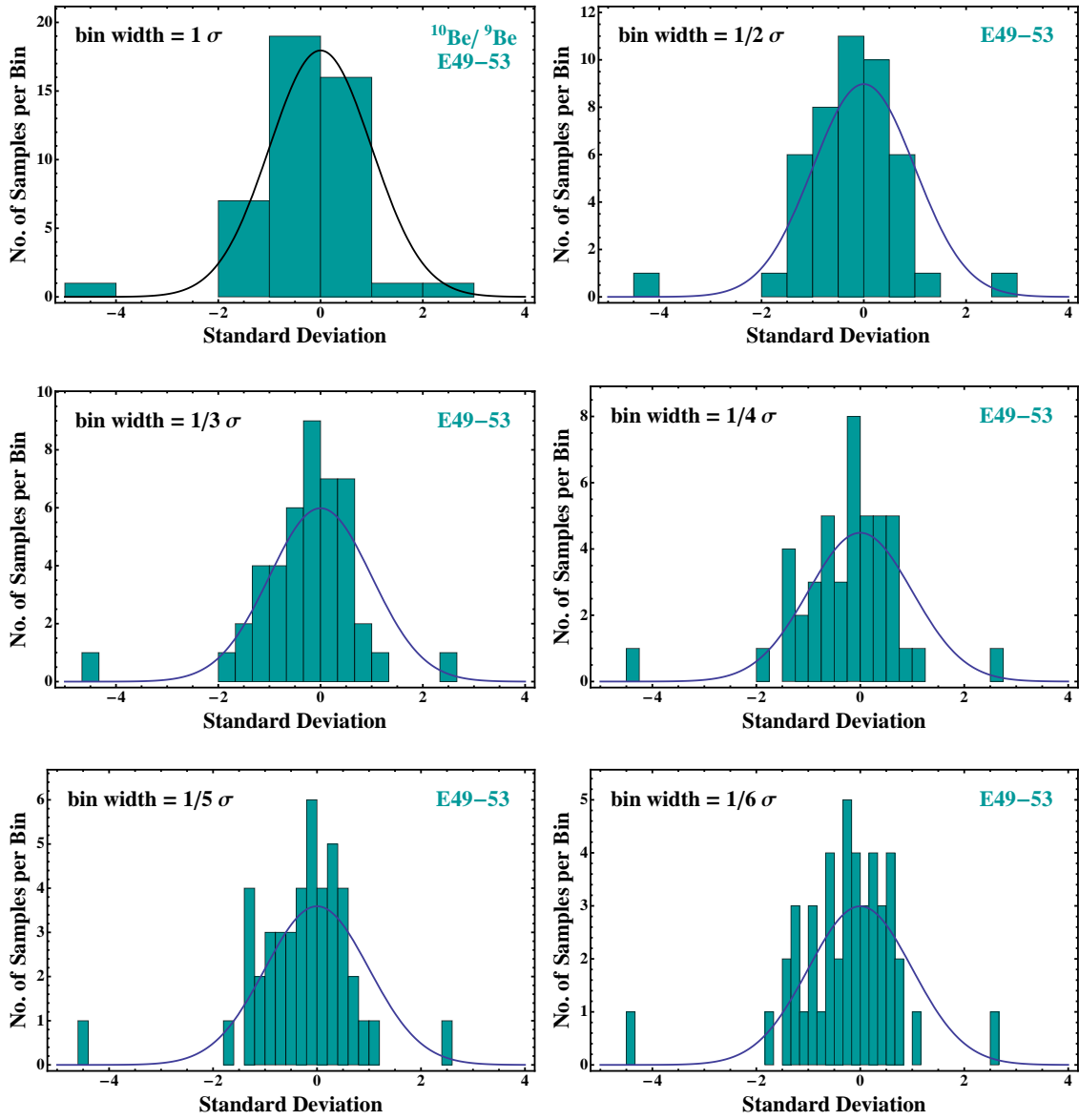
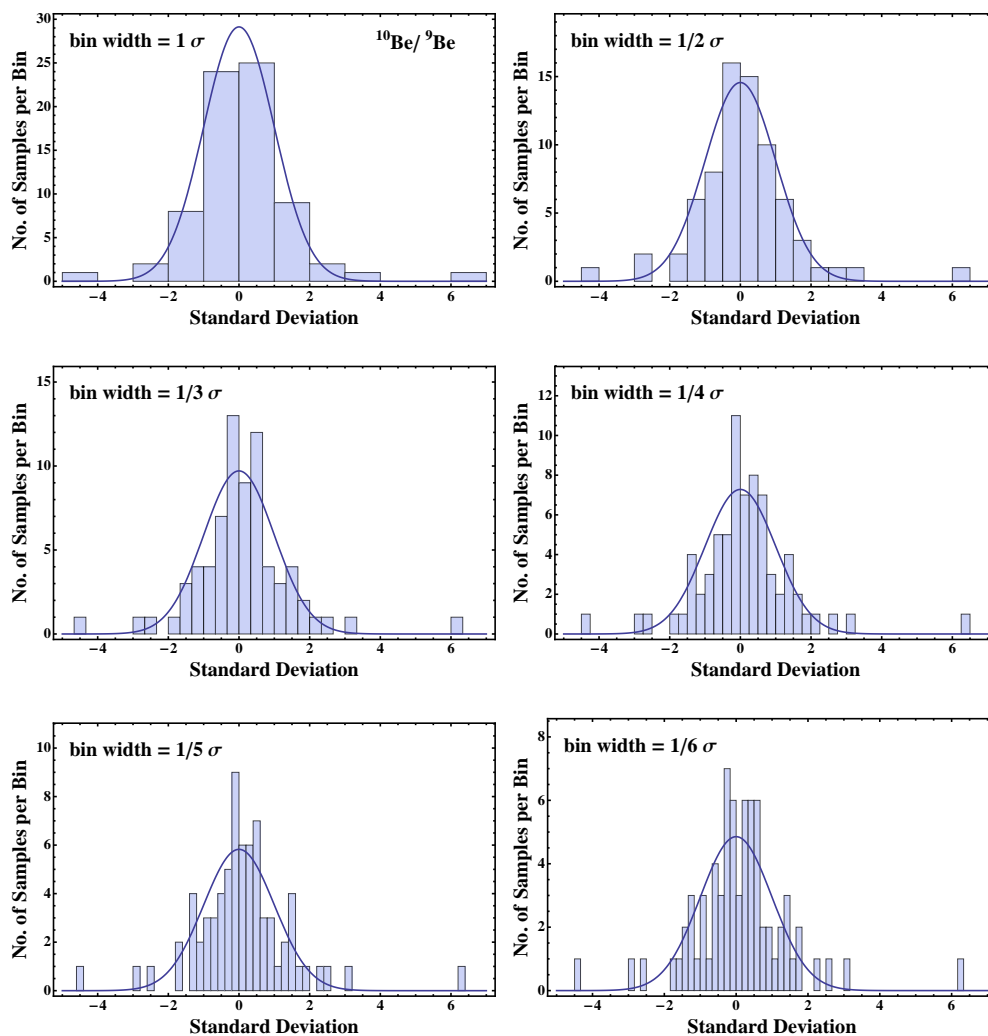**Figure H.5:** Fluctuations of ^{10}Be/^{9}Be displayed as histograms in terms of standard deviations with bin widths varying from 1-1/6 σ. Here, only the data set of E49-53 was taken into account.
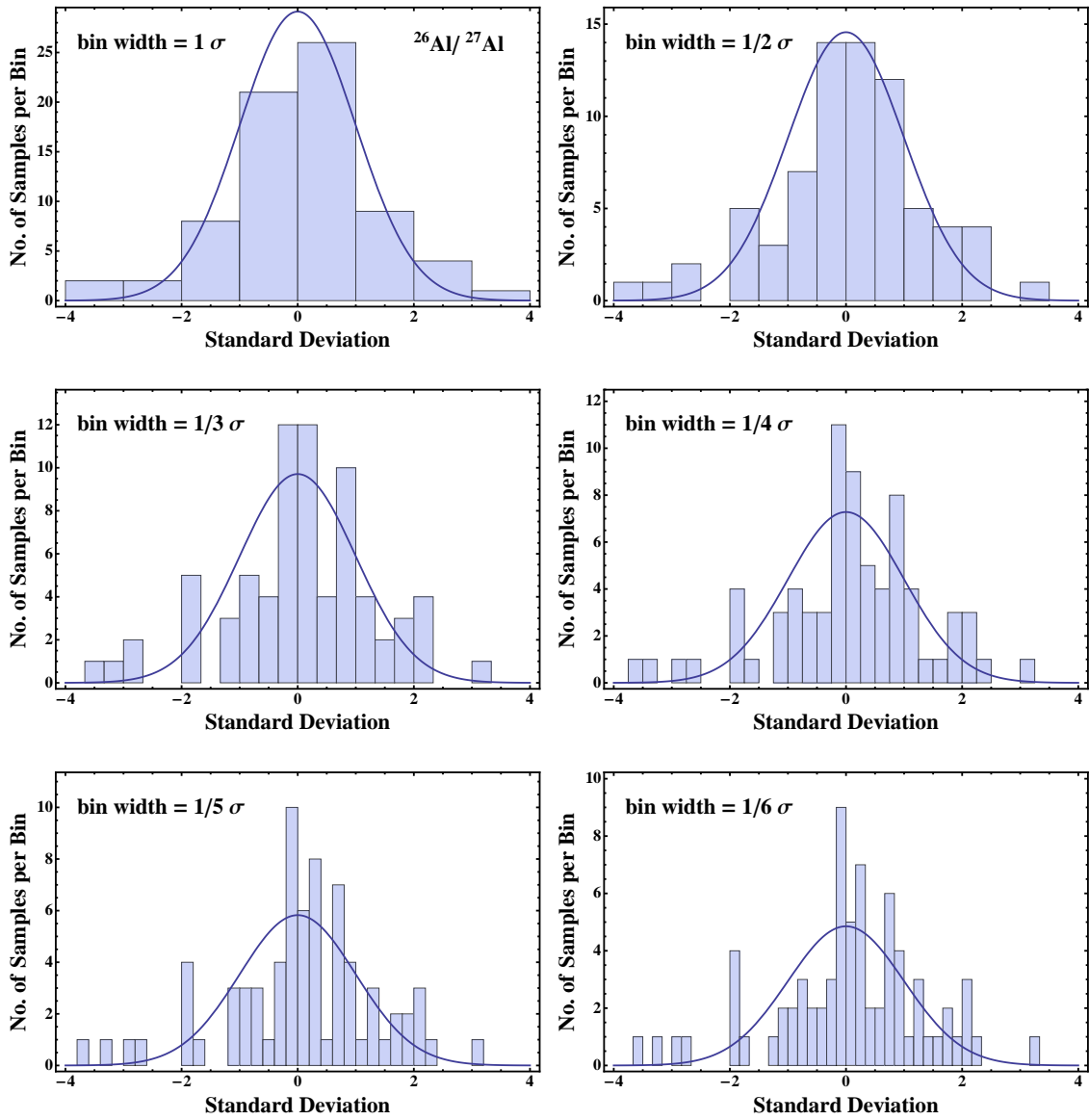
Scattering of ^{26}Al/^{27}Al Ratios (E49-53)
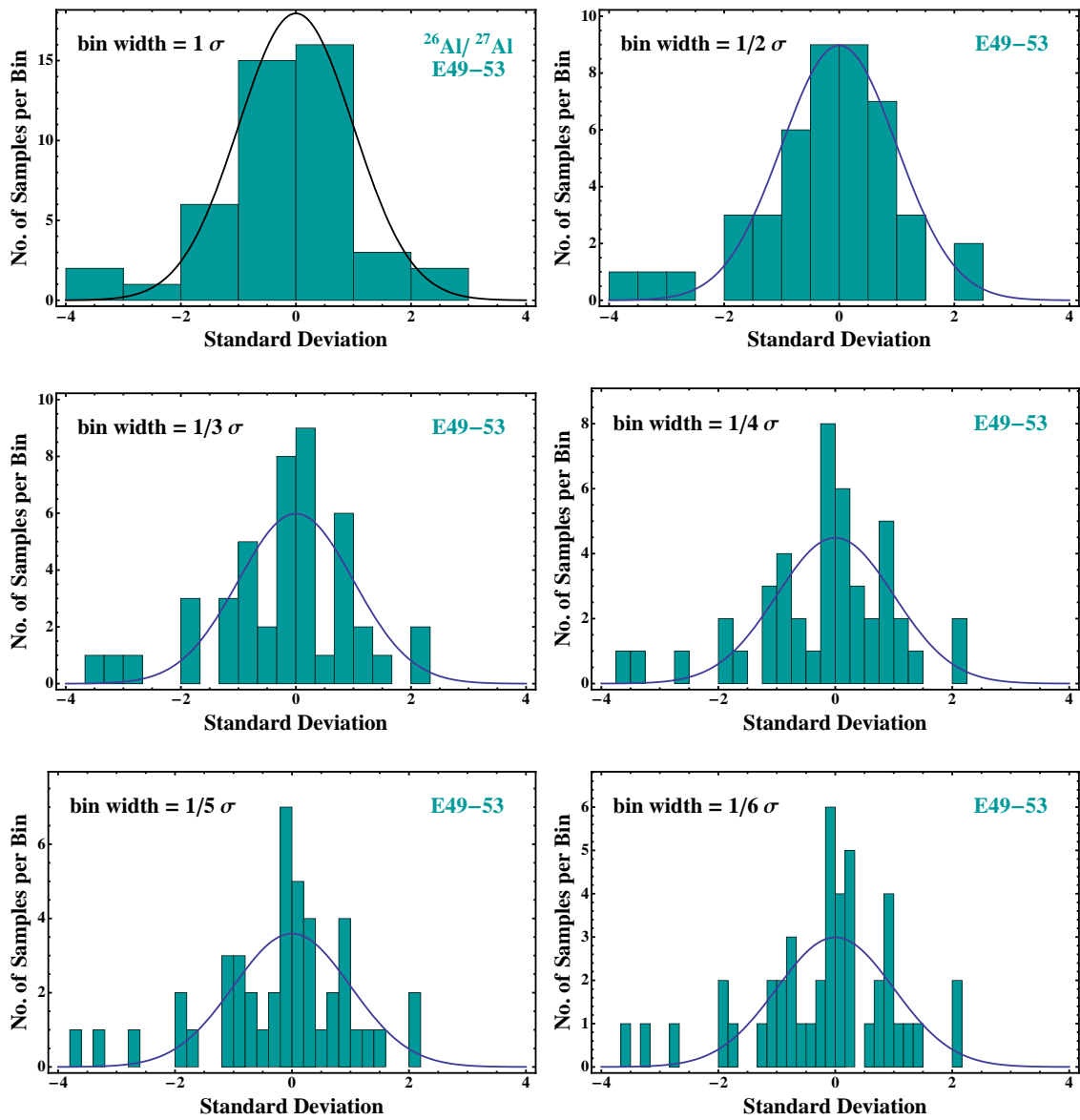
Figure H.6: Fluctuations of ^{26}Al/^{27}Al displayed as histograms in terms of standard deviations with bin widths varying from 1-1/6 σ. Here, only the data set of E49-53 was taken into account.

H.2 Moving Averages of ^{10}Be/^{9}Be and ^{26}Al/^{27}Al Ratios
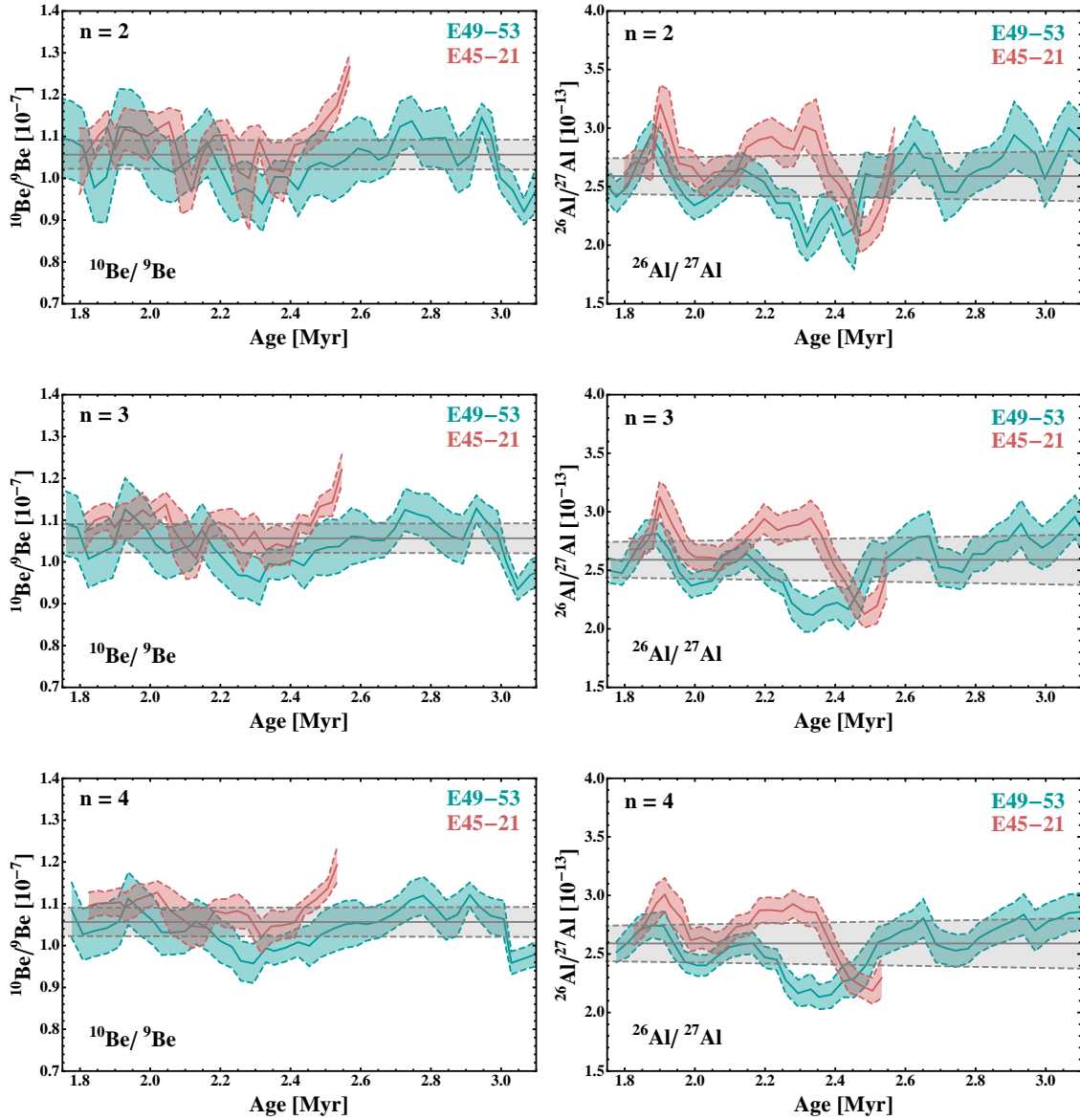
Figure H.7: Running means calculated from weighted averages of subsets of n=2 to n=4 data points of the two half-life corrected isotopic ratios of ^{26}Al/^{27}Al and ^{10}Be/^{9}Be in E45-21 and E49-53.

Figure H.8: Running means calculated from weighted averages of subsets of n=5 to n=8 data points of the two half-life corrected isotopic ratios of ^{26}Al/^{27}Al and ^{10}Be/^{9}Be in E45-21 and E49-53.

APPENDIX I Moving Averages of ^{60}Fe/Fe Ratios
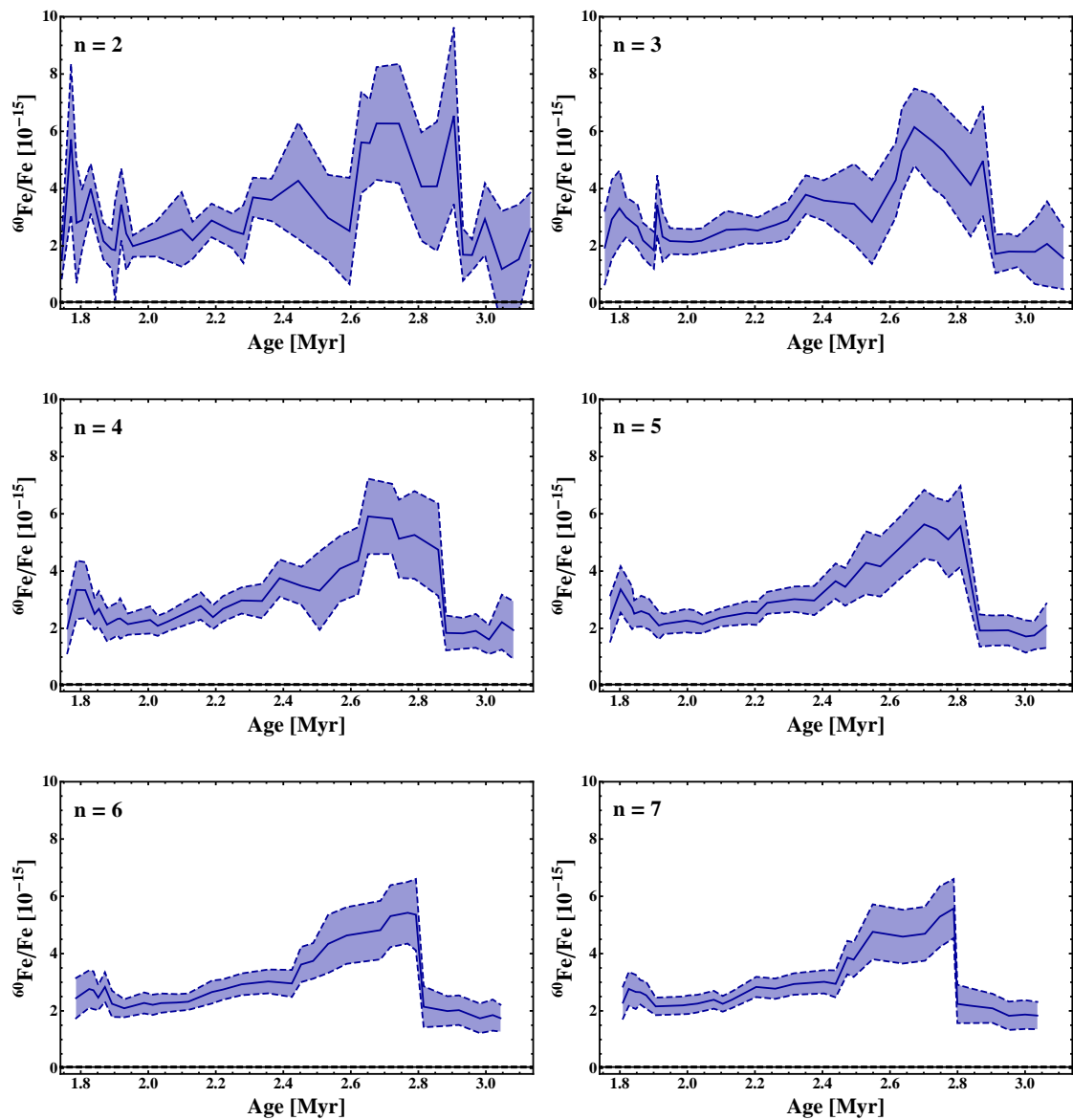
Figure I.1: Moving averages of summarized ^{60}Fe/Fe data points with n=2 to n=7 in the peak area of 1.7-3.2 Myr corrected for half-life. A time profile is shown. The horizontal line corresponds to the background level measured with AMS.

APPENDIX I. Moving Averages of ^{60}Fe/Fe Ratios
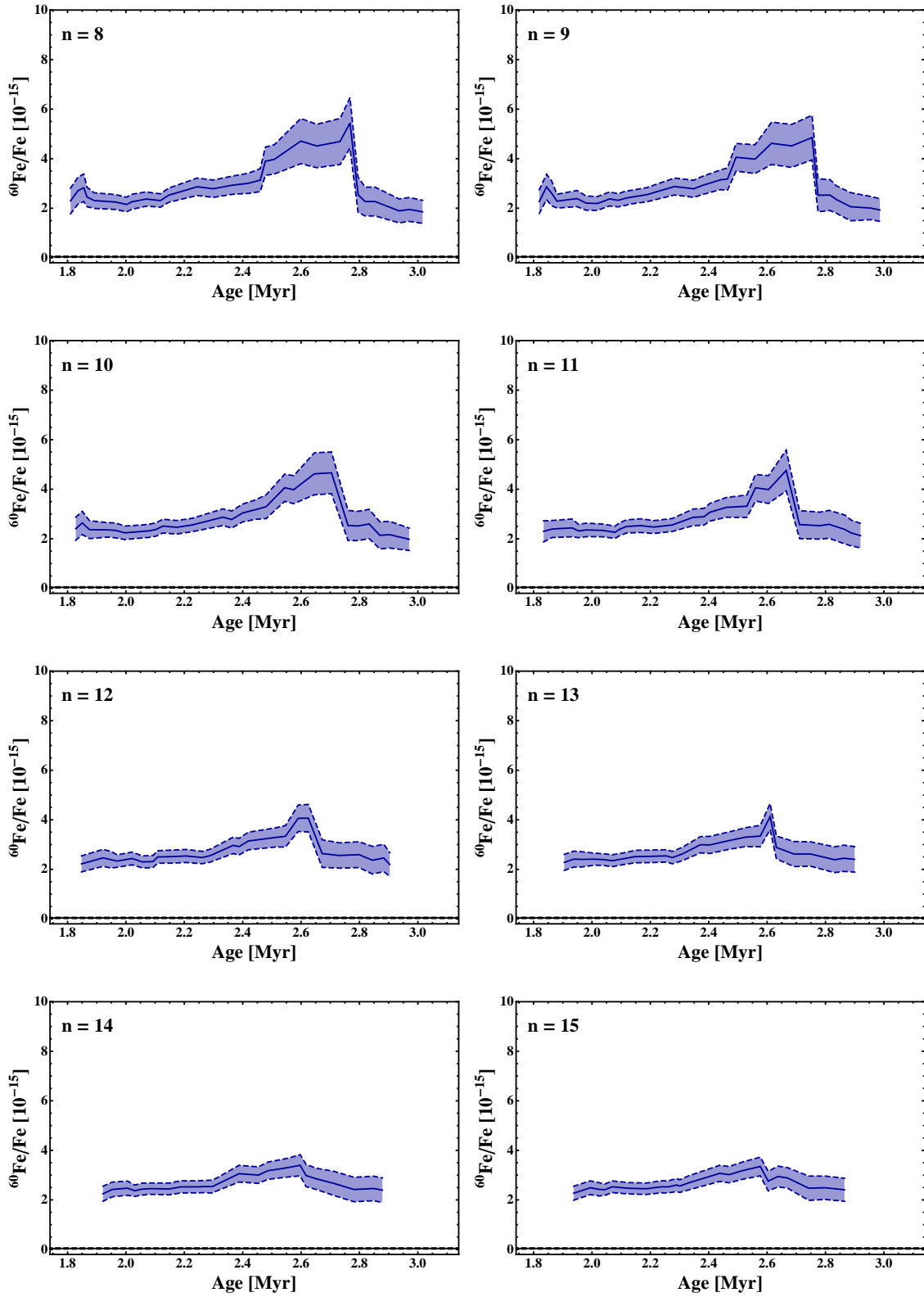
Figure I.2: Moving averages of summarized ^{60}Fe/Fe data points with n=8 to n=15 in the peak area of 1.7-3.2 Myr corrected for half-life. A time profile is shown. The horizontal line corresponds to the background level measured with AMS.

Glossary

Due to the interdisciplinary character of this work, selected terms and abbreviations are briefly explained in this glossary. The literature used for explanations is Robert (2008) (for geological terms), as well as Diehl et al. (2011) and Weigert and Wendker (2001) (for astronomical terms). Some terms are summarized from the text of this thesis. If further publications were taken for particular descriptions, citations will be given explicitly.

AABW
Ant**a**rctic **B**ottom **W**ater: A major water current in the southern Hemisphere partly subsiding with the deep circumpolar current surrounding Antarctica. In the Indian Ocean it flows in north-west direction through the South Australian Basin. Due to the high density of the water, the current moves at depths below 4 km. Therefore it affects the formation of sediments analyzed in this work.

AAS
Atomic **A**bsorption **S**pectrometry: A method to analyze absorption spectra of dissolved sample material to quantify concentrations of elements within this sample (chapter 4.3.2).

AGB-star
Asymptotic **G**iant **B**ranch star: This phase occurs after the RGB-phase of a star. Around the He-exhausted core, which consists mainly of carbon and oxygen, shell burning of helium continues. The star enters the AGB phase, where H and He shell burning alternate. The stellar envelope expands to surface radii 100-1000 times that of the sun. Furthermore, the star experiences enhanced mass loss.

AMS
Accelerator **M**ass **S**pectrometry: A very sensitive method used for detection of trace amounts of long-lived radionuclides. Usually the ratio to the stable isotope is measured; the detection limit can be as low as 10^{-16} (chapter 4.2).

ARF
Antarctic Marine Geology **R**esearch **F**acility: Located at the Florida State University (USA), it is a national repository for geological materials collected in polar regions. Deep-sea sediment cores recovered by the *Eltanin* research vessel from the Indian Ocean are stored in this facility (arf.fsu.edu).

AU
Astronomical **U**nit: the mean distance of the Earth's obit to the sun, 1.5×10^{11} m.

authigenic
Particles that form by chemical or biochemical processes such as precipitation or remineralization. Such particles belong to the secondary minerals. In the deep-sea they precipitate at the water-sediment interface such as the surface of rocks on the sea floor (building up hydrogeneous ferromanganese crusts or nodules) or within pore spaces of a sediment.

autotroph
Organisms that use light (such as plants, algae, phytoplankton) or inorganic matter (e.g. some bacteria and archaea, for instance iron-oxidizing bacteria) to build up organic compounds. Autotrophs are consumed by heterotrophs.

benthic
Organisms (such as bacteria, foraminifera, radiolaria, worms, etc.), which in contrast to planktonic organisms live in and on the surface of marine sediments.

Glossary

biogenic
Deep-sea sediments made of biogenic compounds consist of mineral fragments from fossilized organisms. These are for instance tests of foraminifera (made of calcium carbonate), exoskeletons of radiolaria (silicates) or remains of other organisms, such as pieces of bones or shark teeth.

biostratigraphy
The evolution of fossilized organisms such as radiolaria and foraminifera can be observed throughout the layers of deep-sea sediments. Changes in species can be assigned to ages and serve for dating of a marine sediment (section 2.3.1).

bioturbation
Benthic organisms living in and on the surface of sediments are actively burrowing. For this reason material is transported and the top part of the sediment is homogenized. The extension of the affected layer is called mixing length.

black hole
An area in space, where gravity is so strong, that nothing can escape, not even light.

BP
Before the **P**resent

CAIs
Calcium-**A**luminium **I**nclusions: These particles are found in meteorites and are believed to be among the first solid condensates, that have formed in the protoplanetary disc of the Early Solar System. Decay signatures of ^{26}Al and ^{53}Mn, and ^{60}Fe in CAIs point to the presence of those radionuclides in the Early Solar System.

CCD
Calcite (or **C**arbonate) **C**ompensation **D**epth: The depth, where carbonates are dissolved, on average 3500-5000 m below the sea surface. This depth depends on environmental conditions, such as temperature and water pressure as well as its chemical composition. CO_2 is predominantly responsible for the dissolution of $CaCO_3$. Therefore, in regions with enhanced volcanic activity releasing CO_2, the CCDs are located at shallower depths.

CCSN
Core-**C**ollapse **S**uper**n**ova: This event occurs for stars with masses larger than approximately 10 $M_\odot$. These proceed through all central burning stages, eventually a Fe core is generated. Further fusion processes would not release energy, as Fe (and Ni) has the highest binding energy per nucleon. The core collapses in a highly energetic event, with explosion energies of 10^{51}erg. Depending on the initial mass of the star, a neutron star or a black hole is formed.

chondrules
Spherical inclusions in chondrites, which are stony meteorites. In contrast to their parent bodies, chondrules have been subject to melting in the Early Solar System. Like CAIs, these were among the first solids in the Solar Nebula.

chron
If marine sediments are dated with magnetostratigraphy, a bar code-like pattern is observable with depth. The individual constituents of this pattern correspond to either a normal or a reverse magnetic field of the Earth. Sections with dominating normal or reverse magnetic field fingerprints between major reversals, are called chrons. The appearance of an inverse geomagnetic field section within a chron is referred to as subchron.

clay
Deep-sea sediment can contain large amounts of clay. A clay mineral consist mainly of silicate sheets containing Al, as well as other elements such as Fe and Mg. With sized of 0.2-4 µm, clay minerals belong to the fine grained particles.

CNO-cycle
One of the burning cycles in a star that converts hydrogen into helium, however, the initial abundance of C, N, and O remains unchanged. The CNO-cycle becomes efficient at temperatures higher than required for the pp-chain (>20 MK). In the sun, only a fraction of 0.4 % of helium produced is due to the CNO-cycle.

coccoliths	Autotrophic unicellar algae (phytoplankton) that form an exoskeleton consisting of calcite. Their sizes usually range between 1 and 15 µm. Because they are photosynthetic organisms, they predominantly populate the photic zone. Coccoliths are found as calcareous nannofossils in biogenic sediments.
colloid	Very fine particles of sizes less than 0.2 µm, which are usually associated with a suspension. However, due to their small sizes colloids do not settle.
cosmogenic	Radionuclides, that are produced via the interaction of cosmic rays or their secondary products (neutrons, protons), are called cosmogenic nuclides. Cosmogenic production occurs in space by reactions on meteoroids or asteroids, as well as on Earth, either by spallation reaction on particles in the Earths' atmosphere (producing for instance ^{10}Be from N and ^{26}Al from Ar) or in exposed surfaces to cosmic rays, such as rocks. Within rocks, cosmogenic ^{10}Be is produced mainly from oxygen, and ^{26}Al from Si. Such products are also called in-situ produced cosmogenic radionulices.
detrital	Particles of weathered rocks. These can be eroded and subsequently be incorporated into deep-sea sediments forming the terrigenous component.
diagenesis	Alteration of sediment components, which transforms the soft sediments into sedimentary rocks by biological, chemical, and physical processes. Biological alteration occurs mainly in the upper cm's of the sediment (within the mixing length). Chemical processes become important with greater depths and are facilitated by pore water flows, which transport chemical elements. Physical processes appear for example due to the pressure increase with depth, leading to deformation of the sediment material.
diatoms	Autotropic unicellar algae (phytoplankton) with a cell wall consisting of amorphous silica (opal A). Their sizes usually range between 10 and 100 µm. Because they are photosynthetic organisms, they predominantly populate the photic zone. Diatoms are found as siliceous microfossils in biogenic sediments.
dredge-up	Dredge-up happens in a star, when the convective zone penetrates into inner layers. As a consequence, nucleosynthesis products are transported outwards and mixed with upper layers.
ECSN	Electron-Capture Supernova: This type of SN occurs for a fraction of SAGB-stars, with masses between 7 and 12 $M_\odot$. In contrast to stars that explode in a CCSNe, SAGB-stars do not proceed through all burning stages. They burn H, He, and C in the core, finally their center consists of O, Ne and Mg. Electron capture on ^{20}Ne and ^{24}Mg initiates the collapse of the core, which is, with an explosion energy of 10^{50}erg, an order of magnitude less energetic than a CCSN. The residue of this event is a neutron star.
eolian	This indicates processes involving wind. Eolian erosion causes dust particles to be transported far away from the point of origin. The finest grains (such as silt and clay) may be transported some 1000 km. Eolian dust particles make up the major fraction of the terrigenous component of pelagic sediments.
erosion	Removing of particles from the parent rock after weathering processes. Transport may occur by water flows (fluvial), ice or wind (eolian).
Fe-Mn crust	A very slow-growing (mm Myr^{-1}) type of pelagic sediment, which is formed by hydrogeneous processes. Usually a ferromanganese crust develops in areas, where strong bottom water currents prevent normal sedimentation, such as sea mountains, ridges, and plateaus (chapter 2.1.3).

Fe-Mn nodule	A ferromanganese nodule differs from a crust by its spherical appearance and commonly larger growth rate. In the deep-ocean it is predominantly formed by hydrogeneous or diagenetic processes around a nucleus. Usually a mixture of the two types is observed. The larger the diagenetic component, the more it differs from a ferromanganese crust by chemical composition and growth rate (chapter 2.1.3).
feldspar	Silicate minerals containing aluminium, which make up the main component of the Earth's crust.
feroxyhyte	(Oxyhydr)oxide minerals of iron (δ-FeO(OH)), which are found in ferromanganese crusts and nodules.
flocculation	The tiny suspended particles of terrigenous and biogenic origin form agglomerates due to molecular attraction. These sink as flocculated matter, which can be as large as 1 cm. Most sinking matter in the deep-sea is accumulated in such flocs.
fluence	A fluence is a time-integrated flux and corresponds to a number of particles per area.
fluvial	Processes, which involve water flows such as rivers, are called fluvial. Here, it describes transport of eroded particles via water streams.
foraminifera	Heterotrophic protozoa, which occur predominantly in zooplanktonic, a small fraction in benthic form. The planktonic species produce tests of calcium carbonate (calcite), benthic organisms use terrigenous and organic particles to produce their shells. Their sizes usually range between 50 and 400 μm. Due to their large variation in species since their first appearance in the Late Jurassic, foraminifera are used for biostratigraphy.
FWHM	**F**ull **W**idth **H**alf **M**aximum: For a gaussian normal distribution, the FWHM scales with the standard deviation σ by FWHM = $2\sqrt{2\ln(2)}\,\sigma = 2.355\,\sigma$. It represents the width of the curve at half its height.
GCRs	**G**alactic **C**osmic **R**ays: In contrast to SCRs, GCRs are of extrasolar origin. Possible sources are e.g. SNe, shocks propagating through the ISM, and active galactic nuclei. GCRs consist mainly of protons (87 %), α-particles (12 %) and a small proportion of heavier nuclei (1 %). Their energies range from a few GeV/nucleon up to 10^{20} eV/nucleon (e.g. Simpson (1983)).
heterotrophs	Organisms that consume organic compounds and use it for growth and reproduction. As autotrophs are primary producers, heterotrophs serve as secondary producers of organic matter. Fungi, animals, most bacteria and archaea are heterotrophic organisms.
hydrogeneous	or **hydrogenetic**: Formation processes of ferromanganese crusts and nodules involving precipitation of elements from sea water onto oceanic surface layers (e.g. of an already existing Fe-Mn crust). This happens predominantly in regions, where water currents prevent normal precipitation. Here, fresh elements are transported from elsewhere. These are accreted extremely slow, leading to very small growth rates of mm Myr^{-1}.
hydrothermal	Here, this term refers to hydrothermal deposits. This includes manganese nodules, which grow close to a hydrothermal vent (such as a black smoker). Their composition reflects the chemical constituents of the hydrothermal fluids. These are mixed with the ambient sea water and thus precipitated onto the nodule.
ICP-MS	**I**nductively **C**oupled **P**lasma **M**ass **S**pectrometry: like AAS, it is a method to determine concentrations of elements within a dissolved sample (chapter 4.3.1).

IDPs   Interplanetary Dust Particles: In contrast to ISDs, these originate from within the Solar System from asteroids or comets. These are distinguished from MMs by their smaller sizes of less than 30μm.

ion exchange   Separation of chemical elements can be achieved using ion exchange chromatography (chapter 4.1.3).

ISDs   Interstellar Dust particles: In contrast to IDPs, ISDs originate from outside the Solar System. Major dust producers are AGB-stars and SN explosions. Within the Solar System ISDs are characterized by very high speeds up to $\sim$100 km s^{-1} on hyperbolic or extremely elliptic orbits.

ISM   Interstellar Medium: The medium between the stars in a galaxy, which consists primarily of hydrogen. A mass fraction of 1 % is present as interstellar dust. On average, the ISM has a density of 1 atom cm^{-3}.

isotope   Chemical elements are distinguished from each other by their number of protons in the nucleus. However, the amount of neutrons of a chemical element can vary. Atoms with the same number of protons, but different numbers of neutrons are referred to as isotopes of the element.

leaching   A chemical procedure that does not dissolve a material completely. Instead only the fraction attached to the surface of an insoluble mineral is extracted. An example is dissolution of salt being attached to rock by water.

LB   Local Bubble: A structure in the local ISM, in which the Solar System is embedded. With extensions of $\sim$200 pc in the galactic plane and $\sim$600 pc perpendicular to it, the LB is much smaller than the extension of the Milky Way, with a diameter of $\sim$30 kpc. The LB is characterized by a shell-like structure at its boundary and hot (10^6 K) medium inside. With a particle density of $0.5{\times}10^{-3}$ ats cm^{-3}, the LB gas is much thinner than the average ISM gas. The LB is a superbubble, which was presumably produced by 14-20 SNe within the past 14 Myr. The closest neighbor bubble to the LB is the Loop I superbubble.

LCC   Lower Centaurus Crux: a subgroup of the Sco-Cen association. Some of the stars, that are found within this young OB-association, belonged to the stellar moving group that passed the Solar System at an average distance of 90-100 pc 2-3 Myr ago. The age of LCC is estimated with 20-30 Myr. Stars, that exploded during the last 14 Myr within this stellar moving group, may have caused the formation of the LB as well the ^{60}Fe anomalies found on Earth and on the Moon.

Local Fluff   Also: Local Cloud. This is a region within the LB with less high temperatures ($\sim$$10^4$ K) and less thin medium (on average 0.1 ats cm^{-3}). The Solar System entered this region $\sim$100 kyr ago, and will leave it in some 10 kyr. Although it has a lower temperature than the LB, it is still a very hot environment. The Earth is shielded from the radiation by the heliosphere and by the magnetic field.

magnetostratigraphy   Deep-sea sediment cores contain ferrimagnetic and canted antiferromagnetic particles (mostly magnetite, Fe_3O_4, and hematite Fe_2O_3, with various degrees of Ti-substitution), which hold a magnetic moment that becomes aligned with the Earth's magnetic field during and shortly after sediment deposition. This orientation records the direction of the magnetic field at the time of deposition and is preserved over geological time scales. If the magnetic field becomes unstable or changes its polarity, this is observed in changes of orientation of magnetized particles. Magnetic reversals occur by chance, therefore a unique pattern consisting of normal and reverse polarity is visible with depth of a marine sediment. Established chrons resulting from this pattern can be used for dating (section 2.3.2).

Main Sequence As soon, as a star starts central hydrogen burning via the pp-chain and/or the CNO-cycle, it enters the main sequence. The main sequence phase lasts, until H is used up in the core. Eventually, the star becomes a red giant.

meteorite As soon, as a meteoroid enters the Earth's atmosphere, it is called a meteor (or shooting star). Meteors, that are not fully ablated due to deceleration and heating in the atmosphere, reach the Earth's surface. These are referred to as meteorites.

meteoroid A meteoroid is an object, that travels through space. It can be a fragment of an asteroid or a comet, or lunar/martian debris ejected during an impact. Debris from asteroids originate from collisions occurring in the asteroid belt, cometary debris are assumed to originate from comets in the Oort's cloud. Sizes of meteoroids range between a few µm (micrometeoroids) up to the order of meters.

MMs **M**icro**m**eteorites: small meteorites of sizes less than a millimeter.

mixing length Mixing of the upper parts of a deep-sea sediment is caused by bioturbation and referred to as benthic mixing layer. The average thickness is comprised of between 4 and 10 cm.

MMNs **M**anganese **M**icro**n**odules: microscopically small manganese nodules (with sizes in the range of µm up to mm) growing in areas with low sedimentation rates. They mainly form by diagenetic accretion processes due to remobilization of manganese and other components in the sediment column.

nannofossils These include fossils, which are smaller than 30 µm. Here, coccoliths are referred to as nannofossils, whereas fossils of diatoms, foraminifera, and radiolaria are identified as microfossils.

neutron stars Residue of a SN explosion, which are very compact objects with densities of 10^{15} g cm^{-3}. Neutron stars consist predominantly of neutrons and their sizes are in the order of 10 km for 1 M$_\odot$. Neutron degeneracy pressure prevents these stars from collapsing.

nucleosynthesis The process of generating new elements and their isotopes from protons and neutrons, as well heavier nuclei, is called nucleosynthesis.

OB-association Loose stellar clusters consisting of young, low and intermediate mass stars of the spectral classes O and B, which were formed at the same time. OB associations have about 10-1000 members and are spread over a wide area in space, with diameters of 30-200 pc.

OMZ **O**xygen **M**inimum **Z**one: A layer (200-1000 m) in the ocean deficient of oxygen. From the ocean's surface towards this zone, the concentration of oxygen decreases. Organisms, such as aerobic bacteria, consume oxygen, using it up with increasing depth. Oxygen is provided by cold bottom water flows, leading to an increase of its concentration below the OMZ.

ooze A sediment consisting of mineral products and shells from pelagic organisms is identified as ooze. If the sediment is a mixture of clay and nannofossils, where the latter component dominates, it is referred to as nannofossil ooze. This implies, that the sediment is predominantly of biogenic origin.

pc A pc is a length constrained from the orbit of the Earth around the sun. A star with a distance of 1 pc to the Solar System, "sees" the radius of the Earth's orbit under an angle of 1 arc second. 1 pc corresponds to 3.1×10^{18} cm.

pelagic	The open ocean (regions far from coastal areas) is identified as the pelagic zone. This includes all oceanic layers: from the surface almost down to the sea floor, excluding the benthic zone. However, sediments which form at the bottom of the open ocean are referred to as pelagic sediments.
photic zone	This zone refers to the upper 100-200 m of the ocean. Here, light is able to penetrate the water column. Therefore, it is a zone of high productivity with a large variety of photosynthetic organisms (such as diatoms and coccoliths) and their consumers (radiolaria, foraminifera, etc.) populating that area.
plankton	In contrast to benthic organisms, planktonic species live in the water column. They are not able to move themselves in the horizontal direction against the water flow (some are able to migrate vertically), but drift through the ocean by moving water masses. A distinction is made between phytoplankton (such as algae, diatoms and coccoliths) and zooplankton (including radiolaria, foraminifera, but also larger organisms such as jellyfish).
protozoa	Unicellar organisms; historically this term refers to the "first animal". Today it is mainly used to describe eukaryotic (one or more nulei in the cell), heterotrophic organisms.
pp-chain	This process converts hydrogen to helium in stars. It activates at temperatures of ~10 MK. In the sun, this is the major process, dominating by 99.6 % over the CNO-cycle in central H-burning.
pteropods	These can be found as microfossils in deep-sea sediments. In contrast to coccoliths and foraminifera with exoskeletons made of calcite, pteropods have shells of aragonite. Like calcite, this is a form of calcium carbonate ($CaCO_3$). However, it is less stable and easier dissolved than calcite. Therefore, the corresponding **A**ragonite **C**ompensation **D**epth (ACD) is usually shallower than the CCD.
quartz	After feldspar, this mineral (SiO_2) makes up the second largest component of the Earth's crust.
radiogenic	If a radioactive decay is involved in the production of a nuclide, it is called a radiogenic nuclide. In this work, radiogenic ^{26}Al is produced in deep-sea sediments by reactions involving α-particles, that originate from radioactive decay within the natural decay chains.
radiolaria	Heterotrophic protozoa, which occur as zooplanktonic microorganisms. They are predominantly populating the photic zone, however, radiolaria can be found in all depths of the ocean. Their exoskeleton consists in most cases of amorphous silica (opal A). The sizes of radiolaria usually range between 40 and 400 µm. Due to their diversity in species since their first appearance in the Cambrian, radiolaria are used for biostratigraphy.
radionuclides	In contrast to stable isotopes, radionuclides have an unstable nucleus and decay by emitting radiation. These are also called radioactive isotopes of an element.
RGB-star	**R**ed **G**iant **B**ranch star: After the main-sequence phase, the star converted most of its hydrogen in the core to helium. H-burning shifts to an H-rich envelope around the He-core. Here, energy is predominantly generated via the CNO-cycle. Meanwhile the stellar envelope expands, causing the surface temperature to drop to a few 1000 K. This phase is also called the First Giant Branch phase.
r-process	**r**apid neutron capture **process**: Approximately half of the nuclei heavier than iron are produced with the r-process, via very rapid neutron capture on an isotope. Neutron densities much higher than for the s-process, reaching up to

10^{25} neutrons cm^{-3}, generate the neutron-rich material of the chart of nuclei. The time scale for a β-decay of a nucleus is longer than the time-scale for another neutron capture, which occurs in less than seconds. The r-process is believed to occur during the explosion of a SN and in neutron star mergers.

SAGB-star　　**S**uper **A**symptotic **G**iant **B**ranch star: Masses of progenitor stars are in the range of 7-12 $M_\odot$. These stars ignite carbon in the core. However, they are not able to proceed to central Ne burning. Thus, SAGB-stars consist of an ONeMg core, whose final fate depends on the chandrasekhar mass. If the core is able to reach a mass of ~1.35 $M_\odot$, the star will explode as ECSN. For lower core masses the star will end its life as ONeMg white dwarf.

scavenging　　Removal of an element from the water column. Particle reactive elements such as Al and Be are quickly adsorbed onto particles such as detrital minerals and biogenic material. The efficiency of scavenging depends amongst others on size and composition of the sinking particles. Therefore, particle reactive elements are enriched in regions with high particle flux. Here, they are quickly adsorbed and deposited.

Sco-Cen association　　**Sco**rpius-**Cen**taurus association: The subgroups UCL, LCC, and US belong today to the Sco-Cen association, which is the closest OB-association to the Solar System. Stars belonging to the Sco-Cen association are visible from the southern hemisphere. The most prominent star within this stellar association is Antares, the brightest star in the constellation Scorpius.

SCRs　　**S**olar **C**osmic **R**ays: As this term suggests, this type of cosmic rays originates from the sun. These particles have lower energies than GCRs, with approximately 1-200 MeV/nucleon. They consist predominantly of protons (98 %) and α-particles (2 %) (e.g. Michel et al. (1996)).

silt　　Deep-sea sediments can contain large amounts of silt. With sizes of 4-63 μm, silt is larger than clay minerals. They still belong to the fine grained particles.

SN　　**S**uper**n**ova: literally, SN is translated as "new star". If a star explodes as a SN, it ejects its stellar envelope into space, leaving a residue such as a neutron star or a black hole. The luminosity of a SN can become comparable to that of a whole galaxy. Different types of SNe were observed, e.g. ECSNe, CCSNe, as well as SNe type Ia. The latter results from a white dwarf, that accretes mass from a companion star and collapses when it reaches a mass of about 1.44 $M_\odot$.

SNR　　**S**uper**n**ova **R**emnant: the ejected mass of a SN expanding through the ISM is called SNR. The expansion mechanism of an SNR into a homogeneous ambient medium is usually described by three phases. (i) Free Expansion: after the stellar envelope is ejected with velocities in the order of 10^8 cm s^{-1}, it moves freely through the ISM. When the swept up mass of the ISM equals the ejected mass of the SN, the remnant is decelerated and a reverse shock travels through the expanding shell towards the center of explosion. (ii) Due to the reverse shock, the medium in the shell is heated to large temperatures, and the remnant travels further due to the internal pressure. This phase is called the Sedov-Taylor phase. For calculations made in the work, it was substituted by the Kahn-phase, approximating the SNR expansion into a LB medium. (iii) Temperatures cool down to 10^6 K and elements start to recombine in the SNR, reducing the temperature and the internal pressure. Further evolution is due to momentum conservation of the expanding shell. This lasts until the remnant is stopped, fragments and merges with the ISM. Typical order of extensions of SNRs are a few 10 pc. If more than a single SN explode in a sequence, they can form much larger structures in the ISM, the so-called superbubbles.

spallogenic	Nuclides produced from a spallation reaction are called spallogenic isotopes. During a spallation reaction, a nucleus is fragmented into smaller parts, for instance from the impact of primary or secondary cosmic rays (which can produce cosmogenic radionuclides). The fragments consist of debris from the initial nucleus: neutrons, protons, α-particles, but also heavier products such as the long-lived radionuclides ^{10}Be and ^{26}Al, which are generated from spallogenic reactions.
spicules	Cylindrical structures found in sponges, which can be calcerous or siliceous.
s-process	**s**low neutron capture **process**: Approximately half of the nuclei heavier than iron are produced in the late phases of stars with the s-process, via neutron captures predominantly on stable isotopes. The time scale for a β-decay of a nucleus is shorter than the time-scale for another neutron capture. Neutron densities in the order of 10^7 neutrons cm^{-3} are required for the s-process. Thus, s-process nuclei are produced close to the line of stability of the chart of nuclei.
superbubble	A large (in the order of ~100 pc in diameter) bubble-like structure in the ISM can be produced by a sequence of SNe. These push the ambient ISM outwards, leaving a cavity of thin (~10^{-3} ats cm^{-3}), hot (~10^6 K) gas surrounded by a shell-like boundary. Such a supperbubble is present in the local ISM, which surrounds the Solar System (the LB). Due to a density gradient within the galaxy towards the galactic north and south pole, the superbubble shell might break and release the interior medium, which might escape the galaxy into the intergalactic medium. A galactic chimney is formed. The phenomenon of released matter falling back onto the galaxy as high velocity clouds is called a galactic fountain.
suspension	A mixture of insoluble particles within a substance (e.g. liquid). In contrast to colloids, particle sizes are large enough to settle.
terrigenous	Particles transported into the ocean of continental origin are referred to as terrigenous. These are separated from their parent rock by physical and chemical weathering processes and are subsequently eroded.
todorokite	The major constituent of diagenetic and hydrothermal nodules. It is an iron-free hydrous manganese oxide.
tropopause	In the Earth's atmosphere this is the boundary between troposphere and stratosphere. Its height depends on the latitude. At the poles the tropopause is on average 9 km above the surface of the Earth. Towards the equator its height increases up to 17 km.
UCL	**U**pper **C**entaurus **L**upus: a subgroup of the Sco-Cen association. Some of the stars, that are found within this young OB-association, belonged to the stellar moving group that passed the Solar System at an average distance of 90-100 pc 2-3 Myr ago. The age of UCL is estimated with 20-30 Myr. Stars, that exploded during the last 14 Myr within this stellar moving group, may have caused the formation of the LB as well the ^{60}Fe anomalies found on Earth and on the Moon.
US	**U**pper **S**corpius: a subgroup of the Sco-Cen association. Some of the stars, that are found within this young OB-association, belonged to the stellar moving group that passed the Solar System at an average distance of 90-100 pc 2-3 Myr ago. However, the age for US is, with 5-10 Myr, much younger than of UCL and LCC. With average distances between 130 and 160 pc, US was probably too far away to significantly contribute to the ^{60}Fe anomalies found on Earth and on the Moon.

uptake-factor	Only a fraction of an element present in the ocean is incorporated into a ferro-manganese crust. The fraction incorporated of this element to its total oceanic concentration is referred to as uptake-factor, or uptake-efficiency. The uptake-factor for iron in the ferromanganese crust 237KD was calculated to ~10 % in this work.
vernadite	In hydrogeneous Fe-Mn crusts and nodules, vernadite (δ-MnO_2) is the primary manganese-bearing mineral.
weathering	Separation of particles from parent rock. Breaking the rock surface, for instance by temperature changes and biological activity, is referred to as physical weathering. Alteration of the rock surface or production of new minerals formed of elements released from the rock is called chemical weathering.
White Dwarfs	Star with masses lower than ~8 $M_\odot$ slowly eject their envelopes in a stellar wind with approximately 10^{-8} $M_\odot$ yr^{-1}. A white dwarf remains in the center of a so-called planetary nebula. White dwarfs have diameters of a few 1000 km and are very compact objects, with densities of 10^5-10^7 g cm^{-3}. The electron degeneracy pressure prevents the white dwarf from collapsing.
Wolf-Rayet stars	Massive stars in evolved stages, (with more than 20-30 $M_\odot$) that suffer from such a strong mass loss, that their interior is exposed up to the He or C burning shell. Material of 10^{-6}-10^{-5} $M_\odot$ is ejected in stellar winds with velocities up to 2000 km s^{-1}. The sun only loses a mass of 10^{-14} $M_\odot$ yr^{-1}.

Bibliography

Akhmadaliev, S., Heller, R., Hanf, D., Rugel, G., and Merchel, S. (2013). The new 6 MV AMS-facility DREAMS at Dresden. *Nuclear Instruments and Methods in Physics Research B*, 294:5–10.

Allison, E. and Ledbetter, M. T. (1982). Timing of Bottom-Water Scour Recorded by Sedimentological Parameters in the South Australian Basin. *Marine Geology*, 46:131–147.

Altobelli, N., Kempf, S., Krüger, H., Landgraf, M., Roy, M., and Grün, E. (2005). Interstellar dust flux measurements by the Galileo dust instrument between the orbits of Venus and Mars. *Journal of Geophysical Research (Space Physics)*, 110:7102.

Andersen, A. C. (2007). Dust from AGB Stars. In Kerschbaum, F., Charbonnel, C., and Wing, R. F., editors, *Why Galaxies Care About AGB Stars: Their Importance as Actors and Probes*, volume 378 of *Astronomical Society of the Pacific Conference Series*, page 170.

Arazi, A., Faestermann, T., Niello, J. O. F., Knie, K., Korschinek, G., Poutivtsev, M., Richter, E., Rugel, G., and Wallner, A. (2006). Measurement of $Mg25(p, \gamma)Al26^g$ resonance strengths via accelerator mass spectrometry. *Physical Review C*, 74(2):025802.

Athanassiadou, T. and Fields, B. D. (2011). Penetration of nearby supernova dust in the inner solar system. *New Astronomy*, 16:229–241.

Auer, M. (2008). *Applications of ^{26}Al in Atmospheric Research*. PhD thesis, University of Vienna.

Auer, M., Kutschera, W., Priller, A., Wagenbach, D., Wallner, A., and Wild, E. M. (2007). Measurement of ^{26}Al for atmospheric and climate research and the potential of $^{26}Al/$ ^{10}Be ratios. *Nuclear Instruments and Methods in Physics Research B*, 259:595–599.

Auer, M., Wagenbach, D., Wild, E. M., Wallner, A., Priller, A., Miller, H., Schlosser, C., and Kutschera, W. (2009). Cosmogenic ^{26}Al in the atmosphere and the prospect of a $^{26}Al/^{10}Be$ chronometer to date old ice. *Earth and Planetary Science Letters*, 287:453–462.

Baroni, M., Bard, E., Petit, J.-R., Magand, O., and Bourlès, D. (2011). Volcanic and solar activity, and atmospheric circulation influences on cosmogenic ^{10}Be fallout at Vostok and Concordia (Antarctica) over the last 60 years. *Geochimica et Cosmochimica Acta*, 75:7132–7145.

Bibliography

Basu, S., Stuart, F. M., Schnabel, C., and Klemm, V. (2007). Galactic-Cosmic-Ray-Produced He3 in a Ferromanganese Crust: Any Supernova Fe60 Excess on Earth? *Physical Review Letters*, 98(14):141103.

Beech, M. (2011). The past, present and future supernova threat to Earth's biosphere. *Astrophysics and Space Science*, 336:287–302.

Beer, J., Blinov, A., Bonani, G., Hofmann, H. J., and Finkel, R. C. (1990). Use of Be-10 in polar ice to trace the 11-year cycle of solar activity. *Nature*, 347:164–166.

Benítez, N., Maíz-Apellániz, J., and Canelles, M. (2002). Evidence for Nearby Supernova Explosions. *Physical Review Letters*, 88(8):081101.

Berghöfer, T. W. and Breitschwerdt, D. (2002). The origin of the young stellar population in the solar neighborhood – A link to the formation of the Local Bubble? *Astronomy and Astrophysics*, 390:299–306.

Bianchi, S. and Schneider, R. (2007). Dust formation and survival in supernova ejecta. *Monthly Notices of the Royal Astronomical Society*, 378:973–982.

Bibron, R., Chesselet, R., Crozaz, G., Leger, G., Mennessier, J. P., and Picciotto, E. (1974). Extra-terrestrial ^{53}Mn in Antarctic ice. *Earth and Planetary Science Letters*, 21:109–116.

Bishop, S. and Egli, R. (2011). Discovery prospects for a supernova signature of biogenic origin. *Icarus*, 212:960–962.

Bouchet, P., De Buizer, J. M., Suntzeff, N. B., Danziger, I. J., Hayward, T. L., Telesco, C. M., and Packham, C. (2004). High-Resolution Mid-infrared Imaging of SN 1987A. *The Astrophysical Journal*, 611:394–398.

Bourlès, D., Raisbeck, G. M., and Yiou, F. (1989). ^{10}Be and ^{9}Be in marine sediments and their potential for dating. *Geochimica et Cosmochimica Acta*, 53:443–452.

Bourlès, D., Raisbeck, G. M., Yiou, F., Loiseaux, J. M., Lieuvin, M., Klein, J., and Middleton, R. (1984). Investigation of the possible association of ^{10}Be and ^{26}Al with biogenic matter in the marine environment. *Nuclear Instruments and Methods in Physics Research B*, 5:365–370.

Breitschwerdt, D. and de Avillez, M. A. (2006). The history and future of the Local and Loop I bubbles. *Astronomy and Astrophysics*, 452:L1–L5.

Breitschwerdt, D., de Avillez, M. A., Feige, J., and Dettbarn, C. (2012). Interstellar medium simulations. *Astronomische Nachrichten*, 333:486.

Broekaert, J. A. C. (2005). *Analytical Atomic Spectrometry with Flames and Plasmas*. WILEY-VCH Verlag GmbH & Co.

Brownlee, D. E. (1985). Cosmic dust - Collection and research. *Annual Review of Earth and Planetary Sciences*, 13:147–173.

Cherchneff, I. (2014). Dust production in Supernovae. *ArXiv e-prints*.

Chieffi, A. and Limongi, M. (2013). Pre-supernova Evolution of Rotating Solar Metallicity Stars in the Mass Range 13-120 $M_\odot$ and their Explosive Yields. *The Astrophysical Journal*, 764:21.

Chmeleff, J., von Blanckenburg, F., Kossert, K., and Jakob, D. (2010). Determination of the ^{10}Be half-life by multicollector ICP-MS and liquid scintillation counting. *Nuclear Instruments and Methods in Physics Research B*, 268:192–199.

Christl, M., Vockenhuber, C., Kubik, P. W., Wacker, L., Lachner, J., Alfimov, V., and Synal, H.-A. (2013). The ETH Zurich AMS facilities: Performance parameters and reference materials. *Nuclear Instruments and Methods in Physics Research B*, 294:29–38.

Clarke, C. J. and Carswell, R. F. (2007). *Principles of Astrophysical Fluid Dynamics*. Cambridge University Press.

Cook, D. L., Berger, E., Faestermann, T., Herzog, G. F., Knie, K., Korschinek, G., Poutivtsev, M., Rugel, G., and Serefiddin, F. (2009). ^{60}Fe, ^{10}Be, and ^{26}Al in Lunar Cores 12025/8 and 60006/7: Search for a Nearby Supernova. In *Lunar and Planetary Institute Science Conference Abstracts*, volume 40 of *Lunar and Planetary Institute Science Conference Abstracts*, page 1129.

Dauphas, N., Cook, D. L., Sacarabany, A., Fröhlich, C., Davis, A. M., Wadhwa, M., Pourmand, A., Rauscher, T., and Gallino, R. (2008). Iron 60 Evidence for Early Injection and Efficient Mixing of Stellar Debris in the Protosolar Nebula. *The Astrophysical Journal*, 686:560–569.

deMenocal, P. B. (2011). Climate and Human Evolution. *Science*, 331:540–542.

Diehl, R., Halloin, H., Kretschmer, K., Lichti, G. G., Schönfelder, V., Strong, A. W., von Kienlin, A., Wang, W., Jean, P., Knödlseder, J., Roques, J.-P., Weidenspointner, G., Schanne, S., Hartmann, D. H., Winkler, C., and Wunderer, C. (2006). Radioactive ^{26}Al from massive stars in the Galaxy. *Nature*, 439:45–47.

Diehl, R., Hartmann, D. H., and Prantzos, N., editors (2011). *Astronomy with Radioactivities*, volume 812 of *Lecture Notes in Physics, Berlin Springer Verlag*.

Diehl, R., Lang, M., Kretschmer, K., and Wang, W. (2008). ^{26}Al emission throughout the Galaxy. *New Astronomy Reviews*, 52:440–444.

Doherty, C. L., Gil-Pons, P., Lau, H. H. B., Lattanzio, J. C., and Siess, L. (2014). Super and massive AGB stars - II. Nucleosynthesis and yields - Z = 0.02, 0.008 and 0.004. *Monthly Notices of the Royal Astronomical Society,*, 437:195–214.

Bibliography

Ellis, J., Fields, B. D., and Schramm, D. N. (1996). Geological Isotope Anomalies as Signatures of Nearby Supernovae. *The Astrophysical Journal*, 470:1227.

EPICA community members (2004). Eight glacial cycles from an Antarctic ice core. *Nature*, 429:623–628.

Fabryka-Martin, J. T. (1988). *Production of radionuclides in the Earth and their hydrogeologic significance, with emphasis on chlorine-36 and iodine-129*. PhD thesis, University of Arizona.

Feige, J. (2010). The Connection between the Local Bubble and the ^{60}Fe Anomaly in the Deep Sea Hydrogenetic Ferromanganese Crust. Master's thesis, University of Vienna.

Feige, J., Wallner, A., Fifield, L. K., Korschinek, G., Merchel, S., Rugel, G., Steier, P., Winkler, S. R., and Golser, R. (2013). AMS measurements of cosmogenic and supernova-ejected radionuclides in deep-sea sediment cores. In *European Physical Journal Web of Conferences*, volume 63 of *European Physical Journal Web of Conferences*, page 3003.

Feige, J., Wallner, A., Winkler, S. R., Merchel, S., Fifield, L. K., Korschinek, G., Rugel, G., and Breitschwerdt, D. (2012). The Search for Supernova-Produced Radionuclides in Terrestrial Deep-Sea Archives. *Publications of the Astronomical Society of Australia*, 29:109–114.

Feige, Y., Oltman, B. G., and Kastner, J. (1968). Production rates of neutrons in soils due to natural radioactivity. *Journal of Geophysical Research*, 73:3135–3142.

Fields, B. D., Athanassiadou, T., and Johnson, S. R. (2008). Supernova Collisions with the Heliosphere. *The Astrophysical Journal*, 678:549–562.

Fields, B. D., Hochmuth, K. A., and Ellis, J. (2005). Deep-Ocean Crusts as Telescopes: Using Live Radioisotopes to Probe Supernova Nucleosynthesis. *The Astrophysical Journal*, 621:902–907.

Fifield, L. K., Tims, S. G., Fujioka, T., Hoo, W. T., and Everett, S. E. (2010). Accelerator mass spectrometry with the 14UD accelerator at the Australian National University. *Nuclear Instruments and Methods in Physics Research B*, 268:858–862.

Fimiani, L., Cook, D. L., Faestermann, T., Gomez Guzman, J. M., Hain, K., Herzog, G. F., Knie, K., Korschinek, G., Ligon, B., Ludwig, P., Park, J., Reedy, R. C., and Rugel, G. (2014). Evidence for Deposition of Interstellar Material on the Lunar Surface. In *Lunar and Planetary Science Conference*, volume 45 of *Lunar and Planetary Science Conference*, page 1778.

Fimiani, L., Cook, D. L., Faestermann, T., Gomez Guzman, J. M., Hain, K., Herzog, G. F., Korschinek, G., Ligon, B., Ludwig, P., Park, J., Reedy, R. C., and Rugel, G. (2012). Sources of Live ^{60}Fe, ^{10}Be, and ^{26}Al in Lunar Core 12025, Core 15008, Skim Sample 69921, Scoop Sample 69941, and Under-Boulder Sample 69961. In *Lunar and*

Planetary Science Conference, volume 43 of *Lunar and Planetary Science Conference*, page 1279.

Fischer, H., Severinghaus, J., Brook, E., Wolff, E., Albert, M., Alemany, O., Arthern, R., Bentley, C., Blankenship, D., Chappellaz, J., Creyts, T., Dahl-Jensen, D., Dinn, M., Frezzotti, M., Fujita, S., Gallee, H., Hindmarsh, R., Hudspeth, D., Jugie, G., Kawamura, K., Lipenkov, V., Miller, H., Mulvaney, R., Parrenin, F., Pattyn, F., Ritz, C., Schwander, J., Steinhage, D., van Ommen, T., and Wilhelms, F. (2013). Where to find 1.5 million yr old ice for the ipics "oldest-ice" ice core. *Climate of the Past*, 9(6):2489–2505.

Fitoussi, C. and Raisbeck, G. M. (2007). Chemical procedure for extracting ^{129}I, ^{60}Fe and ^{26}Al from marine sediments: Prospects for detection of a ~2.8 My old supernova. *Nuclear Instruments and Methods in Physics Research B*, 259:351–358.

Fitoussi, C., Raisbeck, G. M., Knie, K., Korschinek, G., Faestermann, T., Goriely, S., Lunney, D., Poutivtsev, M., Rugel, G., Waelbroeck, C., and Wallner, A. (2008). Search for Supernova-Produced Fe60 in a Marine Sediment. *Physical Review Letters*, 101(12):121101.

Frakes, L. A. (1971). USNS Eltanin Cruises 32-45 , core descriptions. *Sedimentology Research Laboratory Contribution*, 33:105.

Frakes, L. A. (1973). USNS Eltanin Cruises 47-54 , sediment descriptions. *Sedimentology Research Laboratory Contribution*, 37:259.

Fry, B. J., Fields, B. D., and Ellis, J. R. (2014). Astrophysical Shrapnel: Discriminating Among Extra-solar Sources of Live Radioactive Isotopes. *ArXiv e-prints*.

Fuchs, B., Breitschwerdt, D., de Avillez, M. A., Dettbarn, C., and Flynn, C. (2006). The search for the origin of the Local Bubble redivivus. *Monthly Notices of the Royal Astronomical Society*, 373:993–1003.

Gall, C., Hjorth, J., Watson, D., Dwek, E., Maund, J. R., Fox, O., Leloudas, G., Malesani, D., and Day-Jones, A. C. (2014). Rapid formation of large dust grains in the luminous supernova 2010jl. *Nature*, 511:326–329.

Gall, L., Williams, H. M., Siebert, C., Halliday, A. N., Herrington, R. J., and Hein, J. R. (2013). Nickel isotopic compositions of ferromanganese crusts and the constancy of deep ocean inputs and continental weathering effects over the Cenozoic. *Earth and Planetary Science Letters*, 375:148–155.

Gehrels, N., Laird, C. M., Jackman, C. H., Cannizzo, J. K., Mattson, B. J., and Chen, W. (2003). Ozone Depletion from Nearby Supernovae. *The Astrophysical Journal*, 585:1169–1176.

Genge, M. J., Engrand, C., Gounelle, M., and Taylor, S. (2008). The classification of micrometeorites. *Meteoritics and Planetary Science*, 43:497–515.

Bibliography

Gladkis, L. G., Fifield, L. K., Morton, C. R., Barrows, T. T., and Tims, S. G. (2007). Manganese-53: Development of the AMS technique for exposure-age dating applications. *Nuclear Instruments and Methods in Physics Research B*, 259:236–240.

Goff, J., Chagué-Goff, C., Archer, M., Dominey-Howes, D., and Turney, C. (2012). The Eltanin asteroid impact: possible South Pacific palaeomegatsunami footprint and potential implications for the Pliocene-Pleistocene transition. *Journal of Quaternary Science*, 27:660–670.

Gomez, H. (2013). Dust in supernova remnants. In *Proceedings of The Life Cycle of Dust in the Universe: Observations, Theory, and Laboratory Experiments (LCDU2013)*.

Gomez, H. (2014). Astrophysics: Survival of the largest. *Nature*, 511:296–297.

Gradstein, F. M. and, O. J. G., Schmitz, M. D., and Ogg, G. M., editors (2012). *The Geological Time Scale 2012*. Elsevier.

Grindlay, G., Mora, J., de Loos-Vollebregt, M., and Vanhaecke, F. (2013). A systematic study on the influence of carbon on the behavior of hard-to-ionize elements in inductively coupled plasma-mass spectrometry. *Spectrochimica Acta*, 86:42–49.

Gruen, E., Gustafson, B., Mann, I., Baguhl, M., Morfill, G. E., Staubach, P., Taylor, A., and Zook, H. A. (1994). Interstellar dust in the heliosphere. *Astronomy and Astrophysics*, 286:915–924.

Halbach, P. (1986). Processes controlling the heavy metal distribution in pacific ferromanganese nodules and crusts. *Geologische Rundschau*, 75:235–247.

Hays, J. D. (1965). Radiolaria and Late Tertiary and Quaternary History of Antarctic Seas. *Antarctic Research Series*, 5:125–183.

Hays, J. D. and Obdyke, N. D. (1967). Antarctic radiolaria, magnetic reversals, and climatic change. *Science*, 138:1001–1011.

Heikkilä, U., Beer, J., Abreu, J. A., and Steinhilber, F. (2013). On the Atmospheric Transport and Deposition of the Cosmogenic Radionuclides (^{10}Be): A Review. *Space Science Reviews*, 176:321–332.

Hein, J. R. and Koschinsky, A. (2014). *Treatise on Geochemistry*, chapter Deep-Ocean Ferromanganese Crusts and Nodules, pages 273–291. Elsevier Ltd, 2nd edition edition.

Hein, J. R., Koschinsky, A., B. M., Manheim, F. T., Kang, J.-K., and Roberts, L. (2000). *Handbook of Marine Mineral Deposits*, chapter Cobalt-rich ferromanganese crusts in the Pacific, pages 239–279. CRC Marine Science Series.

Henderson, G. M., Heinze, C., Anderson, R. F., and Winguth, A. M. E. (1999). Global distribution of the ^{230}Th flux to ocean sediments constrained by GCM modelling. *Deep Sea Research Part I: Oceanographic Research*, 46:1861–1893.

Henken-Mellies, W. U., Beer, J., Heller, F., Hsü, K. J., Shen, C., Bonani, G., Hofmann, H. J., Suter, M., and Wölfli, W. (1990). ^{10}Be and ^{9}Be in South Atlantic DSDP Site 519: Relation to geomagnetic reversals and to sediment composition. *Earth and Planetary Science Letters*, 98:267–276.

Hofmann, H. J., Beer, J., Bonani, G., Von Gunten, H. R., Raman, S., Suter, M., Walker, R. L., Wölfli, W., and Zimmermann, D. (1987). ^{10}Be: Half-life and AMS-standards. *Nuclear Instruments and Methods in Physics Research B*, 29:32–36.

Honda, M. and Imamura, M. (1971). Half-Life of Mn^{53}. *Physical Review C*, 4:1182–1188.

Howe, P., Malcolm, H., and Dobson, S. (2004). Manganese and its compounds: Environmental aspects. *Concise International Chemical Assessment Document 63*.

Huss, G. R., Meyer, B. S., Srinivasan, G., Goswami, J. N., and Sahijpal, S. (2009). Stellar sources of the short-lived radionuclides in the early solar system. *Geochimica et Cosmochimica Acta*, 73:4922–4945.

Imamura, M., Inoue, T., Nishitzumi, K., and Tanaka, S. (1979). ^{53}MN in Deep-Sea Sediment Cores - AN Indicator of Past Solar Activity. *International Cosmic Ray Conference*, 2:304.

Jauhari, P. and Pattan, J. N. (2000). *Handbook of Marine Mineral Deposits*, chapter Ferromanganese Nodules from the Central Indian Ocean Basin, pages 171–195. CRC Marine Science Series.

Jones, A. P., Tielens, A. G. G. M., Hollenbach, D. J., and McKee, C. F. (1994). Grain destruction in shocks in the interstellar medium. *The Astrophysical Journal*, 433:797–810.

Kadko, D. (1980). ^{230}Th, ^{226}Ra and ^{222}Rn in abyssal sediments. *Earth and Planetary Science Letters*, 49:360–380.

Kahn, F. D. (1998). The Galactic Fountain. In Breitschwerdt, D., Freyberg, M. J., and Truemper, J., editors, *IAU Colloq. 166: The Local Bubble and Beyond*, volume 506 of *Lecture Notes in Physics, Berlin Springer Verlag*, pages 483–494.

Kennett, J. P. and Watkins, N. D. (1976). Regional deep-sea dynamic processes recorded by late Cenozoic sediments of the southeastern Indian Ocean. *Geological Society of America Bulletin*, 87:321.

Knie, K., Faestermann, T., and Korschinek, G. (1997). AMS at the Munich gas-filled analyzing magnet system GAMS. *Nuclear Instruments and Methods in Physics Research B*, 123:128–131.

Knie, K., Korschinek, G., Faestermann, T., Dorfi, E. A., Rugel, G., and Wallner, A. (2004). ^{60}Fe Anomaly in a Deep-Sea Manganese Crust and Implications for a Nearby Supernova Source. *Physical Review Letters*, 93(17):171103.

Bibliography

Knie, K., Korschinek, G., Faestermann, T., Wallner, C., Scholten, J., and Hillebrandt, W. (1999a). Indication for Supernova Produced ^{60}Fe Activity on Earth. *Physical Review Letters*, 83:18–21.

Knie, K., Merchel, S., Korschinek, G., Faestermann, T., Herpers, U., Gloris, M., and Michel, R. (1999b). AMS measurements and model calculations of iron-60 production rates in meteorites. *Meteoritics and Planetary Science*, 34:729–734.

Koide, M. and Goldberg, E. D. (1963). Uranium-234/uranium-238 ratios in sea water. *Progress in Oceanography*, 3:173–177.

Korschinek, G., Bergmaier, A., Faestermann, T., Gerstmann, U. C., Knie, K., Rugel, G., Wallner, A., Dillmann, I., Dollinger, G., von Gostomski, C. L., Kossert, K., Maiti, M., Poutivtsev, M., and Remmert, A. (2010). A new value for the half-life of ^{10}Be by Heavy-Ion Elastic Recoil Detection and liquid scintillation counting. *Nuclear Instruments and Methods in Physics Research B*, 268:187–191.

Korschinek, G., Faestermann, T., Knie, K., and Schmidt, C. (1996). ^{60}Fe, a Promising AMS Isotope for Many Applications. *Radiocarbon*, 38(1):68–69.

Koschinsky, A. and Halbach, P. (1995). Sequential leaching of marine ferromanganese precipitates: Genetic implications. *Geochimica et Cosmochimica Acta*, 59:5113–5132.

Kotak, R. (2014). The dusty debate: core-collapse supernovae and dust. In Ray, A. and McCray, R. A., editors, *IAU Symposium*, volume 296 of *IAU Symposium*, pages 144–150.

Kozasa, T., Nozawa, T., Tominaga, N., Umeda, H., Maeda, K., and Nomoto, K. (2009). Dust in Supernovae: Formation and Evolution. In Henning, T., Grün, E., and Steinacker, J., editors, *Cosmic Dust - Near and Far*, volume 414 of *Astronomical Society of the Pacific Conference Series*, page 43.

Ku, T.-L., Knauss, K. G., and Mathieu, G. G. (1977). Uranium in open ocean: concentration and isotopic composition. *Deep Sea Research*, 24:1005–1017.

Kubik, P. W. and Christl, M. (2010). ^{10}Be and ^{26}Al measurements at the Zurich 6 MV Tandem AMS facility. *Nuclear Instruments and Methods in Physics Research B*, 268:880–883.

Kutschera, W., Billquist, P. J., Frekers, D., Henning, W., Jensen, K. J., Xiuzeng, M., Pardo, R., Paul, M., Rehm, K. E., Smither, R. K., Yntema, J. L., and Mausner, L. F. (1984). Half-life of ^{60}Fe. *Nuclear Instruments and Methods in Physics Research B*, 5:430–435.

Kutschera, W., Collon, P., Friedmann, H., Golser, R., Hille, P., Priller, A., Rom, W., Steier, P., Tagesen, S., Wallner, A., Wild, E., and Winkler, G. (1997). VERA: A new AMS facility in Vienna. *Nuclear Instruments and Methods in Physics Research Section B: Beam Interactions with Materials and Atoms*, 123(1-4):47–50.

Lachner, J. (2013). *Environmental Applications of Low-Energy Accelerator Mass Spectrometry*. PhD thesis, ETH Zürich.

Lal, D., Gallup, C. D., Somayajulu, B. L. K., Vacher, L., Caffee, M. W., Jull, A. J. T., Finkel, R. C., Speed, R. C., and Winter, A. (2005). Records of cosmogenic radionuclides ^{10}Be, ^{26}Al and ^{36}Cl in corals: First studies on coral erosion rates and potential of dating very old corals. *Geochimica et Cosmochimica Acta*, 69:5717–5728.

Lal, D. and Peters, B. (1967). Cosmic Ray Produced Radioactivity on the Earth. *Handbuch der Physik*, 46:551–612.

Lebatard, A.-E., Bourlès, D. L., Duringer, P., Jolivet, M., Braucher, R., Carcaillet, J., Schuster, M., Arnaud, N., Monié, P., Lihoreau, F., Mackaye, A. L. H. T., Vignaud, P., and Brunet, M. (2008). Cosmogenic nuclide dating of sahelanthropus tchadensis and australopithecus bahrelghazali: Mio-pliocene hominids from chad. *Proceedings of the National Academy of Sciences of the United States of America*, 105(9):3226–3231.

Leya, I., Lange, H.-J., Neumann, S., Wieler, R., and Michel, R. (2000). The production of cosmogenic nuclides in stony meteoroids by galactic cosmic ray particles. *Meteoritics and Planetary Science*, 35:259–286.

Limongi, M. and Chieffi, A. (2006). The Nucleosynthesis of ^{26}Al and ^{60}Fe in Solar Metallicity Stars Extending in Mass from 11 to 120 M$_{\odot}$: The Hydrostatic and Explosive Contributions. *The Astrophysical Journal*, 647:483–500.

Love, S. G. and Brownlee, D. E. (1991). Heating and thermal transformation of micrometeoroids entering the earth's atmosphere. *ICARUS*, 89:26–43.

L'Annunziata, M. F., editor (2012). *Handbook of Radioactivity Analysis*. Elsevier, Academic Press.

Ludwig, P., Egli, R., Bishop, S., Chernenko, V., Frederichs, T., Rugel, G., Merchel, S., and Orgeira, M. J. (2013). Characterization of primary and secondary magnetite in marine sediment by combining chemical and magnetic unmixing techniques. *Global and Planetary Change*, 110:321–339.

Lugaro, M., Heger, A., Osrin, D., Goriely, S., Zuber, K., Karakas, A. I., Gibson, B. K., Doherty, C. L., Lattanzio, J. C., and Ott, U. (2014). Stellar origin of the 182Hf cosmochronometer and the presolar history of solar system matter. *ArXiv e-prints*.

Lugaro, M. and Karakas, A. I. (2008). ^{26}Al and ^{60}Fe yields from AGB stars. *New Astronomy Reviews*, 52:416–418.

Lyle, M. W. and Dymond, J. (1976). Metal accumulation rates in the southeast pacific - errors introduced from assumed bulk densities. *Earth and Planetary Science Letters*, 30:164–168.

Bibliography

Maíz-Apellániz, J. (2001). The Origin of the Local Bubble. *The Astrophysical Journal*, 560:L83–L86.

Masarik, J. and Beer, J. (2009). An updated simulation of particle fluxes and cosmogenic nuclide production in the Earth's atmosphere. *Journal of Geophysical Research (Atmospheres)*, 114:11103.

Meisel, D. D., Janches, D., and Mathews, J. D. (2002). Extrasolar Micrometeors Radiating from the Vicinity of the Local Interstellar Bubble. *The Astrophysical Journal*, 567:323–341.

Ménabréaz, L., Bourlès, D. L., and Thouveny, N. (2012). Amplitude and timing of the Laschamp geomagnetic dipole low from the global atmospheric ^{10}Be overproduction: Contribution of authigenic ^{10}Be/^{9}Be ratios in west equatorial Pacific sediments. *Journal of Geophysical Research (Solid Earth)*, 117:11101.

Merchel, S., Faestermann, T., Herpers, U., Knie, K., Korschinek, G., Leya, I., Michel, R., Rugel, G., and Wallner, C. (2000). Thin- and thick-target cross sections for the production of ^{53}Mn and ^{60}Fe. *Nuclear Instruments and Methods in Physics Research B*, 172:806–811.

Merchel, S. and Herpers, U. (1999). An Update on Radiochemical Separation Techniques for the Determination of Long-Lived Radionuclides via Accelerator Mass Spectrometry. *Geochimica et Cosmochimica Acta*, 84:215–219.

Meyer, B. S. (2005). Synthesis of Short-lived Radioactivities in a Massive Star. In Krot, A. N., Scott, E. R. D., and Reipurth, B., editors, *Chondrites and the Protoplanetary Disk*, volume 341 of *Astronomical Society of the Pacific Conference Series*, page 515.

Michel, R., Leya, I., and Borges, L. (1996). Production of cosmogenic nuclides in meteoroids: Accelerator experiments and model calculations to decipher the cosmic ray record in extraterrestrial matter. *Nuclear Instruments and Methods in Physics Research B*, 113:434–444.

Middleton, R. (1990). *A Negative-Ion Cookbook*.

Middleton, R., Klein, J., Raisbeck, G. M., and Yiou, F. (1983). Accelerator mass spectrometry with ^{26}Al. *Nuclear Instruments and Methods in Physics Research*, 218:430–438.

Morgan, H. L. and Edmunds, M. G. (2003). Dust formation in early galaxies. *Monthly Notice of the Royal Astronomical Society*, 343:427–442.

Murray, S. J. and Renard, A. F. (1891). *Report on deep-Sea Deposits Based on the Specimens Collected During the Voyage of H. M. S. Challenger in the Years 1872 to 1876.*

Neuhäuser, R., Tetzlaff, N., Eisenbeiss, T., and Hohle, M. M. (2012). On identifying the neutron star that was born in the supernova that placed ^{60}Fe onto the Earth. *Journal of Physics Conference Series*, 337(1):012052.

Norman, E. B., Chupp, T. E., Lesko, K. T., Schwalbach, P., and Grant, P. J. (1982). ^{26g,m}Al production cross sections from the ^{23}Na(α, n) ^{26}Al reaction. *Nuclear Physics A*, 390:561–572.

Norris, T. L., Gancarz, A. J., Rokop, D. J., and Thomas, K. W. (1983). Half-life of ^{26}Al. *Journal of Geophysical Research*, 88:331.

Nozawa, T., Kozasa, T., Umeda, H., Maeda, K., Nomoto, K., Tominaga, N., Yamasawa, D., Habe, A., and Hirashita, H. (2012). Supernovae as sources of dust in the early universe. *Memorie della Societa Astronomica Italiana*, 83:77.

Orians, K. J. and Bruland, K. W. (1986). The biogeochemistry of aluminum in the Pacific Ocean. *Earth and Planetary Science Letters*, 78:397–410.

Ott, U. and Hoppe, P. (2007). Pre-solar grains in meteorites and interplanetary dust: an overview. *Highlights of Astronomy*, 14:341–344.

Overholt, A. C. and Melott, A. L. (2013). Cosmogenic nuclide enhancement via deposition from long-period comets as a test of the Younger Dryas impact hypothesis. *Earth and Planetary Science Letters*, 377:55–61.

Paul, M., Glagola, B. G., Henning, W., Keller, J. G., Kutschera, W., Liu, Z., Rehm, K. E., Schneck, B., and Siemssen, R. H. (1989). Heavy ion separation with a gas-filled magnetic spectrograph. *Nuclear Instruments and Methods in Physics Research A*, 277:418–430.

Paul, M., Valenta, A., Ahmad, I., Berkovits, D., Bordeanu, C., Ghelberg, S., Hashimoto, Y., Hershkowitz, A., Jiang, S., Nakanishi, T., and Sakamoto, K. (2003). A window on nucleosynthesis through detection of short-lived radionuclides. *Nuclear Physics A*, 719:29.

Paul, M., Valenta, A., Ahmad, I., Berkovits, D., Bordeanu, C., Ghelberg, S., Hashimoto, Y., Hershkowitz, A., Jiang, S., Nakanishi, T., and Sakamoto, K. (2007). An upper limit to interstellar ^{244}Pu abundance as deduced from radiochemical search in deep-sea sediment: An account. *Journal of Radioanalytical and Nuclear Chemistry*, 272:243–245.

Pavicevic, M. K., Wild, E. M., Amthauer, G., Berger, M., Boev, B., Kutschera, W., Priller, A., Prohaska, T., and Steffan, I. (2004). AMS measurements of ^{26}Al in quartz to assess the cosmic ray background for the geochemical solar neutrino experiment LOREX. *Nuclear Instruments and Methods in Physics Research B*, 223:660–667.

Petuch, E. J. (1995). Molluscan Diversity in the Late Neogene of Florida: Evidence for a Two-Staged Mass Extinction. *Science*, 270:275–277.

Poutivtsev, M. (2007). *Extraterrestrisches ^{53}Mn in hydrogenetischen Mangankrusten*. PhD thesis, Technische Universität München.

Bibliography

Poutivtsev, M., Dillmann, I., Faestermann, T., Knie, K., Korschinek, G., Lachner, J., Meier, A., Rugel, G., and Wallner, A. (2010). Highly sensitive AMS measurements of ^{53}Mn. *Nuclear Instruments and Methods in Physics Research B*, 268:756–758.

Raisbeck, G. M. and Yiou, F. (1984). Production of long-lived cosmogenic nuclei and their applications. *Nuclear Instruments and Methods in Physics Research B*, 5:91–99.

Raisbeck, G. M., Yiou, F., Fruneau, M., Loiseaux, J. M., Lieuvin, M., and Ravel, J. C. (1981). Cosmogenic Be-10/Be-7 as a probe of atmospheric transport processes. *Geophysical Research Letters*, 8:1015–1018.

Raiswell, R. (2011). Iron Transport from the Continents to the Open Ocean: The Aging-Rejuvenation Cycle. *Elements*, 7:101–106.

Rauscher, T., Heger, A., Hoffman, R. D., and Woosley, S. E. (2002). Nucleosynthesis in Massive Stars with Improved Nuclear and Stellar Physics. *The Astrophysical Journal*, 576:323–348.

Reeves, H. (1994). On the origin of the light elements (Z<6). *Reviews of Modern Physics*, 66:193–216.

Rho, J., Kozasa, T., Reach, W. T., Smith, J. D., Rudnick, L., DeLaney, T., Ennis, J. A., Gomez, H., and Tappe, A. (2008). Freshly Formed Dust in the Cassiopeia A Supernova Remnant as Revealed by the Spitzer Space Telescope. *The Astrophysical Journal*, 673:271–282.

Robert, C. M., editor (2008). *Developments in Marine Geology Vol. 3, Global Sedimentology of the Ocean:An Interplay between Geodynamics and Paleoenvironment*. Elsevier.

Robertson, H. P. (1937). Dynamical effects of radiation in the solar system. *Monthly Notices of the Royal Astronomical Society*, 97:423.

Rowlands, K., Gomez, H. L., Dunne, L., Aragón-Salamanca, A., Dye, S., Maddox, S., da Cunha, E., and Werf, P. v. d. (2014). The dust budget crisis in high-redshift submillimetre galaxies. *Monthly Notice of the Royal Astronomical Society*, 441:1040–1058.

Rugel, G., Faestermann, T., Knie, K., Korschinek, G., Poutivtsev, M., Schumann, D., Kivel, N., Günther-Leopold, I., Weinreich, R., and Wohlmuther, M. (2009). New Measurement of the Fe60 Half-Life. *Physical Review Letters*, 103(7):072502.

Salpeter, E. E. (1955). The Luminosity Function and Stellar Evolution. *The Astrophysical Journal*, 121:161.

Samworth, E. A., Warburton, E. K., and Engelbertink, G. A. (1972). Beta Decay of the ^{26}Al Ground State. *Physical Review C*, 5:138–142.

Sarangi, A. and Cherchneff, I. (2013a). Condensation of dust in supernova ejecta. In *Proceedings of The Life Cycle of Dust in the Universe: Observations, Theory, and Laboratory Experiments (LCDU2013)*.

Sarangi, A. and Cherchneff, I. (2013b). The Chemically Controlled Synthesis of Dust in Type II-P Supernovae. *The Astrophysical Journal*, 776:107.

Schmidt, E. (2013). AMS detection of ^{10}Be with a SiN-foil stack. Master's thesis, University of Vienna.

Scholten, J., Scott, S. D., Garbe-Schönberg, D., Fietzke, J., Blanz, T., and Kennedy, C. B. (2004). *Oceanic Hotspots*, chapter Hydrothermal iron and manganese crusts from the Pitcairn hot-spot region, pages 375–405. Springer Verlag, Berlin-Heidelberg.

Sedov, L. I. (1993). *Similarity and Dimensional Methods in Mechanics, 10th Edition*. CRC Press, Inc.

Segl, M., Mangini, A., Bonani, G., Hofmann, H. J., Nessi, M., Suter, M., Wölfli, W., Friedrich, G., Plüger, W. L., Wiechowski, A., and Beer, J. (1984). ^{10}Be-dating of a manganese crust from Central North Pacific and implications for ocean palaeocirculation. *Nature*, 309:540–543.

Sharma, P., Klein, J., Middleton, R., and Church, T. M. (1987a). ^{26}Al and ^{10}Be in authigenic marine minerals. *Nuclear Instruments and Methods in Physics Research B*, 29:335–340.

Sharma, P., Mahannah, R., Moore, W. S., Ku, T. L., and Southon, J. R. (1987b). Transport of ^{10}Be and ^{9}Be in the ocean. *Earth and Planetary Science Letters*, 86:69–76.

Sharma, P. and Middleton, R. (1989). Radiogenic production of ^{10}Be and ^{26}Al in uranium and thorium ores: Implications for studying terrestrial samples containing low levels of ^{10}Be and ^{26}Al. *Geochimica et Cosmochimica Acta*, 53:709–716.

Sharma, P. and Somayajulu, B. L. K. (1982). ^{10}Be dating of large manganese nodules from world oceans. *Earth and Planetary Science Letters*, 59:235–244.

Shibata, Y., Tanaka, A., Yoneda, M., Uehiro, T., Kawai, T., Morita, M., and Kobayashi, K. (2000). ^{26}Al/ ^{10}Be method for dating of sediment core samples from Lake Baikal. *Nuclear Instruments and Methods in Physics Research B*, 172:827–831.

Shuvalov, V. and Gersonde, R. (2014). Constraints on interpretation of the Eltanin impact from numerical simulations. *Meteoritics and Planetary Science*, 49:1171–1185.

Silvia, D. W., Smith, B. D., and Shull, J. M. (2010). Numerical Simulations of Supernova Dust Destruction. I. Cloud-crushing and Post-processed Grain Sputtering. *The Astrophysical Journal*, 715:1575–1590.

Simpson, J. A. (1983). Introduction to the galactic cosmic radiation. In Shapiro, M. M., editor, *NATO ASIC Proc. 107: Composition and Origin of Cosmic Rays*, pages 1–24.

Snowden, S. L., Cox, D. P., McCammon, D., and Sanders, W. T. (1990). A model for the distribution of material generating the soft X-ray background. *The Astrophysical Journal*, 354:211–219.

Bibliography

Steier, P., Golser, R., Liechtenstein, V., Kutschera, W., Priller, A., Vockenhuber, C., and Wallner, A. (2005). Opportunities and limits of AMS with 3-MV tandem accelerators. *Nuclear Instruments and Methods in Physics Research B*, 240:445–451.

Stoffers, P., Glasby, G. P., and Frenzel, G. (1984). Comparison of the characteristics of manganese micronodules from the equatorial and South-West Pacific. *TMPM Tschermaks Mineralogische und Petrographische Mitteilungen, Volume 33, Issue 1, pp.1-23*, 33:1–23.

Stuart, F. M. and Lee, M. R. (2012). Micrometeorites and extraterrestrial He in a ferromanganese crust from the Pacific Ocean. *Chemical Geology*, 322.

Temim, T., Sonneborn, G., Dwek, E., Arendt, R. G., Gehrz, R. D., Slane, P., and Roellig, T. L. (2012). Properties and Spatial Distribution of Dust Emission in the Crab Nebula. *The Astrophysical Journal*, 753:72.

Tetzlaff, N., Torres, G., Neuhäuser, R., and Hohle, M. M. (2013). The neutron star born in the Antlia supernova remnant. *Monthly Notices of the Royal Astronomical Society*, 435:879–884.

Thomas, J. H., Rau, R. L., Skelton, R. T., and Kavanagh, R. W. (1984). Half-life of ^{26}Al. *Physical Review C (Nuclear Physics)*, 30:385–387.

Timmes, F. X., Woosley, S. E., Hartmann, D. H., Hoffman, R. D., Weaver, T. A., and Matteucci, F. (1995). 26Al and 60Fe from Supernova Explosions. *The Astrophysical Journal*, 449:204.

Todini, P. and Ferrara, A. (2001). Dust formation in primordial Type II supernovae. *Monthly Notices of the Royal Astronomical Society*, 325:726–736.

Trappitsch, R. and Leya, I. (2013). Cosmogenic production rates and recoil loss effects in micrometeorites and interplanetary dust particles. *Meteoritics and Planetary Science*, 48:195–210.

von Stackelberg, U. (2000). *Handbook of Marine Mineral Deposits*, chapter Manganese Nodules of the Peru Basin, pages 197–238. CRC Marine Science Series.

Wallner, A., Ikeda, Y., Kutschera, W., Priller, A., Steier, P., Vonach, H., and Wild, E. (2000). Precision and accuracy of ^{26}Al measurements at VERA. *Nuclear Instruments and Methods in Physics Research B*, 172:382–387.

Wallner, C., Faestermann, T., Gerstmann, U., Hillebrandt, W., Knie, K., Korschinek, G., Lierse, C., Pomar, C., and Rugel, G. (2000). Development of a very sensitive AMS method for the detection of supernova-produced longliving actinide nuclei in terrestrial archives. *Nuclear Instruments and Methods in Physics Research B*, 172:333–337.

Wallner, C., Faestermann, T., Gerstmann, U., Knie, K., Korschinek, G., Lierse, C., and Rugel, G. (2004). Supernova produced and anthropogenic ^{244}Pu in deep sea manganese encrustations. *New Astronomy Reviews*, 48:145–150.

Wang, L., Ku, T. L., Luo, S., Southon, J. R., and Kusakabe, M. (1996). ^{26}Al-^{10}Be systematics in deep-sea sediments. *Geochimica et Cosmochimica Acta*, 60(1):109–119.

Wang, W. (2008). ^{60}Fe and Massive Stars. In Deng, L. and Chan, K. L., editors, *IAU Symposium*, volume 252 of *IAU Symposium*, pages 333–338.

Weigert, A. and Wendker, H. (2001). *Astronomie und Astrophysik*. VCH Verlagsgesellschaft mbH.

Welz, B. and Sperling, M. (1997). *Atomabsorptionsspektrometrie*. WILEY-VCH Verlag GmbH.

Westphal, A. J., Bechtel, H. A., Brenker, F. E., Butterworth, A. L., Flynn, G., Frank, D. R., Gainsforth, Z., Hillier, J. K., Postberg, F., Simionovici, A. S., Sterken, V. J., Stroud, R. M., Allen, C., Anderson, D., Ansari, A., Bajt, S., Bastien, R. K., Bassim, N., Borg, J., Bridges, J., Brownlee, D. E., Burchell, M., Burghammer, M., Changela, H., Cloetens, P., Davis, A. M., Doll, R., Floss, C., Grün, E., Heck, P. R., Hoppe, P., Hudson, B., Huth, J., Hvide, B., Kearsley, A., King, A. J., Lai, B., Leitner, J., Lemelle, L., Leroux, H., Leonard, A., Lettieri, R., Marchant, W., Nittler, L. R., Ogliore, R., Ong, W. J., Price, M. C., Sandford, S. A., Tresseras, J.-A. S., Schmitz, S., Schoonjans, T., Silversmit, G., Solé, V. A., Srama, R., Stadermann, F., Stephan, T., Stodolna, J., Sutton, S., Trieloff, M., Tsou, P., Tsuchiyama, A., Tyliszczak, T., Vekemans, B., Vincze, L., Korff, J., Wordsworth, N., Zevin, D., and Zolensky, M. E. (2014). Final reports of the Stardust Interstellar Preliminary Examination. *Meteoritics and Planetary Science*, 49:1720–1733.

Willenbring, J. K. and von Blanckenburg, F. (2010). Long-term stability of global erosion rates and weathering during late-Cenozoic cooling. *Nature*, 465:211–214.

Witze, A. (2013). Supernova left its mark in ancient bacteria. Nature News, Nature Publishing Group.

Woosley, S. E. and Heger, A. (2007). Nucleosynthesis and remnants in massive stars of solar metallicity. *Physics Reports*, 442:269–283.

Woosley, S. E., Heger, A., and Weaver, T. A. (2002). The evolution and explosion of massive stars. *Reviews of Modern Physics*, 74:1015–1071.

Woosley, S. E. and Weaver, T. A. (1995). The Evolution and Explosion of Massive Stars. II. Explosive Hydrodynamics and Nucleosynthesis. *The Astrophysical Journal Supplement Series*, 101:181.

Young, E. D. (2014). Inheritance of solar short- and long-lived radionuclides from molecular clouds and the unexceptional nature of the solar system. *Earth and Planetary Science Letters*, 392:16–27.

Ziegler, J. F., Ziegler, M. D., and Biersack, J. P. (2010). SRIM - The stopping and range of ions in matter (2010). *Nuclear Instruments and Methods in Physics Research B*, 268:1818–1823.

Acknowledgements

There are many people who deserve to be thanked for their support throughout this work, and I hope I didn't forget anyone important. I would like to thank:

Acknowledgements

- The AMS team at TUM for AMS measurements of ^{60}Fe: Peter Ludwig, Leticia Fimiani, Gunther Korschinek, and Thomas Faestermann.

- The people who carried out the stable isotope measurements: Aline Ritter and Sabrina Gurlit (HZDR) and Valéry Guillou (CEREGE).

- The Geologists who kindly answered my questions: Axel Renno, Ramon Egli (thank you for proof-reading the geology part of this thesis), Matthias M.M. Meier, and also the people at ASTER: Didier Bourlès, Regis Braucher, and Maurice Arnold, for dating and dancing in the accelerator hall.

- Helga Vincro and Anne Elisabeth Viehauser, who managed to keep an overview over all my travel accounts, when even I did not see through anymore.

- The staff at the VERA workshop: Ewald Friedl, Johann Lukas, Wolfgang Hieß, and Gabriela Obstmayer.

- Dieter Breitschwerdt, Christian Dettbarn and Michi Schulreich, who continued collaborating with me after my master thesis was finished.

- All other people at VERA who supported me: Oliver Forstner, Walter Kutschera, and the generations of students and postdocs that came and disappeared again, while I was constantly here, for lots of fun and entertainment, but also for good advice and cookies: Claudia Lederer (also thank you for proof reading of parts of this thesis), Martin Martschini, Jakob Liebl, Edith Schmidt, Josef Buchriegler (Good luck for the future!), Thomas Wieninger, Karin Eisenhuth, Leonhard Michlmayr, Kerstin Rumpelmayr, Franz Weninger, Stefan Pavetich, Johannesse (Lahner (thank you for the Port wine) & Lachner (thank you for funny Sherlock and BTTF nights)), Johanna Pitters, Magdalena Kasberger, Marco Ploner, and Tobias Moreau.

- Susi Schramm for proof reading my application for the Abschlussstipendium, which was accepted. You've done well!

- The people at the Observatory, who did not forget me, even though I cheated on them.

- My family and my friends, who were always there for me and supported my decisions.

- I attach utmost importance on thanking all the people, who drank coffee with me at different places around the world!

Curriculum vitae

Education and Work Experience

1988 – 1996	Grund- und Gesamtschule Woltersdorf, Rüdersdorf
1996 – 1998	Gymnasium Erkner
1998 – 1999	High Pavement College, Nottingham, England
1999 – 2002	Gymnasium Erkner and final exams
2002 – 2005	Bachelor studies at the University of Vienna, Austria (Astronomy), thesis title: *Extrasolare Planeten* (advisor: Univ. Prof. Dr. Rudolf Dvorak)
07 - 08 2005	Work experience at the Astrophysikalisches Institut Potsdam (AIP), Germany, topic: *AGN-Hostgalaxien im Great Observatories Origins Deep Survey* (advisor: Prof. Dr. Lutz Wisotzky)
2005 – 2010	Magister studies at the University of Vienna, Austria (Astronomy), thesis title: *The Connection between the Locabl Bubble and the ^{60}Fe Anomaly in the Deep Sea Hydrogenetic Ferromanganese Crust* (advisor: Prof. Dr. Dieter Breitschwerdt)
W. sem. 08/09	Studies at Albanova in Stockholm, Sweden
since 2010	PhD studies at the University of Vienna (Physics)
2011 – 2014	Teaching assistant at the University of Vienna (Nuclear Physics)

Conferences and Workshops

2009   Joint Annual Meeting of APS, SPS with SSAA and ASAA
Innsbruck, Austria
2-4 September 2009 (Poster Presentation)

Annual Fall Meeting of the Astronomischen Gesellschaft
Potsdam, Germany
21-25 September 2009, (Talk and Poster Presentation)

2010   11th Symposium on Nuclei in the Cosmos (NIC XI)
Heidelberg, Germany
19-23 Juli 2010

First EuroGENESIS Workshop, Origins of the elements and nuclear history of the universe
Dubrovnik, Croatia
24-26 November 2010, (Poster Presentation)

2011   Astronomy with Radioactivities VII
Phillip Island, Victoria, Australia
1-3 March 2011 (Talk)

AMS-12
Wellington, New Zealand
20-25 March 2011

Joint Annual Meeting of APS, SPS with SSAA and ASAA
Lausanne, Switzerland
15-17 June 2011 (Talk, Diploma Award Ceremony)

Annual meeting of the Astronomische Gesellschaft
Heidelberg, Germany
19-23 September 2011 (Poster Presentation)

CoDustMas Intra-CRP Workshop
Vienna, Austria
21-22 November 2011 (Talk)

2012   62nd Annual Meeting of the Austrian Physical Society
Graz, Austria
18-21 September 2012 (Talk)

Joint meeting "Paneth Kolloquium"
"The first 10 million years of the solar system"
Nördlingen, Germany
9-12 October 2012 (Poster Presentation)

Dust in Core-Collaps Supernovae near & far:
understanding its formation and evolution
Monte Verita - Ascona, Switzerland
5-8 November 2012 (Talk)

Dust in EuroGENESIS environments:
from primitive, massive stars to novae
Perugia, Italy
11-14 November 2012 (Talk)

2013   Heavy Ion Accelerator Symposium on Fundamental
and Applied Science - 2013 (HIAS)
Canberra, Australia
8-12 April 2013 (Plenary Talk)

THE ORIGIN OF COSMIC ELEMENTS
Past and Present Achievements, Future Challenges
Barcelona, Spain
12-15 June 2013 (Talk)

Annual MASCHE Meeting
Darmstadt, Germany
3 December 2013

2014   78th Annual Meeting of the DPG and DPG Spring Meeting
Berlin, Germany
17-21 March 2014 (2 Talks)

ATHENA Final Workshop
Menaggio, Italy
13-16 May 2014 (Talk)

13th Symposium on Nuclei in the Cosmos (NIC XIII)
Debrecen, Hungary
7-11 Juli 2014 (Poster Presentation)

AMS-13
Aix-En-Provence, France
25-29 August 2014 (Talk)

Kick-Off Meeting IBC User Selection Panel
Helmholtz-Zentrum Dresden-Rossendorf, Germany
15 October 2014 (Talk)

Summer Schools and Seminars

2010   First Summerschool of the Swiss Commission for Astronomy:
"Stars and Supernovae in galaxies"
St-Luc, Switzerland
13-17 September 2010

2011   Nuclear Reaction Networks School 2011
Abtei Frauenwörth, Frauenchiemsee, Germany
10-17 April 2011

2012	496. WE-Heraeus Seminar on "Astrophysics with modern small-scale accelerators" Physikzentrum Bad Honnef, Germany 6-10 February 2012 (Poster Presentation)
2013	Satellite School of THE ORIGIN OF COSMIC ELEMENTS Past and Present Achievements, Future Challenges Institut d'Estudis Espacials de Catalunya (IEEC), Barcelona, Spain 10-11 June 2013

Seminar Talks

2009	TU Berlin, Germany Department of Astronomy and Astrophysics (ZAA) *Supernova Relikte in der Tiefseemangankruste*
	University of Vienna, Austria Institute of Astronomy *Supernova Relics in the Deep-Sea Ferromanganese Crust*
2010	University of Heidelberg, Germany Astronomisches Rechen-Institut *The connection between the Local Bubble and the ^{60}Fe anomaly in the deep-sea hydrogenetic ferromanganese crust*
	University Jena, Germany Astrophysical Institute and University Observatory *Expansion of a Supernova-Remnant*
2011	The University of Sydney, Australia Sydney Institute for Astronomy *The Connection between the Local Bubble and the ^{60}Fe Anomaly in the deep Ocean's Crust*
	Helmholtz-Zentrum Dresden-Rossendorf, Germany Institute of Ion-Beam Physics and Material Research *Supernova-produzierte Radionuklide in Tiefseesedimenten*
2012	ETH Zurich, Switzerland Laboratory of Ion Beam Physics *The Search for Supernova-Produced Radionuclides in New Deep-Sea Sediment Samples and Preparation for AMS Measurements*
	University of Vienna, Austria Faculty of Physics – Isotope Research *Deep-Sea Astronomy: Searching for Signals of Recent Nucleosynthesis in the Local Universe with AMS*

2013	Monash University, Australia Faculty of Science *AMS Measurements of Cosmogenic and Supernova-Ejected Radionuclides in Deep-Sea Sediment Cores*
	Helmholtz-Zentrum Dresden-Rossendorf, Germany Institute of Ion-Beam Physics and Material Research *AMS Measurements of Cosmogenic and Supernova-Ejected Radionuclides in Deep-Sea Sediment Cores*
2014	Centre Européen de Recherche et d'Enseignement des Géosciences de l'Environnement (CEREGE) Aix-En-Provence, France *^{26}Al and ^{10}Be in 2 Myr old Sediment Cores from the Indian Ocean*
	University of Vienna, Austria Institut für Astrophysik *Injection of Supernova Dust into the Solar System: Exploring Traces in Deep-Sea Sediments*

Publications

2012	Breitschwerdt, D., de Avillez, M. A., **Feige, J.**, Dettbarn, C. *Interstellar medium simulations* Astronomische Nachrichten, Vol.333, Issue 5-6, p.486 (2012)
	Feige, J., Wallner, A., Winkler, S. R., Merchel, S., Fifield, L. K., Korschinek, G., Rugel, G., Breitschwerdt, D. *The Search for Supernova-Produced Radionuclides in Terrestrial Deep-Sea Archives* Publications of the Astronomical Society of Australia (PASA), Volume 29, Issue 2, pp. 109-114 (2012)
	Wallner, A., Buczak, K., Dillmann, I., **Feige, J.**, Käppeler, F., Korschinek, G., Lederer, C., Mengoni, A., Ott, U., Paul, M., Schätzel, G., Steier, P., Trautvetter, H. P. *AMS Applications in Nuclear Astrophysics: New Results for $^{13}C(n,\gamma)^{14}C$ and $^{14}N(n,p)^{14}C$* Publications of the Astronomical Society of Australia (PASA), Volume 29, Issue 2, pp. 115-120 (2012)
2013	**Feige, J.**, Wallner, A., Fifield, L. K., Korschinek, G., Merchel, S., Rugel, G., Steier, P., Winkler, S. R., Golser, R. *AMS measurements of cosmogenic and supernova-ejected radionuclides in deep-sea sediment cores* EPJ Web of Conferences, Volume 63, id. 03003 (2013)

2014	Wallner, A., Faestermann, T., **Feige, J.**, Feldstein, C., Knie, K., Korschinek, K., Kutschera, W., Ofan, A., Paul, M., Quinto, F., Rugel, G., Steier, P. *New limit of ^{244}Pu on Earth points to rarity of actinide nucleosynthesis* Nature Communications, accepted for publication

Public Outreach Activities

2009	Science Blogs (scienceblogs.de): *Tiefseeastronomie*, author: Florian Freistetter (Astrodicticum Simplex)
2013	Kix! Dein KinderuniXpress 04/2013, *Sternenstaub am Meeresgrund*, author: Susanne Schramm
2014	Bild der Wissenschaft 06/2014, *Expedition zu den Nachbarn - Die explosive Blase*, author: Thorsten Dambeck
	Science Slam Frankfurt - Goethe Slam (www.scienceslam.physikalischer-verein.de), *Tiefseeastronomie - Sternenstaub am Meeresgrund*, 4. June 2014

Awards and Research Grants

2011	Diploma Award of the Austrian Society of Astronomy and Astrophysics
2012	Best Poster Award at 496. Wilhelm und Else Heraeus-Seminar Bad Honnef, Germany
2014	Stipend (Abschlussstipendium) of the University of Vienna, period of sponsorship: March - August 2014
	Best Poster Award at Nuclei in the Cosmos (NIC XIII), Debrecen, Hungary

Further Activities

2007 – 2010	Employment at the Planetarium Vienna and the Urania Public Observatory in Vienna
2009	Illustrations of the children's book "Die kleine Sonne auf großer Fahrt" by Werner Gruber, Natascha Riahi, and Christian Rupp
2011	Member of Local Organization Committee of CoDustMas Intra-CRP Workshop, Vienna, Austria, 21-22 November 2011
since 2011	Illustrations for booklets of Die Wiener Volkshochschulen, VHS Kindersommer (www.vhs.at/sommerprogramm/kindersommer.html)
since 2012	Camera operator for *Es werde Licht - humanistisch fernsehen*, OKTO (www.eswerdelicht.tv)

Languages

German (native), English